

N° d'Ordre : DU 1975  
EDSF : 594

**UNIVERSITÉ BLAISE PASCAL**  
U.F.R. Sciences et Technologies

**ÉCOLE DOCTORALE DES SCIENCES FONDAMENTALES**

# THÈSE

Présentée pour obtenir le grade de

**DOCTEUR D'UNIVERSITÉ**  
SPECIALITÉ : PHYSIQUE DES PARTICULES

par

**Astrid CHANTELAUZE**  
Maître ès-sciences, Master 2

**Investigation of the muon-induced background  
of the EDELWEISS-II experiment**

Soutenue publiquement le 4 novembre 2009,  
devant la commission d'examen composée de :

J.	BLÜMER	Directeur de thèse
J.	ORLOFF	Président du jury
J.	JOCHUM	Rapporteur
H.	KRAUS	Rapporteur
G.	GERBIER	Examineur



*Things change.  
They always do, it's one of the things of nature.  
Most people are afraid of change,  
but if you look at it as something you can always count on,  
then it can be a comfort.*  
Robert Kincaid

*But I will run until my feet no longer run no more  
And I will kiss until my lips no longer feel no more  
And I will love until my heart it aches  
And I will love until my heart it breaks  
And I will love until there's nothing more to live for.*  
Amy Macdonald



# Acknowledgement

I would like to thank Prof. Dr. Johannes Blümer who gave me the opportunity to come at Forschungszentrum Karlsruhe and to participate in the EDELWEISS-II project. I also would like to thank Dr. Gilles Gerbier who welcomed me at CEA/Saclay for some long stays to exchange knowledge about bolometers and muon veto and who first got me acquainted with EDELWEISS and this weird dark matter thing, when I was looking for a PhD. I also would like to thank Prof. Dr. Hans Kraus and Prof. Dr. Josef Jochum who kindly accepted to serve as referee and also Prof. Dr. Jean Orloff who coordinated the administrative PhD paperwork for the Université Blaise Pascal.

I would like to thank Klaus Eitel for his day-to-day support, advices and physics discussions and without whom this PhD would not have been so successful. Computing at IK or cabling in LSM, mad-driving to conference or missing trains to Modane, I could not have imagined having a better advisor.

I would like to thank anyone from the EDELWEISS collaboration, whose discussions helped me to progress in my thesis or who participated to create a lively and nice atmosphere in meetings. I would especially like to thank Eric Armengaud, Jules Gascon, Alex, Alex B., Maryvonne, Corinne, Véronique, Bernard, Xavier and of course Silvia.

I would like to give a special thank to Markus, who had been the best office mate one can imagine. I would also like to thank the EDELWEISS Karlsruhe crew: Holger K., Holger N. and Valentin. We did not have as awesome adventures as we had when the group was only 2 and a half people, but it was great to work with you, guys. I would like to thank the European smala at FZK: Fabiana, Ioana, Sven, Florian, Paolo and others and RISE and ISAPP students, who make life lighter, always ready to party. I would also like to thank heartily R.B. et F.K., anonymous but supportive people about my PhD work and my future.

Sans vous, la vie serait drôlement moins bien, alors je remercie mon frère Hervé et mes meilleurs amis Cath, Claire, MarieNo et Yann. Je tiens aussi à remercier Maty et Romy pour la formidable semaine passée chez eux dans les Alpes pendant la rédaction du Chapitre 3. Par contre, je remercie moins les vaches et leur cloche. Plus sérieusement, j'aimerais remercier mes parents Elisabeth et Bernard qui m'ont toujours soutenue et qui m'ont laissée libre de développer mes projets, même quand cela impliquait de partir loin. Et je tiens à remercier mon parrain Christian sans qui rien n'aurait commencé, s'il ne m'avait emmenée, il y a 15 ans de ça, à une réunion des Astronomes Amateurs d'Auvergne.

Et enfin, je remercie Julien. Pour sa patience, pour son énergie, pour sa cuisine, pour son soutien, pour les mots bleus et pas que ceux qu'on dit avec les yeux. I would also like to add to the interested whom that I've written the main and only paper worth publishing in my physics life. I can switch name now.



# Contents

<b>1</b>	<b>The Dark Matter problem</b>	<b>3</b>
1.1	Cosmological Framework . . . . .	4
1.2	Evidence at Scales of Galaxies . . . . .	5
1.2.1	Spiral Galaxies . . . . .	5
1.2.2	Elliptical Galaxies . . . . .	7
1.3	Clusters of Galaxies . . . . .	7
1.4	Gravitational Lensing . . . . .	9
1.5	Studies of the Early Universe . . . . .	10
1.5.1	Big Bang Nucleosynthesis . . . . .	10
1.5.2	The Cosmic Microwave Background Radiation . . . . .	14
1.6	Observations of Type Ia Supernovae . . . . .	17
1.7	Large-scale Structure Formation . . . . .	17
1.8	Dark Matter particle candidates . . . . .	20
1.8.1	Axions . . . . .	23
1.8.2	WIMPs . . . . .	24
<b>2</b>	<b>Detecting the WIMP</b>	<b>29</b>
2.1	High energy collider production . . . . .	29
2.2	Indirect detection . . . . .	30
2.2.1	Gamma ray searches . . . . .	30
2.2.2	Neutrino detectors . . . . .	32
2.2.3	Antimatter detection . . . . .	33
2.2.4	WMAP haze . . . . .	34
2.3	Direct detection . . . . .	34
2.3.1	WIMP elastic scattering . . . . .	34
2.3.2	Spin-independent scattering . . . . .	35
2.3.3	Spin-dependent scattering . . . . .	36
2.3.4	Event rate . . . . .	37
2.3.5	Background suppression techniques . . . . .	39
2.3.6	Current experiments . . . . .	41
2.3.7	The DAMA claim . . . . .	43
<b>3</b>	<b>The EDELWEISS-II experiment</b>	<b>47</b>
3.1	Bolometers . . . . .	47
3.1.1	Ionization channel . . . . .	49
3.1.2	Heat channel . . . . .	52
3.1.3	Case of: Germanium NbSi bolometer . . . . .	55
3.1.4	Case of: Interdigitised bolometer . . . . .	55
3.1.5	Event-by-event discrimination . . . . .	58
3.1.6	Bolometer conventions . . . . .	60
3.1.7	Data acquisition . . . . .	61
3.1.8	Online monitoring . . . . .	64

3.2	EDELWEISS-II cryostat and shielding . . . . .	66
3.2.1	Reversed cryostat . . . . .	66
3.2.2	Lead and polyethylene shielding . . . . .	66
3.3	Muon veto system . . . . .	67
3.3.1	Mechanical setup . . . . .	68
3.3.2	Data acquisition . . . . .	70
3.3.3	Online monitoring . . . . .	72
3.4	Neutron counters . . . . .	74
3.4.1	Ambient neutron counter . . . . .	74
3.4.2	Muon-induced neutron counter . . . . .	75
3.5	Results of EDELWEISS-I . . . . .	76
<b>4</b>	<b>Muon detection</b>	<b>81</b>
4.1	Muon veto conventions . . . . .	81
4.2	Life time of the muon veto . . . . .	83
4.3	Muon rate . . . . .	84
4.4	Mean muon energy deposit per module . . . . .	87
4.5	Tracking muon candidates . . . . .	88
4.5.1	Position of the event along the module axis . . . . .	88
4.5.2	Through going muon candidates . . . . .	90
<b>5</b>	<b>Analysis of Run 8</b>	<b>95</b>
5.1	Status of the experiment . . . . .	95
5.2	Muon veto data . . . . .	97
5.3	Bolometer data . . . . .	99
5.4	Coincidences between the muon veto and the bolometers . . . . .	104
5.4.1	Definition of coincidence region and rates . . . . .	105
5.4.2	Identification of the coincidence events . . . . .	109
5.4.3	Discussion: Comparison with the pure bolometer analysis and position of the peak . . . . .	114
5.5	Summary . . . . .	116
<b>6</b>	<b>Analysis of Run 10</b>	<b>119</b>
6.1	Status of the experiment . . . . .	119
6.2	Muon veto data . . . . .	121
6.3	Bolometer data . . . . .	123
6.4	Coincidences between the muon veto and the bolometers . . . . .	129
6.4.1	Definition of coincidence region and rates . . . . .	129
6.4.2	Identification of the coincidence events . . . . .	133
6.5	Summary and conclusion . . . . .	133
<b>A</b>	<b>Parameters of Run 8</b>	<b>139</b>
A.1	Resolution parameters . . . . .	139
A.2	Figure of merit . . . . .	139
A.3	List of events in the coincident region . . . . .	139
<b>B</b>	<b>Parameters of Run 10</b>	<b>143</b>
B.1	Calibration factor of conversion . . . . .	143
B.2	Adaptative threshold . . . . .	143
B.3	Resolution parameters . . . . .	143

---

B.4	List of events in the coincident region . . . . .	145
<b>C</b>	<b>Definition of the bolometer timing</b>	<b>149</b>
C.1	Time variables from the ntp . . . . .	150
C.2	Time variables from the analysis . . . . .	150
C.3	An example for Run 8 . . . . .	152
C.4	An example for Run 10 . . . . .	154
C.5	Conclusion . . . . .	154
<b>Bibliography</b>		<b>157</b>



# List of Figures

1.1	Rotation curves of the spiral galaxy M33 . . . . .	6
1.2	Snapshots of the simulation of two equal mass spiral galaxies merging into a single elliptical galaxy . . . . .	8
1.3	Comparison of measured and predicted velocity dispersion profiles . . . . .	8
1.4	Galaxy Cluster Abell 2218 with Giant Luminous Arcs and many arclets . . . . .	9
1.5	Comparison between the dispersion velocities of the galaxies as obtained by X-ray measurements against those as obtained from weak lensing . . . . .	11
1.6	Mass-to-light ratio as a function of scale . . . . .	11
1.7	Hubble diagram of distance <i>vs.</i> velocity by the Hubble Space Telescope Key Project . . . . .	12
1.8	Light element abundances as predicted by the standard model of big-bang nucleosynthesis . . . . .	13
1.9	Spectrum of the Cosmic Microwave Background as measured by the FIRAS instrument on board of the COBE satellite . . . . .	15
1.10	North and South full sky maps of the temperature fluctuations of the Cosmic Microwave Background as from five years of WMAP data . . . . .	15
1.11	Temperature power spectrum of primary CMB anisotropies as estimated from WMAP 5-year data . . . . .	16
1.12	The normalized matter $\Omega_m$ versus the energy density $\Omega_\Lambda$ for three independent sets of observations: High-redshift supernovae, galaxy cluster surveys and cosmic microwave background . . . . .	18
1.13	Projected distribution of the galaxies measured by the 2dFGRS team . . . . .	21
1.14	Sloan Digital Sky Survey (SDSS) galaxy power spectrum . . . . .	21
1.15	The bullet cluster passing through another cluster . . . . .	23
1.16	Evolution of the WIMP's comoving number density as function of temperature in the early Universe. . . . .	26
2.1	“First light” image of the gamma ray sky from the Fermi Gamma-ray Space Telescope . . . . .	32
2.2	Main detection techniques to track a WIMP signal . . . . .	40
2.3	The DAMA claim . . . . .	44
3.1	Schematic overview of an EDELWEISS heat and ionization Germanium detector . . . . .	49
3.2	Example of filtered pulses for the ionization from the center electrode and for the heat channel in a Germanium bolometer . . . . .	51
3.3	The EDELWEISS Germanium bolometers: Standard and NbSi . . . . .	54
3.4	The EDELWEISS-II Germanium bolometers: Interdigitised and Fiducial Interdigitised . . . . .	56
3.5	Configuration of bolometers during the physics Run 8 . . . . .	62
3.6	Configuration of bolometers during the physics Run 10 . . . . .	62
3.7	Configuration of bolometers during the physics Run 12 . . . . .	63

3.8	Examples of plots from the online monitoring of bolometers . . . . .	65
3.9	Pictures of the cryostat of the EDELWEISS-II experiment . . . . .	67
3.10	Schematic view of the passive shielding, the mechanical construction and the muon veto detector of EDELWEISS-II . . . . .	69
3.11	Muon veto system of EDELWEISS-II . . . . .	69
3.12	Electronic chain of the muon veto system . . . . .	71
3.13	Muon veto monitoring wesite . . . . .	73
3.14	Schematic of the side view of the muon-induced neutron counter . . .	75
3.15	EDELWEISS-I results . . . . .	77
3.16	Current and expected limits from various direct Dark Matter search experiments . . . . .	79
4.1	Energy deposit in the North side of the Top module #4 . . . . .	83
4.2	Life time of the muon veto during three years of data acquisition . . .	84
4.3	Muon candidate rates of the Top and North side in coincidence with the lower level . . . . .	85
4.4	Simulated total energy deposit and relative contribution of gammas, electrons and muons . . . . .	86
4.5	Time difference of the TDCs from both ends of a module in coinci- dence with the other level per sets of modules per size . . . . .	91
4.6	Time difference within the neighboring module $n + 1$ versus the time difference within module $n$ of a level, further in coincidence with the other level of the veto system . . . . .	92
4.7	Time difference of through going muon candidates . . . . .	93
5.1	Run 8 - Electronic chain of the bolometers and distribution of the time over the EDELWEISS-II experiment . . . . .	96
5.2	Run 8 - Rate of the muon veto per 8-hour file . . . . .	98
5.3	Run 8 - Timeline of the veto events . . . . .	98
5.4	Run 8 - Time difference of consecutive muon veto events . . . . .	99
5.5	Run 8 - 3-D visualization of the selected bolometers for the muon veto-bolometer coincidence analysis . . . . .	100
5.6	Run 8 - Shift applied to reconstruct the time stamp of $s1$ and of $s3$ to correspond to this of $s2$ . . . . .	102
5.7	Run 8 - Time difference of the events which are in coincidence between the three sets of bolometers . . . . .	102
5.8	Run 8 - Quality of the bolometer system events . . . . .	104
5.9	Run 8 - Muon veto-bolometer events in coincidence . . . . .	106
5.10	Run 8 - Muon veto-bolometer events in coincidence at high heat en- ergy $E_H > 6.5$ MeV . . . . .	106
5.11	Run 8 - Muon veto-bolometer events in coincidence with $multi_{\text{veto}} > 3$	107
5.12	Run 8 - Geant-4 simulation of muon-induced Germanium hits . . . . .	109
5.13	Run 8 - Q-plot of events in coincidence with $E_R < 250$ keV inside and outside the coincidence time interval $\Delta t_{\text{coinc}} \in (+15, +35)$ ms . . . . .	111
5.14	Run 8 - 3-D visualization of the four coincidence events in the region $E_R < 250$ keV in the nuclear recoil band in $\Delta t_{\text{coinc}} \in (+15, +35)$ ms .	112
5.15	Run 8 - Examples of coincidence events in the region $E_R \geq 250$ keV in $\Delta t_{\text{coinc}} \in (+15, +35)$ ms in 3-D visualization . . . . .	113

5.16	Run 8 - Q-plot on different energy scales and plot of the multiplicity of events in coincidence with $E_R \geq 250$ keV inside the coincidence time interval $\Delta t_{\text{coinc}} \in (+15, +35)$ ms . . . . .	115
6.1	Run 10 - Electronic chain of the bolometers and distribution of the time over the EDELWEISS-II experiment . . . . .	120
6.2	Run 10 - Rate of the muon veto per 8-hour file . . . . .	122
6.3	Run 10 - Timeline and time difference of consecutive muon veto events	122
6.4	Run 10 - 3-D visualization of the selected bolometers for the muon veto-bolometer coincidence analysis . . . . .	125
6.5	Run 10 - Biplot of the heat channel versus the sum of the ionization channels from guard and center from $s1$ , $s2$ and $s3$ . . . . .	127
6.6	Run 10 - Time difference of coincidences between $s1-s2$ and $s1-s3$ . .	128
6.7	Run 10 - Muon veto-bolometer events in coincidence per data set $s1$ , $s2$ , $s3$ . . . . .	128
6.8	Run 10 - Quality of the bolometer system events . . . . .	129
6.9	Run 10 - Muon veto-bolometer events in coincidence . . . . .	130
6.10	Run 10 - Muon veto-bolometer events in coincidence with $multi_{\text{veto}} > 3130$	
6.11	Run 10 - Muon veto-bolometer events in coincidence at high heat energy $E_H > 6.5$ MeV . . . . .	131
6.12	Run 10 - Q-plot of events in coincidence with $E_H < 250$ keV inside the coincidence time interval $\Delta t_{\text{coinc}} \in (-15, +5)$ ms . . . . .	135
6.13	Run 10 - Q-plot on different energy scales and plot of the multiplicity of events in coincidence with $E_H \geq 250$ keV inside the coincidence time interval $\Delta t_{\text{coinc}} \in (-15, +5)$ ms . . . . .	136
C.1	Schematic of the signals induced in different sub-systems by a coincidence event in the EDELWEISS-II experiment . . . . .	155



# List of Tables

1.1	Spectrum of particles predicted by the Minimal Supersymmetric Standard Model . . . . .	25
1.2	The cosmological parameters as estimated by the three year data set from the WMAP experiment . . . . .	28
3.1	Data structure of the muon veto electronic . . . . .	71
4.1	Comparison of the rates of muon candidates and simulation for rates of muon candidates in different sides of the upper level . . . . .	87
4.2	Mean muon energy deposit (simulation and experimental) . . . . .	89
5.1	Run 8 - Bolometer status . . . . .	100
5.2	Run 8 - Measured and extrapolated rate of accidental coincidences . .	108
5.3	Run 8 - Events at $E_R < 250$ keV and $E_R \geq 250$ keV in the coincidence region . . . . .	108
5.4	Run 8 - Evaluation of the coincidence interval . . . . .	108
5.5	Run 8 - Number of events outside and inside the coincidence interval $\Delta t = (+15, +35)$ ms in 4 different regions defined by the conditions $E_R \geq 50$ keV or $E_R < 50$ keV and $Q \geq 0.6$ or $Q < 0.6$ . . . . .	110
5.6	Run 8 - Summary of the results for the muon veto-bolometer coincidence analysis . . . . .	117
6.1	Run 10 - Bolometer status . . . . .	124
6.2	Run 10 - Evaluation of the coincidence interval . . . . .	131
6.3	Run 10 - Measured and extrapolated rate of accidental coincidences .	132
6.4	Run 10 - Events at $E_R < 250$ keV and $E_R \geq 250$ keV in the coincidence regions . . . . .	132
6.5	Run 10 - Summary of the results for the muon veto-bolometer coincidence analysis . . . . .	134
A.1	Run 8 - Resolutions of heat and ionization channels per bolometer during calibration and physics runs . . . . .	140
A.2	Run 8 - Figure of merit per bolometer . . . . .	140
A.3	Run 8 - Short list of parameters of coincidence events at $E_R < 250$ keV	141
A.4	Run 8 - Short list of parameters of coincidence events at $E_R \geq 250$ keV	142
B.1	Run 10 - Calibration conversion table of heat and ionization channels per bolometer . . . . .	144
B.2	Run 10 - Mean adaptative threshold on heat channel per bolometer .	144
B.3	Run 10 - Resolutions of heat and ionization channels per bolometer during calibration and physics runs . . . . .	145
B.4	Run 10 - Short list of parameters of coincidence events at $E_H < 250$ keV	146
B.5	Run 10 - Short list of parameters of coincidence events at $E_R \geq 250$ keV	147

C.1	Time variables from the ntp files . . . . .	150
C.2	Useful time variables for the heat channel . . . . .	151
C.3	Useful time variables for the ionization channel . . . . .	151
C.4	Time variables from the analysis files . . . . .	151

# Introduction

SINCE COPERNICUS AND GALILEO suggested that the Earth is not the center of the universe, the human race slowly slides away the cosmic significance. At first, we were not the center of the Solar system, and then the Sun just became another star in the Milky Way. We are not even in the center of our galaxy, a galaxy which is nothing but special, one among others. And now, we are told that we are not even made of the same content as most of the universe, which is predominantly made of darkness.

Detailed investigations of the cosmic microwave background radiation, galaxy surveys as well as measurement of distant supernovae, as reviewed in Chapter 1, leads to derive a cosmological concordance model in which the most prominent contribution to the cosmological energy density comes from the cosmological constant  $\Lambda$  or often called Dark Energy. Ordinary matter would only contribute to 4 %, whereas the second biggest fraction would consist of Dark Matter.

The favorable dark matter candidate is in the form of weakly interacting massive particles, so-called WIMPs. The expected properties of this candidate are discussed in Chapter 2, as well as the different possibilities of detection: Direct detection in underground experiments, or indirect detection of their products, in space-based experiments. Prospects for producing WIMPs at future high-energy colliders are also discussed.

The direct detection EDELWEISS (Expérience pour DEtecter Les Wimps En SIte Souterrain) experiment, see Chapter 3, situated in the Modane Underground Laboratory uses monocrystals of Germanium at a working temperature of  $T \sim 20$  mK, so-called bolometers. Such a configuration allows reading out an energy deposit in two distinct channels, the heat channel and the ionization channel. Whereas the heat channel reflects the total energy deposit, the amount of ionization strongly depends on the particle type, which permits a strong suppression of radioactive background. However, nuclear recoils induced by neutrons manifest a background source which can mimic in its heat-to-ionization ratio a scattering process of a WIMP off a Germanium nucleus. Neutrons, therefore, have to be discriminated by other experimental means. Sources for neutrons are radioactivity in the detector material and its surroundings as well as cosmic muons entering the detector environment.

Though, there is a reduction of the cosmic muon flux by the rock overburden of more than  $10^6$  compared to sea level, neutrons produced in deep inelastic scattering (DIS) of cosmic muons are the most prominent background in the upcoming second generation experiments searching directly for Dark Matter. The identification of muons in the vicinity of the Germanium detectors allows a significant suppression of this background source and hence an improvement in experimental sensitivity. The group at Forschungszentrum Karlsruhe and Universität Karlsruhe built and operates an active muon veto system, see Chapter 3, which properties in terms of muon detection are developed in Chapter 4. Muon veto-bolometer coincidences analysis results are presented for two physics runs of 2007 and 2008 in Chapter 5 and Chapter 6.



# 1

## The Dark Matter problem

### Contents

- 1.1 Cosmological Framework
- 1.2 Evidence at Scales of Galaxies
- 1.3 Clusters of Galaxies
- 1.4 Gravitational Lensing
- 1.5 Studies of the Early Universe
- 1.6 Observations of Type Ia Supernovae
- 1.7 Large-scale Structure Formation
- 1.8 Dark Matter particle candidates

*Make things as simple as possible,  
but not simpler.*

A. Einstein.

1

**W**HAT IS THE WORLD MADE OF? What is the Universe made of? How did the Universe evolve? These questions have always raised a great enthusiasm in science and philosophy throughout ages. Today, these questions are not going to be solved any sooner or faster, but the technology is more on our side than ever. With the most state-of-the-art telescopes, we look up at the sky watching the electromagnetic spectrum to try to understand the cosmos. And with our most powerful microscopes, *i.e.* particle accelerators, we look down into matter to understand how it has formed and what it is made of.

Big-bang conditions are recreated in laboratory with the use of particle accelerators to search for new phenomena that will improve our understanding of particle physics, and then yield to a better understanding of the cosmos. The Dark Matter problem is a good example of the interplay between particle physics and cosmology into what has become today Astroparticle physics.

California, 1933. The Swiss astronomer Fritz Zwicky [1] reported the observation that the galaxies of the Coma cluster move faster than expected. Taking into account the sole luminosity of the cluster, *i.e.* taking into account the only sort of particles we know, to deduce its mass, the cluster should have moved slower than observed. During the last 70 years, this observation has only undergone a small correction and still holds today. Vast observations from scales of galaxies ( $\lesssim 100$  kpc) to clusters of galaxies (hundreds of Mpc), have the same problem: The mass that shines falls short in accounting for the gravitational effect. As a solution, Zwicky proposed that there should be a non-luminous matter component that was later referred to as “Dark Matter”.

In this chapter a brief introduction to the motivation for dark matter is reviewed, attempting to answer a simple question: Why has something invisible become an accepted part of modern astrophysics?

## 1.1 Cosmological Framework

The current cosmological picture is based on two (seemingly reasonable) assumptions:

- **Universal Isotropy:** The position of the Earth (or Milky Way) is assumed to be not atypical in the Universe. Consequently, the observed isotropy (on large scales) leads to the conclusion that the Universe must appear to be isotropic from any arbitrary location. This in fact requires the Universe to be homogeneous.
- **The Equivalence Principle:** The laws of physics (as expressed within special relativity) are assumed to hold in all local inertial frames.

The resulting metric must then obey the following form

$$ds^2 = -dt^2 + a(t)^2 \left[ d\chi^2 + \Sigma^2(\chi) d\Omega^2 \right] \quad (1.1)$$

known as the Robertson-Walker metric. In the above equation  $\chi$  is a dimensionless radial coordinate,  $d\Omega$  is an infinitesimal solid angle element, and  $a$  is a scaling factor.  $\Sigma$  may be either  $\sin(\chi)$  describing a closed, spheroidal universe, or  $\sinh(\chi)$  describing an open, hyperboloid universe with a radius of curvature  $a$ . In the limit of  $\chi \rightarrow 0$  or  $a \rightarrow \infty$ ,  $\Sigma(\chi)$  reduces to  $\chi$  giving a flat, Euclidean universe.

To consider the evolution in time of the scale factor,  $a$ , a specific theory of gravitation must be invoked. General Relativity yields the following two equations:

$$H(t)^2 \equiv \left( \frac{1}{a} \frac{da}{dt} \right)^2 = \frac{8\pi G}{3} \rho + \frac{\Lambda}{3} - \frac{k}{a^2} \quad (1.2)$$

$$\frac{1}{a} \frac{d^2 a}{dt^2} = -\frac{4\pi G}{3} (\rho + 3p) + \frac{\Lambda}{3} \quad (1.3)$$

where  $H(t)$  is the expansion rate of the universe,  $G$  is the Newtonian gravitational constant,  $\Lambda$  is the cosmological constant, and  $k = -1$  for an open infinite universe,  $k = 0$  for a flat infinite universe,  $k = +1$  for a closed and finite universe.  $\rho$  and  $p$  represent the density and pressure of the Universe's constituents.

Defining

$$\Omega_m \equiv \frac{8\pi G \rho_0}{3H_0^2} \quad (1.4)$$

$$\Omega_k \equiv \frac{-k}{a_0^2 H_0^2} \quad (1.5)$$

$$\Omega_\Lambda \equiv \frac{\Lambda}{3H_0^2} \quad (1.6)$$

as the normalized densities of the matter, curvature and cosmological constant terms, where the 0 subscript denotes present day values, Equation 1.2 reduces to:

$$\Omega_{\text{tot}} = \Omega_m + \Omega_k + \Omega_\Lambda = 1 \quad (1.7)$$

for a flat universe (which also means  $\Omega_k = 0$ ). For a Universe dominated by non-relativistic matter in the recent past, Equation 1.2 can be recast as

$$\left(\frac{H}{H_0}\right)^2 = \Omega_m \left(\frac{a_0}{a}\right)^3 + \Omega_k \left(\frac{a_0}{a}\right)^2 + \Omega_\Lambda \quad (1.8)$$

The time evolution of the scale parameter is then fully determined if three independent parameters, *e.g.*  $H_0$ ,  $\Omega_m$ , and  $\Omega_\Lambda$ , can be measured. However, it can be seen that for small values of  $a$  the matter density dominates the expansion of the Universe, while for large values of  $a$  a non-zero cosmological constant drives the expansion.

This model, called  $\Lambda$ CDM model as an abbreviation for Lambda-Cold Dark Matter [21], has formed from the convergence of many independent investigations. It is the simplest known model that is in general agreement with the observed phenomena, such as those described in the Sections 1.2–1.7.  $\Lambda$  stands for a now dominating contribution to the overall energy content by  $\Omega_\Lambda$ , which is a dark energy term that allows for the current accelerating expansion of the universe. Cold dark matter is the model where the dark matter is explained as being cold, *i.e.* non relativistic at the epoch of radiation-matter equality, possibly non-baryonic, dissipationless (can not cool by radiating photons) and collisionless (*i.e.* the dark matter particles interact with each other and other particles very weakly or even only through gravity). The characteristics of the dark matter are discussed in Section 1.8 and the detection techniques for the favorable candidate, the Weakly Interactive Massive Particle (WIMP) (*cf.* Section 1.8.2), are described in Chapter 2.

## 1.2 Evidence at Scales of Galaxies

This section presents the evidence from galaxy dynamics both for spiral and elliptical galaxies. Evidence of Dark Matter halos from galaxies was first presented about 30 years ago when V. Rubin and W.K. Ford [2] measured the rotation curves of the outermost stars of the Andromeda galaxy.

### 1.2.1 Spiral Galaxies

Spiral galaxies have billions of stars. A spiral galaxy such as our own consists of a central bright bulge surrounded by a rotating disk of younger stars. They correspond to about 80% of light galaxies in areas of low density, while in core areas of galaxy clusters they are very rare, about 10%. Measurements of the galactic rotation speed as a function of radius have now been conducted for many spiral galaxies. Assuming that the stars in the spiral galaxy have a circular orbit around the center of the galaxy, we can calculate the rotation velocity by equating the gravitational and centrifugal forces using Newtonian dynamics as

$$F = \frac{GmM}{r_s^2} = \frac{mv^2}{r_s} \quad (1.9)$$

where  $M$  is the mass contained by the orbit of radius  $r_s$ . Therefore, the velocity of the star would be

$$v(r_s) = \sqrt{\frac{GM}{r_s}} \quad (1.10)$$

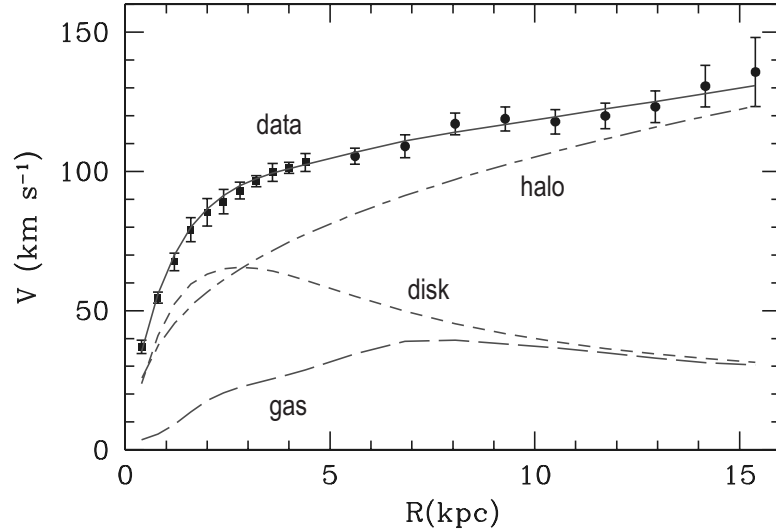


Figure 1.1: *M33* rotation curve (points) compared with the best fit model (continuous line). One expect the rotation curve to follow the contribution of the stellar disk (short dashed line) where is concentrated most of the known visible matter. However, the halo contribution (dash-dotted line) is dominant after  $\sim 5$  kpc, and the halo does not correspond to the gas contribution (long dashed line). Thus, it indicates the existence of a large amount of an unknown non-visible mass extending around the center of the galaxy. Figure adapted from [3].

where the mass of the bulge can be written as  $M = \rho V \sim \rho r_s^3$ . Therefore, the velocity of a star as a function of the distance from the center of the galaxy can be written as  $v(r) \sim r$  for  $r < r_s$  and  $v(r) \sim r^{1/2}$  for  $r > r_s$ . However, the observations of spiral galaxy rotation curves, for example for the spiral galaxy M33 shown in Figure 1.1, show that  $v(r) \approx \text{constant}$  after  $\sim 5$  kpc, which means that  $M \sim r$ . Or in other words, it indicates the existence of a large amount of mass extending around the center of the galaxy and far beyond the visible region, but this mass by itself is optically invisible.

The rotation curves constitute some of the most robust evidence for dark matter halos in galaxies and can be fit to a Universal Rotation Curve (URC). The URC is determined only by the galaxy luminosity ( $\sim$  velocity) as a function of radius [4].

Moreover, Navarro, Frenk and White [5] (hereafter NFW) have done N-body simulations to predict the structure of dark matter halos on kiloparsec and sub-kiloparsec scales, where it can be compared to observations of galactic dynamics. They have found a universal structure between the density profiles of dark matter halos of galaxies. This structure is independent of mass and of the value of cosmological parameters. The universal density profile proposed by NFW can be written as

$$\frac{\rho(r)}{\rho_{\text{crit}}} = \frac{\delta_c}{(r/r_s)(1 + r/r_s)^2} \quad (1.11)$$

and describes the density profile of *any* halo with only two parameters, a characteristic density contrast  $\delta_c$ , and a scale radius  $r_s$ .

### 1.2.2 Elliptical Galaxies

Elliptical galaxies are believed to originate from major mergers of spiral galaxies. Therefore, they should also contain dark matter halos [6, 7, 8, 9]. The initial galaxies had each a spherical bulge and a thin exponential disk, as well as a thin gaseous disk and a spherical NFW dark matter halo. The galaxies disturb one another to eventually collide, see Figure 1.2, and the final merger followed after 2-3 Gyr. The similarity between the observed and simulated velocity dispersion profiles is shown in Figure 1.3. It shows that the simulations, including certain amounts of dark matter, reproduce the observed velocity dispersion profiles.

## 1.3 Clusters of Galaxies

Galaxy clusters, the largest bound structures in our universe, are also an excellent laboratory in which to observe the effects of unseen matter. They are formed from the gravitational collapse of relatively large regions of several Mpc of the early universe. Clusters may be more representative of the average composition of the universe than smaller structures. They contain hundreds to thousands of galaxies to form a total mass up to  $10^{15}$  solar masses. One of the first confrontations between luminous and gravitational matter came from the analysis of the Coma cluster by Zwicky in 1937 [12]. Zwicky used the Doppler effect to measure the line-of-sight velocities of galaxies in the Coma cluster. He found that the measurement of the velocities and distance of the galaxies yield an estimate on the gravitational mass of the cluster. Based upon the galaxies' velocity dispersion and an estimate of the cluster's size based upon its apparent angular size and a (very inaccurate) value of Hubble's constant, Zwicky inferred a mass-to-light ratio of several hundred using the virial theorem. The virial theorem for a central force states

$$2\langle E_{\text{kin}} \rangle + \langle E_{\text{pot}} \rangle = 0 \quad (1.12)$$

However, the use of the virial theorem implies that the system is closed and in mechanical equilibrium. If we write the kinetic energy of  $N$  galaxies in a cluster by  $\langle E_{\text{kin}} \rangle = \frac{1}{2}N\langle mv^2 \rangle$  then the potential energy of the cluster would be

$$\langle E_{\text{pot}} \rangle = -\frac{1}{2}GN(N-1)\frac{\langle m^2 \rangle}{\langle r \rangle} \quad (1.13)$$

hence the dynamic mass is given by

$$M \simeq \frac{2\langle r \rangle \langle v^2 \rangle}{G} \quad (1.14)$$

where for large number of galaxies  $(N-1) \simeq N$ , and  $N\langle m \rangle = M$ . Then, an estimate on the mass of the cluster  $M$  can be done measuring  $r$  and  $v$ . Zwicky's result was very crude and numerically-inaccurate, but modern calculations with better data and more sophisticated techniques support the same basic conclusion: Galaxy clusters are strongly dominated by unseen matter. Another method to estimate the mass of the cluster is the use of gravitational lensing and the Sunyaev-Zeldovich effect, which are discussed in Section 1.4 and 1.5.2 respectively. All of these methods yield a gravitational mass that is significantly higher than the luminous mass.

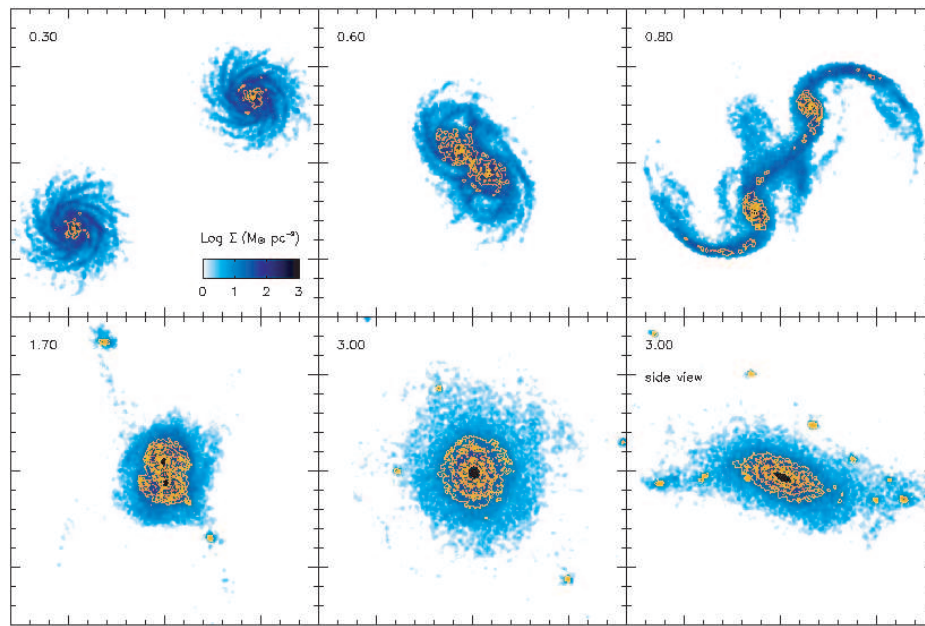


Figure 1.2: *Snapshots of the simulation of two equal mass spiral galaxies merging into a single elliptical galaxy, in Gyr after big bang. The lighter zones in the central regions of the galaxies represents the young stars formed during the simulation, while the remaining smooth greyscale are the old stars. Figure from [10].*

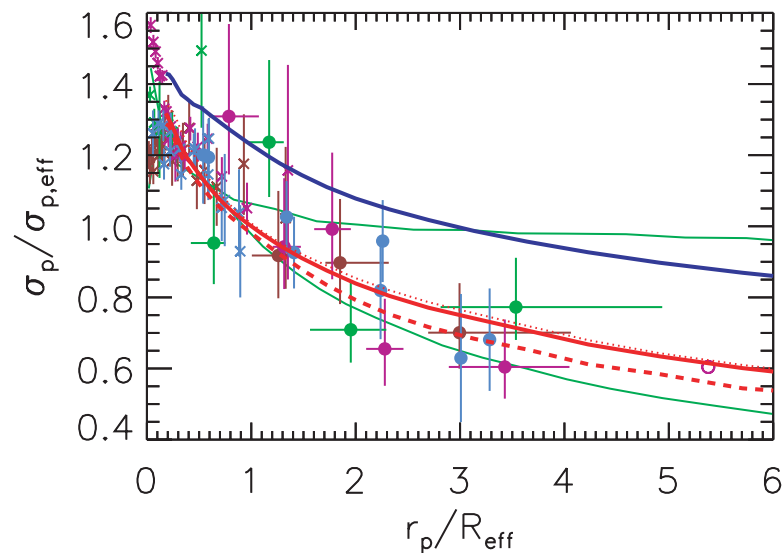


Figure 1.3: *Comparison of measured and predicted velocity dispersion profiles. The line-of-sight velocity dispersion is shown versus the projected radius  $r_p$ , normalized to the half-projected light (mass) radius, i.e. the effective radius  $R_{\text{eff}}$ . The lower and upper thin (green) curves represent the predictions of Romanowsky et al. [11], respectively without and with dark matter. Dark matter are the upper solid (blue) curve, stars are the lower curves (old, young and 'all' are dotted, dashed and solid). Figure adapted from [10].*

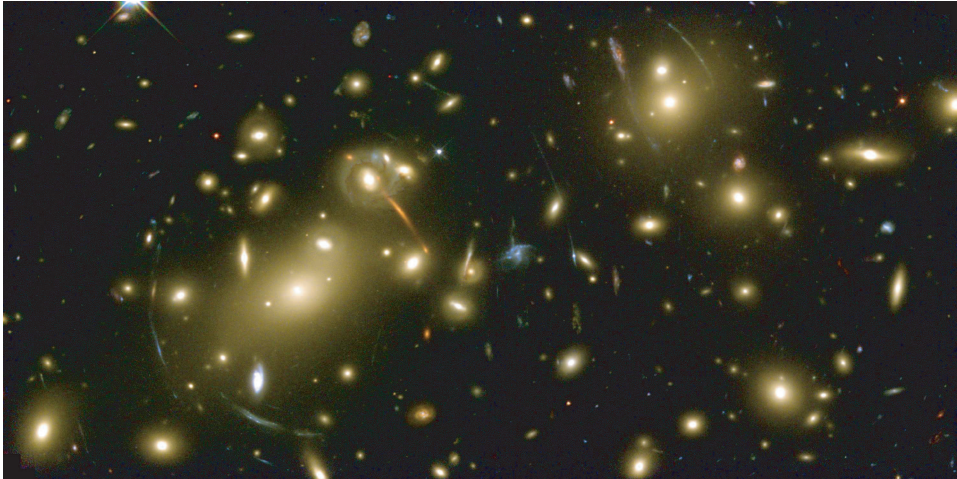


Figure 1.4: *Galaxy Cluster Abell 2218 with Giant Luminous Arcs and many arclets. Light from distant galaxies passes by the gravitational mass of the cluster and gets bent, creating a lensing effect. Picture from the Hubble Space Telescope [16].*

## 1.4 Gravitational Lensing

Cluster masses can also be inferred from their effect upon light rays from distant sources [13, 14]. Einstein deduced with his theory of General Relativity that the deflection angle  $\alpha$  of a light ray passing at a distance  $r$  from a body of mass  $M$  is

$$\alpha = \frac{4GM}{c^2} \frac{1}{r} \quad (1.15)$$

where  $G$  is the gravitational constant and  $c$  is the velocity of light. More advanced observations have measured and confirmed the predicted value to better than 0.02% [15]. Today, gravitational lensing – the deflection of light by matter – is a widely used astrophysical tool that is used, for example, to estimate the amount of dark matter in clusters.

The gravitational potential well of a galaxy cluster or other massive object thus acts as a complex lens, distorting the images of more distant galaxies or quasars. Thus, weak gravitational lensing is a method that can be used to measure the mass of a body knowing these distortions. The images of background galaxies that are near a cluster of galaxies are deflected away from the cluster, becoming enlarged while preserving the surface brightness and distorted tangentially to the center of the potential, also known as gravitational shear. Figure 1.4 shows the galaxy cluster Abell 2218 with luminous arcs of the background galaxy. The gravitational shear effects are used to measure the mass of the structure(s) causing the lensing. This technique does not assume anything about the dynamical state of the mass and therefore it is particularly robust when applied to a system with an unknown dynamical perturbation. Dahle et al. [17] found, for a sample of 40 clusters, a mass-to-light ratio derived using gravitational lensing of  $M/L = 377 \pm 17$ .

Since many of the clusters in the sample studied by Dahle et al. have also been studied using X-ray temperature measurements or galaxy velocity dispersion measurements, it is possible to compare the weak lensing measurements to the velocity dispersion measurements. It is done by fitting an isothermal sphere model to the measured shear profiles around the clusters. Figure 1.5 shows the comparison between the dispersion velocities of the galaxies as obtained by X-ray measurements

against the dispersion velocities as obtained from weak lensing. There is a good agreement between these two methods that further supports the dark matter hypothesis of Zwicky. Figure 1.6 shows the inferred mass-to-light ratio of many systems that have scales ranging from galaxies ( $10^{-2}$  Mpc) to superclusters (100 Mpc). Bahcall et al. [20] have found that mass-to-light ratio remains flat at  $\Omega_m = 0.3$  after  $R \simeq 1$  Mpc.

## 1.5 Studies of the Early Universe

In the previous sections, astrophysical evidence for Dark Matter has been described from scales of galaxies to clusters. In the following sections are described the studies of the early universe, starting with big-bang nucleosynthesis, which sheds light on the nature of dark matter, and following with measurements of the cosmic microwave background radiation (CMB). CMB has opened the field of precision observational cosmology and has become one of the best tools to study the composition of the universe.

The age of the Universe can be measured in a variety of different ways [21]. It can be measured by using the expansion rate and computing the time back to the big bang, by dating the oldest stars in globular clusters and by dating the radioactive elements such as  $^{238}\text{Th}$  (mean life time  $\tau = 20.27$  Gyr). All techniques yield results consistently within the range of 10 to 20 Gyr. The current best estimate is  $13.73 \pm 0.15$  Gyr [22].

The understanding of the early Universe begins with a very basic observation: Almost all galaxy spectra are red shifted. The light that we see today was emitted when the Universe was a few billion years old. Defining the Hubble constant,  $H_0 \equiv (dR/dt)/R(t_0)$  as the expansion rate of the Universe at present time, and  $q_0 \equiv -(d^2R/dt^2)/R(t_0)H_0^2 \equiv -R(t_0)\ddot{R}/\dot{R}^2$  as the deceleration parameter, which measures the rate at which the Universe is slowing down, this redshift  $z$  and the luminosity distance  $d_L$  of a galaxy can be written in power series

$$H_0 d_L = z + \frac{1}{2}(1 - q_0)z^2 + \dots \quad (1.16)$$

where  $d_L \equiv (L/4\pi F)^2$  and  $L$  being the luminosity of the object and  $F$  the measured flux. Therefore we can write

$$z = H_0 d_L + \frac{1}{2}(q_0 - 1)(H_0 d_L)^2 + \dots \quad (1.17)$$

The present day Hubble expansion rate has a value of [23]

$$H_0 = 100 \cdot h = 72 \pm 8 \text{ km}\cdot\text{sec}^{-1}\cdot\text{Mpc}^{-1} \quad (1.18)$$

$$\text{and } h = 0.73 \pm 3 \quad (1.19)$$

with  $h$  is the present day normalized Hubble expansion rate [22].

The Hubble diagram, shown in Figure 1.7, is the most direct evidence of the expansion of the Universe.

### 1.5.1 Big Bang Nucleosynthesis

To study nature on its largest scales, we turn to observations related to the early universe. Studies of big bang nucleosynthesis lead to robust and independent measurements of the baryon density of the Universe, and therefore it is a cornerstone for

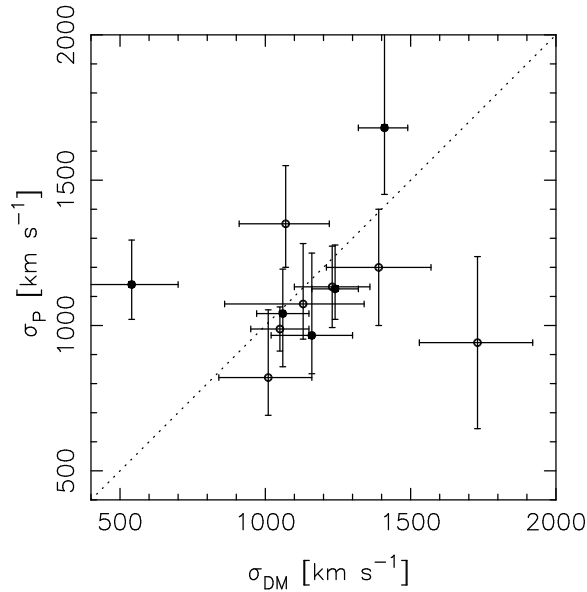


Figure 1.5: *The spectroscopically measured velocity dispersion  $\sigma_P$  from X-ray measurements vs. the dark matter velocity dispersion  $\sigma_{DM}$  from weak lensing measurements. The error bars shown are at  $1\sigma$ . The dotted line indicates a slope of one. Figure from [18].*

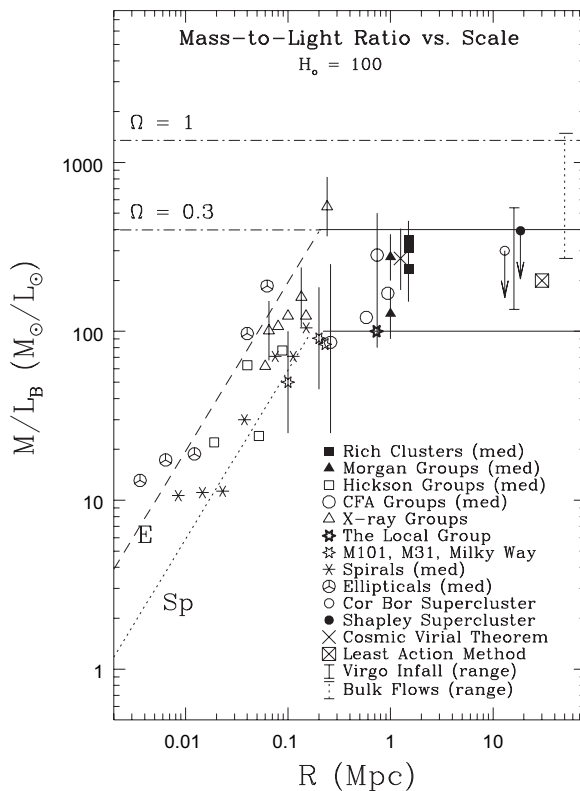


Figure 1.6: *Mass-to-light ratio as a function of scale. The horizontal dashed lines correspond to different matter densities. The mass-to-light ratios stay constant at approximately  $\Omega = 0.3$  after  $R \simeq 1$  Mpc. The plotted points for rich clusters, Morgan groups, Hickson groups, CFA groups, spiral and elliptical are median values of these samples. The plotted circles are values for the clusters studied by [17]. Figure from [18, 19, 20].*

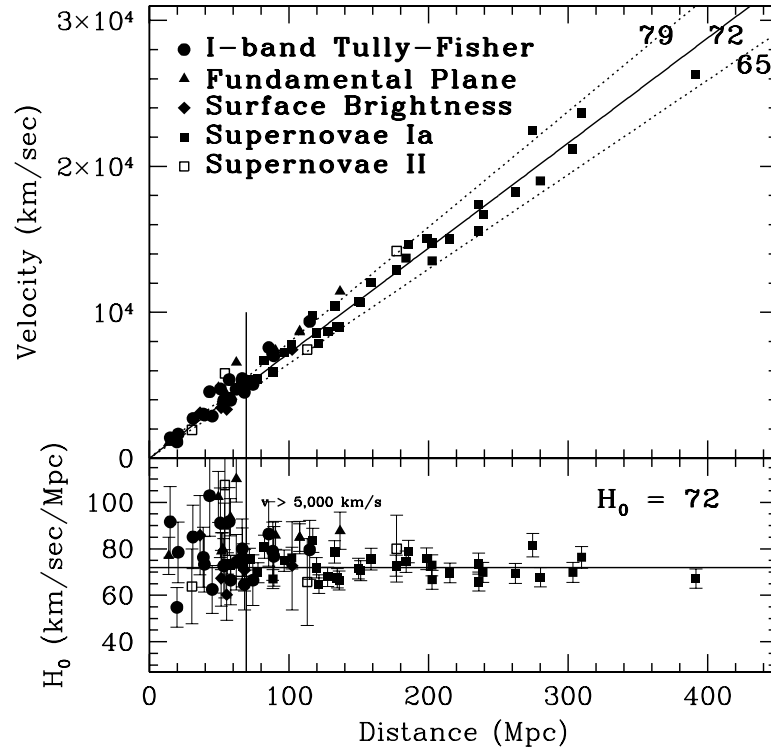


Figure 1.7: Hubble diagram of distance vs. velocity by the Hubble Space Telescope Key Project. A slope of  $H_0 = 72$  is shown with its  $\pm 10\%$  lines. The bottom box shows the Hubble constant vs. distance and the horizontal line is the best fit to data. Figure from [23].

the existence of nonbaryonic dark matter. Big bang nucleosynthesis is a nonequilibrium process that took place over the course of a few minutes in an expanding, radiation-dominated plasma with high entropy and many free neutrons [24].

The predictions of big bang nucleosynthesis for the light element abundances are shown in Figure 1.8, in which the boxes and arrows show the current estimates for the light element abundances and they are consistent with the corresponding predictions. The primordial abundances of these elements depend critically upon the conditions during the period when such fusion was possible, and in particular on the baryon-to-photon number ratio  $\eta \equiv n_b/n_\gamma \times 10^{10}$ .

At times much less than a second after the big bang, there were roughly equal numbers of electrons, positrons, neutrinos, antineutrinos and photons. The ratio of photons to nucleons, *i.e.* protons and neutrons, was more than a billion to one. The nuclei had not been formed and the ratio of neutrons and protons was unity due to the weak processes that interconvert them. At about one second, when the Universe had cooled to around  $10^{10}$  K, the weak processes were not able to keep the same number of neutrons and protons. And at the temperature of  $\sim 10^9$  K the first formation of D,  $^3\text{H}$ ,  $^3\text{He}$  and  $^4\text{He}$  took place. As the Universe continued to expand and cool, the processes maintaining equilibrium slowed down relative to the temperature evolution and, after five minutes, most neutrons were in  $^4\text{He}$  nuclei, and most protons remained free. There was also formation, in much smaller amounts, of D,  $^3\text{He}$ ,  $^7\text{Li}$  but the low density and temperature caused the elemental composition of the Universe to remain unchanged until the formation of the first stars several billion years later.

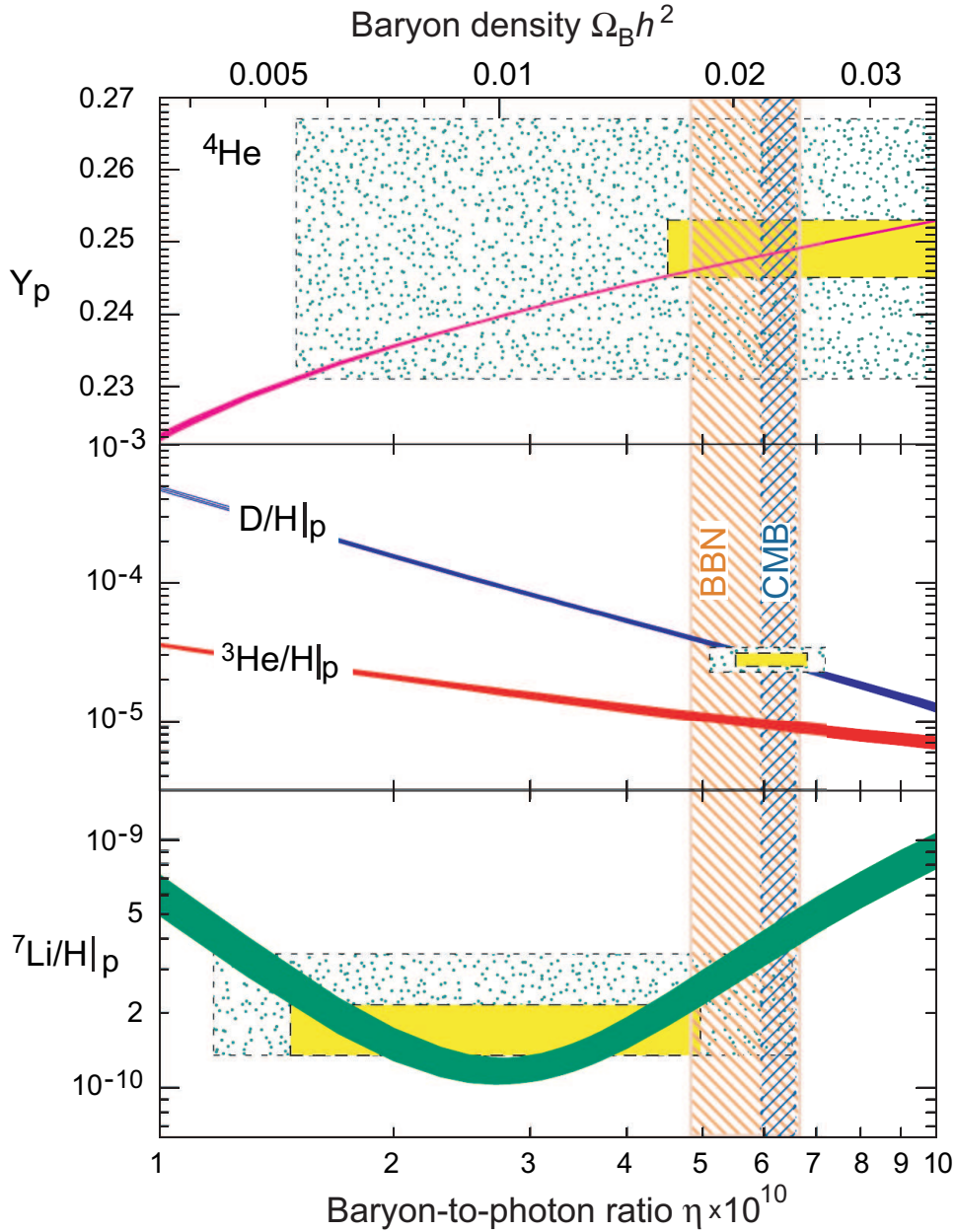


Figure 1.8: The abundances of  $^4\text{He}$ ,  $\text{D}$ ,  $^3\text{He}$ , and  $^7\text{Li}$  as predicted by the standard model of big-bang nucleosynthesis – the bands show the 95% CL range. Boxes indicate the observed light element abundances (smaller boxes:  $\pm 2\sigma$  statistical errors; larger boxes:  $\pm 2\sigma$  statistical and systematic errors). The narrow vertical band indicates the CMB measure of the cosmic baryon density, while the wider band indicates the BBN concordance range (both at 95% CL). Figure from [25].

The photon density sets the time and interval of nucleosynthesis through its control of the universe's expansion rate; given equal photon densities, a greater baryon density leads to a faster rate of fusion to  ${}^4\text{He}$  and fewer nucleons left over in  ${}^2\text{H}$  and  ${}^3\text{He}$ . Since the photon density is well-known from the microwave background's black body temperature, light element ratios thus provide an excellent "baryometer" with which to measure the abundance of ordinary matter.

Deuterium is the most powerful of these baryometers. Deuterium is a delicate nucleus, easily destroyed within stars and therefore no longer created in the modern universe. Since the deuterium abundance is sensitive to  $\eta$  and decreases with time, any measurement of deuterium yields a direct upper limit on  $\eta$ . Current deuterium measurements from quasar absorption lines [25] indicate  $4.7 \leq \eta \leq 6.5$  (95% CL), implying a modern baryon density of  $0.017 \leq \Omega_b h^2 \leq 0.024$  (95% CL), that is  $\Omega_b \simeq 0.05$ . This means that all the baryonic matter that we are made of and that we study at particle accelerators constitutes only less than 5% of the energy density of the universe.

## 1.5.2 The Cosmic Microwave Background Radiation

Nowadays, a photon is likely to travel several Hubble distances, 3700-4700 Mpc, before being scattered or absorbed. However, the expansion of the Universe implies that at earlier times, the Universe was hotter and denser.

At the early age of a temperature above  $\sim 3000$  K, the formation of stable atoms was hindered, as matter and radiation were in thermal equilibrium. Matter existed in an opaque plasma state of ionized atoms, which strongly absorbed electromagnetic radiation of all wavelengths. When the plasma cooled below the temperature of  $\sim 3000$  K, it was cool enough for Hydrogen and Helium nuclei to collect electrons and become stable atoms. Stable atoms absorb only those frequencies characteristic of those atoms or frequencies high enough to ionize them. This means the expanding universe became transparent to almost all wavelengths, at least for photons with quantum energy less than the ionization energy of the atoms. That is called the era of decoupling of matter and radiation.

If the Universe began in a hot and dense state, then it should be filled with a relic background of the last scatterings before decoupling. This remnant of the transparency point, at which the expanding universe dropped below about 3000 K, so that radiation could escape, should have the Planck black-body spectrum:

$$\int_0^\infty \frac{\nu^3 d\nu}{\exp(h\nu/kT_r) - 1} \propto T_r^4 \quad (1.20)$$

where  $T_r$  is the radiation temperature. This microwave radiation, so-called Cosmic Microwave Background (CMB), is isotropic and constant with time.

The FIRAS instrument (Far Infrared Absolute Spectrophotometer) inside the COBE satellite (COsmic Background Explorer) measured, at any angular position on the sky, the spectrum of the CMB to be an ideal blackbody up to 1 part in  $10^4$ . Figure 1.9 shows the spectrum measured by the FIRAS instrument [26].

However, the DMR instrument (Differential Microwave Radiometer) also inside COBE found for the first time that the CMB have intrinsic anisotropies at a level of a part in 100,000. Full sky maps of the CMB were created with a resolution of only  $7^\circ$ , which was the full width at half maximum (FWHM) of the beam of the DMR horn antennas. Later, the Wilkinson Microwave Anisotropy Probe (WMAP)

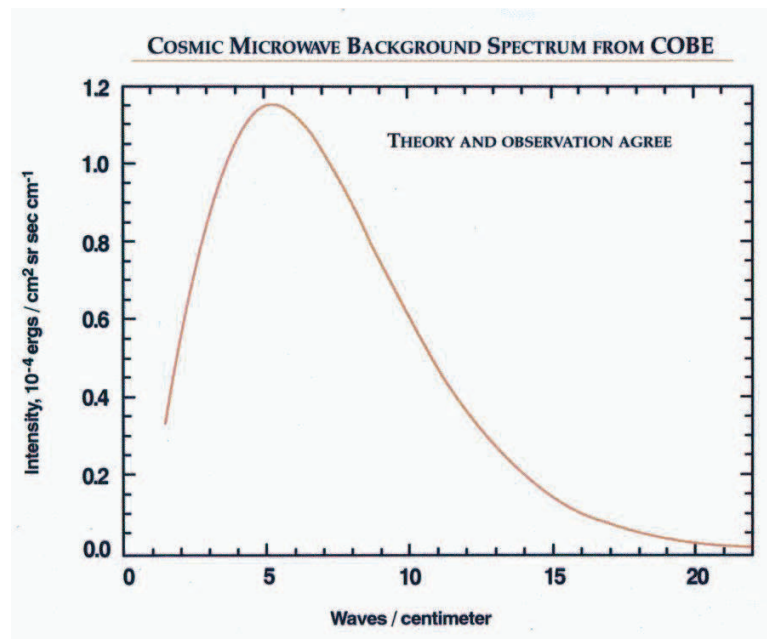


Figure 1.9: *Spectrum of the Cosmic Microwave Background as measured by the FIRAS instrument on board of the COBE satellite. The measured temperature by the COBE team was  $2.728 \pm 0.004$  K. Error bars on the measurement are smaller than the thickness of the line. Figure from [26].*

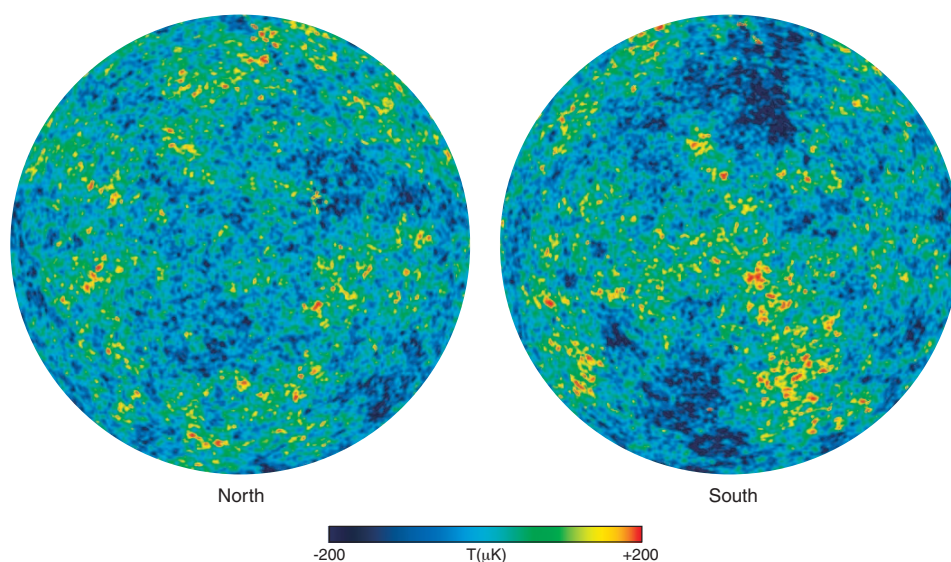


Figure 1.10: *North (left) and South (right) full sky maps of the temperature fluctuations of the Cosmic Microwave Background as from five years of WMAP data. The image reveals 13.7 billion year old temperature fluctuations (shown as color differences in a temperature range of  $\pm 200$  mK) that correspond to the seeds that grew to become the galaxies. The Galactic foreground contribution to the sky signal is minimized to provide a low-contamination image of the CMB anisotropy. Figure from [27].*

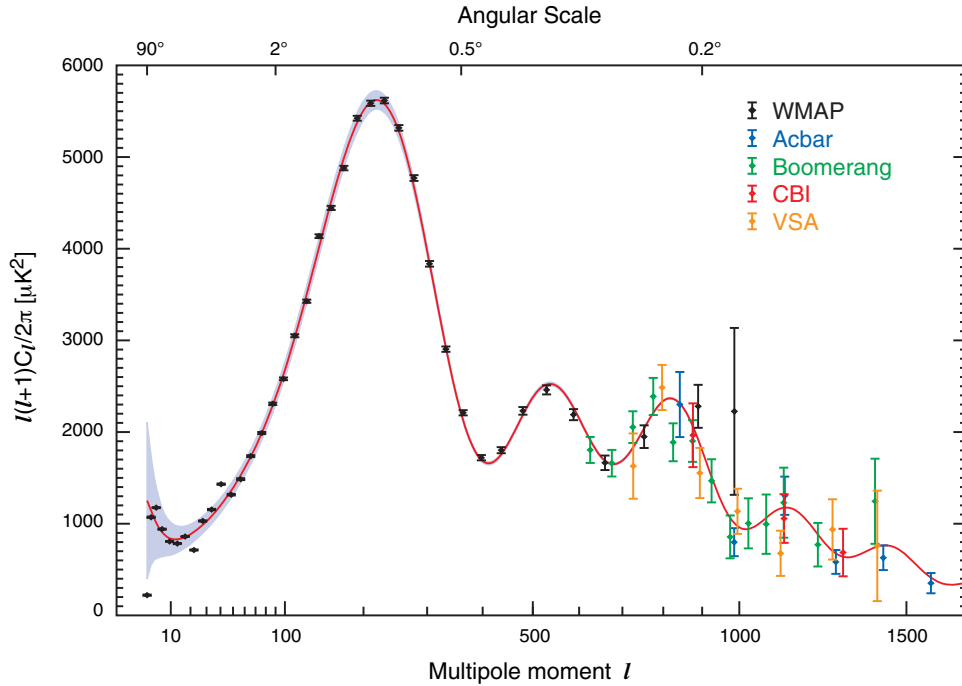


Figure 1.11: *Temperature power spectrum of primary CMB anisotropies as estimated from WMAP 5-year data. WMAP power spectrum in black and a best fit  $\Lambda$ CDM cosmology model, compared with other measurements of the CMB power spectrum such as Boomerang [28], Acbar [29], CBI [30] and VSA [31]. Figure from [27] and references therein.*

mission is designed to determine the geometry, content, and evolution of the universe via a 13 arcminute FWHM resolution full sky map of the temperature anisotropy of the CMB. Figure 1.10 shows the temperature fluctuations of the CMB anisotropy in the full sky as measured by WMAP.

The microwave background's temperature fluctuations record inhomogeneities in the photon-baryon fluid at the era of last-scattering. These inhomogeneities can be seen as incoherent acoustic waves in the photon-baryon fluid of the last-scattering surface, and the densities of baryonic and non-baryonic matter have strong effects upon these oscillations: Baryons increase the inertia of the oscillating photon-baryon fluid, while dark matter reduces the driving effect of those oscillations upon the gravitational potential. Figure 1.11 shows the CMB power spectrum as a function of multipole  $l$  from various experiments.

The position of the first peak in Figure 1.11 probes spatial geometry. The position at  $1^\circ$  means the anisotropies have at most an angular resolution of  $1^\circ$ . And to have anisotropies in today universe as large as  $1^\circ$ , the universe has to be flat:  $\Omega_k = 0$ . Thus,  $\Omega_{\text{tot}}$  corresponds exactly to  $\Omega_m + \Omega_\Lambda$  in the  $\Lambda$ CDM model. WMAP measurement leads to an experimental value of  $\Omega_{\text{tot}}$  [22]:

$$\Omega_{\text{tot}} = 1.011 \pm 12 \quad (1.21)$$

Then, the relative height of peaks in Figure 1.11 probes baryon density. Using WMAP data only, the best fit values for cosmological parameters for the flat  $\Lambda$ CDM

model [22] are

$$\Omega_m h^2 = 0.128 \pm 0.008 = 0.24 \quad h^{-2} \quad (1.22)$$

$$\Omega_b h^2 = 0.0223 \pm 0.0007 = 0.0425 \quad h^{-2} \quad (1.23)$$

The result of  $\Omega_b$  is in agreement with estimations using arguments from big bang nucleosynthesis that we have described in Section 1.5.1. The contribution of baryonic matter is very little compared with the total of matter in the universe. Approximately 85% of the matter density of the universe is thus not baryonic and therefore a natural solution is to search for undiscovered particles.

## 1.6 Observations of Type Ia Supernovae

In the late 1930's, Walter Baade, working closely with Fritz Zwicky, pointed out that supernovae were extremely promising candidates for measuring the cosmic expansion. Their peak brightness seemed to be very uniform, and they were bright enough to be seen at extremely large distances [32]. Supernovae with no Hydrogen features in their spectra are classified as type I. This class is then subdivided into types Ia and Ib, depending on the presence or absence of a silicon absorption feature at 6150 Å in the spectrum of the supernovae. A remarkable consistency between the type Ia supernovae was found, and this was further confirmed and improved when their spectra were studied in detail as they brightened and then faded. The detailed uniformity of the type Ia supernovae implies that they must have some common triggering mechanism. This uniformity provides standard spectral and light-curve templates to measure the expansion rate of the cosmos, or the Hubble constant  $H_0$  [33, 34].

The best fit to measurements of supernovae Ia implies that, at present days, the dark/vacuum energy density  $\rho_\Lambda$  is larger than the energy density associated with mass  $\rho_m c^2$ . As the universe expands, the matter density drops due to continual space being added between all matter. What is more interesting is that dark energy has a negative pressure which is distributed relatively homogeneously in space. And this negative pressure hold by the vacuum counters to the attractive gravitational effect at cosmological scale. Thus, as dark energy dominates, the universe is expanding and accelerating.

If the Universe has no large-scale curvature, as indicated by the WMAP data [22], we can conclude that about 70% of the total energy density is vacuum energy and 30% is mass [33, 34]. Figure 1.12 shows the normalized matter as a function of energy density, obtained using high-redshift supernovae, galaxy clusters, and the cosmic microwave background. This Figure also shows how all the three types of observations converge into the  $\Lambda$ CDM model where  $\Omega_\Lambda + \Omega_m = 1$ .

## 1.7 Large-scale Structure Formation

A final argument for the existence of non-baryonic dark matter comes from attempts to link our observations of the primordial universe with those of its modern configuration. We know that the cosmic microwave background shows anisotropies at the  $10^{-5}$  level, as described in Section 1.5.2. Since photons and baryons were tightly coupled at that era, this gives a snapshot of the level of baryon inhomogeneities,

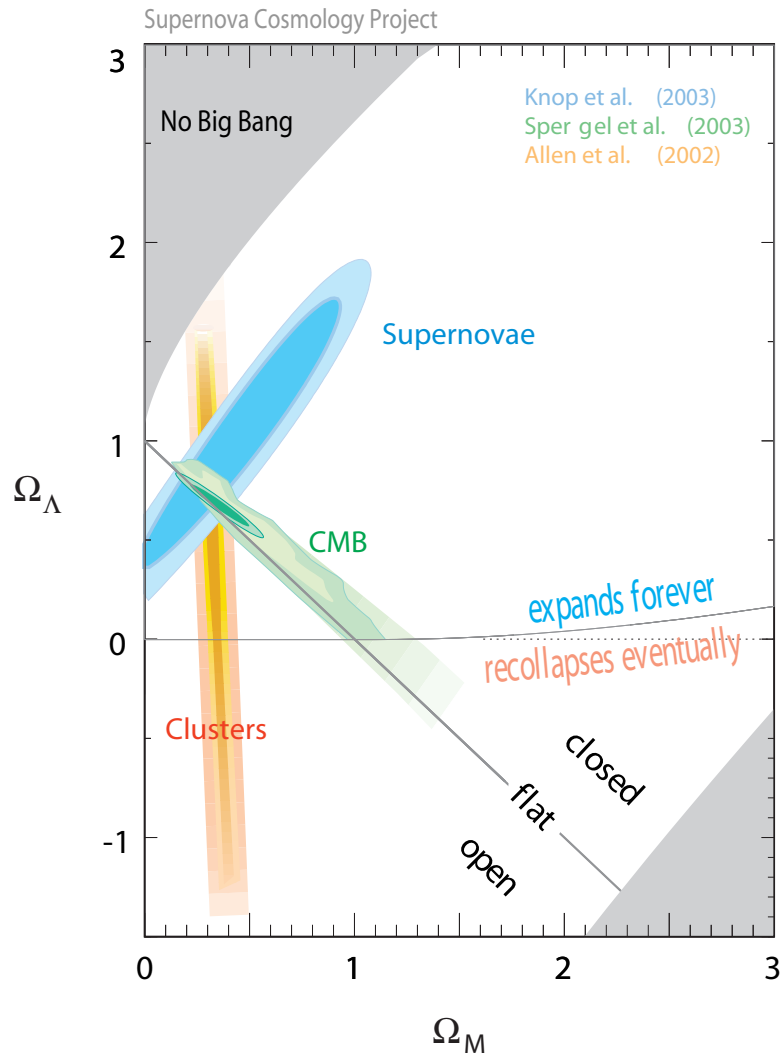


Figure 1.12: The normalized matter  $\Omega_m$  versus the energy density  $\Omega_\Lambda$  for three independent sets of observations: High-redshift supernovae, galaxy cluster surveys and cosmic microwave background. These three independent observations converge near  $\Omega_m = 0.25$  and  $\Omega_\Lambda = 0.75$ . The black diagonal with a negative slope indicates the expectation from a flat cosmos ( $\Omega_\Lambda + \Omega_m = 1$ , with a dominant contribution of  $\Omega_\Lambda$ , thus  $\Lambda$ CDM model). The small yellow contour in this region indicates how SNAP, a satellite experiment, is expected to deliver on the sensitivity to this parameters. Figure from [36].

when the universe was only a few hundred thousand years old ( $z \approx 1000$ ). Since then the scale factor  $a$  of the universe has grown by a factor of  $\sim 1000$ , and today we see a wealth of galaxies and galaxy clusters. Bright galaxies are visible back to redshifts of at least  $z \approx 7.6$  [35], indicating that large structures formed in the first few hundred million years after the Big Bang.

The 2dF Galaxy Redshift Survey (2dFGRS team) measured the redshifts of about a quarter million galaxies in order to have a detailed picture of the galaxy population and of its large-scale structure in the nearby Universe. The 2dFGRS team has measured the galaxy power spectrum  $P(k)$  on scales up to a few hundred Mpc. It has filled the gap between the small scales where  $P(k)$  is known from previous galaxy redshift surveys and the largest scales where  $P(k)$  is well-determined by observations of the cosmic microwave background anisotropies [37]. Figure 1.13 shows the projected distribution of the galaxies measured by the 2dFGRS team and provides the first detection of the redshift-space clustering anisotropy on large scales. Using only the WMAP data, a prediction can be made of the amplitude and shape of the power spectrum of matter.

The large-scale structure of the Universe is sensitive to the energy and matter it contains. A model that can predict measurements of the large-scale structure of the nearby Universe needs the energy and matter content of the Universe as input parameters. In the standard theory of structure formation, the structures we see in the universe today originate from quantum fluctuations in the local energy density of the inflation field. Regions with slightly higher energy densities than their surroundings collapsed under their own gravity, eventually forming the seeds of galaxies and galaxy clusters. These over- and under-densities are characterized by the density contrast field

$$\delta(\vec{x}, t) \equiv \frac{\rho(\vec{x}, t) - \bar{\rho}(t)}{\bar{\rho}(t)} \quad (1.24)$$

where  $\bar{\rho}(t)$  is the universe's mean energy density at time  $t$ . In practice, it is most convenient to consider the statistical distribution of the density contrast at different length scales, given by the power spectrum of  $\delta$ :

$$\delta(\vec{k}, t) \equiv \frac{1}{(2\pi)^{3/2}} \int \delta(\vec{x}, t) e^{-i\vec{k}\vec{x}} d^3\vec{x} \quad (1.25)$$

For small density contrasts ( $\delta \ll 1$ ), we can solve for the evolution of  $\delta(\vec{k}, t)$  using linear perturbation theory. The various values of  $\vec{k}$  decouple from one another in this regime, which lasts until  $\delta \approx 1$ . Propagation to later epochs requires numerical simulations. The full relativistic theory of gravitational collapse in an expanding universe is beyond the scope of this work; for a full discussion, *cf.* [21].

The observation of nonlinear structure at the present day demands  $\delta \gtrsim 10^{-3}$  at  $z \sim 1000$ , far greater than that observed. The small anisotropies observed in the microwave background at small scales ( $l \sim 1000$  corresponds to the scale of observed galaxy clusters) have not had time to grow into the structures we see in the modern universe. Non-baryonic cold dark matter solves this problem very neatly by decoupling the microwave background from the total matter density. When the dark matter scattering rate drops below the expansion rate of the universe, dark matter particles no longer scatter off the thermal bath efficiently and start to cool, free-stream, and then gravitationally cluster. The smooth baryon distribution seen

in the small-scale CMB anisotropies rapidly follows the larger dark matter overdensities, which had more time to grow.

The points in the Figure 1.14 show the Sloan Digital Sky Survey (SDSS) galaxy power spectrum [38] with the amplitude of the fluctuations normalized by the galaxy lensing measurements of the 2dFGRS data [39]. This Figure 1.14 shows that the  $\Lambda$ CDM model accurately predicts the large-scale properties of the matter distribution in the nearby Universe when normalized to observations at  $z \sim 1100$ , which is the scale at which the CMB was formed.

We can discriminate between *hot* and *cold* non-baryonic dark matter. A dark-matter candidate is called hot, if it was moving at relativistic speeds at the time galaxies form, when the horizon first contained about  $10^{12} M_{\odot}$ . If it was moving at nonrelativistic speeds at that time, then it is called *cold* dark-matter.

Studies with N-body simulations of structure formation in a Universe dominated by hot dark-matter cannot reproduce the observed structure [40]. The hypothetical nonbaryonic cold-dark-matter candidates are particles that have not yet been discovered. The leading nonbaryonic cold-dark-matter candidates are axions and weakly interacting massive particles (WIMPs) and are going to be discussed in the next section.



## 1.8 Dark Matter particle candidates

Our current model of dark matter embraces four main facts about its nature:

- Dark matter is predominantly **non-baryonic** in nature. This is supported by evidence from nucleosynthesis and the microwave background, as described in previous sections.
- Non-baryonic dark matter is also **very weakly interacting**. This is supported by upper limits on self-interaction from astrophysical observations, *e.g.* the Bullet cluster, see after, and terrestrial searches.
- Dark matter must be essentially **stable**, or at least have a life time long compared to the present age of the universe.
- Finally, dark matter is apparently **cold**, read slow-moving. More precisely, a cold dark matter candidate must be non-relativistic throughout the formation of largescale structure.

Beyond these four conditions, very little about dark matter is known. In particular, the identity of the particle(s) which accounts for it remains a mystery.

There is a wide range of possible dark-matter candidates. Their mass could be as small as that of axions with  $m = 10^{-5} \text{ eV} = 9 \times 10^{-72} M_{\odot}$  to black holes of mass  $m = 10^4 M_{\odot}$ . First, there are historical candidates, which do not fit one of the condition above. Baryonic candidates, for example, are massive compact halo objects (MACHOs) [41, 42, 43] such as brown dwarfs (balls of H and He with masses below  $0.08 M_{\odot}$ ), jupiters (masses near  $0.001 M_{\odot}$ ), stellar back-hole remnants (masses near  $100 M_{\odot}$ ) and neutron stars. But astronomical surveys for MACHOs indicate that these objects cannot make up all the amount of dark matter that is needed in our galactic halo. The EROS collaboration [44] has placed an upper limit on the

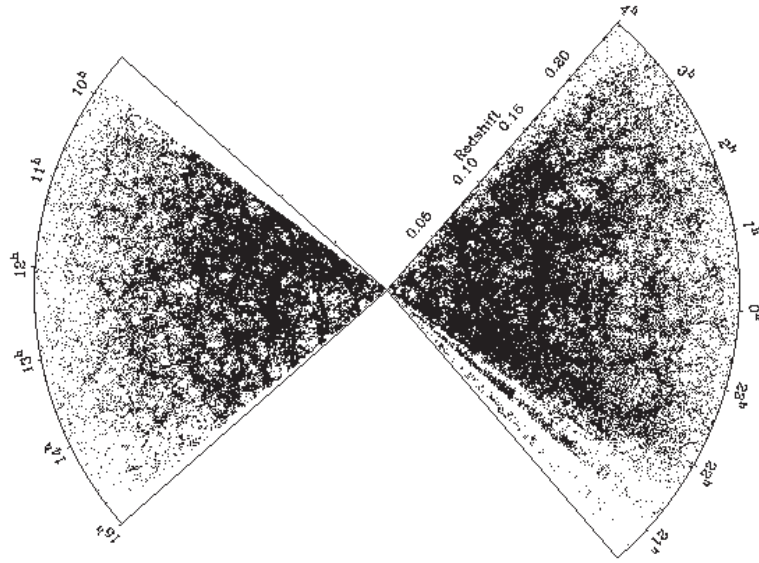


Figure 1.13: *The 2dF Galaxy Redshift Survey (2dFGRS) projected distribution of galaxies (about 250,000) as a function of redshift. The 2dFGRS has provided the first clear detection the redshift-space clustering anisotropy on large scales. Figure from [37].*

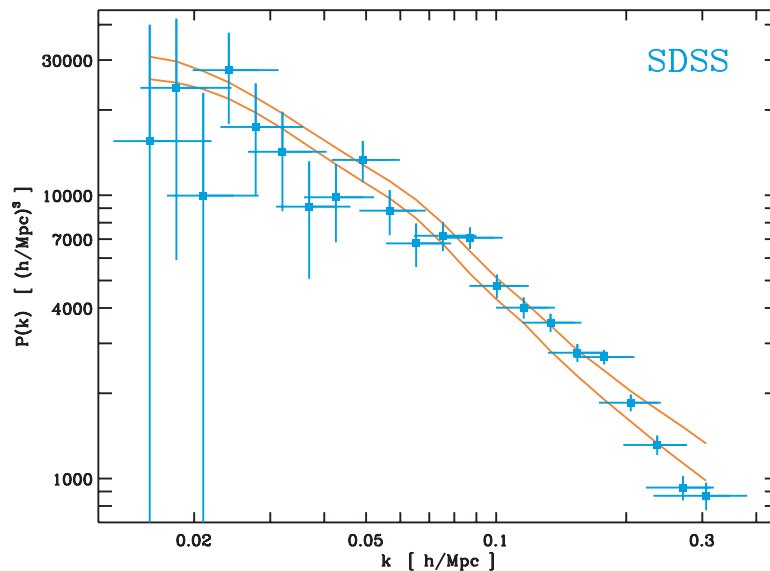


Figure 1.14: *The mass power spectrum predicted with a range of parameters consistent with the WMAP-only parameters (shown as the band with a width determined by the 68% confidence interval) compared with the mass power spectrum as measured by the SDSS galaxy survey [38]. The figure shows that the  $\Lambda$ CDM model, when normalized to observations at  $z \sim 1100$ , accurately predicts the large-scale properties of the matter distribution in the nearby Universe. Figure adapted from [22].*

halo fraction  $f < 0.2$  (95% CL) for objects in the mass range between  $2 \cdot 10^{-7} M_{\odot}$  and  $1 M_{\odot}$ , dismissing earlier claims of a significant halo fraction of compact objects by the MACHO collaboration [45]. Compact objects within this mass range cannot account for more than 25% of a standard halo.

Another example of candidates for Dark Matter are the light neutrinos. They are hot dark matter (HDM), rather than cold, and then would have substantial effects on the formation of large-scale structure. The investigation of the still open role of neutrino HDM in the evolution of large scale structure is one of the main motivations for the proposed next-generation tritium  $\beta$  decay experiment KATRIN [46], which is designed to measure the absolute mass of the electron neutrino with sub-eV sensitivity (a discovery potential down to about  $0.35 \text{ eV}/c^2$ ). Correspondingly, KATRIN would be sensitive to a neutrino HDM contribution down to a value of  $\Omega_{\nu} = 0.025$ , thus significantly constraining the role of neutrino HDM in structure formation. With its sensitivity, KATRIN will either detect a neutrino mass of cosmological relevance or exclude (in case of a negative result) any significant contribution of neutrinos to the universe's matter content and structures.

There is also the possibility that the dark matter problem could be explained by non-Newtonian gravity models, in which the strength of the gravitational force decreases less rapidly than  $r^{-2}$  at large distance. However, gravitational lensing by the colliding galaxy clusters 1E0657-56 is a convincing dynamic system giving theory-independent proof of dark matter dominance at large scales [47]. It is made up of two subclusters in the process of merging, which appear to have passed directly through one another, shown in Figure 1.15. The space between galaxies is large enough so that the galaxies in each subcluster have passed through the other subcluster without collisions. The intracluster medium (ICM), on the other hand, has been shocked and heated by the interaction, and remains concentrated closer to the collision point. This sets the stage for a very beautiful test of the dark matter model: If the mass of the clusters is dominated by collisionless dark matter, then weak lensing will show two centers near the concentrations of galaxies. If, on the other hand, the mass is mainly in the ICM, with the high mass-to-light ratio of galaxies and clusters explained by modified gravity, then weak lensing should show one center, near the gas. When this system is studied and mapped with weak lensing, it shows that the lensing mass is concentrated in the two regions containing the galaxies, rather than in the two clouds of stripped gas which contain most of the baryonic mass and significantly separated from the highest intensity of X-rays [47, 48]. Weakly interacting dark matter would move together with the galaxies, and therefore explains the observed system. The bullet cluster of 1E0657-56 is not a sole example, more cases have been studied since, see [49, 50, 51]. And all agree to a non-baryonic cold dark matter. These observations present a difficulty for alternative gravity theories.

Nonetheless, there is a strong consensus in the astrophysics community that non-baryonic cold dark matter best explains the wealth of cosmological observations available to us, and is a real component of the universe in which we live. The leading nonbaryonic cold-dark-matter candidates are axions and weakly interacting massive particles (WIMPs). The following sections describe the properties of these two main particle candidates for cold dark matter.

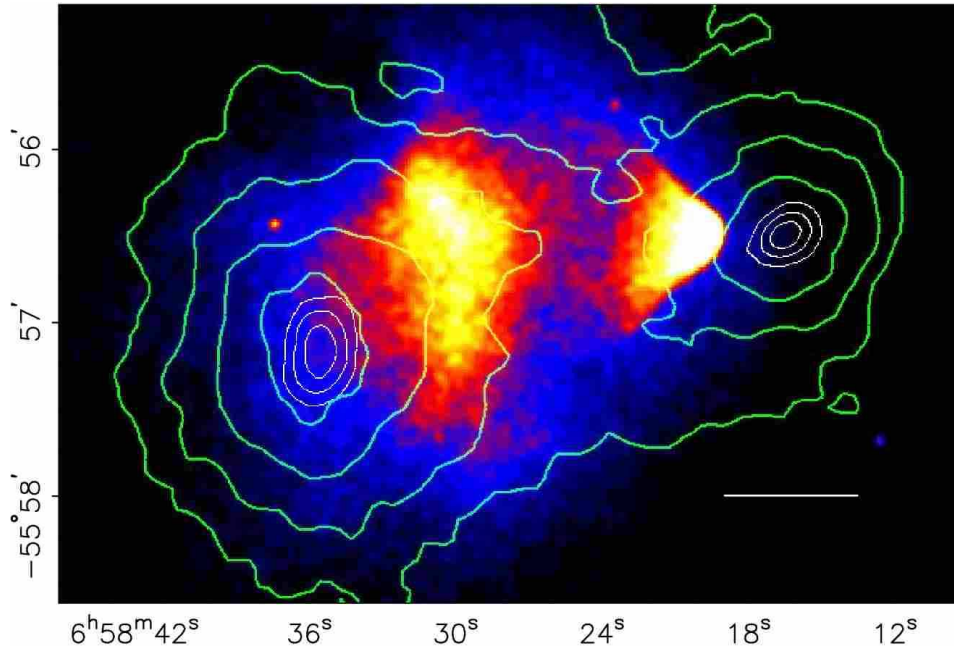


Figure 1.15: *The bullet cluster (right) passing through the cluster on the left. The hot gas that is stripped off the colliding clusters is colored in red-yellow. The white bar indicates 200 kpc at the distance of the cluster. Shown in green contours are the levels surfaces of gravitational lensing convergence. The two peaks of this do not coincide with those of the gas X-ray image which is mostly all the known mass, but point in the direction of the galaxy concentrations. Figure from [48].*

### 1.8.1 Axions

The axion is a dark matter particle candidate that arises as a consequence of a theory by Peccei and Quinn [52] that proposes a dynamical mechanism to conserve strong  $CP$  symmetry. This symmetry, according to the Standard Model of particle physics, should be violated and therefore produce a neutron electric dipole moment 10 orders of magnitude larger than the current experimental lower limit of  $10^{-26}$  ecm [53]. Therefore, this upper limit requires a mechanism to preserve  $CP$  symmetry.

The axion is described by the spontaneous symmetry breaking scale of the Peccei-Quinn symmetry,  $f_a$ , and is related to the mass,  $m_a$ , as

$$m_a \simeq 6\mu\text{eV} \left( \frac{10^{12}\text{GeV}}{f_a} \right) \quad (1.26)$$

and the axion-photon coupling  $g_{a\gamma\gamma}$  is defined as

$$g_{a\gamma\gamma} \equiv \frac{\alpha g_\gamma}{\pi f_a} \quad (1.27)$$

where  $\alpha$  is the fine structure constant and  $g_\gamma$  is a dimensionless model dependent coupling parameter.

Axions may be created in the early universe as a non-relativistic condensate through the “misalignment” mechanism [54]. The average axion relic density is

$$\Omega_a h^2 \sim \left( \frac{f_a}{10^{12}\text{GeV}} \right)^{7/6} \quad (1.28)$$

where  $h$  is the current Hubble parameter in units of 100 km/s/Mpc. This implies that an axion of mass  $m_a \approx 10 \mu\text{eV}$  can constitute the universe's dark matter, while lighter axions are cosmologically excluded. Note that axions are in general produced non-thermally, and so are cold (non-relativistic) dark matter despite their very low masses.

At present times, we expect axions to be gravitationally bound in our own galaxy, forming a large halo of particles moving with relative velocities of order  $10^{-3}c$  [55]. For an axion to be gravitationally bound to our galaxy means they are moving slower than the escape velocity of  $2 \cdot 10^{-3}c$ . In principle, a flux of axions traversing a microwave cavity permeated by a strong magnetic field could be converted to radio frequency (RF) photons when the cavity is tuned to the resonant frequency determined by their mass. This detection principle, based on the axion-photon coupling, was first proposed by Pierre Sikivie in 1983 [56] and has marked the way to the most sensitive searches to date of the cosmological axions. The leading such experiment at  $\mu\text{eV}$  masses is ADMX [57], which has already begun to probe cosmologically-interesting axion masses.

## 1.8.2 WIMPs

Although the composition of dark matter remains unknown, one natural candidate is a weakly interacting, massive particle. These so-called WIMPs have several advantages: They arise naturally in supersymmetric models and as Kaluza-Klein particles in theories with extra dimensions; they are cold, as required for structure formation; and they can be generated as a thermal relic of the big bang, with approximately the required density.

### SUSY motivations

The Standard Model (SM) of particle physics has been tested since the 1970's over a wide range of experiments and energies that have supported its validity. Nevertheless, it remains to find the Higgs boson, a missing ingredient of the Standard Model. And the SM suffers from some unnaturalness, such as the hierarchy problem, for which the Supersymmetry introduces a solution. Solving the hierarchy problem means that Supersymmetry explains how the weak and gravitational scales are determined. Supersymmetry was not conceived or crafted to solve the hierarchy problem in particular, but it did. Furthermore, Supersymmetry can explain one of the central problems of the standard model of how electroweak symmetry is broken. If Supersymmetry is relevant to electroweak-symmetry breaking, it should manifest in physics near the electroweak scale,  $E \lesssim O(\text{TeV})$ .

And this is quite remarkable: With no detailed input from particle physics, cosmological data points to a possible connection between dark matter and the weak nuclear force. Any stable, massive (GeV-TeV) particle interacting through the weak nuclear force would quite naturally be the observed dark matter. Such a particle would also satisfy constraints from large-scale structure observations, since it is cold enough to steer structure formation.

The feature that gives rise to a supersymmetric cold dark matter candidate is  $R$ -parity:

$$R = -1^{3(B-L)+2S} \quad (1.29)$$

Usual particles		SUSY partners	
Symbol	Name	Symbol	Name
$q = u, c, t$	up quarks	$\tilde{q}_u^1, \dots, \tilde{q}_u^6$	up squarks
$q = d, s, b$	down quarks	$\tilde{q}_d^1, \dots, \tilde{q}_d^6$	down squarks
$l = e, \mu, \tau$	leptons	$\tilde{l}_1, \dots, \tilde{l}_6$	sleptons
$\nu$	neutrinos	$\tilde{\nu}_1, \dots, \tilde{\nu}_3$	sneutrinos
$g$	gluons	$\tilde{g}$	gluinos
$W^\pm$	W boson	$\tilde{\chi}_1^\pm, \tilde{\chi}_2^\pm$	charginos
$H^\pm$	charged Higgs		
$\gamma$	photon		
$Z^0$	Z boson		
$h^0$ ( $H_2^0$ )	light scalar Higgs	$\tilde{\chi}_1^0, \dots, \tilde{\chi}_4^0$	neutralinos
$H^0$ ( $H_1^0$ )	heavy scalar Higgs		
$A^0$ ( $H_3^0, P_0$ )	pseudoscalar Higgs		

Table 1.1: *Spectrum of particles predicted by the Minimal Supersymmetric Standard Model (MSSM) [58]. The neutralino is most probably the lightest supersymmetric particle in the MSSM and a good WIMP candidate [59].*

where  $B$ ,  $L$  and  $S$  are the baryon, lepton and spin number operators respectively. When  $R = 1$  this corresponds to ordinary particles and if  $R = -1$  to the corresponding superpartners. If  $R$ -parity is broken, it means that there are no selection rules to prevent the decay of the supersymmetric particles in the spectrum with masses of order a few GeV or heavier. The scale of  $R$ -parity violation regulates the strength of baryon- and lepton-number violation processes, which have not been observed in nature so far and severe constraints on  $R$ -parity violation arise. For each fermionic degree of freedom, there is a bosonic degree of freedom and vice-versa, causing an extension of the particle spectrum (see Table 1.1). For example, quarks have spin  $\frac{1}{2}$ , and the supersymmetric partners would be the squarks and would be bosons. The neutralino is most probably the lightest supersymmetric particle in the MSSM (Minimal Supersymmetric Standard Model) [59]. The neutralino would be stable and weakly interacting and therefore a good WIMP dark-matter candidate.

### Expected WIMP relic density

If a WIMP-like stable particle ( $\chi$ ) would have existed in thermal equilibrium and in abundance in the early Universe, when the temperature of the expanding Universe exceeds the mass  $m_\chi$  of the particle, then it could have a significant cosmological abundance today [60, 61, 62]. A simple estimate of the cosmological abundance of WIMPs can be found in the review paper by Jungman, Kamionkowski and Griest [58] and has been first proposed by Lee and Weinberg [63].

Suppose that in the early Universe, in addition to the known particles of the standard model, there is a new stable or long-lived  $\chi$ . The equilibrium abundance would be conserved by the annihilation of the particle with its antiparticle into lighter particles and also through the inverse reaction  $\chi\bar{\chi} \leftrightarrow l\bar{l}$ . In thermal equilibrium, the number density of  $\chi$ -particles is

$$n_\chi^{\text{eq}} = \frac{g}{(2\pi)^3} \int f(\tilde{\mathbf{p}}) d^3\tilde{p} \simeq g \left( \frac{M_\chi kT}{2\pi\hbar^2} \right) e^{-\frac{M_\chi c^2}{kT}} \quad (1.30)$$

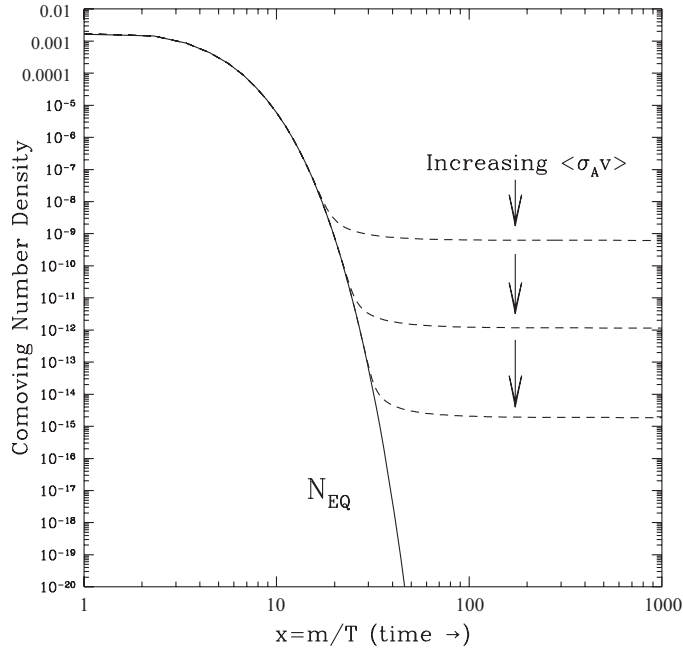


Figure 1.16: *Evolution of the WIMP's comoving number density as function of temperature (in units of the WIMP mass  $m$ ) in the early Universe. The solid curve represents the equilibrium abundance, while the dashed lines correspond to actual abundances for various choices of velocity-weighted annihilation cross section. The temperature of the freeze out occurs when the reaction rate drops below the expansion rate. Figure from [21].*

where  $g$  is the number of internal degrees of freedom of the particle and  $f(\vec{p})$  is the Fermi-Dirac or Bose-Einstein distribution. At high temperatures ( $T \gg m_\chi$ ),  $n_\chi^{\text{eq}} \propto T^3$ , so that the number of photons and WIMPs is roughly the same. As the Universe expands and cools down to a temperature below  $m_\chi$ , ( $T \ll m_\chi$ ), the WIMP density is  $n_\chi^{\text{eq}} \propto g(m_\chi T/2\pi)^{3/2} \exp(-m_\chi/T)$ , that is Boltzmann suppressed. At  $T \sim m_\chi$ , the number density of WIMPs falls exponentially, and the rate for annihilation  $\chi$ 's ( $\Gamma = \langle\sigma_A v\rangle n_\chi$ ) drops below the expansion rate,  $\Gamma \lesssim H$ . At this moment, WIMPs can no longer annihilate. The interactions, which maintained the thermal equilibrium, *freeze out*, forming a relic cosmological abundance that remains at present times [58].

The quantitative way of describing this process is done by using the Boltzmann equation, which describes the time evolution of the number density  $n_\chi(t)$  of WIMPs:

$$\frac{dn_\chi}{dt} + 3Hn_\chi = -\langle\sigma_A v\rangle((n_\chi)^2 - (n_\chi^{\text{eq}})^2) \quad (1.31)$$

where  $H = \dot{a}/a$  is the Hubble expansion rate, and  $a$  is the scale factor of the Universe. The second term on the left-hand side accounts for the expansion of the Universe. The first term in brackets on the right-hand side accounts for depletion of WIMPs due to annihilation, and the second term arises from creation of WIMPs from the inverse reaction. This equation can be derived by imposing that, in equilibrium, the rate for annihilation and creation of WIMPs is equal. Accurate calculations require a numerical solution of the Boltzmann equation, but an approximate solution for

the relic density in the relevant regime is [21, 58]

$$\Omega_\chi h^2 = \frac{s_0}{\rho_c/h^2} \left( \frac{45}{\pi g_*} \right)^{1/2} \frac{x_f}{m_{\text{Pl}}} \frac{1}{\langle \sigma v \rangle} \quad (1.32)$$

where  $s_0$  is the current entropy density of the universe,  $\rho_c$  is the critical density,  $h$  is the scaled Hubble constant ( $H_0 = 100h$  km/sec/Mpc),  $g_*$  is the number of relativistic degrees of freedom at the time the WIMP falls out of equilibrium,  $m_{\text{Pl}}$  is the Planck mass,  $x_f \approx 25^*$  and  $\langle \sigma v \rangle$  is the thermal average of the dark matter pair annihilation cross section times the relative velocity. Figure 1.16 indicates the general character of this solution. The equilibrium (solid line) and actual (dashed lines) abundances per comoving volume are plotted as a function of  $x \equiv m_\chi/T$ . The relic density is determined by the thermally-averaged annihilation cross section at decoupling. A particle with a larger annihilation cross section can remain in equilibrium slightly longer, leading to further Boltzmann-suppression and a smaller relic abundance is formed. The annihilation cross section, which depends on the kinetic energy and mass of the WIMP, produces a temperature of the freeze out to be  $T_f \simeq m_\chi/20 \ll m_\chi$ . Hence, WIMPs are moving at nonrelativistic velocities when they freeze out. The resulting density is the *relic density* of the WIMP.

Using  $\Omega_\chi = 0.2$ , we find that  $\langle \sigma v \rangle \sim 3 \cdot 10^{-26}$  cm<sup>3</sup>/s. In terms of mass, this means for example that if  $\langle \sigma v \rangle = \pi \alpha^2/8m^2^\dagger$ , then  $m \sim 100$  GeV, giving the order of magnitude for the WIMP mass.

According to the  $\Lambda$ CDM model the universe is expanding and accelerating, has a spatially flat geometry, and consists of three types of element: Normal visible matter, dark matter, and dark energy. Dark, or vacuum, energy is a repulsive force that constitutes approximately 75% of the total energy density. The usual visible matter, we deal with every day, represents less than 5% of the universe's total energy density. The final 20% of the universe's energy density is made of dark matter. The normalized densities of the total, the cosmological constant, the matter, the baryons and the dark matter, as well as the expansion rate and the age of the universe, from WMAP results, are summarized in Table 1.2.

Thus, although almost 85% of the matter in the universe is unknown and in a form never seen so far, the dark matter problem is a very real one. Its presence has been confirmed by the study of rotation curves of galaxies and clusters, gravitational lensing, cosmic microwave background and others as described in this chapter. Expectations for non-baryonic dark matter are founded principally in Big Bang nucleosynthesis calculations, which indicate that the missing mass of the universe is not likely to be baryonic.

The most favorable candidate is the non-baryonic Weakly Interactive Massive Particle (WIMP), corresponding to the lightest natural supersymmetric theory candidate, the neutralino. The WIMP's mass is expected to be of hundreds of GeV/c.

\*  $x_f = x$  at the time of the 'freeze out' which is when the rate of annihilation is equal to the cosmic expansion.

† which is the way to calculate a generic electroweak mass particle annihilating through the exchange of the electroweak gauge or Higgs bosons [65]

parameter	value
$\Omega_{\text{tot}}$	$1.011 \pm 0.012$
$\Omega_{\Lambda}$	$0.73 \pm 0.03$
$\Omega_m$	$0.128 \pm 0.008 \quad h^{-2} = 0.24$
$\Omega_b$	$0.0223 \pm 0.0007 h^{-2} = 0.0425$
$\Omega_{dm}$	$0.105 \pm 0.008 \quad h^{-2} = 0.20$
Hubble constant $H_0$	$72 \pm 8 \text{ km}\cdot\text{sec}^{-1}\cdot\text{Mpc}^{-1}$
Age of Universe $t_0$	$13.73 \pm 0.15 \text{ Gyr}$

Table 1.2: The cosmological parameters as estimated by the three year data set from the WMAP experiment [22].

To be consistent with an early-universe annihilation rate, which leaves proper relic abundances, the WIMP should have a small, but measurable, interaction cross section with ordinary matter of the order of the electro-weak scale. A nucleus interacting cross section of 10 pb would be consistent with a meaningful cosmological role for the particle.

# 2

## Detecting the WIMP

### Contents

- 2.1 High energy collider production
- 2.2 Indirect detection
- 2.3 Direct detection

*The secret is to gang up on the problem,  
rather than each other.*

Thomas Stallkamp.

THE CURRENT proposed detection techniques are reviewed in this chapter, distinguishing between three major classes of experimental signatures: Collider production of WIMPs, indirect detection of WIMP annihilation, and direct detection of WIMP scattering. The first two are discussed briefly in order to more fully describe the third, which is the focus of this dissertation, and we will also see how all these measurements could complement each other to measure the properties of the WIMP as dark matter.

2

### 2.1 High energy collider production

Particle accelerators are the traditional tools to investigate the phenomenology of new elementary particles. Hadron colliders, like the CERN's Large Hadron Collider (LHC), as well as electron-positron colliders such as the proposed International Linear Collider (ILC), will push the energy frontier of the Standard Model. These instruments are designed to characterize particle phenomena at the TeV energy scale, the regime associated with electroweak symmetry breaking. Particles with TeV scale masses, which originate in models of electroweak symmetry breaking, also have QCD color, therefore, any particle with these properties will be pair-produced at the LHC with a cross section in the tens of picobarns [64]. If dark matter is related to these new phenomena, accelerators may produce WIMPs in the laboratory and illuminate the associated theory.

Due to their small interaction cross sections, WIMPs are expected to escape particle detectors unnoticed. The primary signatures of a WIMP are thus similar to those of a neutrino: Missing energy and momentum from a particle collision. The signature of WIMPs at the LHC would be events with many hadronic jets and an imbalance of measured momentum [65]. Direct collider constraints upon the lightest neutralino or other WIMP candidates tend to be somewhat model-dependent, since the most probable WIMP-generating pathways are generally the decay chains of heavier charged or colored particles. Measurements at high-energy accelerators will then be used to determine the microscopic properties of the dark matter.

If a measurement of the supersymmetric particles is done at the LHC, this can provide the cross check for measurements from direct and indirect detection. Thus, far no absolute lower bound on the WIMP mass exists from collider constraints, but accelerator constraints generally favor masses of order 100–1000 GeV/c<sup>2</sup>.

## 2.2 Indirect detection

If the WIMP model of dark matter is correct, the same WIMP annihilation processes that determined the relic density in the early universe, *cf.* Section 1.8.2, may continue today in regions of high dark matter density. Indirect detection experiments aim to detect the annihilation products of the dark matter particles [58, 66].

The rate of WIMP annihilation is proportional to the square of the local WIMP density  $\Gamma_{\chi\chi\rightarrow X} \propto n_\chi^2$ , so the observable flux is vastly enhanced in regions of high WIMP density. The WIMP density is high in the central regions of expected dark matter halos, ranging from large galactic halos to the mini-halos of dwarf galaxies [67] or in the substructure of our own galaxy [68]. Elastic scattering may also concentrate WIMPs in the centers of massive bodies such as the Sun and the Earth, leading to enhanced annihilation there as well [69, 70].

Though the total WIMP annihilation cross section in the hot early universe is well-known from the WIMP's relic density, different annihilation processes may dominate in today's cold universe. And the annihilation rate into a specific detectable channel (e.g.  $\chi\chi \rightarrow \gamma\gamma$ ) is model-dependent. But even if these annihilation rates vary significantly between WIMP models, these quantities can be calculated precisely within a given model. In the following subsections will be discussed the WIMP annihilation through gamma ray, neutrino, antimatter and synchrotron radiation signals.

### 2.2.1 Gamma ray searches

Gamma rays are particularly promising as dark matter signatures because they are relatively easy to detect and retain their directionality over extragalactic distances [71]. In principle, a sensitive gamma ray detector may not only identify the annihilation signature of dark matter but also map its distribution in the local universe. One of the standard models, which is due to Navarro, Frenk and White (NFW) gives a density profile that peaks at the galactic center. This region has long been considered to be one of the most promising windows to search for gamma rays from dark matter annihilations. However, the understanding of astrophysical backgrounds is essential in order to understand a potential signal. Furthermore, not only is the galactic center expected to enhance the probability of detection, but any high-density objects nearby such as dwarf spheroidals [72] or other dark matter structures [73] could also enhance the rate. If the WIMP can annihilate to a two-body final state containing a photon, this process will appear as a monoenergetic gamma ray line at GeV-TeV energies. This is an ideal “smoking gun” signature of WIMP annihilation: Easily distinguishable from continuum backgrounds and difficult to mimic with conventional astrophysical processes. Unfortunately, gamma ray telescopes have generally poor resolution, making it difficult to distinguish narrow, dim features above bright continuum backgrounds. Gamma ray observatories have already yielded several excesses from the galactic signal which may be interpreted as

a result of WIMP annihilation. To date, however, none of these has been positively confirmed as a dark matter signal.

There are two main types of detectors that can look for WIMP-induced energetic gamma rays: Space based telescopes and the ground based Atmospheric Cerenkov Telescopes (ACT). These two classes of experiments play complementary roles in the search for dark matter.

An ACT is a large array of optical telescopes, which each is generally a large mirror focusing light upon an array of photomultiplier tubes (PMTs), used to monitor Cerenkov light emissions over a wide area of the sky. ACTs reconstruct the Cerenkov light patterns from particle showers produced in the atmosphere by high-energy gamma rays (and cosmic rays). Performance is roughly limited by the light-collection area of each telescope (larger dishes can detect dimmer, low-energy events), the area of the array (larger arrays can collect more events in the same exposure time), and background rejection (more dishes and more pixels means better tracks, and thus easier rejection of cosmic rays and meteors). Prominent instruments in this category include HESS [74], MAGIC [75], VERITAS [76] and CANGAROO-II [77]. In 2006, the H.E.S.S. collaboration reported an excess of TeV gamma rays from the galactic center, consistent with a near-pointlike source [78]. The authors have proposed this as a possible signature of heavy ( $\sim 10 \text{ TeV}/c^2$ ) WIMP annihilation. The observed spectrum is only marginally consistent with expectations from WIMP annihilation, however, and more closely resembles a power law typical of astrophysical sources. Although this gamma ray source represents a formidable background for experiments searching for dark matter annihilation radiation [79], it may be possible to reduce the impact of this and other backgrounds by studying the angular distribution of gamma rays from this region of the sky [80].

Space-based gamma ray telescopes will continuously observe a large fraction of the sky, but with an effective area far smaller than possessed by ground based telescopes. Ground based telescopes, in contrast, study the emission from a small angular field, but with far greater exposure. Furthermore, while ground based telescopes can only study gamma rays with energy greater than  $\sim 100 \text{ GeV}$ , Fermi will be able to directly study gamma rays with energies over the range of  $100 \text{ MeV}$  to  $300 \text{ GeV}$ .

The first result from space-based experiment is from EGRET (Energetic Gamma Ray Experiment Telescope) aboard the Compton Gamma Ray Observatory. The EGRET telescope has produced the most extensive measurements to date on the gamma ray sky between  $\sim 20 \text{ MeV}$  and  $30 \text{ GeV}$ . The collaboration has noted an excess of GeV-scale gamma rays in EGRET data and have proposed a WIMP interpretation of this excess [81]. However, the observed gamma ray excess seems inconsistent with limits on antimatter production from WIMP annihilation [82]. The authors' proposed WIMP density profile traces the galaxy's visible matter more closely than expected for a WIMP halo, as well as demanding an anomalously-large boost factor of  $B \sim 100$ . Finally, several EGRET collaborators have proposed that instrumental calibration errors could explain the proposed signal [83].

The satellite based Fermi gamma ray space telescope [84] (formerly known as GLAST), launched on June 11<sup>th</sup> 2008, will provide an important leap in sensitivity for indirect searches in the next few years. Through its main instrument, a large silicon tracker known as the Large Area Telescope (LAT), Fermi promises unprecedented sensitivity to gamma rays in the  $10 \text{ MeV}$ – $300 \text{ GeV}$  regime. The LAT improves upon EGRET with an increased field of view, greater target area, superior energy

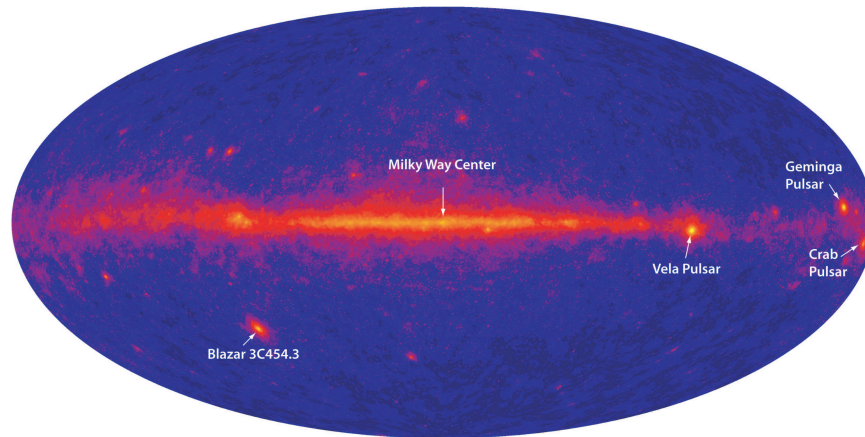


Figure 2.1: “First light” image of the gamma ray sky from the Fermi Gamma-ray Space Telescope. Image from [85].

resolution, and an improved anti-coincidence shield to limit the self-vetoing which plagued EGRET. Fermi has already released its first image of the gamma ray sky, see Figure 2.1.

## 2.2.2 Neutrino detectors

Neutrinos are another leading tracer for WIMP annihilation. Like gamma rays, neutrinos retain directional and spectral information over cosmological distances. Their extremely low scattering cross section renders them vastly more difficult to detect, but also allows them to penetrate dense matter. This makes neutrinos ideal probes of WIMP annihilation in the cores of massive objects such as the Sun and the Earth [69, 70]. Neutrinos are also a possible signature of WIMP annihilation in the galactic center, but the observable signal is greatly suppressed by the small solid angle of the Earth as seen from the galactic center.

The SuperKamiokande neutrino detector [86] or the IceCube experiment [87] can set limits on the rate of WIMP annihilations in the Sun. As particles of dark matter travel through the solar system, some will elastically scatter inside the Sun. If they lose enough energy to become gravitationally bound, they will eventually settle into the center of the Sun, where the WIMP density can grow high enough for annihilations to occur. Among other products, the annihilation can yield neutrinos. If a high-energy ( $\sim 1$  GeV) muon neutrino reaches the Earth, it may scatter in material near the surface to produce an energetic muon, that will propagate all the way through the SuperK chamber, for example. This daughter muon will be emitted in a direction well-aligned with that of the incident neutrino, thus retaining directional information about the annihilation source. Upward-going muons of this sort are easily distinguished from solar neutrinos by their far greater energies (solar neutrinos have energies characteristic of nuclear processes: keV-MeV) and from atmospheric neutrinos by their directional correlation with the Sun’s position in the sky.

When completed, the IceCube experiment will possess a full square kilometer of effective area and kilometer depth, and will be sensitive to muons above approximately 50 GeV [88]. The Deep Core extension of IceCube will be sensitive down to 10 GeV. The Super-Kamiokande detector, in contrast, has  $10^{-3}$  times the effective area of IceCube and a depth of only 36.2 meters [89]. For low mass WIMPs,

however, Super-Kamiokande benefits over large volume detector such as IceCube by being sensitive to muons with as little energy as  $\sim 1$  GeV.

In many ways, neutrino-based WIMP searches are more similar to direct detection experiments than to indirect searches with gamma rays. Under the assumption of capture-annihilation equilibrium, the annihilation rate in the solar center depends upon the cross section for WIMP-nucleon elastic scattering rather than the annihilation cross section. Since the Sun is composed primarily of Hydrogen, the spin-dependent WIMP-proton cross section generally dominates the capture rate for SUSY neutralinos. The good indirect detection sensitivity of neutrino detectors to WIMPs with spin-dependent coupling to unpaired protons is especially convenient, as it explores the one type of coupling that is not well covered by direct detection experiments with Ge targets, such as the one described in the body of this thesis.

### 2.2.3 Antimatter detection

Anomalous populations of antimatter in cosmic rays, such as positrons, antiprotons, and antideuterons, are also a possible signature of WIMP annihilation in the cosmos [58]. When WIMPs annihilate in the galactic halo, they can produce quarks, leptons, gauge bosons, Higgs bosons and gluons. The origin of positrons comes when these particles either decay and/or hadronize, *i.e.* produce hadron jets. WIMP annihilation is then expected to produce an equal mixture of electrons and positrons, but this raises the (generally low) electron-positron ratio from more trivial background processes. Therefore WIMP annihilation should generally appear as a broad excess of high-energy positrons, inconsistent with the declining power laws expected from background processes.

Since antimatter particles are usually secondary annihilation products, they generally lack strong spectral features. The propagation of antimatter through the galactic magnetic field is complex and diffusive, erasing directional information and producing large theoretical uncertainties in the expected antimatter flux. Antimatter can nonetheless be a prominent tracer for WIMP annihilation in energy regimes where astrophysical backgrounds are low. Multiple experiments have recently announced results which have been interpreted as possible products of WIMPs.

The PAMELA experiment, which began its three-year satellite mission in June 2006, recently reported an anomalous rise in the cosmic ray positron fraction (the positron to positron-plus-electron ratio) above 10 GeV [90], confirming earlier indications from HEAT [91] and AMS-01 [92]. Additionally, the ATIC balloon experiment has recently published data revealing a feature in the cosmic ray electron (plus positron) spectrum between approximately 300 and 800 GeV, peaking at around 600 GeV [93]. These observations suggest the presence of a relatively local (within  $\sim 1$  kpc) source(s) of energetic cosmic ray electrons and positrons. Furthermore, in addition to the observations of PAMELA and ATIC, the WMAP experiment has revealed an excess of microwave emission from the central region of the Milky Way. This excess has been interpreted as synchrotron emission from a population of electrons/positrons with a hard spectral index [94]. Taken together, these observations suggest that energetic electrons and positrons are surprisingly ubiquitous throughout our galaxy.

Although the origin of these electrons and positrons is not currently known, interpretations of the observations have focused two possibilities: Emission from pulsars and dark matter annihilations. However, a large fraction of the annihilations

must proceed to electron-positron pairs, or possibly to  $\mu^+\mu^-$  or  $\tau^+\tau^-$  [95] in order to produce a spectrum with a shape similar to that observed by PAMELA and ATIC for dark matter annihilations throughout in the Milky Way halo. Furthermore, WIMPs annihilating to other final states typically exceed the observed flux of cosmic ray antiprotons if normalized to generate the PAMELA and ATIC signals [96].

Dark matter particles which annihilate directly to  $e^+e^-$  are predicted to generate a distinctive feature in the cosmic ray electron spectrum: an edge that drops off suddenly at  $E_e = m_\chi$ . On the other hand, pulsars and other astrophysical sources of cosmic ray electrons are expected to produce spectra which fall off more gradually. Although the current data from ATIC is not detailed enough to discriminate between a feature with a sudden edge (dark matter-like) or graduate cutoff (pulsar-like), such a discrimination could become possible, if the electron spectrum were measured with greater precision. Interestingly, such a measurement should be possible for ground based gamma ray telescopes such as HESS or VERITAS [97].

### 2.2.4 WMAP haze

The Wilkinson Microwave Anisotropy Probe (WMAP) has observed an unknown source of microwaves within  $20^\circ$  of the galactic center, known as the “WMAP haze”. This excess signal is not associated with any known source, and is not well explained by standard types of microwave emission in the interstellar medium, such as dust or synchrotron radiation of electrons and positrons from supernovae. The haze has been interpreted as synchrotron radiation by electrons and positrons from WIMP annihilation in the galactic center [94]. The annihilation of heavy WIMPs can produce such a population, which makes the haze a very intriguing candidate for indirect detection.

## 2.3 Direct detection

Because of the Earth’s position within the dark matter halo of the Milky Way, WIMP interactions are not only an astronomical phenomenon, but also a terrestrial one. Once in a *great* while (current upper limits are less than one event per day in one kilogram of Ge), a WIMP should scatter elastically upon any material sample, and a sufficiently sensitive detector may be able to observe this interaction [98, 99]. This is the goal of the EDELWEISS-II experiment and a host of other direct detection experiments: To observe the rare interactions of galactic WIMPs in (underground) laboratory particle detectors.

### 2.3.1 WIMP elastic scattering

Even without knowing the details of any specific WIMP model, there are several general conclusions we can draw about WIMP-nucleus elastic scattering. WIMPs are bound within the galactic halo, hence they should travel at typical galactic velocities in the solar neighborhood:  $v \approx 270 \text{ km/s} \sim 10^{-3}c$ . A WIMP, which have a mass of  $M = 100 \text{ GeV}/c^2$ , has thus a kinetic energy of  $E_\chi \approx 50 \text{ keV}$ . In an elastic collision with a stationary target of mass  $m$ , the mean kinetic energy of the recoiling target is

$$E_{\text{recoil}} = \frac{2m/M}{(1 + m/M)^2} E_\chi \quad (2.1)$$

The maximum recoil energy is twice this amount. An elastic collision between a  $100 \text{ GeV}/c^2$  galactic WIMP and a Ge nucleus ( $m_{\text{Ge}}c^2 \approx 72.64 \text{ u}$ ) leads the nucleus to recoil with a typical kinetic energy of  $E_{\text{kin}} \sim 25 \text{ keV}$ . This energy deposition is detectable in a variety of low-threshold particle detectors. To compare, a WIMP-electron collision typically endows the electron with  $E_{\text{kin}} < 1 \text{ eV}$  - not enough to ionize a single charge carrier, and thus a challenging target for any massive detector technology. Direct detection efforts thus focus upon WIMP-induced nuclear recoils.

The slow speed of an incident WIMP has also important implications for its scattering cross section. A  $100 \text{ GeV}/c^2$  galactic WIMP has a De Broglie wavelength of  $\lambda = h/(M_\chi v) \approx 12 \text{ fm}$ , the diameter of a large atomic nucleus. So an incident WIMP interacts coherently with an entire atomic nucleus rather than scattering off single nucleons. Cross section computations must account for constructive or destructive interference among the individual WIMP-nucleon scattering amplitudes. Roughly speaking, a WIMP's long wavelength means that it "sees" the nucleus at this scale of resolution and cannot resolve individual nucleons.

The WIMP-nucleon scattering amplitude can take a variety of different forms depending on the WIMP's spin and the symmetries of its couplings: Scalar, pseudoscalar, vector, axial-vector, tensor, or pseudotensor. Kurylov and Kamionkowski have shown [100] quite generally, however, that only scalar and axial-vector terms survive in the extreme non-relativistic limit. The remaining terms are either suppressed by large factors or can be absorbed into these two. In this limit, the general interaction Lagrangian becomes

$$\mathcal{L}_{\chi N} = 4\chi^\dagger\chi\left(f_p\eta_p^\dagger\eta_p + f_n\eta_n^\dagger\eta_n\right) + 16\sqrt{2}G_F\chi^\dagger\frac{\vec{\sigma}}{2}\left(a_p\eta_p^\dagger\frac{\vec{\sigma}}{2}\eta_p + a_n\eta_n^\dagger\frac{\vec{\sigma}}{2}\eta_n\right) + \mathcal{O}\left(\frac{q}{M_{p,\chi}}\right) \quad (2.2)$$

where  $\chi$  is the WIMP wavefunction,  $\eta_{p(n)}$  is the proton (neutron) Weyl spinor,  $\vec{\sigma}$  is the spin operator from Pauli spin matrices, and  $q$  is the recoil energy. The WIMP-nucleon interaction is thus characterized by five parameters: The WIMP mass  $M_\chi$ , the "spin-independent" (SI) couplings  $f_p$  and  $f_n$ , and the "spin-dependent" (SD) couplings  $a_p$  and  $a_n$ .

### 2.3.2 Spin-independent scattering

A spin-independent WIMP-nucleon interaction corresponds to a coupling to the nucleon density operators, characterized by coupling constants  $f_p$  and  $f_n$  to protons and neutrons, respectively. In the limit of vanishing momentum transfer, *i.e.* an extremely soft collision, the scattering amplitudes with individual nucleons add coherently, giving a total scattering amplitude  $M_{\text{SI}} \propto (Zf_p + (A-Z)f_n)$  for a nucleus with atomic number  $Z$  and atomic mass  $A$ . Squaring the amplitude and adding in kinematic factors, we obtain the spin-independent WIMP-nucleus cross section

$$\sigma_{\text{SI}}^0 = \frac{4}{\pi}\mu_{\chi N}^2(Zf_p + (A-Z)f_n)^2 \quad (2.3)$$

where  $\mu_{\chi N} = (M_\chi M_N)/(M_\chi + M_N)$  is the collision's reduced mass. Most supersymmetric and similar models predict  $f_p \approx f_n$  [58], giving a cross section  $\sigma_{\text{SI}} \propto A^2$ . The cross-section does not scale linearly with the size of the nucleus, but quadratically. This coherent enhancement can be enormous ( $A_{\text{Ge}}^2 \sim 5000$ ), so a WIMP target built of heavy nuclei is greatly more sensitive to WIMP interactions than one composed of lighter nuclei.

The differential cross-section of the spin-independent or scalar interactions is then [58]:

$$\frac{d\sigma_{\text{SI}}}{dq^2} = \frac{4}{\pi} \mu_{\chi N}^2 (Z f_p + (A - Z) f_n)^2 F^2(q) \quad (2.4)$$

When  $q$  corresponds to a wavelength much larger than the nucleus, the scattering is fully coherent. As  $q$  rises, the nuclear structure becomes important, with the exact dependence encoded in  $F(q)$ . A convenient approximation to  $F^2(q)$  for a wide range of nuclides under the assumption that protons and neutrons are similarly distributed and  $f_p \approx f_n$  is the Helm form factor from Lewin & Smith [101]:

$$F(q) = \frac{3j_1(qr_n)}{qr_n} e^{-q^2 s^2/2} \quad (2.5)$$

where  $j_1 = \sin(x)/x^2 - \cos(x)/x$  is a spherical Bessel function of the first kind,  $r_n = c^2 + 7/3\pi^2 a^2 - 5s^2$  is an effective nuclear radius,  $s = 0.9$  fm is the nuclear skin thickness,  $a = 0.52$  fm is the Bohr radius, and  $c = 1.23A^{1/3} - 0.60$  fm. These values have been chosen to make Equation 2.5 approximately equal to the Fourier transform of the Woods-Saxon formula, which is a two-parameter Fermi distribution giving the spatial distribution of charges in the nucleus. Our selected  $F(q)$  therefore amounts to a ‘‘fit of a fit’’. Although more sophisticated approaches are available, based on electron elastic scattering data rather than model-dependent parameterizations, the Lewin & Smith formula has been found to be an acceptably close match [102] and has been adopted as a working standard by many direct-detection experiments.

### 2.3.3 Spin-dependent scattering

On the other hand, in the non-relativistic limit, axial-vector couplings (characterized by coefficients  $a_p$  and  $a_n$ ) give amplitudes proportional to the inner product of the WIMP and nucleon spins. Since the interaction amplitude switches signs when the nucleon spin is flipped, a WIMP’s spin-dependent (SD) interaction amplitudes with two nucleons of opposite spin will interfere destructively in the zero-momentum-transfer limit. Nucleons align into spinsinglet pairings within nuclei, so spin-dependent cross sections are dominated by unpaired nucleons and vanish entirely for spinless nuclides. This leads to very different constraints on experimental design: Experiments targeting SD interactions generally use light odd-proton or odd-neutron nuclides to maximize the nuclear spin per unit mass, rather than the heavy nuclides preferred for SI-sensitive detectors.

At vanishing momentum transfer, the WIMP-nucleon spin-dependent interaction cross section is [103]

$$\sigma_{\text{SD}}^0 = \frac{32(J+1)}{\pi J} G_F^2 \mu_{\chi N}^2 (a_p \langle S_p \rangle + a_n \langle S_n \rangle)^2 \quad (2.6)$$

where  $J$  is the nuclear spin and  $\langle S_{p(n)} \rangle$  is the expectation value for the nucleus of the proton (neutron) spin. The spin expectation values must be obtained from detailed nuclear structure calculations [104, 105]. Such calculations also show that an odd-neutron nucleus may have a small but non-zero  $\langle S_p \rangle$ , or vice versa, due to polarization effects within the nucleus.

In the case of spin-dependent scattering, we cannot generally take  $a_p \approx a_n$ . Their ratio may vary in sign and magnitude among neutralino models. This means that

we must generally consider a three-parameter space:  $a_p$ ,  $a_n$ , and  $M_\chi$ . Furthermore, it means that the finite-momentum-transfer effects of the form factor cannot be factored out of the cross section in a model-independent fashion. The distributions of proton and neutron spin may be very different in a given nucleus, and so finite momentum effects may be very model-dependent. The preferred way to deal with this is to follow [106] by writing the WIMP-nucleus differential cross section in the form

$$\frac{d\sigma_{\text{SD}}}{dq^2} = \frac{8G_F^2}{(2J+1)v^2} S(q) \quad (2.7)$$

where  $v$  is the incident velocity and

$$S(q) \equiv a_0^2 S_{00}(q) + a_0 a_1 S_{01}(q) + a_1^2 S_{11}(q) \quad (2.8)$$

with  $a_0 \equiv a_p + a_n$  and  $a_1 \equiv a_p - a_n$ .  $S(q)$  encompasses the effects of finite momentum transfer, as well as values for the neutron and proton spin expectations\*. There is no universal form of  $S(q)$ . It must be computed separately for each nuclide using nuclear structure models [104, 105].

Although neutralinos often have intrinsically larger spin-dependent than spin independent couplings to nucleons, due to the great power of coherent enhancement – Equation 2.4 shows that scalar interactions are enhanced by the square of the target nuclear mass, while the spin-dependent cross-section in Equation 2.7 does not increase with  $A$  –, spin independent WIMP-nucleus cross sections are generally much greater. Because of this, and because of the relative rarity of heavy spin-sensitive isotopes, spin-independent interactions are targeted by most leading direct searches.

### 2.3.4 Event rate

The differential rate for scalar interactions can be written in terms of  $\sigma_{\text{SI}}^0$  from Equation 2.3:

$$\frac{dR}{dE} = \frac{\rho_0 \sigma_{\text{SI}}^0 |F(q)|^2}{2M_\chi \mu^2} \int_{v>q/2\mu} \frac{f(\vec{v}, t)}{v} d^3v \quad (2.9)$$

The lower limit of integration is the minimum WIMP velocity required in order to be kinematically possible for an energy  $E$  to be transferred to the nucleus. For the velocity profile, we assume a Maxwellian distribution truncated at the galactic escape velocity  $v_{\text{esc}}$ . However,  $v_{\text{esc}}$  is large enough, so that it has little effect on the calculation, and so we have omitted it here. The Maxwellian distribution is

$$f(v) d^3v = \frac{1}{v_0^3 \pi^{3/2}} e^{-v^2/v_0^2} d^3v \quad (2.10)$$

with a characteristic velocity  $v_0 = 270$  km/s in the solar neighborhood and truncated at a galactic escape velocity of  $v_{\text{esc}} \approx 650$  km/s. Substituting this form into Equation 2.9 gives an energy spectrum that is a falling exponential modified by  $F(q)$ . Then, the differential rate is

$$\frac{dR}{dE} = \frac{\rho_0 \sigma_{\text{SI}}^0 |F(E)|^2}{\sqrt{\pi} v_0 M_\chi \mu^2} \exp\left(-\frac{EM_N}{2\mu^2 v_0^2}\right) \quad (2.11)$$

---

\* There is a variation on this method advocated by some authors [58, 101] in which the scattering expressions are made to look more similar to those in the SI case by multiplying the above expression for  $\sigma_{\text{SD}}$  by a model-dependent form factor  $F^2(q) = S(q)/S(0)$ . This is equivalent in principle, but the division by  $S(0)$  may increase numerical errors in practice.

Here are not included the small corrections for the galactic escape velocity, the Earth's motion around the Sun, and the Sun's motion around the galactic center. A treatment including these effects can be found in Lewin & Smith [101]. In order to compare results across experiments, it is useful to express rates in terms of the cross section for scattering on a single nucleon  $\sigma_{\text{SI}}^{0,n}$ . The cross section for a nuclear species  $i$  is  $\sigma_{\text{SI}}^{0,i} = \sigma_{\text{SI}}^{0,n} \mu_i^2 / \mu_n^2 \cdot A^2$ , where  $\mu_i$  and  $\mu_n$  are the reduced masses for the WIMP-nucleus and WIMP-nucleon systems, respectively. Putting all together,

$$\frac{dR}{dE} = \frac{\rho_0 \sigma_{\text{SI}}^{0,n} |F(E)|^2}{\sqrt{\pi} v_0 M_\chi \mu_n^2} \exp\left(-\frac{EM_N}{2\mu_i^2 v_0^2}\right) \quad (2.12)$$

The expected scattering rates depend on several assumptions about the precise properties of the Milky Way's dark matter halo. N-body simulations have been performed to study the dark matter halo of the Milky Way. These simulations are being used to understand the fine-scale structure predicted around the Milky Way by the standard structure formation model, and as the basis for simulation by various techniques of the growth of the stellar components of our Galaxy. The question is to determine whether the annihilation signal will be dominated by emission from very small clumps, which would be most easily detected where they cluster together in the dark matter halos of satellite galaxies, or whether the dominant and likely most easily detectable signal will be produced by diffuse dark matter in the main halo and consequently in the central region of the Milky Way. The simulations from the Via Lactea Project [107] and the Aquarius Project [108] leads to a same conclusion such small-scale structure will, in fact, have a negligible impact on dark matter detectability. The local velocity distribution is very smooth, but it differs systematically from a (multivariate) Gaussian distribution. This is not due to the presence of individual clumps or streams, but to broad features in the velocity modulus and energy distributions that are stable both in space and time and reflect the detailed assembly history of each halo. Different choices of parameters can change the expected rates by a significant amount, up to factors of a few [109, 110]. This is acceptable, as the theoretical properties of WIMPs are subject to even larger uncertainties. And comparisons between the sensitivities of competing direct detection experiments are not strongly sensitive to halo uncertainties

Thus, a "standard halo" can be defined under astrophysically reasonable assumptions, but subject to uncertainties as estimated by the simulations. The standard halo follows these local properties: first  $\langle v_0 \rangle \approx 270$  km/s, which is the mean velocity of a Maxwellian velocity distribution in the vicinity of the Earth, and then a local WIMP density of  $\rho_0 = 0.3$  GeV/c<sup>2</sup>/cm<sup>3</sup>. The true value of  $v_0$  may range from 170–270 km/s, and  $\rho_0$  from 0.2–0.4 GeV/cm<sup>3</sup>.

If now we add up the WIMP-nucleon scattering cross section assumed to be  $\sigma_{\chi p} \sim 1$  pb, we can estimate the approximate event rate we might expect from a generic WIMP. For a 100 GeV/c<sup>2</sup> WIMP, this corresponds to a scattering rate of a few events per day in a one-kilogram Hydrogen target mass. This event rate can be altered enormously by model-dependent considerations, but we are nonetheless led to a general experimental design: A search for rare WIMP impacts occurring once or less per month of exposure and kilogram of target.

### 2.3.5 Background suppression techniques

Based on the discussion above, a leading direct detection experiment must be able to identify a spectrum of  $\mathcal{O}(10)$  keV nuclear recoils occurring less than once a month in each kilogram of target material. Unfortunately, this energy regime is awash with background events from natural radioactivity and cosmic rays. Direct WIMP detection is thus a low background enterprise, demanding exquisite protection from these non-welcomed events. The ultimate sensitivity of a WIMP experiment is set by its rate of background events which are indistinguishable from WIMP candidates.

Radioactive and cosmogenic background rates may be reduced by a variety of shielding and material-handling techniques, many of which are described in a review article by Heusser [111]. I discuss several of the techniques in use by EDELWEISS in Chapter 3. Some rate of background events invariably remains, however, and the most competitive experiments generally pursue some scheme to separate the WIMP signal from these background events. These techniques take two general forms: statistical signatures of WIMP interactions or event-by-event identification of WIMP recoils.

#### Statistical signatures of WIMP interactions

Even if individual WIMP events cannot be identified among a lingering background, the WIMP population may possess statistical signatures which can identify its presence. The two signatures discussed most prominently in the literature are the annual modulation in the WIMP recoil spectrum and the daily modulation of the incident WIMP direction. Both signatures take advantage of the extraterrestrial origin of the WIMP signal, and so should provide strong evidence that an observed signal is indeed related to dark matter. As statistical signatures, however, both require an enormous sample of WIMP recoils.

The Earth's motion around the Sun introduces an annual modulation in the velocity distribution of WIMPs incident upon a terrestrial detector. The Earth's net velocity through the galactic halo is greatest in June and lowest in December. Then, a WIMP detector should observe a slightly higher rate of candidate events above its energy threshold in June than in December, generally by a few percent [112, 113].

WIMPs should also show a diurnal modulation in recoil energy direction with the Earth's daily rotation [114]. Due to the orientation of the Earth's axis with respect to our motion through the halo, this corresponds to a shift of  $\sim 90^\circ$  in the mean recoil direction every 12 sidereal (not solar) hours. This effect should be very strong, but its detection is complicated by the enormous difficulty of measuring the direction of the short track produced by a low-energy nuclear recoil.

#### Event-by-event identification of WIMP recoils

Rather than looking for statistical signatures among a large sample of candidate events, we may instead try to identify individual WIMP-induced recoils on an event-by-event basis. A sufficiently accurate discrimination technique can reduce an experiment's background rate low enough to maintain operation in the zero-background

regime, even at very large WIMP-search exposures. This requires a powerful particle identification technique that operates at low energies, but the benefits of low-background operation allow one to extract enormous sensitivity from relatively small detector exposures in this way.

Most modern direct-detection experiments use event-by-event discrimination techniques to identify nuclear recoils from WIMPs, or neutrons, among a far larger rate of electron recoils from radioactive decay and cosmogenic processes. Some experiments, notably bubble chambers and other phase-transition detectors, use the difference in  $dE/dx$  between electron- and nuclear-recoil tracks to make their detectors unresponsive to electron recoils, thus achieving a particularly simple sort of event-by-event discrimination. Discrimination is more commonly accomplished by measuring each event in two or more distinct detection channels and using their ratio to identify the recoil type. When the recoil occurs, the energy is partitioned in the ionization, the heat/phonons and the scintillation channels. In Figure 2.2, the main detection techniques are shown around a triangle that depicts the energy from the interaction of a WIMP-nuclear recoil. These channels differ enormously in the mean nuclear recoil energy needed to create the individual quanta: A few meV per phonon,  $\sim 10$  eV per charge carrier, and  $\sim 100$  eV per scintillation photon. Each detection technique exploits one or more of these channels or degrees of freedom to make the discrimination between nuclear recoils (neutrons and WIMPs) and electron recoils (majority of backgrounds).

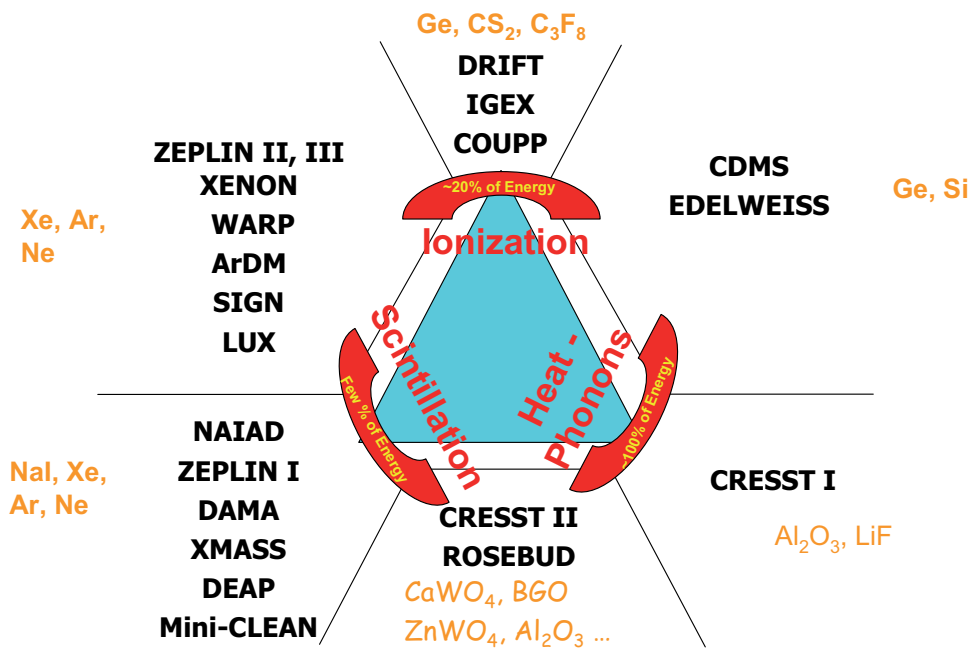


Figure 2.2: Main detection techniques to track a WIMP signal. The triangle depicts the energy after a nuclear recoil interaction from a WIMP, each corner represents a channel where the energy from the interaction appears. Each detection technique exploits one or more of these channels. Most of the energy goes into phonons and ionization, the two channels used by CDMS and EDELWEISS. Figure from [115].

### 2.3.6 Current experiments

**XENON** Liquid Xenon is the most obviously promising of the noble liquid targets. It has the highest boiling point, the largest light yield, no long-lived radioisotopes, and scintillation light which can be detected using ordinary PMTs without wavelength-shifting. Its large atomic mass gives it a large cross section for spin-independent interactions (though form factor effects can counteract this at high energy transfers). Its high density allows for compact detectors and makes for very effective self-shielding: Most background events cannot penetrate more than a few cm into the detector volume. Xenon is not well-suited to pulse shape discrimination, however, due to its extremely short scintillation times.

The XENON experimental program [116] aims to detect cold dark matter particles via their elastic collisions with Xenon nuclei in two-phase time projection chambers (TPCs). XENON10 was the first prototype developed within the XENON dark matter program to prove the concept of a two-phase Xenon time projection chamber (XeTPC) for dark matter searches to discriminate signal from background down to 4.5 keV nuclear recoil energy. The XENON10 collaboration [116] announced its first WIMP-search results in April 2007. Using a 15-kg dual-phase detector located at Gran Sasso, a blind analysis of 58.6 live days of data and a fiducial mass of 5.4 kg, the collaboration reached a sensitivity of  $8.82 \cdot 10^{-44} \text{ cm}^2$  for a WIMP mass of 100 GeV/c<sup>2</sup>, and  $4.5 \cdot 10^{-44} \text{ cm}^2$  for a WIMP mass of 30 GeV/c<sup>2</sup>. These data set then-world-leading limits on WIMP-nucleon spin-independent couplings and spin-dependent interactions with neutrons.

The 100 kg XENON100 detector [117] is currently running and taking data at Gran Sasso, scaling up the same basic design as XENON10. This new, ultra-low background detector, has a total of 170 kg of Xenon (65 kg in the target region and 105 kg in the active shield). With a raw exposure of 6000 kg·d, free of background events, XENON100 is designed to reach a WIMP-nucleon cross section of  $\sim 2 \cdot 10^{-45} \text{ cm}^2$  at a WIMP mass of 100 GeV/c<sup>2</sup>. An upgraded XENON100 will improve this sensitivity by another order of magnitude by 2012.

The 300 kg LUX experiment [118] adds an active water shield to further enhance neutron rejection; this instrument is under construction for deployment at the Sanford Underground Science and Engineering Lab (SUSEL) in South Dakota. In Japan, the XMASS collaboration is developing an 800 kg single-phase detector, focusing on self-shielding and good position reconstruction to eliminate backgrounds. Each of these instruments has an expected sensitivity at or below  $10^{-45} \text{ cm}^2$ , and designs for yet larger detectors are well underway.

**ZEPLIN-III** The ZEPLIN-III [119] experiment in the Palmer Underground Laboratory at Boulby uses liquid Xe as its target mass and discriminates between nuclear recoils and electron recoils. The detector uses a 12 kg two-phase Xenon time projection chamber and measures both scintillation and ionization produced by radiation interacting in the liquid to differentiate between the nuclear recoils expected from WIMPs and the electron recoil background signals down to  $\sim 10$  keV nuclear recoil energy. An analysis of 847 kg·d of data has excluded a WIMP-nucleon elastic scattering spin-independent cross-section above  $10^{-44} \text{ cm}^2$  at 60 GeV/c<sup>2</sup> with a 90% confidence limit. It has also demonstrated that the two-phase Xenon technique is capable of better discrimination between electron and nuclear recoils at low-energy than previously achieved by other Xenon-based experiments.

**Argon** The WARP collaboration has published limits with a 2.3 liter two-phase

prototype detector at Gran Sasso [120], using both ionization and pulse-shape discrimination. The WARP collaboration is pursuing similar two-phase technology on a larger scale (140 kg).

**CRESST** The CRESST dark matter experiment [121] uses cryogenic solid state detectors. CRESST simultaneously measures both the scintillation and the athermal phonons produced by a recoil. A CRESST detector is a  $\text{CaWO}_4$  crystal instrumented with two TES (Transistor Edge Superconducting) thermometers: One to measure the crystal temperature, the other to measure the temperature of an associated light-absorbing Si wafer. CRESST uses the ratio of scintillation to phonon energy, similar to the CDMS and EDELWEISS approach using the ratio of ionization to phonon energy, to discriminate between electron and nuclear recoils. But unlike the detectors for CDMS and EDELWEISS, the CRESST detector does not suffer from a background due to electron recoils near the detector surface. However, the presence of three different nuclei within the crystal makes it difficult to fully characterize the crystal's response through the use of in-situ calibrations. CRESST has set limits on spin-independent WIMP-nucleon interactions at the  $5 \cdot 10^{-43} \text{ cm}^2$  level and is also proceeding with a larger experimental installation (CRESST-II).

CRESST and EDELWEISS have joined the EURECA project [122], a pan-European effort to develop a next generation cryogenic WIMP search experiment up to 1 t. The aim of EURECA project is to reach a sensitivity of  $10^{-46} \text{ cm}^2$ .

**CDMS-I** The detector technology for EDELWEISS and CDMS-I is virtually identical. The target mass is Germanium. Electrodes on the detector surface measure the ionization produced by a recoil while thermistors simultaneously measure the heat that is produced. These detectors can discriminate between nuclear recoils and electron recoils on an event-by-event basis since the heat measurement is an absolute measurement of the recoil energy while the ionization is reduced or quenched for nuclear recoils. The detectors have one electromagnetic background. Electron recoils near the electrodes can have deficient charge collection resulting in reduced ionization measurements. Neither experiment observes a signal from dark matter. The sensitivity of CDMS-I was limited by an irreducible cosmogenic neutron background at the Stanford Underground Facility.

**CDMS-II** The CDMS collaboration [123] has developed another detector technology for dark matter detection. The detectors are crystals of Ge and Si with sensors that simultaneously measure the ionization and athermal phonons produced by a recoil. The detectors are designed to also measure timing information from the athermal phonon signal making it possible to reconstruct the location of the interaction. The ability to reconstruct the position of an event enables the rejection of the background from electron recoils near the surface. The use of both Si and Ge detectors allows for an estimate of neutron backgrounds, since the cross section for neutron is 5–7 times larger in Si than in Ge.

First results from CDMS-II experiment running with its full complement of 30 cryogenic particle detectors at the Soudan Underground Laboratory have been released in [123]. The analysis is based on data acquired between October 2006 and July 2007 from 15 Ge detectors (3.75 kg), giving an effective exposure of 121.3 kg·d (averaged over recoil energies 10–100 keV, weighted for a weakly interacting massive particle (WIMP) mass of  $60 \text{ GeV}/c^2$ ). A blind analysis, incorporating improved techniques for event reconstruction and data quality monitoring, resulted in zero observed events.

This analysis sets an upper limit on the WIMP-nucleon spin-independent cross

section of  $6.6 \cdot 10^{-44} \text{ cm}^2$  ( $4.6 \cdot 10^{-44} \text{ cm}^2$  when combined with previous CDMS Soudan data) at the 90 % confidence level for a WIMP mass of  $60 \text{ GeV}/c^2$ . By providing the best sensitivity for dark matter WIMPs with masses above  $42 \text{ GeV}/c^2$ , this work significantly restricts the parameter space for some of the favored supersymmetric models.

The current limits of all these experiments can be found in the WIMP mass – WIMP-nucleon cross section (normalized to nucleon) plane on Figure 3.16 at the end of Chapter 3.

### 2.3.7 The DAMA claim

The aim of the Italian-Chinese collaboration DAMA is to exploit the expected annual modulation signature of dark matter caused by the Earth orbit around the Sun. This experiment expects a larger flux around June 2<sup>nd</sup> when the orbital velocity of the Earth is summed to the orbital velocity of the solar system around the Galaxy, and expects a smaller rate around December 2<sup>nd</sup>, when the orbital velocities of the Earth and of the Sun are anti-parallel [124]. The signal counting rate in the  $k^{\text{th}}$  energy interval as a function of time  $t$  can be written as:

$$S_k = S_{0,k} + S_{m,k} \cos(\omega(t - t_0)) \quad (2.13)$$

where  $S_{0,k}$  is the constant part of the signal,  $S_{m,k}$  is the modulation amplitude,  $\omega$  is the frequency and  $t_0$  the phase [124]. The expected DAMA annual modulation signature from dark matter particles will have the following features [124]:

- the modulation of the rate follows a cosine function with a period of one year,
- the phase of the signal modulation should be close to June 2<sup>nd</sup> and produce an effect of  $\simeq 7\%$ , depending on the properties of the galactic dark matter halo,
- the signals producing the modulation must be low energetic single hits.

The DAMA collaboration sees this approach as model-independent because nothing is assumed about the nature of the particle causing the energy deposition and the modulation, in contrast to all the other direct detection methods that assume that the dark matter is the WIMP and scatters from nuclei. In 1996, the DAMA/NaI experiment was proposed [125] and was the first to claim [126] direct-detection model-independent evidence for the presence of dark matter particles in the Milky Way halo. Recently, the DAMA/LIBRA collaboration has reinforced the claim of evidence for dark matter from an observed annual modulation of the detected single rates at very low energies ( $\lesssim 10 \text{ keV}$ ) [127].

They claim they have done a model independent analysis of the residual rates of the single-hit events in the lowest energy regions. The residual singles rates are calculated from the measured rate after some efficiency corrections and after subtracting the constant part defined by  $\langle r_{ijk} - flat_{jk} \rangle_{jk}$ , where  $r_{ijk}$  is the rate in the  $i^{\text{th}}$  time interval for the  $j^{\text{th}}$  detector in the  $k^{\text{th}}$  energy bin, and  $flat_{jk}$  is the rate of the  $j^{\text{th}}$  detector in the  $k^{\text{th}}$  energy bin averaged over the cycles. The average is made on all detectors ( $j$  index) and on all the 1 keV energy bins ( $k$  index). In Figure 2.3, the residual rates for single-hits in the DAMA/LIBRA experiment are shown over four annual cycles, adding to 0.53 ton-year. The rates from the previous experiment,

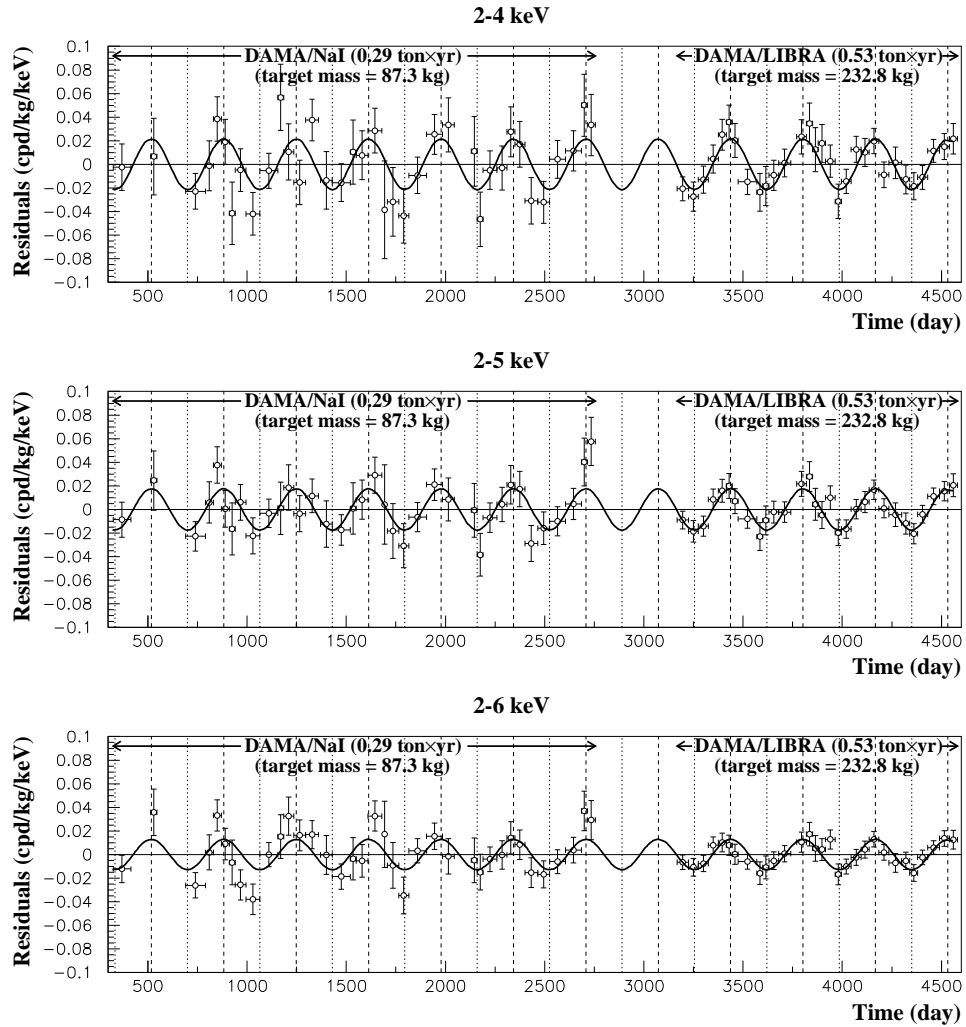


Figure 2.3: The residual single-hit events in the 2–4, 2–5 and 2–6 keV energy intervals as a function of the time for the DAMA/NaI and DAMA/LIBRA experiments with an exposure of 0.53 and 0.29 ton-year, respectively. The zero of the time scale is January 1<sup>st</sup>. The solid lines correspond to the superimposed cosinusoidal functions  $A\cos(\omega(t - t_0))$  with a period of one year, a phase  $t_0 = 152.5$  days (June 2<sup>nd</sup>) and with modulation amplitudes of  $A = (0.0215 \pm 0.0026)$  cpd/kg/keV,  $(0.0176 \pm 0.0020)$  cpd/kg/keV and  $(0.0129 \pm 0.0016)$  cpd/kg/keV for the (2–4) keV, (2–5) keV and (2–6) keV energy intervals, respectively. Figure from [127].

the DAMA/NaI which accumulated an exposure of 0.29 ton-year, are also shown. The improved signal due to increased statistics is clear in this plot and an annual modulation is evident. Other possible systematic effects such as temperature effects on the noise of the photomultiplier tubes, humidity related backgrounds, radon or other systematic effects has not been conclusively established.

Assuming a spin-independent interaction and a WIMP mass of tens of  $\text{GeV}/c^2$  or higher, the WIMP-nucleus cross section extracted from the annual modulation in the DAMA/NaI experiment would correspond to  $\sim 10^{-5}$  pb. This claim has been ruled out by previous CDMS experiment results [123] and by many other experiments, including various targets and radically different techniques, such as the XENON 10 experiment [116]. Nevertheless, due to the insufficiently-low energy threshold of the majority of the other experiments, it has been proposed that light WIMPs ( $\sim 10 \text{ GeV}/c^2$ ) could cause the observed modulation and still be undetected by the other experiments [128, 129]. Recently, the COUPP collaboration, using an improved bubble chamber technology, has ruled out the WIMP hypothesis for spin-dependent WIMP-nucleus interactions [130]. The remaining possibility that low-mass WIMPs undergo spin-independent interactions has been ruled out more recently by the CoGeNT collaboration [131] employing a new type of Germanium radiation detector with a very low electronic noise [132]. And finally a latest attempt to reconcile the detection of annual modulation observation of DAMA experiment and null results from all other experiments was to introduce inelastic dark matter. Inelastic dark matter model explored the possibility of an altered kinematics of the collision between the  $\chi$  and the nuclei. This scenario seems to be also ruled out by the noble liquid Xenon detector of the ZEPLIN-II experiment [133].

The DAMA results have not been solved yet. The collaboration has not been able to identify any other systematic effects capable of producing this signal. However, the claim that this signal is the result of dark matter interactions is in direct conflict with any other experiments. The DAMA results may be an artificial, one dare say a false, result or may lead to a non-MSSM dark matter candidate, as long as the results are not reproduced, the claim is not conclusive.

Direct detection of dark matter encompasses all those experiments that search for a dark matter particle interacting directly with the detector, via elastic scattering, for example, with a target nucleus causing a nuclear recoil of about 15 keV. Indirect detection experiments search for a non-WIMP particle originating from WIMPs that interact with the detector. In collider experiments a new particle may be produced and be detectable in a twist of looking for “missing energy” or missing transfer momentum.

However, a measurement of the couplings is highly unlikely in collider, and it will not be possible to determine if the “missing particle” has the necessary stability to be a “freeze out” product from the Big-Bang. Moreover, the production rate and detectability of WIMPs at colliders depends primarily upon the masses of the WIMP and related new particles: If the particles are too heavy, they cannot be produced. Thus, primary annihilation processes that set the relic density in some WIMP models are temperature-dependent. The annihilation rates of such models are greatly

reduced in the cold modern universe, making indirect detection less promising given equivalent halo models. Finally, the “crossing symmetry” argument posits that the dominant WIMP annihilation and scattering processes have comparable amplitudes. Direct detection is less promising if this relationship is broken, as when annihilation occurs on resonance.

Different WIMP models answer these questions differently, and thus have different detection prospects. Some models generate robust signals for all three search strategies, others in only a subset. These three investigations can also provide complementary information about the same WIMP, opening up new opportunities for elucidating its nature. That’s why collider, indirect, and direct investigations of WIMPs provide three complementary probes of the nature of dark matter. Each of the three asks a fundamentally distinct question about the properties of the dark matter particle.

# 3

## The EDELWEISS-II experiment

### Contents

- 3.1 Bolometers
- 3.2 EDELWEISS-II cryostat and shielding
- 3.3 Muon veto system
- 3.4 Neutron counters
- 3.5 Results of EDELWEISS-I

*In the final analysis, though, Zwicky probably didn't care whether people believed his ideas or not. Zwicky knew. That was enough.*

S. M. Mauer.

THIS CHAPTER is dedicated to the description of the direct dark matter search experiment called EDELWEISS (Expérience pour DEtecter Les Wimps en Site Souterrain). The EDELWEISS collaboration consists of about 50 scientists from universities and research centers in France, Germany and Russia. Among those are the University of Karlsruhe (TH) and the Forschungszentrum Karlsruhe, currently merging into the Karlsruhe Institute of Technology (KIT). The experiment is installed since 1994 at the Laboratoire Souterrain de Modane (LSM), an underground laboratory settled in the highway tunnel of Fréjus between France and Italy. The EDELWEISS experiment looks for direct interaction of dark matter in Germanium crystals. The first 320 g Germanium detector has been installed in the EDELWEISS cryostat in 2000 [134]. In 2001, the EDELWEISS-I phase started with 3 detectors [135]. The experiment has since been upgraded step by step in terms of shielding and bolometers [136]. With a complete new set-up since 2005, the so-called EDELWEISS-II experiment [137] intends to have up to 120 bolometers to reach a mass of Germanium of  $\sim 30$  kg.

This chapter deals with the description of the detectors used in EDELWEISS-II, *i.e.* Ge bolometers for dark matter search in the ionization and heat channels, muon veto scintillators to suppress muon-induced background, and neutron detectors to monitor neutron background. At the end, the EDELWEISS-I results are reviewed and compared with the goals of EDELWEISS-II.

### 3.1 Bolometers

The goal of the EDELWEISS-II experiment is to detect nuclear recoil events of the well-motivated Dark Matter candidate, the Weakly Interacting Massive Particle (WIMP), *cf.* Section 1.8.2 for details. The event rate of the WIMP can be as low

as  $10^{-6}$  event/kg/d, which is a very low event rate if one refers to the natural radioactivity of a human body ( $10^7$  decays/kg/d), for example. The recoil energy of a WIMP in a detector is also very low. A WIMP with a mass  $M = 100 \text{ GeV}/c^2$  has a kinetic energy of  $E_{\text{kin}} \approx 50 \text{ keV}$ . An elastic collision between a  $100 \text{ GeV}/c^2$  galactic WIMP and a Germanium nucleus, for example, then gives the nucleus to recoil with typical kinetic energy of  $\sim 25 \text{ keV}$ , *cf.* Section 2.3.1. A very low event rate plus a low recoil energy require special precaution in terms of background, which has then to be maintained as low as possible.

As first step, the EDELWEISS experiment is located underground in the LSM laboratory which provides an approximately 4600 meter-water-equivalent (mwe) rock shielding against cosmic ray muons, see Chapter 4 for more details on muon-induced background issues.

A second step is to have, passive or active, shielding around the detectors which is discussed later in Section 3.2. Then, when the background is hardwarely maintained as low as possible, the next step is to find ways to clearly distinguish the WIMP from other signals in the bolometers.

The possible signatures used in the EDELWEISS-II experiment to discriminate the recoil spectrum of the WIMPS from those of background particles are:

- Type of interaction: WIMPs scatter off the nuclei of the detector material (nuclear recoils), while background particles, mainly  $\beta$  and  $\gamma$  through Compton scattering, scatter off the electrons of the target (electronic recoils).
- Location in the detector: The WIMPs have a long free mean path, which means that the events due to the WIMPs are uniformly spread in the detector. On the other hand, events from the ambient radioactivity of the laboratory happen close to the surface: High energy  $\gamma$  have a mean free path less than a cm, and low energy  $\gamma$ ,  $\beta$  and  $\alpha$  of the order of a mm.
- Multiple interactions: Neutrons also produce nuclear recoils. But the WIMP as it is written in its name is a weakly interacting particle, which is not likely to make multiple interactions, while the neutron-nucleus scattering cross section is  $\sigma_n \approx 1 \text{ b}$  with a distance in between two interactions in a solid of the order of a centimeter.

Therefore, WIMP events are classified as single non surface nuclear recoil events. When a WIMP interacts with a nucleus of the target, the kinetic energy of the recoil nucleus is partially converted into three possible energies, the ionization, the heat/phonons and the scintillation ones. The measurable quantities are then an electric current, a temperature rise, and light. The Ge bolometers of the EDELWEISS experiment, which do not scintillate, measure the signal in the ionization and in the heat channel.

Choosing two channels of detection allows to discriminate between WIMPs and background events. The mean free path of an electron of 50 keV in a solid is a few  $\mu\text{m}$  while a nucleus of the same energy recoils only a few tens of nm. A nuclear recoil produces then proportionally less ionization than an electronic recoil of equal energy. This effect is quantified in a factor, the so-called quenching factor  $Q$ , which is the ratio of the signal of a nuclear recoil over that of an electronic recoil of equal energy, as described empirically in [138]. In the ionization channel for Germanium, the quenching factor is  $Q_{\text{Ge}} \simeq 0.33$  [139, 140]. It is important, however, to note

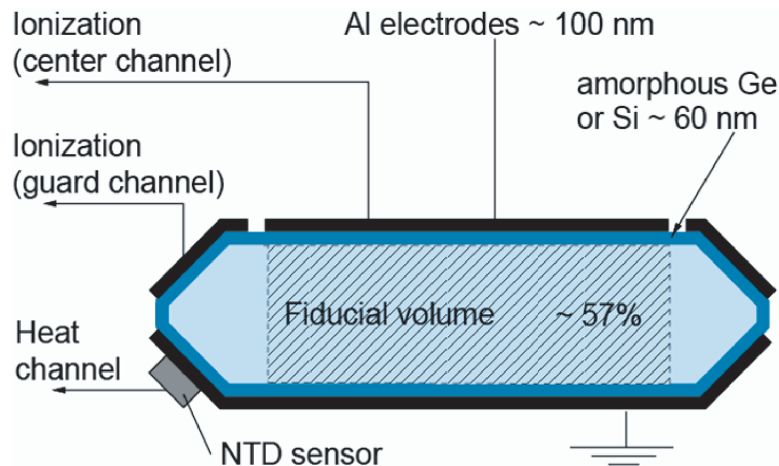


Figure 3.1: Schematic overview of an EDELWEISS heat and ionization Germanium detector. The electrodes, the amorphous layer and the NTD thermometer are not represented to scale. Figure from [141].

that there is no quenching in the heat channel:  $Q'_{\text{Ge}} \simeq 1$  [139, 140], which means that the heat signal does not depend on the origin of the particle. This is the great advantage of the cryogenic Ge bolometer, the energy scale comes from heat and thus is independent on particle. The second great advantage is that the quenching in the ionization channel allows an event-by-event discrimination of electronic and nuclear recoils by the simultaneous measurement of the two signals, *cf.* Section 3.1.5.

Because of the different quenching factors  $Q_{\text{Ge}}$ , the energy calibration using the ionization channel depends on the origin of the signals, whether electronic or nuclear. As it is difficult to have mono-energetic sources of nuclear recoils, most of the time the detectors are calibrated with gamma sources, in keV-electron-equivalent  $\text{keV}_{ee}$ . One keV-electron-equivalent corresponds to 1 keV for an energy deposit of a  $\gamma$  or a  $\beta$ , *i.e.* an electronic recoil, but to  $1/Q$  keV for the WIMPs or neutrons nuclear recoils.

The EDELWEISS collaboration uses cryogenic Germanium crystals. The high-purity Germanium detectors, as shown in Figure 3.1, have a mass of  $m = 320$  g and are of cylindrical shape. The diameter is 70 mm and the height is 20 mm. On the sides, the thickness reduces to 4 mm due to beveled edges in a  $45^\circ$  angle [142]. The detectors of EDELWEISS detect simultaneously two signals per event, the ionization signal, Section 3.1.1, and the heat signal, Section 3.1.2, per event. The double detection allows to deduce the deposited energy as it is described in Section 3.1.5.

### 3.1.1 Ionization channel

Bolometers are semi-conductor crystals in ultra-pure Germanium. The Germanium has a lot of advantages. First, it is possible to have crystals of an extremely intrinsic purity of  $N_{\text{acceptor}} < 10^{-10}$  and of a relatively high mass (kg). Furthermore the small gap between the conduction band and the valence band,  $0.75 eV_{ee}$  at 0 K [143], allows a great conversion efficiency of electronic energy into electron-hole pairs. The intrinsic fluctuation of the Germanium due to free charges, fluctuation which depends on  $T$ , is low,  $\sim 100 eV_{ee}$  for a deposit of 10  $\text{keV}_{ee}$  [144], and therefore

detection thresholds of the order of a few  $\text{keV}_{ee}$  are possible.

In Figure 3.1 is represented a Germanium detector as used in EDELWEISS-I and the first phase of EDELWEISS-II. On top and on bottom of bolometers are planar electrodes to collect charges. The electrodes are made of 100 nm thick Aluminum layers sputtered on the upper and lower side of the detectors. The top electrode is divided into a central part and a guard ring, electrically decoupled for radial localisation of the charge collection. Between the electrodes a moderate voltage between  $\pm 3$  V and  $\pm 9$  V is applied. The charge carriers (*i.e.* electron-hole pairs) created in the crystal by the particle interaction drift along the electrical field lines towards the electrodes where they are collected. The time interval between the interaction and the collection of charges depends on the location of the interaction relative to the electrodes [145].

The complete charge collection is essential to determine the type of interaction, whether electronic or nuclear recoil. However, incomplete charge collection can occur with three main causes:

- Presence of impurities: During their migration towards the electrodes, charge carrier can be trapped by impurities and induce the formation of space charges. To limit this effect, degradation or regeneration phases are conducted with  $^{60}\text{Co}$ , which emits two high energy  $\gamma$  (1.17 et 1.33 MeV). A regeneration lasts at least one hour between two data acquisitions, and occurs at minimum every 24 hour-period [146].
- Surface events: As already mentioned, electrons and  $\alpha$ -particles (with kinetic energies of several tens of keV) have a mean free path of only a few  $\mu\text{m}$ , a few nm, respectively. Therefore the interaction of these particles takes place in principle very close to the surface of the crystals [147]. It is possible that the created charge carriers are collected by the inadequate (or wrong-signed) electrode due to the proximity of the interaction to the electrodes. For these near-surface events, the measured ionization signal may represent for example only a half of the actual energy of the charge carriers. In [148] it is shown that introducing an additional amorphous layer between the electrodes and the crystal significantly reduces the collection of wrong-signed charges. An amorphous dead layer of either Germanium or Silicon is used for all EDELWEISS detectors and has a thickness of  $d \sim 60$  nm, see Figure 3.1.
- Electric field line irregularities: On the lateral sides, electric field lines can escape before they reach the electrodes. Therefore the lateral sides of the surface are beveled and a segmented electrode (center and guard ring electrodes, see Figure 3.1) is used to additionally acquire information on the position of the interaction. The beveled surfaces allow to have a more homogeneous field under the central electrode. Miscollection due to field inhomogeneities are on the guard ring and can be rejected afterwards. Moreover, the guard ring collects the radioactive background from the holders of the detectors and of the electronics, which are intentionally localised in this region.

To limit these effects, the electric field is maintained at a few V/cm. Altogether, in the data analysis a fiducial volume is defined, where the electric field is the most uniform, where a reliable charge collection is expected and where the detector is better shielded from its environment.

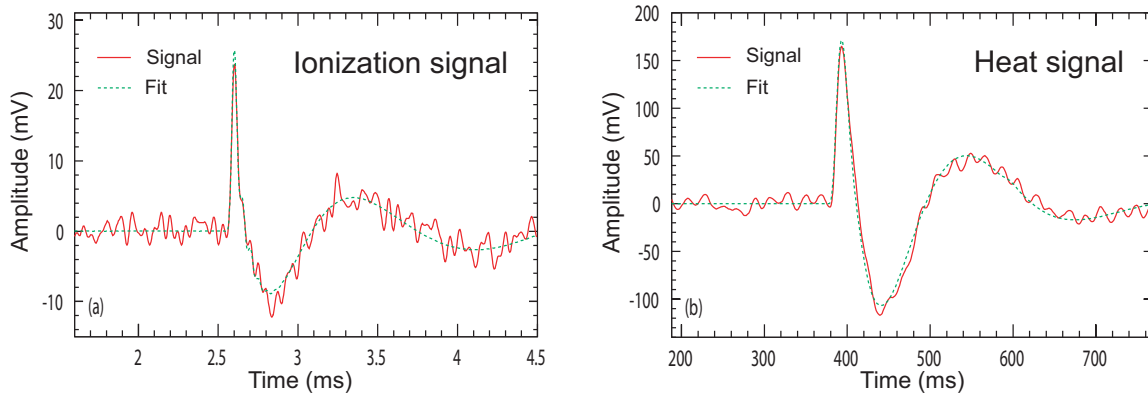


Figure 3.2: Example of filtered pulses for the ionization from the center electrode (left) and for the heat channel (right) from signals with an energy of  $\sim 10$  keV (full line) in a Germanium bolometer. The green dotted line is the corresponding fit. Figures from [149].

When an interaction occurs, depending on the type of recoil induced in the target, the number of electron-holes created per unit of energy is different:

$$N_I = \frac{E_r}{\epsilon} \quad (3.1)$$

where  $E_r$  is the initial energy deposit of the particle and the needed energy to create a charge carrier is  $\epsilon \simeq 3$  eV for an electronic recoil, and  $\epsilon \simeq 9$  eV for a nuclear recoil. For an equal energy deposit, a nuclear recoil will create 3 times less pairs than an electronic recoil. This difference is represented by the quenching factor  $Q = \epsilon_\gamma / \epsilon_n$ . We define then two numbers for the pair creation  $N_I^\gamma$  and  $N_I^n$ :

$$N_I^\gamma = \frac{E_r}{\epsilon_\gamma} \quad (3.2)$$

$$N_I^n = \frac{E_r}{\epsilon_n} = Q \frac{E_r}{\epsilon_\gamma} \quad (3.3)$$

The ionization signal is measured in mV after amplification in a charge amplifier, see Figure 3.2. It is then normalized thanks to calibration runs to be expressed in keV. Conventionally, for electronic recoils, we consider  $E_R = E_I$ , where  $E_I$  is the ionization energy in keV<sub>ee</sub>. Practically, the ionization signal is measured and then transformed in ionization energy thanks to an ionization normalization factor. This factor is determined during calibration runs with a well-known gamma source. This calibration procedure allows to express the ionization energy for any incident particle  $E_I \equiv \epsilon_\gamma N_I$ . Hence, the ionization energy for an electronic recoil  $E_I^\gamma$  and a nuclear recoil  $E_I^n$  are:

$$E_I^\gamma = \epsilon_\gamma \frac{E_r}{\epsilon_\gamma} = E_R \quad (3.4)$$

$$E_I^n = \epsilon_\gamma Q \frac{E_r}{\epsilon_\gamma} = Q E_R \quad (3.5)$$

with  $E_I = E_R$  for  $\gamma$ -particles.

### 3.1.2 Heat channel

In the following, the terms of temperature, heat and phonon often refer to the same quantity. The heat increase  $\delta Q$  is indeed linked to the variation of temperature  $\Delta T$  through the equation  $\delta Q = C \cdot \Delta T$ , where  $C$  is the heat capacity of a body. The phonon is a fictitious particle corresponding in quantum mechanics to the excitation of a vibration mode in a crystal. These excitations, once thermalized, carry the heat  $\delta Q$ . Immediately after the collision, the phonons are not thermalized,  $\delta Q$  and  $\Delta T$  are then not defined. The fastest thermic sensors can then be sensitive to athermal phonons, out of equilibrium; we then would talk about “phonon signal”. The slowest sensors are sensitive to thermalized phonons only; we then would talk about “heat signal”.

The principle of the measurement of the heat induced by the interaction of a particle is to measure the energy deposit of the particle in the target, which is entirely converted into phonons. A bolometer is made of two elements: An absorber in which the particles interact and deposit energy (where also the ionization energy is created) and a thermal resistor (or thermistor) which measures the induced rise of temperature, Figure 3.3b. The relation between the deposited energy and the rise of temperature is:

$$\Delta T = \frac{\Delta E}{C(T)} \quad (3.6)$$

where  $C$  is the total (absorber and sensor) heat capacity of a bolometer. The heat capacity of the absorber at very low temperature follows Debye’s law:  $C \propto (T/T_D)^3$ . For Germanium crystal, the Debye temperature is approximately  $T_D \simeq 360$  K. Consequently, to lower the heat capacity and achieve a measurable temperature rise for very small energy deposits, the crystals need to be operated at very low temperatures. In the EDELWEISS experiment, the base temperature is 10–20 mK. For example, for a Germanium bolometer of 300 g at a temperature of 20 mK, the interaction of a particle of 10 keV energy deposit induces a temperature rise of  $\sim 10 \mu\text{K}$ .

These detectors allow to reach a very low detection threshold ( $\sim 1$  keV) and energy resolutions of  $\sim 100$  eV. One technical challenge, however, is to reach detector masses of the order of 1 kg and to maintain  $C$  as low as possible to reach very low temperatures.

Depending on the type of sensor, as already mentioned, two types of phonons are detected: the primary phonons, called out-of-equilibrium or athermal, which conserve the information about the history of the event, such as the location of the interaction; and the thermalized phonons, for which the amplitude of the measured signal is directly linked to the energy deposit. In both cases, the energy deposit in the absorber induces a measurable variation of the impedance of the thermistor. The relation between  $R$  and  $T$  is [150]:

$$R = R_0 e^{\sqrt{T_0/T}} \quad (3.7)$$

where  $T_0$  is the characteristic temperature of the sensor. The values of  $R_0$  and  $T_0$  depend on the type the thermometer; typically a few Ohms for  $R_0$  and a few Kelvins for  $T_0$ . For a temperature of  $\sim 20$  mK, the impedance is of the order of 1 M $\Omega$ .

The thermistors of the EDELWEISS standard bolometers are 7 mm<sup>3</sup> Neutron Transmutation Doped (NTD) Germanium crystals glued on a sputtered gold pad on the main Germanium crystal, see Figure 3.3b. These NTD sensors are sensitive to the global temperature variations of the absorber, having no resolution power of the time evolution of the phonon signal and thus without the possibility to determine the position of the interaction, in contrast to the sensors described in Section 3.1.3.

The NTD sensors are polarised by individual constant currents  $I$ . In this manner the rise of temperature in the absorber gives rise to a variation  $\Delta R$  of the thermal resistance and induces a voltage fluctuation  $\Delta V$ , as shown in Figure 3.2 right, corresponding to the heat signal:

$$\Delta V = \Delta R \cdot I \quad (3.8)$$

For example, for the above mentioned temperature rise of  $\Delta T \sim 10 \mu\text{K}$ , the voltage change is  $\Delta V \sim 1 \mu\text{V}$ .

Though increasing the applied voltage, and thus the electrical field, would in principle improve charge collection for ionization, a moderate voltage, typically between  $\pm 3 \text{ V}$  and  $\pm 9 \text{ V}$  depending on the detector, is essential to limit additional heating of the crystal. This effect is generally known as the Neganov-Luke-effect [151]. It is analog to the Joule effect in metals. The charge carriers acquire energy during their drift in the crystal and release this energy via phonons. The released energy is proportional to the number of charge and to the applied voltage of polarisation:

$$E_{\text{Luke}} = N_I V = \frac{E_R}{\epsilon} V \quad (3.9)$$

The total measured energy  $E_{\text{tot}}$  is then equal to the sum of  $E_{\text{Luke}}$  and the recoil energy  $E_R$ , reduced by a potential heat quenching factor  $Q'$  in the case of a nuclear recoil:

$$E_{\text{tot}}^\gamma = E_R + \frac{E_R}{\epsilon_\gamma} V = E_R \left( 1 + \frac{V}{\epsilon_\gamma} \right) \quad (3.10)$$

$$E_{\text{tot}}^n = Q' E_R + \frac{E_R}{\epsilon_n} V = E_R \left( Q' + \frac{QV}{\epsilon_\gamma} \right) \quad (3.11)$$

Note that in Ge, as already mentioned,  $Q' \approx 1$ , see Equation 3.17.

For any incident particle, the normalized heat energy in keV is:

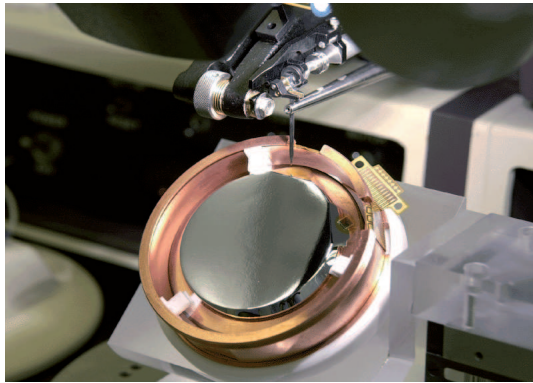
$$E_H = \frac{E_{\text{tot}}}{1 + V/\epsilon_\gamma} \quad (3.12)$$

Hence, the heat energy for an electronic recoil  $E_H^\gamma$  and for a nuclear recoil  $E_H^n$  is

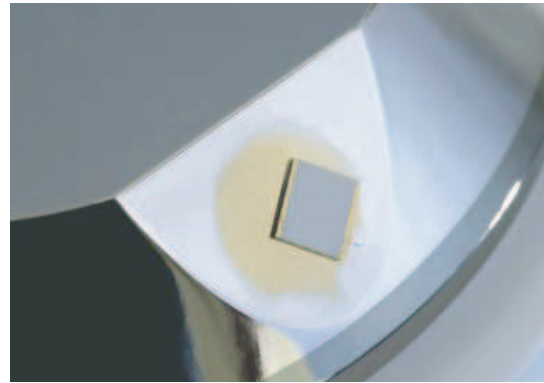
$$E_H^\gamma = E_R \frac{1 + V/\epsilon_\gamma}{1 + V/\epsilon_\gamma} = E_R \quad (3.13)$$

$$E_H^n = E_R \frac{Q' + QV/\epsilon_\gamma}{1 + V/\epsilon_\gamma} \quad (3.14)$$

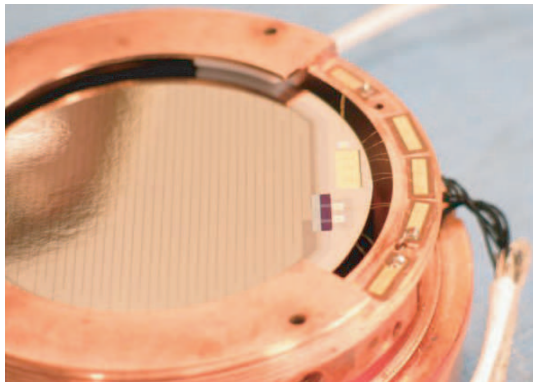
And note that  $E_H = E_R$  still holds for  $\gamma$ -particles.



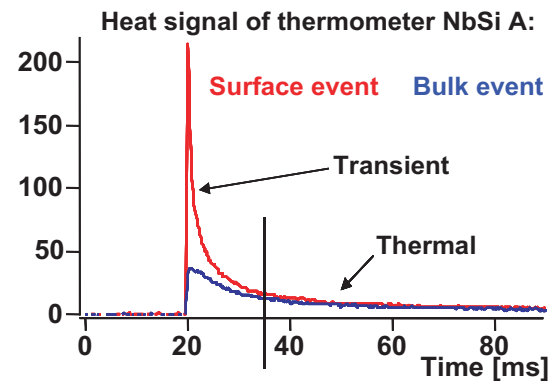
(a) Picture of a standard Germanium bolometer within holder structure and the NTD thermistor glued on a golden pad on the beveled part of the crystal.



(b) Close-up of the NTD thermistor.



(c) Picture of one of the 400 g Germanium detectors with NbSi thin film sensors as used in the EDELWEISS-II experiment.



(d) Heat signal as measured by one thermometer, called NbSi A, for two different event types (near-surface and bulk event).

Figure 3.3: The EDELWEISS Germanium bolometers. First line: Standard Germanium bolometer (GGA or GSA) as used in EDELWEISS-I and -II. Second line: The first new generation of bolometer for EDELWEISS-II, the Germanium NbSi detectors (NbSi). Pictures courtesy LSM & J.J. Bigot (CEA/IRFU), schematic from the EDELWEISS collaboration.

### 3.1.3 Case of: Germanium NbSi bolometer

To achieve the  $10^{-8}$  pb goal for the spin-independent WIMP-nucleon scattering cross section, the EDELWEISS-II experiment has to accumulate  $o(1000)$  kg·d of data without any event in the nuclear recoil band. Therefore, the contribution of background within the nuclear recoil band has to be less than  $0.001$  events·(kg·d) $^{-1}$ . However, if the contribution from  $\gamma$ -particles and neutrons (neutrons after vetoing from the muon veto) is  $< 0.001$  events·(kg·d) $^{-1}$  for each, *cf.* Chapter 4, the rate of  $\beta$ -particles, in the nuclear recoil band, is of  $0.04$  events·(kg·d) $^{-1}$  (2 events·(kg·d) $^{-1}$  in total) [153]. These  $\beta$  are mainly from  $^{210}\text{Pb}$  and are low penetrating events ( $\sim 700$   $\mu\text{m}$  for 1 MeV  $\beta$ -particle,  $\sim 25$   $\mu\text{m}$  for 100 keV) with a low ionization signal, which means most likely surface events with a miscollected charge. A standard Germanium bolometer without any device to reject surface events will get  $\sim 2000$  events during the 1000 kg·d of exposure.  $2000 \times 0.02 = 40$  events in the nuclear recoil band above 30 keV [153], which is not acceptable. Hence, bolometers which can localise precisely the position of events in the detectors to efficiently reject surface events have been developed for and tested in the EDELWEISS-II experiment.

The first new generation of detectors, called Germanium NbSi bolometers, are operated combining the two sensors for charge collection and temperature rise into one. Two heat channels and two ionization channels are measured simultaneously. This is achieved by an amorphous thin film, typically of 10–100 nm thickness, replacing the NTD-thermometer and the Aluminum electrodes on both sides of the Germanium crystal [150, 152]. These films are obtained by evaporating  $\text{Nb}_x\text{Si}_{1-x}$ , on the surface of the crystals, whose electric resistance is strongly dependent on the temperature. The variable  $x$  is the relative contribution of the elements and is typically around  $x \sim 0.085$ . The thin film electrodes are divided in a guard ring electrode and a central part through 0.5 mm spaced interleaved NbSi electrodes with 50  $\mu\text{m}$  digit width in a comb-like structure, see Figure 3.3c.

The advantage of these thin film phonon detectors is the possibility to determine the position of the interaction by comparing the signal ratio of each side of the crystal, which was not possible with the NTD sensors. A particle interaction in the Germanium crystal will produce out-of-equilibrium phonons diffusing away from the impact zone. In the case of a near-surface event, a large amount of these high-energy phonons will be trapped by the nearby NbSi layer and induce an athermal heat signal. This signal, as illustrated in red on Figure 3.3d, will be much larger than the one created by a bulk event of the same energy, illustrated in blue, while the thermal part related to the total energy deposit does not change. Using pulse shape analysis of the two NbSi thermometers allows effective identification of near-surface events [154, 155], which bad charge collection can be misinterpreted as nuclear recoil events.

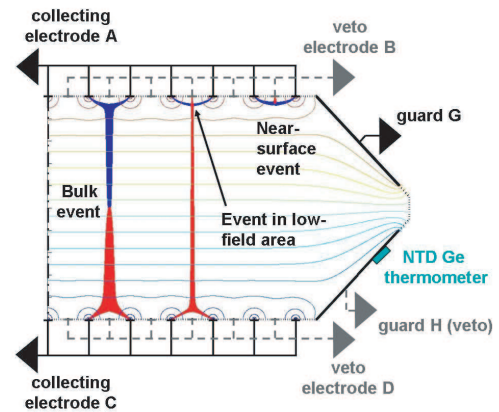
However, the results of the test phase at the LSM laboratory were not as successful as expected, and this detector development is not pursued any more.

### 3.1.4 Case of: Interdigitised bolometer

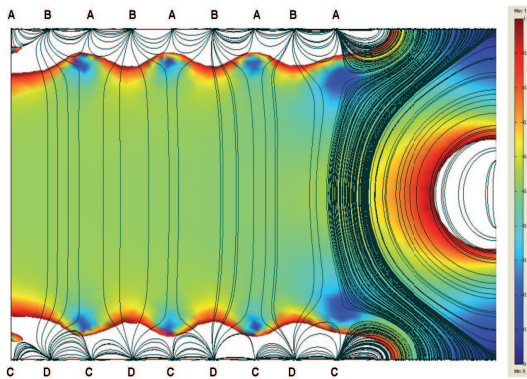
In addition to the new NbSi athermal phonon detectors, the collaboration developed for the EDELWEISS-phase II a new method of surface event rejection based on the ionization signal. The first prototype of this new InterDigitised bolometer (ID), called ID201, has been realized at CSNSM (Orsay) in the context of the R&D



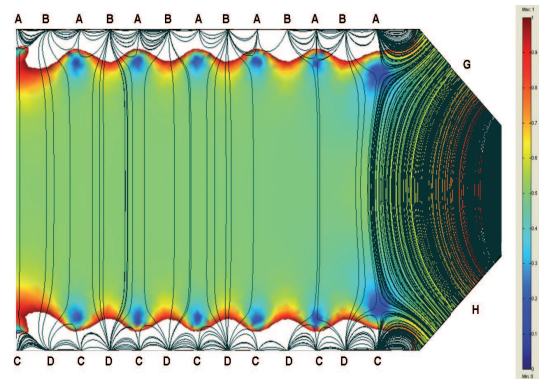
(a) Picture of one of the 400 g Interdigitised Germanium detectors.



(b) Schematic side view of half a Germanium crystal, shown are charge carrier trajectories for three representative events.



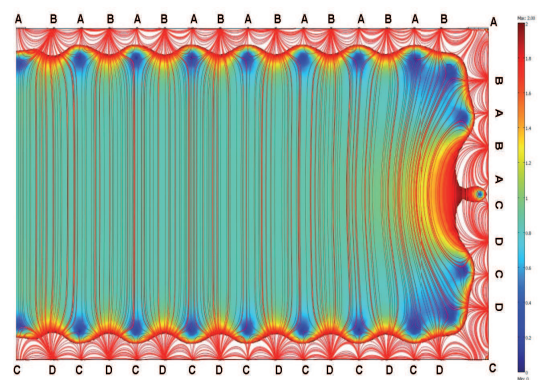
(c) Simulated field for an ID bolometer, if the edges were not 45°-beveled.



(d) Simulated field for an ID bolometer as used in the experiment.



(e) Picture of a 400 g Fiducial Interdigitised Germanium detectors.



(f) Simulated field for a FID bolometer.

Figure 3.4: The EDELWEISS-II Germanium bolometers. First line: Germanium InterDigitised detectors (ID). Second line: Simulated field for an ID bolometer, with and without beveled edges. Note that in the experiment ID do have beveled edges. Third line: Germanium Fiducial InterDigitised detectors (FID). Pictures courtesy LSM & J.J. Bigot (CEA/IRFU), schematic from [156], simulation pictures courtesy S. Marnieros.

program of EDELWEISS. ID201 is a Germanium crystal of a mass of  $\sim 200$  g, 48 mm-length diameter and 2 cm-height with a new electrodes design. The classical disk-shaped central Aluminum electrodes are replaced by interleaved concentric rings with typical width of  $200 \mu\text{m}$  in a distance of 2 mm, centered around a central disk of 1 mm diameter. The strips are alternately connected by ultrasound bonding to make two alternated subsets, see Figure 3.4a. Both faces are identical. As for standard bolometers, guard electrodes and a neutron transmutation-doped (NTD) Germanium thermometer complete the device. So there is a total of 6 different electrodes (2 subsets of strips on top, 2 subsets of strips on bottom, plus 2 guards, 1 on top and 1 on bottom) which can be independently polarised and read for the ionization channel, plus one heat channel, as shown in Figure 3.4b.

Different voltages of polarisation are applied on the electrodes to modulate the electric field inside the detectors. Symmetrically for each face, there is one collecting electrode and one veto electrode. One face collects electrons, and vetoes holes, the other one collects holes and vetoes electrons. The two guard electrodes are separated into one collecting electrode on top, and one veto on bottom. Charge carriers produced by a particle interaction are drifted along the field lines towards the collecting electrodes. Depending on the place of the energy deposition, different event populations are then obtained in the electrodes, see Figure 3.4b. In principle, one can discriminate four different types of events [153]:

- Bulk events deliver signals on both sides of the crystal: Electrons (holes) on the collecting electrode of one (the other) side.
- Near-surface events deliver signals only on one side: Electrons on the collecting electrode of a side, holes on the veto electrodes of the same side.
- Low field area events, which happen at the limit of the bulk and surface events, result in charge division between three measurement channels because of Coulomb's law: Electrons and holes are collected as for bulk events, but additionally holes or electrons are also collected in the corresponding veto electrodes of a side.
- Lateral events which occur in the guard area are collected in the specific electrodes of the guard.

It is thus possible to select potential signal events, for which there is no collection of charge on the veto electrodes and in guards. A fiducial volume can then also be defined as a volume in which there is no event with a miscollected charge. Apart from this technique, this bolometer type, as well as other ID with larger masses, *cf.* Section 3.1.6, have the same readout principle (ionization/heat combination) as other standard Germanium crystals, except that the number of electrodes allow to have a good rejection of surface events.

With Germanium NbSi bolometers, 2% of the  $\beta$  background still make a signal in the nuclear recoil band due to bad charge collections, which means 98% of passive rejection. With interdigitised bolometer, the obtained passive rejection is 99.998% [157], less than one  $\beta$  over 2000 events makes an event in the nuclear recoil band. And the threshold has been improved from 30 keV for standard bolometer to 10 keV [153, 157].

If, in terms of surface passive rejection, the interdigitised bolometers are the best tuned detectors so far in EDELWEISS-II, the fiducial volume of an ID is only of 50%

of the available Germanium volume, because of the beveled edges. The interdigitised bolometers have therefore been developed a step further. The beveled edges are used to homogenize the electric field. New bolometers, so-called Fiducial InterDigitised bolometer (FID), have their interleaved concentric strips continuing on the side, which is not beveled any more, as shown in Figure 3.4e. Figure 3.4c shows the simulated field inside an ID bolometer, if the edges were not beveled. One can see the field is not uniform on the side of bolometers (same problem with standard bolometers). To avoid this problem, the edges of all bolometers were so far beveled as shown in Figure 3.4d, but the available volume with a uniform field is reduced because of the slope of the edges. New FID bolometers have a pure cylinder shape. The field inside FIDs is more homogeneous than in ID and the available volume for the detection of “good events” is thus greater, Figure 3.4f.

The interdigitised bolometer type has been installed in 2008 for test purposes in EDELWEISS-II, at that time there were 3 ID among 30 bolometers. But since mid-2009 (from Run 12 on, which is not the study of this work), more than half of the detectors used are interdigitised bolometers. The rest is half fiducial interdigitised bolometers and half standard Germanium bolometers.

### 3.1.5 Event-by-event discrimination

From the interaction of a particle in the detector medium to the collection of the created charges into the different channels, the ionization and the heat energies,  $E_I$  and  $E_H$ , of the incident particle are defined and known, *cf.* Section 3.1.1 and Section 3.1.2, respectively. In this chapter, based on the experimental values  $E_I$  and  $E_H$ , we deduce how the recoil energy and the quenching factor of events can be extracted and used to discriminate between electronic and nuclear recoil.

#### Recoil energy $E_R$ and quenching factor $Q$

In summary, the ionization and heat energies after calibration and normalization can be written as

$$E_I = QE_R \quad (3.15)$$

$$E_H = E_R \frac{Q' + QV/\epsilon_\gamma}{1 + V/\epsilon_\gamma} \quad (3.16)$$

The recoil energy  $E_R$  is the value to be determined for the WIMP search. But the Equations 3.15 and 3.16 do not allow to determine  $E_R$  without any hypothesis on the ionization quenching factor  $Q$  and on the heat quenching factor  $Q'$ .

As we already mentioned, in Germanium [139, 140],  $Q'$  is expected to be 1. However, since the determination of the energy calibration for nuclear recoils, and then the energy threshold of the detectors, rely on the value of  $Q'$ , thorough investigations have been performed [140]. The heat quenching factor is indirectly measured combining direct measurements of  $Q$  and measurements of the ratio  $Q/Q'$  by neutron calibrations. For recoil energies between  $20 < E_R < 100$  keV, the result for the heat quenching factor is

$$Q' = 0.91 \pm 0.03 \pm 0.04 \simeq 1 \quad (3.17)$$

where the two errors are the contribution from the  $Q$  and  $Q/Q'$  measurements, respectively. In the following, we consider  $Q' = 1$ . The ionization quenching factor

$Q$  depends on the recoil energy. For Germanium, we use the Lindhard model [138]:

$$Q = \frac{k \cdot g(\epsilon)}{1 + k \cdot g(\epsilon)} \quad (3.18)$$

with  $\epsilon = \frac{11.5}{Z^{7/3}} E = 0.00354 E$  (keV),  $k = 0.133 \frac{Z^{2/3}}{A^{1/2}} = 0.157$ , and  $g = 3\epsilon^{0.15} + 0.7\epsilon^{0.6} + \epsilon$ . All into one, it corresponds to a quenching factor for ionization of

$$Q = 0.16(E_R)^{0.18} \quad (3.19)$$

This relation has been tested with direct measurements and holds at a 10 % level [139, 140, 149].

As  $Q' \approx 1$ , it is possible\* to determine a pair  $(E_R, Q)$  for each event from the ionization and the heat energy:

$$E_R = \left(1 + \frac{V}{\epsilon_\gamma}\right) E_H - \frac{V}{\epsilon_\gamma} E_I \quad (3.20)$$

$$Q = \frac{E_I}{E_R} \quad (3.21)$$

In case of miscollection of charges, the collected charges for a surface events correspond to only a fraction of the value of what they should be, *cf.* Section 3.1.1. The quenching factor becomes  $Q = Q_m < 1$ , typically  $0.3 \leq Q_m \leq 0.8$ , while the recoil energy remains the same.

$$E_I^m = Q_m E_R \quad (3.22)$$

$$E_H^m = E_R \frac{1 + Q_m V / \epsilon_\gamma}{1 + V / \epsilon_\gamma} \quad (3.23)$$

then plugging these equations in Equation 3.20, we have  $E_R^m = E_R$ . Surface events are thus translated into the  $(Q, E_R)$  plane with  $Q < 1$ , getting closer to the nuclear recoil region, but with correct reconstruction of the recoil energy  $E_R$ .

## Resolutions

Knowing the recoil energy  $E_R$  and the corresponding quenching factor  $Q$ , it is possible to make the so-called Q-plot. This plot gets even clearer, if the lines representing *e.g.* the  $1\sigma$ - and  $2\sigma$ -resolutions of the expected  $Q(E_R)$  for electron(gamma)-like events and for the neutron-like events are also shown.

For each channel, two values of resolutions are measured, one for the baseline during physics runs, one for the photo-electric peak of Barium during calibration runs.  $^{133}\text{Ba}$  emits  $\gamma$ 's of  $E_\gamma = 356$  keV. These  $\gamma$ -particles are penetrating enough to reach the detectors inside the cryostat, *cf.* Section 3.2. The resolutions vary together with the energy such as [158]

$$\sigma_{I,H} = \sqrt{\sigma_{I,H}^2(0) + a_{I,H}^2 E_{I,H}^2} \quad (3.24)$$

---

\* If  $Q' \neq 1$ , we need to define a new pair  $(x, y) = (Q' E_R, Q/Q')$ ,  $x \doteq E_R$  and  $y = E_I/x$ . If  $Q' > 1$ ,  $y$  is lower than the true value of  $Q$ , and  $x$  overestimates  $E_R$ . And vice-versa, if  $Q' < 1$ . In this case, the cross-section of interaction is overestimated [149].

with  $a_{I,H}$  being a factor determined from the resolution at 356 keV obtained with  $^{133}\text{Ba}$  calibration:

$$a_{I,H} = \frac{\sqrt{\sigma_{I,H}^2(356) - \sigma_{I,H}^2(0)}}{356} \quad (3.25)$$

$\sigma_I(356)$  is from the Gaussian fit in the ionization channel for Barium runs.  $\sigma_H(356)$  is deduced from the distributions of  $E_H/E_I$ , once  $\sigma_I(356)$  is measured.

The resolution of the ionization and heat baselines  $\sigma_{I,H}(0)$  is determined by looking at the distribution of the amplitude of events which trigger on another channel than the one under consideration. Events which are triggered by the studied channel are excluded. The value is then obtained from the Gaussian fit of this distribution. The resolution of the total ionization baseline is

$$\sigma_I^2(0) = \sigma_{\text{center}}^2(0) + \sigma_{\text{guard}}^2(0) \quad (3.26)$$

This equation is also true for  $\sigma_I^2(356)$  at 356 keV.

Finally, the equations allowing to express the variation of  $\sigma_{Q_{\gamma,n}}$  and  $Q_{\gamma,n}$  depending on  $E_R$ ,  $\sigma_I$  and  $\sigma_H$  are

$$\langle Q_{\gamma} \rangle = 1 \quad (3.27)$$

$$\sigma_{Q_{\gamma}} = \frac{1 + V/3}{E_R} \sqrt{\sigma_I^2 + \sigma_H^2} \quad (3.28)$$

$$\langle Q_n \rangle = \alpha (E_R)^{\beta} \quad (3.29)$$

$$\sigma_{Q_n} = \frac{1}{E_R} \sqrt{\left[ \left( 1 + \frac{V}{3} \right) \langle Q_n \rangle \sigma_H \right]^2 + \left[ \left( 1 + \frac{V}{3} \langle Q_n \rangle \right) \sigma_I \right]^2 + C^2 E_R^2} \quad (3.30)$$

These resolutions define the so-called gamma band and nuclear recoil or neutron band in a Q-plot. The ionization quenching factor of  $\gamma$ -like events, in the Equation 3.27, is set to 1 by definition. The Equation 3.29 corresponds to the Equation 3.19 with  $\alpha = 0.16$  and  $\beta = 0.18$ . They are the mean values for the electronic and nuclear recoil regions. The constant  $C = 0.035$  in Equation 3.28 is introduced in the reference [154, 159] to describe the fluctuations of the quenching factor  $Q_n$ . These fluctuations are due to the multiple diffusion and to the stochastic nature of the process of stopping nuclear recoil in Germanium. These effects add up to the width  $\sigma_{Q_n}$ . Furthermore,  $Q_n$  and  $Q_n/Q_{\gamma}$  are estimated by neutron calibrations, as previously mentioned. Multiple scatterings of neutrons alter a bit the nuclear recoil band by decreasing  $Q_n$  and increasing  $\sigma_{Q_n}$  [159]. As WIMPs do not multiply scatter, we should then redefine our nuclear recoil region. This work has been made in [154]. The conclusion is that to consider the nuclear recoil band for WIMPs to be the same than the one for neutrons is acceptable and conservative.

### 3.1.6 Bolometer conventions

The different detectors are named and consecutively numbered according to their composition. GGA crystals are Germanium crystal with an additional hydrogenated amorphous Germanium layer under the Aluminum electrodes, while GSA detectors have an amorphous Silicon layer. PGSA are the same kind of bolometer, but of smaller size (*petit* GSA for small GSA). Ge73 is also a small bolometer, but made of the Ge isotope  $^{73}\text{Ge}$ . Gc bolometers are Ge crystals with only a heat channel.

(F)ID stands for (Fiducial) Interdigitised detector, with a numbering less than 100 for a mass of 320 g, greater than 200 for a mass of 200 g, and greater than 400 for a mass of 400 g, *cf.* Section 3.1.4.

In EDELWEISS-II, there are too many bolometers to be handled by only one computer. Thus, bolometers are combined in group of up to 10 per acquisition computer. Each computer has its proper and independent DAQ. When one channel of a detector of a DAQ computer triggers, the data of the bolometers on this computer are registered independently from what happens in the DAQ of other computers. There are as many runs as DAQ computers.

But note that a run is not a Run. In the data acquisition language, a measuring period over a few weeks/months is called a Run. A Run is made up from typically day-long runs intersected by regeneration periods of  $\sim 1$  h. In between two physics Runs are generally a Research and Development (R&D) Run to install and test more bolometers and improve the setup. Therefore the numbering of Runs is odd for R&D Runs and even for physics data Runs.

The configuration of bolometers during the physics Run 8, 10 and 12 are shown in Figure 3.5, 3.6 and 3.7, respectively. There are exclusively standard bolometers during Run 8, except for one ID, which was implemented for test purpose. Run 8 reproduced EDELWEISS-I on a larger scale. The number of bolometers is growing in between Run 8 and Run 10, with the installation of NbSi and ID bolometers. However, there are less bolometers during Run 12, as the system switched to almost exclusively high performing ID bolometers. During Run 12, as they are well known, the standard bolometers are in as reference bolometer to witness the system behavior and test the new electronics.

### 3.1.7 Data acquisition

For each detector, the data acquisition (DAQ) has to generate from 3 up to 7 channels per bolometer: heat, ionization from the center electrode and ionization from the guard electrode in the case of a standard Germanium bolometer; ionization from the collecting electrode of a side, ionization from the veto electrode of the same side, these two but for the other side, and the same again which correspond to the guard and finally heat in the case of an interdigitised bolometer. The DAQ of EDELWEISS is described in detail in [149, 160].

Basically when one channel of one detector triggers, all the other channels of all detectors are registered and read out as one event. The ionization signal is saved in a time window of 10 ms, the heat signal over 1 s. Besides the physics signal, the baseline before the event is also registered, which is called the pre-trigger. The main action is to choose between an ionization or a heat trigger.

The risetime of the ionization signals is  $\sim 1000$  times faster than the one for the heat signals. The advantage is that the time of an event can be known very accurately, and the search for the heat signal is then facilitated. However, the data considered in this work have a heat trigger because of the following reasons:

- The baseline resolutions of the heat channel are typically twice as good as those of the ionization channel.
- The ionization signal of a nuclear recoil event in Germanium is 3 times lower than the one of an electronic recoil with the same energy deposit, while the heat signals have the same amplitude. Therefore the trigger is more efficient

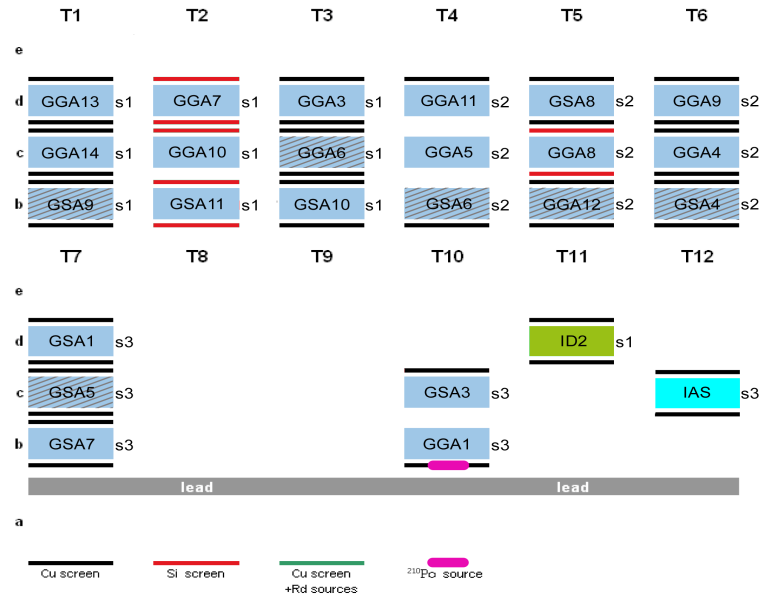


Figure 3.5: Configuration of bolometers during the physics Run 8. Only three lower layers are used (one can add up to 10 layers of bolometers). There are exclusively standard bolometers (in blue) in the first six column, and one ID (in green) in column T11, which was implemented for test purpose, and a sapphire bolometer (in turquoise blue) in column T12. The striped bolometers are troubled bolometers (a channel missing, electronic problems), which finally did not record data. The labeling starting with a “s” on the right of a detector corresponds to the DAQ computer, with which the detector is linked: s1 for computer 1, s2 for computer 2 ...

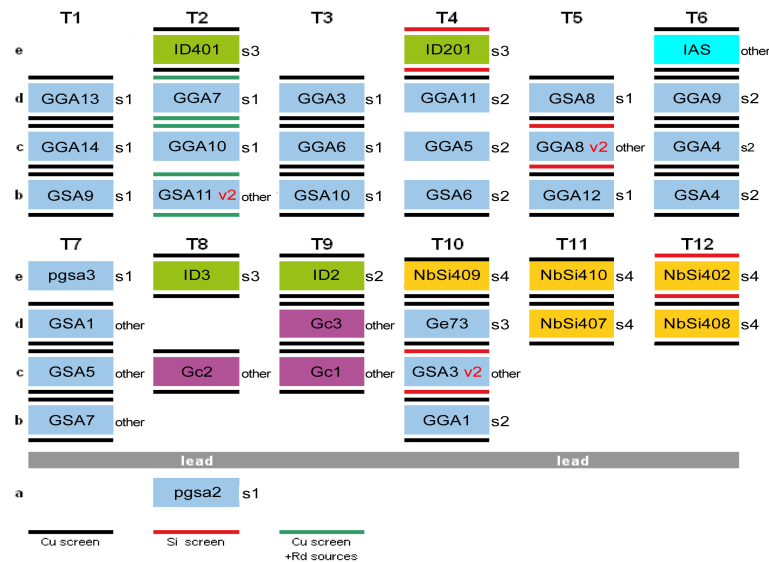


Figure 3.6: Configuration of bolometers during the physics Run 10. In addition to the standard Germanium bolometer (in blue), more detectors are installed, especially NbSi (in yellow) and ID (in green) bolometers. In purple are pure heat Germanium bolometers, and in turquoise blue is a sapphire bolometer. Detectors with the label “v2” are those mounted with a new readout electronic card and the label “other” is for those with a new readout electronic chain for test purposes.

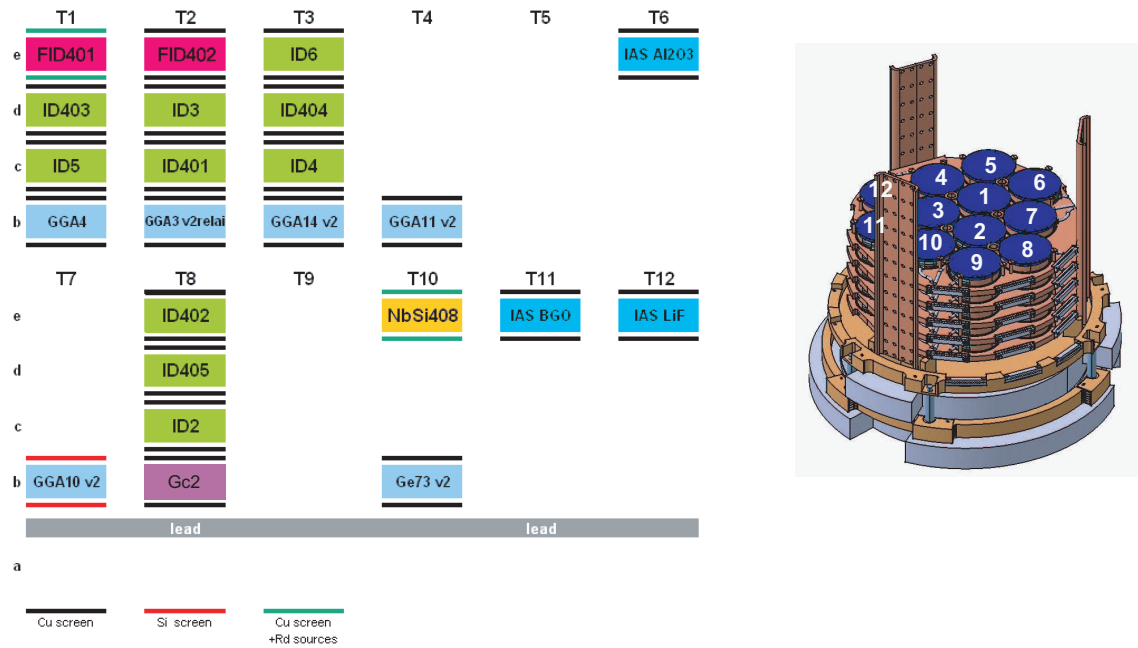


Figure 3.7: *Left: Configuration of bolometers during the physics Run 12. For Run 12, the system switched to almost exclusively high performing ID (in green) and FID (in magenta) bolometers. They are still some standard Germanium (in blue), one NbSi (in yellow) and one pure heat (in purple) bolometers, and different sapphire bolometers (in turquoise blue). During Run 12, as they are well known, the standard bolometers are in as reference bolometer to witness the system behavior and test the new electronics. Detectors with the label “v2” are those mounted with a new readout electronic card. Right: Schematic of the opened cryostat of the EDELWEISS-II experiment. The cryostat can house up to 10 layers of 12 bolometers.*

for the small amounts of energy deposit and does not inherently depend on the type of interaction.

The main problem of the heat trigger is the search of the corresponding ionization signal which occurs before the heat signal because of its very fast risetime. This problem has been worked out in [160]. The conclusion is that the maximum time interval between an ionization and a heat signal is 20 ms. Thus, as soon as a heat signal passes the threshold, the acquisition software looks back up to 20 ms in the ionization signal buffer for the corresponding signals. This is made by comparing the data with a reference event built during the calibration runs. Once the event with the highest amplitude is found, all other events are synchronized to this one and saved on disk.

The data are saved in different formats per run:

- raw files: There are some event files per run, with all the necessary information for the analysis.
- log file: There is one “log” file, which is the monitoring file of the DAQ.
- seuils file: From the Run 10 on of EDELWEISS-II, there is one “seuils” file, which enumerates regularly the thresholds applied for each bolometer during the physics run. This threshold can be changed during a run, this is the so-called adaptative threshold.
- ntp file: There is one “ntp” file per run. Ntp files are sort of pre-analysed event files to monitor the behavior of bolometers.

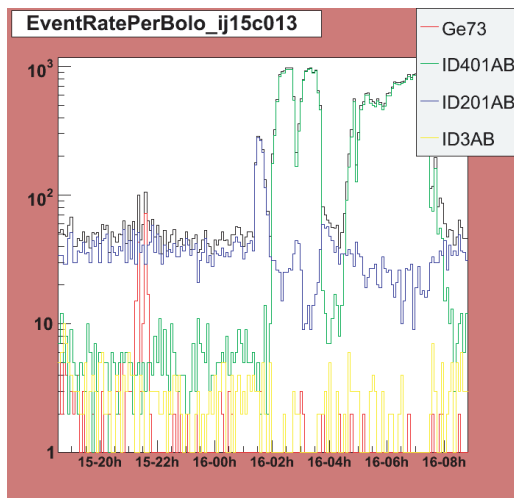
### 3.1.8 Online monitoring

The ever growing number of bolometers (and channels) leads to develop an automatic online monitoring to supervise the bolometers’ behavior during data acquisition and to fast and timely check the quality of the acquired data. To get acquainted with the bolometer system of EDELWEISS-II, for which coincidences with the muon veto are later described, *cf.* Chapters 5 and 6, the online monitoring software was tackled within this work during two 3-month stays at the IRFU<sup>†</sup> CEA/Saclay (France) in winter 2007 and winter 2008, and was further developed by Eric Armengaud.

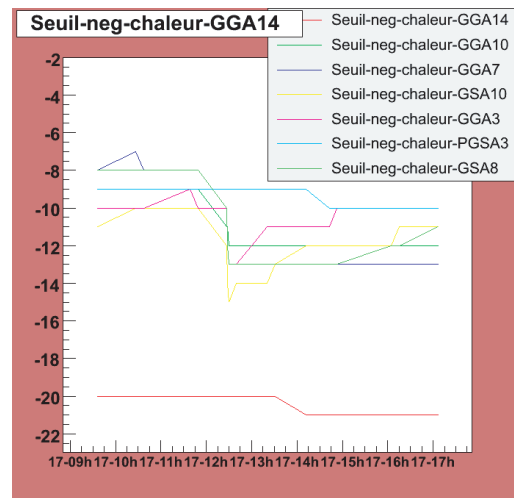
The monitoring software transforms the latest ntp files into ROOT-files [162] and creates usual plots, which are then published online on an internal EDELWEISS website [163]. All data remain local on a computer in the data acquisition room at LSM. The bolometer monitoring runs every hour. These plots are as various as the global rate of the system, bolo-per-bolo event rates (Figure 3.8a), thresholds per bolo (Figure 3.8b), ionization signal from guard *vs.* center per bolo (Figure 3.8c), heat from one temperature sensor *vs.* the other one for NbSi bolometer (Figure 3.8d), heat *vs.* ionization (*cf.* Chapter 6), baselines ... The monitoring script also copies every night the run files of the day to the IN2P3<sup>‡</sup> Computer Center in Lyon, where all EDELWEISS data are stored, and provides a backup for CEA/Saclay.

<sup>†</sup> IRFU: Institut de Recherche sur les lois Fondamentales de l’Univers, CEA: Commissariat à l’Énergie Atomique.

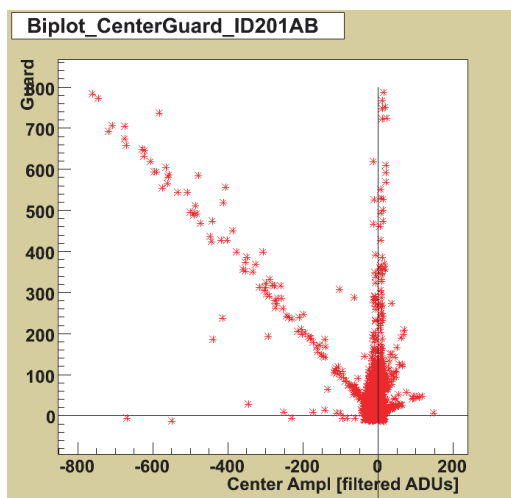
<sup>‡</sup> IN2P3: Institut National de Physique Nucléaire et de Physique des Particules



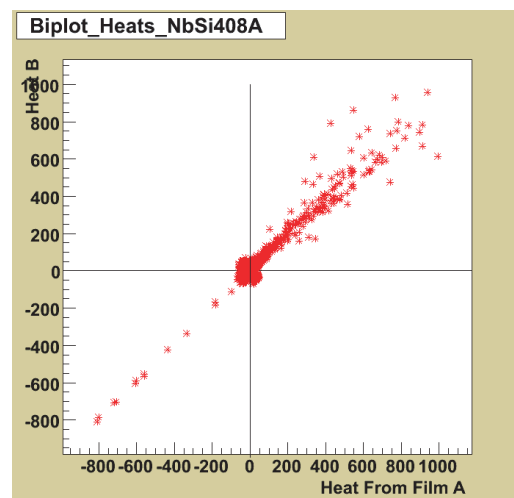
(a) Histogram of the event rate per bolometer during run "ij15c013" (2008, November 15<sup>th</sup>, DAQ on the 3<sup>rd</sup> computer, 13<sup>th</sup> file of the run). 4 different bolometers are superimposed.



(b) Plot of the threshold per bolometer during a run. 7 different bolometers are superimposed.



(c) Biplot of the ionization signal from guard vs. the ionization signal from center for the interdigitised bolometer ID201, in ADC unit (ADU).



(d) Biplot of the heat signal from the temperature sensor B vs. the heat signal from the temperature sensor A for the Germanium NbSi bolometer NbSi408, in ADC unit (ADU).

Figure 3.8: Examples of plots from the online monitoring of bolometers. The plots of the online monitoring allow a fast and timely cross-checked of the acquired data.

## 3.2 EDELWEISS-II cryostat and shielding

In the WIMPs hunting, the principal limitation is the background, especially from neutron-like events. To be shielded against most of the cosmic rays, the EDELWEISS experiment is sheltered under  $\sim 4600$  *mwe* rock shielding. Still there is natural radioactivity in the rock and in material around bolometers, that need further reduction strategies. The following sections describe the EDELWEISS-II setup. A brief description of EDELWEISS-I is made while recalling the results in Section 3.5.

### 3.2.1 Reversed cryostat

The EDELWEISS-II cryostat has a total volume of  $V \sim 100$  l and can accommodate up to 120 bolometers with a total mass of approximately 30 kg. It is a nitrogen-free system, using three pulse tubes to cool the 100 K and 20 K copper screens around the detectors and a He reliquifier to reduce the He consumption. Its operating temperature of  $T = 10$  mK with fluctuations less than  $\pm 10$   $\mu$ K is reached by the principle of a dilution refrigerator.

The characteristic of this cryostat is that it has an inverted geometry, with the experimental chamber on the top of the structure, see Figure 3.9. It simplifies the installation and maintenance of the detectors as well as reduces the susceptibility to vibrations by the pumping system. Furthermore, since the complete cryogenic pumping system with all supply tubes is below the bolometers, the shielding of the detectors is more uniform. The copper walls of the cryostat are the so-called self-shielding. Nevertheless, inside the cryostat, in addition to the radiopurity selection of materials, bolometers have individual copper casings, plus some archaeological lead underneath to protect against noise and radioactivity from the electronics nearby the crystals.

### 3.2.2 Lead and polyethylene shielding

Then, from inside to outside, 20 cm of lead and 50 cm of polyethylene follow. Since all materials in the close vicinity of the detectors are subject to radiopurity limitations, the innermost 3 cm of the total 36 tons of lead comes from archaeological sources to avoid the 46 keV gammas from the decay of  $^{210}\text{Pb}$ . [164].  $^{210}\text{Pb}$  has a half-life of  $t_{1/2} \sim 22.3$  y. Aged over several centuries, the  $^{210}\text{Pb}$  content is then negligible. The archaeological lead used for EDELWEISS was retrieved from a sunken antique roman ship [165]. The contamination by  $^{238}\text{U}$  in this lead is less than 1 ppb.

Polyethylene is a Hydrogen-rich moderator, which moderates and absorbs neutrons from natural radioactivity in the rock surrounding the underground laboratory. The mean neutron energy of these processes is of a few MeV. Then, after the moderator material, most of the neutrons have an energy which is not sufficient to penetrate the lead shielding. For neutrons with a kinetic energy less than 10 MeV, the use of 50 cm of polyethylene allows to reduce the rate of neutrons by a factor of  $\sim 1000$  [166].

To allow easy access to the cryostat for installation and maintenance purposes, the experimental setup of EDELWEISS-II is separated into two horizontal levels. The lower part at ground floor houses most of the cryogenic system. The upper part, first floor, is placed in a permanent cleanroom of class 10,000 <sup>§</sup> and consists of

<sup>§</sup> Cleanrooms are classified according to the number and size of particles permitted per volume



Figure 3.9: *Cryostat of the EDELWEISS-II experiment, closed (left) and opened (right). The cryostat can house up to 10 layers of 12 bolometers. On the picture on right, the copper casings for each bolometer and the layer of archaeological lead are to shield against the innermost electronics. Pictures courtesy M. Horn and courtesy LSM & J.J. Bigot (CEA/IRFU).*

two movable wagons with the lead and polyethylene shielding as well as the muon veto mounted on tracks. If the cryostat has to be opened, an additional cleanroom environment is set to a temporary class 100.

Furthermore the clean room is in a “deradonised” air flow. Radon is a radioactive noble gas, produced during the decay chain of  $^{238}\text{U}$ .  $^{222}\text{Rn}$  mixes itself with the air of the laboratory and can then contaminate the Germanium bolometers. With a half-life of 3.8 days, it decays into  $^{210}\text{Po}$  and  $^{210}\text{Pb}$ , leading to surface events in the detectors. The Radon rate is of  $10 \text{ Bq/m}^3$  in the LSM laboratory. In the clean room, the deradonised air contains  $\leq 0.01 \text{ Bq/m}^3$  and is monitored by a dedicated detector.

### 3.3 Muon veto system

Everywhere in the rock, as well as everywhere in the set-up (especially in high-Z materials such as the anti- $\gamma$  lead shielding), muons interact and induce neutrons. The muon-induced neutrons have an energy of far more than 10 MeV, but can lead to the production of secondary neutrons with energies below 10 MeV, which will then fall into the region of interest for WIMPs. Tagging the original muon reduces significantly the effect of this background.

The group at Forschungszentrum Karlsruhe and Universität Karlsruhe built and operates an active muon veto system [167]. The muon veto is the extreme outside

---

of air. Class 10,000 or class 100 (US FED STD 209E) denotes the number of particles of size  $0.5 \mu\text{m}$  or larger permitted per cubic feet ( $\text{ft}^3$ ) of air, corresponding to the ISO-146441-1 standards ISO-7 and ISO-5, respectively.

layer of the EDELWEISS-II experiment, as shown in Figure 3.10.

The installation of the muon veto system in the Modane Underground Laboratory started in May 2005 with the mounting of the lower part of the veto surface. In August 2005, the second and final part of the veto modules was installed. This comprises the electronics system and cabling of almost all modules, so that the muon veto system was ready for data taking in September 2005. The muon veto system is the central study of this work and is therefore discussed in detail in the following subsections.

### 3.3.1 Mechanical setup

The veto system consists of 42 plastic scintillator modules of 65-cm width, 5-cm thickness and lengths between 2 m and 4 m, as illustrated in Figure 3.11. The total surface is about 100 m<sup>2</sup> surrounding almost hermetically the outer polyethylene shielding of the cryostat to maximize the muon detection efficiency. Each scintillator module is read out at both ends, yielding 84 channels for the muon veto data acquisition system.

The modules have been used similarly as a muon veto counter in the KARMEN experiment [168]. A complete description of the modules, measurements of the effective attenuation length and spectral quantum efficiency can be found in [169] and references therein. However, for the EDELWEISS-II setup, a complete new mechanical construction has been developed for the scintillator modules.

The muon veto is built on two levels, and the modules separates into two open cubes. The lower level, at ground floor, is made by four sides and one bottom wall and houses the cryogenic pumping system. Except for the Bottom modules, all modules of the lower level are vertically oriented along their longer side. The North lower side has one module missing in its middle to let the cryogenic tubes reach the He bottle. The upper level, on the first floor, is made by four sides and one top wall and surrounds the passive shielding in the clean room. The modules of the East and NEMO<sup>¶</sup> upper sides are also vertically oriented along their longer side. However, the modules of the North and South upper sides are vertically oriented along their shorter side, so that the system can be opened in two symmetric wagons to access the cryostat and the bolometers, if needed. The Top and Bottom walls are horizontally oriented and have their modules directed perpendicularly in the North-South and East-NEMO directions, respectively. The different orientations lead to different track length in the muon veto, and to different energy deposit, as detailed in Chapter 4. The muon flux dependence on the zenith and azimuthal angle due to the rock overburden leads also to different rates in the different veto modules.

Both ends of the 42 modules have individual and specific high voltage settings, which were fixed during the calibration of the module at Forschungszentrum Karlsruhe [170]. These voltages have been tuned slightly (a few tens of Volts with typical values of  $-1500$  V) since the installation in the underground lab for optimization, *i.e.* reducing sparks on the photomultipliers, or due to the ageing of the veto module, *cf.* Section 4.2.

<sup>¶</sup> East/Ost/Est opposing to West/West/Ouest were too confusing during the building in the lab. To simplify the communication and to avoid accent confusion, the West side of the EDELWEISS experiment is called NEMO, which is the closest (and biggest) experiment standing in the West direction.

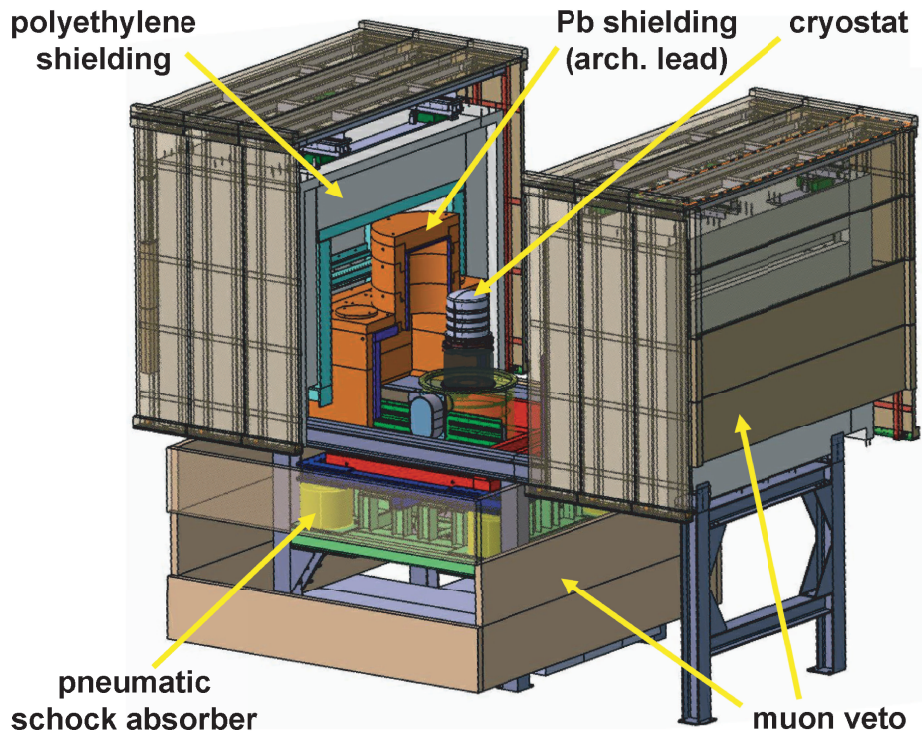


Figure 3.10: Schematic view of the passive shielding, the mechanical construction and the muon veto detector of EDELWEISS-II.

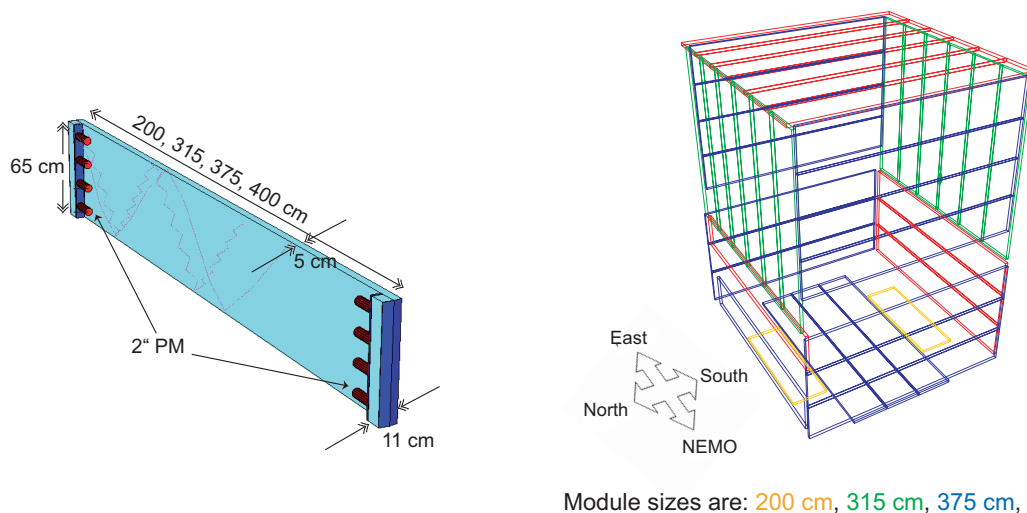


Figure 3.11: Muon veto system of EDELWEISS-II. Left: Schematic overview of a single plastic scintillator module. When installed, modules are wrapped into Aluminum, an individual black plastic protective foil against light, and another thick foil, which also enclosed the whole side the module belongs to. Right: Simulation of the muon veto realized in C++/ROOT. In the simulation, the shape of the modules is simplified to rectangular parallelepiped (box). The color are according to the length of the module as mentioned in the picture.

The electronic readout and data acquisition has also been adjusted to the new setup. The electronics as well as the data read-out of the muon system are fully independent from the bolometer system but linked via a fiber connection transferring the overall experiment clock as well as some restricted information about muon hits. The veto data are stored unrestrictedly and rejection of bolometer events with veto activity is performed offline, as described in Chapters 5 and 6.

### 3.3.2 Data acquisition

Basically, when a particle hits a muon veto module, it creates a scintillation signal collected by the photomultipliers at each side of a module. Then, this electronic signal goes through an electronic chain to be recorded, see Figure 3.12.

The signal from the photomultipliers is duplicated: One will be recorded as scaler data, see Section 3.3.3, the other one as event data, *cf.* Chapter 4. The signals coming from the 84 channels are split into 6 discriminator cards, which have all a threshold specified to 150 mV. Then, the discriminator cards spread the signal to send a copy to the scaler cards, another one to the time-to-digital converter (TDC) and a last one to the logical units (LU). The scaler cards count the number of events happening on a side of a module, no coincidence required, and then it is saved in a scaler data file. The TDC provides time information along the module axis about the events. The LU transfers the signal after selection to the central veto logic card, which makes the decision to save the events. In the same time, the signal passes through the analog-to-digital converters (ADC) to collect energy information about the events.

A signal is saved as an event in an event data file, when the central veto logic card has an internal coincidence in a module (the signals from each side of a module in coincidence) within a 100 ns time window. This coincidence creates a particular TDC channel, called the common stop, which will trigger back the TDC. In parallel, the real time of the event, coming from the time board and connected to the time board of the bolometer system, is also saved in a 10  $\mu$ s scale (for further coincidence(s) with bolometers for example, *cf.* Chapters 5 and 6). To save an event, the whole system is controlled by a trigger of the veto central logic card, so that TDC, ADC and time information are saved together in an event data file.

The DAQ has been further developed since the installation of the modules in the lab. On the contrary to bolometers, the muon veto DAQ is very light. Ssh-tunnel connection and a *screen* script are enough to run the program. *Screen* is a full-screen window manager that multiplexes a physical terminal between several processes, creating virtual shells. The program continues to run when its window is currently not visible and even when the whole *screen* session is detached from the user's terminal. Thus, the DAQ runs as a background process on the computer of the veto system at LSM. The parameters (length of DAQ, thresholds, online printout of events, registration of the scaler file ...) of a new DAQ are specified in an input file. And the DAQ software stores in an output file the messages created during the running of the data acquisition, such as the initialization of the cards and the printout of typically every 50<sup>th</sup> event, as specified in the input file, for monitoring purpose. The specification of the high voltage (HV) of the modules is set and controlled by a different dedicated software.

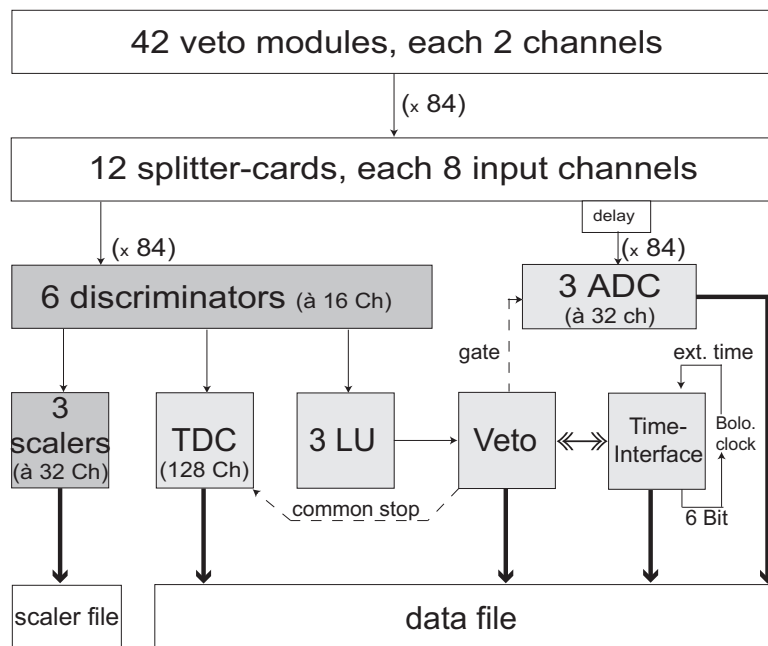


Figure 3.12: *Electronic chain of the muon veto system.*

Bit31				Bit0
<i>Event number</i>				
	<i>Geometry</i>	<i>Multiplicity</i>	<i>Size</i>	
Time stamp 1				
Time stamp 2				
Time stamp 3				
TDC Header				
Channel #1				
...				
TDC EOB				
ADC Header				
Channel #1				
...				
ADC EOB				

Table 3.1: *Structure of the header (2 first lines) and of the data blocks of the muon veto events. Each line is a 32-bit word.*

The data are saved in three different formats per Run<sup>||</sup>: some data event files, a scaler file and a parameter file.

The data files have all necessary information for data analysis, as detailed in the Table 3.1. The header of an event is made of the variables event number, geometry, multiplicity and size. The geometry gives a reference to the side(s) of the muon veto system which got a hit. The multiplicity is the number of TDC with a signal, plus the TDC of the common stop. For example, an event, which makes an internal coincidence in a module, has the two TDC of each sides, plus the common stop, which means a multiplicity  $multi_{\text{veto}} = 3$ . The size is the size of the data blocks. After the header is registered the time stamp of the event, which comes from the bolometer system via a fiber connection. The time stamp is a pattern of 48 bits of 64-ns width with an additional start bit. As the veto system runs on a 32-bit processor, the time stamp is split into three times 16 bits and saved into three 32-bit words. The time stamp has a precision of 10  $\mu\text{s}$ . The local computer time, which have only a precision of the order of 1 s, is not registered with the event, except in the very rare case when no time is transferred from the bolometer system. In this case, the time is registered using all the 32 bits of the first word. Then, are saved the data blocks, which contain the information about the TDC and ADC entries. Data files have a 8-hour-length, and there are up to 99 event files in a Run. If more, a new Run starts (so a new Run does not mean a restart of the DAQ).

The scaler file is used for monitoring and is registered every 15 min, or as specified into the input file of the DAQ software. If a new Run starts during a continuous running period, a new scaler file is created in the new Run folder. The parameter file summarizes the parameters of a running period. It is created at the beginning of the DAQ program from the input file and is then exported to the new Run folder.

Data acquisition typically runs continuously but is interrupted *e.g.* when the HV has to be switched off. HV are switched off for the safety of the people in the clean room and to protect the veto system from disturbances, when critical works are being performed or when there are maintenance periods on the bolometers. On Figure 3.13, one can see long periods with almost continuous data acquisition interrupted by electric power cuts in the LSM laboratory as well as extensive work going on in the clean room of the experiment, when the high voltage of the veto system was switched off for safety reasons. Above the rather constant raw data rate, there are periods with much higher event rates which could be identified as maintenance intervals of the cryostat/clean room in which the upper (mobile) veto modules were moved with the polyethylene shielding, or when radioactive sources were being manipulated.

Since July 2006, the muon veto system is stable in terms of hardware, we consider the recorded event data as exploitable since then.

### 3.3.3 Online monitoring

The monitoring of the muon veto system is made with the data collected through the scaler cards. A scaler card is a counter. The scaler data are raw data made of any hit in the system, where no module coincidence is required, and are helpful to monitor the system. With a rate of 8 kHz for the overall system, which can be arbitrary changed with the settings of the threshold, these are mainly composed

<sup>||</sup> On the contrary to the bolometers, a Run is made of some files and a continuous period of data acquisition, *i.e.* a running period, can stretch over several Runs during some months.

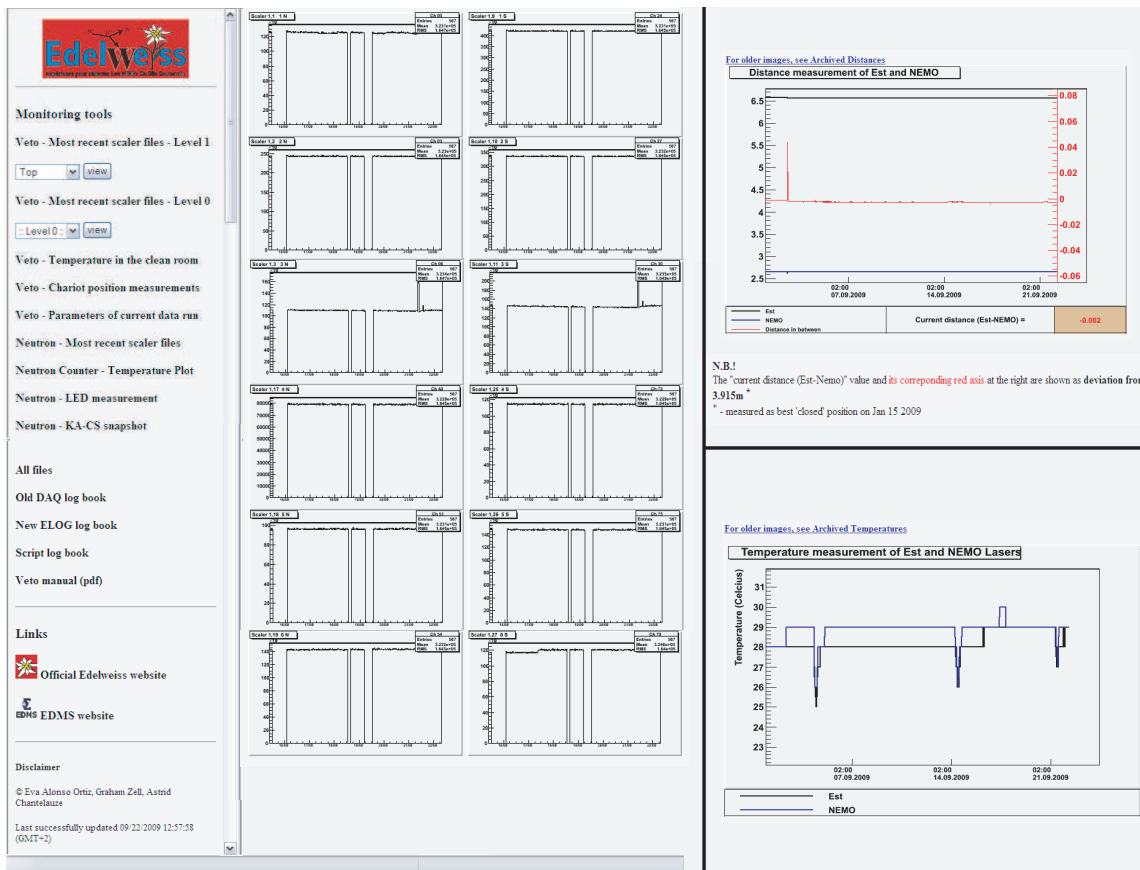


Figure 3.13: *Muon veto monitoring website. Left: Plots from the scaler files for the Top modules. Top-right: Measurement of the position of the veto wagons via the two laser devices. Bottom-right: Temperature in the clean room from the thermometers of the two laser devices. Figure from [171].*

of background. These data are saved into scaler files, usually read out and reset every 15 min.

The monitoring program developed within this work creates the plots associated with each side of each module to have an overview of the modules' behavior over long periods, see Figure 3.13. The monitoring runs every two hours. Every two hours, the updated plots of the latest scaler file(s) are created and then transformed via html routines to be online [171]. A history of the plots of the completed Runs is saved and is also available online, as well as the parameters of the current running period. The script, the plots and the website are on a server at Forschungszentrum Karlsruhe (FZK), while the data are stored at LSM. The script deals with all the passwords of the different servers, and backups the latest event files at FZK. Moreover, if the scaler files or the event files are not increasing, it sends and creates on the website alert messages to warn the users.

This day-after-day monitoring is needed to check the status of the veto and notice if troubles occur. With the help of the scaler plots, one could identify the high peaks as working periods in the clean room or as movements of the upper parts of the muon veto system. One can also notice if there is a problem with one module (accidental shock, sparks, tears in the light-tight covering foil), the scaler rate decreases or increases immediately. More reliable than any logbook, even if sometimes not resolved afterwards, the scaler plots keep tracks of what happens in or nearby the muon veto system.

Whenever physics data are taken, the system is supposed to be closed. However, the detection efficiency of passing muon candidates depends on the position of the system. To know "how close we are closed", since March 2008, two laser devices measure every 15 min the real position of the mobile wagons of the upper level. The stored data of these measurements are then transformed into plots and published online as part of the monitoring program.

8

## 3.4 Neutron counters

The EDELWEISS-II collaboration performs a wide variety of measurements of neutrons in the proximity of the experimental setup together with MC studies [172].

### 3.4.1 Ambient neutron counter

Monitoring of the ambient neutron flux in proximity of the EDELWEISS experimental set-up is performed with the help of four low background  $^3\text{He}$  gas detectors [173]. Each proportional counter [174] has a working length of 860 mm with an internal diameter of 31 mm. The counter is filled with 400 kPa of  $^3\text{He}$  and 500 kPa of  $^{36}\text{Ar}$  as working gas. In proportional counters, the main background arises from  $\alpha$ -decays of  $^{238}\text{U}$  and  $^{233}\text{Th}$  in the walls of the detector. To reduce this background, a 50-60  $\mu\text{m}$  thick layer of Teflon followed by a 1  $\mu\text{m}$  layer of electrolytic copper are inserted in between the wall and the gas.

The thermal neutron monitoring system has been installed in the LSM in November 2008. The detector was positioned next to the eastern wall of the LSM laboratory between the clean room and the rock at the upper level, a few meters away from the EDELWEISS-II setup. The close proximity to the wall provides a solid angle of  $2\pi$  for the emerging thermal neutrons from the rock. The thermal neutrons coming

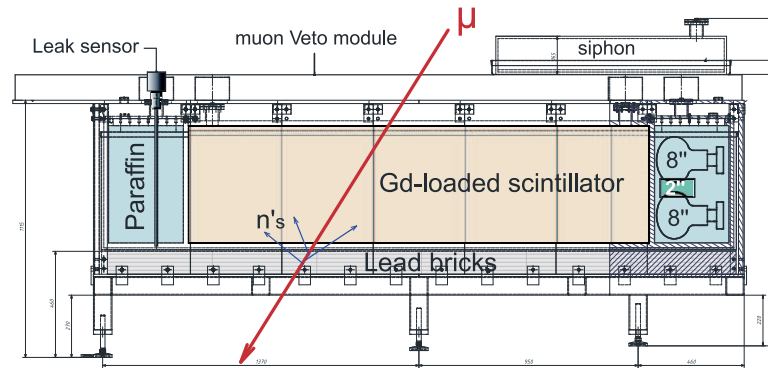


Figure 3.14: *Schematic of the side view of the muon-induced neutron counter. One ton of Gd-loaded liquid scintillator in the center is viewed by 16 PMTs of 8 inch-diameter and 6 PMTs of 2 inch-diameter. A layer of lead bricks below the liquid scintillator volume acts as an effective target for muons and high energy neutrons. Figure from [176].*

from the other  $2\pi$  are likely to come from materials inside the laboratory, especially from the anti-neutron massive polyethylene shielding of the EDELWEISS-II setup.

The neutron detector makes possible a continuous day by day monitoring of the thermal neutron flux in the vicinity of the EDELWEISS-II experiment. This measurement yields to a flux of about  $2 \cdot 10^{-6}$  neutrons/cm<sup>2</sup>/day [173] which is in good agreement with the previously measured value [141].

### 3.4.2 Muon-induced neutron counter

A second neutron detector has been developed by the Karlsruhe group to measure muon-induced neutrons [175, 176]. So far the rate of muon-induced neutrons was evaluated with muon veto-bolometer coincidences, *cf.* Chapters 5 and 6. But despite its high efficiency, it is possible that some muons pass through the muon veto without being tagged as muon-like events, and induce neutrons, which can reach the bolometers. Furthermore, the total mass of bolometers is of few kg, the coincidence rate with the muon veto is very low and dependent of the position of the bolometers inside the cryostat. Therefore, a dedicated detector was designed to access to the global rate of muon-induced neutrons.

The neutron counter registers two quantities: Events from thermalized neutrons in coincidence with the through going muon, and multiple neutron events from muon-induced particle showers. The dedicated detector is based on a liquid scintillator of  $\sim 1 \text{ m}^3$  volume ( $50 \times 100 \times 200 \text{ cm}^3$ ) loaded with 2 g/l Gadolinium (St. Gobain Bicorn BC525), which is used as a core of the detector. This is a 1 t compact detector, with an expected count rate of  $\sim 1$  muon-induced neutron per day.

The neutron capture process on Gd results in several gammas with 8 MeV sum energy. Then, at both end of the module, 8 photomultiplier tubes (PMT) of 8 inch-diameter are installed, see Figure 3.14. These PMTs are optimized to register the light produced after the neutron capture. One expects also muons to pass through the scintillating core. Since muons create much more light than neutrons, the 8 inch PMTs will saturate. The system is then equipped with 6 smaller PMTs (2 inch-

diameter) to register passing-through muons. The scintillator and PMTs are placed in one plexiglas container divided into three parts: A central one for the scintillator itself and two side ones filled with paraffin in which the PMTs are immersed. This plexiglas chamber is then placed in an aluminum vessel as secondary safety container. To reduce the loss of neutrons on the edge of the scintillator, iron plates surround the system to reflect a fraction of neutrons back into the scintillator. Finally, in order to enhance the neutron production, up to a factor of 10 compared to rock, a 10 cm thick layer of lead bricks is put underneath the detector. And on top of the counter, a plastic scintillator module, same type as those of the muon veto, is installed for coincidence measurements.

The neutron counter detector is also equipped with a LED system to monitor over time the light properties of the scintillator and the stability of PMTs. The LED system is made of 8 LEDs ( $\lambda = 425$  nm) placed at different positions, and regularly fired one by one. And because of the pseudocumene based scintillator, vapor sensors to check the internal and surrounding atmosphere, two leak sensors in the aluminum vessel, two temperature-meters (one immersed in the paraffin volume and one outside) monitor constantly the detector. In case of failure, these sensors, which are incorporated into the LSM safety system, give an alarm in the lab (vapor sensors) and/or notify users by email (all devices). These sensors, as well as the LED system are integrated into the muon veto monitoring webpage and are available anytime online.

The complete system is installed since end of 2008 at LSM. It is positioned right near the western (NEMO) wall of the muon veto at ground floor (lower level).

### 3.5 Results of EDELWEISS-I

In the first phase of the EDELWEISS experiment, up to three 320 g Germanium detectors were operated in a low-background dilution cryostat at a temperature of 17 mK. The experimental setup is described in detail in [134, 135, 149, 154]. Inside the cryostat, the detectors were shielded from the radioactivity of the electronic components by 7 cm of archaeological lead. The cryostat was made mostly out of ultrapure copper, considering background issues in terms of natural radioactive isotopes. To shield the cryostat from the radioactive environment, the cryostat was surrounded by 10 cm of copper, 15 cm of lead [164], and pure nitrogen gas circulated to reduce Radon accumulation. A further external 30 cm of polyethylene protected the experiment from neutrons created in the surrounding rock. To minimize intrinsic contamination, as well as EDELWEISS-II, the radioactivity of all materials in the close vicinity of the detectors was measured using a dedicated low-background Germanium  $\gamma$ -ray detectors, the GENTIANE experiment located at LSM and driven by l'Institut d'Astrophysique de Paris (IAP).

The accumulated data of EDELWEISS-I represents a total fiducial exposure of 62 kg·d. The accumulated events of the three detectors together in stable running conditions with a heat trigger and a reduced sensitivity to microphonics represents a total exposure of 22.7 kg·d, as shown in Figure 3.15 (left). However, in the total exposure of 62 kg·d, 59 nuclear recoil candidates are recorded between 10 and 200 keV. Out of these candidates, three are in the critical energy range for establishing limits on WIMP interactions between 30 and 100 keV [136], which makes an average count rate of  $6 \cdot 10^{-4}$  counts/keV/kg/d.

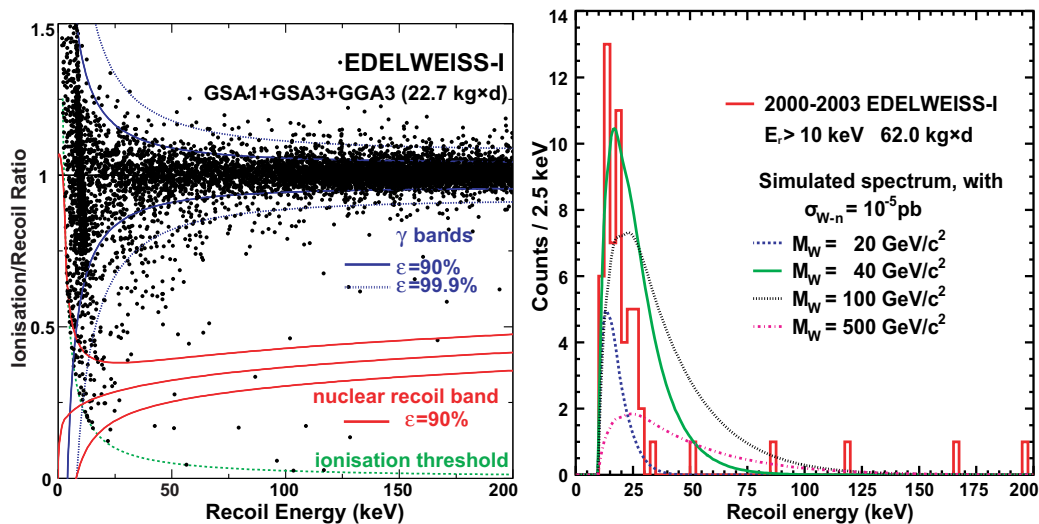


Figure 3.15: *EDELWEISS-I* results. Left: Accumulated events in the fiducial volume of three detectors (*GSA1*, *GSA3* and *GGA3*) in stable running conditions with a heat trigger and a reduced sensitivity to microphonics. The 90% (solid) and 99.9% (dotted) confidence level zones for the electron and nuclear recoil bands are also shown. The hyperbolic dashed curve represents the ionization threshold. Right: Recoil energy spectrum of events with  $E_R > 10$  keV, which are in the nuclear recoil band for a total fiducial exposure of 62 kg·d, compared with simulated WIMP spectra. Figures from [136].

In Figure 3.15 (right) are shown the simulated WIMP spectra for WIMP masses  $M_\chi = 20, 40, 100$  and  $500$  GeV/c<sup>2</sup>, using a WIMP-nucleon scattering cross-section  $\sigma_{\chi-n} = 10^{-5}$  pb. As can be seen, the distribution of the EDELWEISS-I remaining events is not consistent with such WIMP-recoil spectra. Thus, these events may be interpreted as background. Two likely sources of background have been identified: A residual neutron background and surface electron recoil events [172, 177].

In the presence of these background events, the Yellin optimum interval method [149, 178] was used to extract an upper limit on a WIMP signal, *i.e.* on the spin-independent WIMP-nucleon cross section as a function of the WIMP mass. The final result of EDELWEISS-I, which was the best limit at that time, is illustrated in Figure 3.16 (blue line).

The EDELWEISS-I experiment also used Germanium bolometers with natural abundances on <sup>73</sup>Ge (7.8%). Measurements with this high-spin Ge isotope set also limits on the spin-dependent WIMP-nucleon cross section. The complete data set of the first phase contains a fiducial exposure of 4.8 kg·d. The determined sensitivity is competitive in comparison to other spin-sensitive WIMP Dark Matter experiments, but is still two orders of magnitude higher than the most optimistic supersymmetric model predictions [179].

Since the EDELWEISS-I experiment was limited by background, a new setup including better shielding, larger detector masses and new techniques to suppress surface events was proposed to overcome the limitation.

The first phase of the EDELWEISS experiment successfully proved the detection method of the heat-and-ionization Germanium crystals. However, the experimental volume was limited to one liter. To significantly increase the size of the experiment, the second phase of the experiment, EDELWEISS-II [137] uses a larger size dilution cryostat which can house up to 120 detectors ( $\sim 30$  kg), as described in Section 3.2.1. Then, the shielding (Section 3.2) and the performance of the detectors (Section 3.1.3 and Section 3.1.4) have been improved. A muon veto detector (Section 3.3) and two neutron counters (Section 3.4) have been built to further lower and understand the background in the nuclear recoil band.

In this second phase of the experiment, the effective exposure time will be increased by a factor 100, while the background rate should not exceed the level of  $\Gamma_{\text{bg}} < 2 \cdot 10^{-3}$  kg·d to reach the aimed sensitivity goal. The goal is to achieve a sensitivity of better than  $10^{-8}$  pb on the spin-independent WIMP-nucleon cross-section, *cf.* Figure 3.16. After several commissioning runs in 2006 and improvements on hardware components, data acquisition has started in 2007 with 28 bolometers ( $\sim 9$  kg).

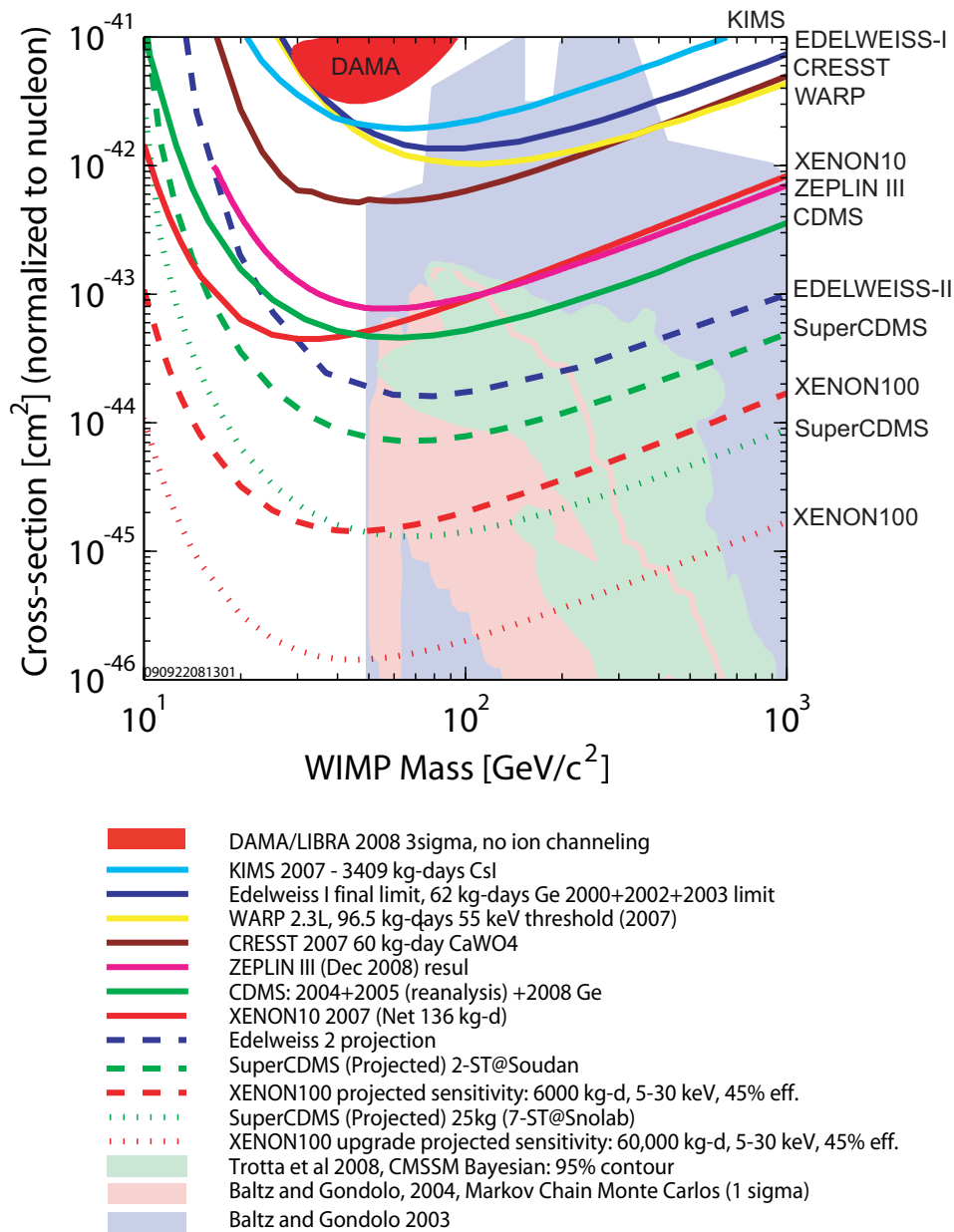


Figure 3.16: *Current and expected limits from various direct Dark Matter search experiments in the WIMP mass–WIMP-nucleon cross section (normalized to nucleon) plane. The expected projected sensitivity for EURECA is of the order of the one of XENON100 with 60,000 kg·d (dotted red). The theoretical expectations from supersymmetric models are from [180, 181, 182]. Figure generated using [183].*



# 4

## Muon detection

### Contents

- 4.1 Muon veto conventions
- 4.2 Life time of the muon veto
- 4.3 Muon rate
- 4.4 Mean muon energy deposit per module
- 4.5 Tracking muon candidates

*Who ordered that?*

I. I. Rabi.

MUONS are the only component of the primary cosmic ray interactions in the atmosphere that survives underground beyond the  $\sim 10$  mwe scale. And though there is a reduction of the cosmic muon flux by the rock overburden in LSM and equivalent laboratories of more than  $10^6$  compared to sea level, neutrons produced in deep inelastic scattering (DIS) of cosmic muons are the most prominent background in the upcoming second generation experiments searching directly for Dark Matter. The identification of muons in the vicinity of the Germanium detectors allows a significant suppression of this background source and hence an improvement in the experimental sensitivity.

The muon veto consists of 42 plastic scintillator modules, read out at both ends with an electronics and a data read-out fully independent from the bolometer system, except for a fiber connection transferring the overall experiment synchronization as well as some restricted information about muon hits, as detailed in Section 3.3. The muon veto is the extreme outside layer of EDELWEISS-II, surrounding almost hermetically the experimental setup with a total surface of  $\sim 100$  m<sup>2</sup>, see Figures 3.10 and 3.11, page 69. The muon veto has been installed since May 2005 at the underground laboratory LSM in Modane, ready for data taking since September 2005 and stable in terms of long term measuring conditions since July 2006.

### 4.1 Muon veto conventions

The muon veto registers two kinds of data files: The scaler files made of raw data and the event data file.

The raw data from the scaler cards correspond to any signal collected by the photomultipliers at the end of a side of a module and above the threshold of the discriminator cards. It is the number of hits per channel per 15 min, with no other information. They are used to monitor the system, *cf.* Section 3.3.3. With a rate

of  $\Gamma_{\text{scaler}} = 8$  kHz for the overall system, these scaler hits are mainly composed of background.

The event data correspond to selected events, *cf.* Section 3.3.2, when there is at least one coincidence of both sides of a module within a 100 ns time window. The event data have all necessary information for further analysis such as the timing (TDC) and the energy (ADC) of the event per end of modules, and the time of the event ( $t_{10\mu s}$ ) from the bolometer system via a fiber connection in 10  $\mu s$ -beat. Although the real time of an event is not known, it can be extrapolated from the time of creation of a file with the precision of the order of 1 s.

An event is thus defined by an internal coincidence within a module, which means that both sides of the module have a signal in terms of TDC and ADC. It can be translated by the condition:

$$\left(TDC[i] \neq 0 \wedge TDC[j] \neq 0\right) \wedge \left(ADC[i] \neq 0 \wedge ADC[j] \neq 0\right) \quad (4.1)$$

with  $i$  and  $j$  corresponding to both ends of a module. The multiplicity is the number of TDC channels with a hit, plus the TDC channel which triggers the system (the so-called common stop). Thus, if we have an internal coincidence within a module, this means we expect a multiplicity  $multi_{\text{veto}} = 3$ , within two modules  $multi_{\text{veto}} = 5$ .

Requiring the event-defining coincidence, the hit rate of 8 kHz for raw data drops to an event data of the full muon veto system of

$$\Gamma_{\text{veto}} = 0.2 \text{ Hz} \quad (4.2)$$

which means 1 event every 5 s. Even with a very generous veto interval of  $\pm 50$  ms around each veto event, this would lead to only 2% dead time.

As the muon veto is on two floors, a set of candidates of through going muons can be simply selected by requiring a coincidence between one module of the upper level and a module from the lower level, *e.g.* one module of the Top side and any module of the Bottom side for very vertical muon candidates, or *e.g.* one module of the Top side and any module of the lower level. To be even more general, muon candidates can be selected by requiring a multiplicity  $multi_{\text{veto}} > 3$ , which means that there are strictly more than one internal coincidence. The rate of muon candidates with  $multi_{\text{veto}} > 3$  is

$$\Gamma_{\text{veto}}^{multi_{\text{veto}} > 3} = 5 \text{ mHz} \quad (4.3)$$

The event rate of these entries is still much higher than the expected muon rate of some  $\mu\text{Hz}$  for the full veto system [184, 185] due to a deliberately low threshold not to miss any muons.

These different conditions are shown in Figure 4.1, which is the energy deposit recorded in a side of a Top module (#4) in ADC channel. Events, which have a very high energy deposit of more than 4096 ADC channels, are stored in the overflow channel at position 4100. The distribution in red represents all events which make an internal coincidence, following the condition of Equation 4.1. One can see it is largely dominated by background, only cut by the hardware threshold at low energy. In blue are represented muon candidates which make an internal coincidence in module #4 and an internal coincidence in one module of the lower level, the distribution can be well fit with a Landau distribution without requiring any background subtraction. In green are the muon candidates which make an internal coincidence in module #4 and totalize a multiplicity  $multi_{\text{veto}} > 3$ . As this

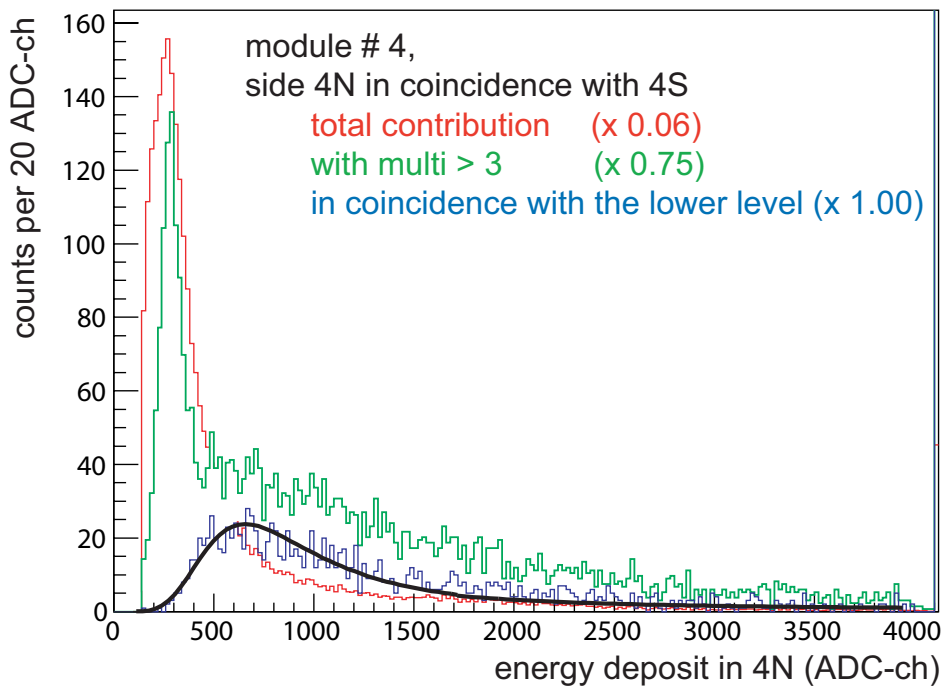


Figure 4.1: *Energy deposit in the North side of the Top module #4. In red are shown events which make an internal coincidence in the module. In green are the muon candidates which make an internal coincidence in module #4 and totalize a multiplicity  $multi_{veto} > 3$ . In blue with the Landau fit is represented muon candidates which make an internal coincidence in module #4 and an internal coincidence in one module of the lower level. The plots are multiplied by the factor in brackets. At 4100 ADC channels is the overflow bin, where are stored very high energy events.*

condition is looser than the preceding one, it also includes coincidences of module #4 with the upper level, but also background below 500 ADC-ch. The Landau spectrum of muons can be distinguished, but is hidden at low energy. See Figure 4.4 for more details about the background.

In the following, the multiplicity condition  $multi_{veto} > 3$  or the “upper modules in coincidence with the lower ones” condition is used to define our set of muon candidates. These conditions are more stringent than the internal module coincidence condition used during data acquisition in order to define a simple and clear sample for  $\mu$  investigations.

## 4.2 Life time of the muon veto

Since muon candidates are defined as coincidence of at least two modules, the muon rate depends on the actual position of the upper wagons, *i.e.* how well the system is closed. The muon veto is defined as close if:

- Before March 2008, the muon veto is known as closed only by manual entries into the logbook. The muon veto system is considered as closed, if the opening is less than 2 hours in an 8-hour muon veto data file.

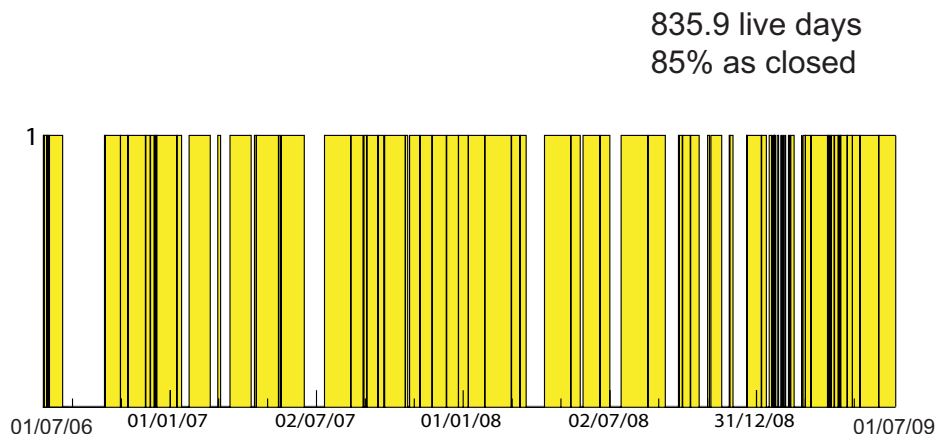


Figure 4.2: *Life time of the muon veto during three years of data acquisition. In yellow are continuous periods of data acquisition, the black thick lines are actually short runs.*

- After March 2008, the position of the wagons of the upper level of the muon veto is precisely known thanks to laser measurements, which are made every 15 min. If the space between the two wagons is less than 28.5 cm, the system is closed.

The condition of 28.5 cm is large, but actually or the system is widely opened of more than 1 m or it is tiny closed on less than 1 cm.

On Figure 4.2 is shown the life time of the muon veto for the full data acquisition time from July 2006 to July 2009. The muon veto ran almost continuously. Interruptions happen mainly during extensive work periods in the clean room, *e.g.* bolometer extensions, or upgrade of the muon veto, when the high voltage of the modules are switched off for safety reasons. The muon veto ran for 835.9 live days over three years of data (76.3% of life time), and as close 85% of this time.

### 4.3 Muon rate

As an example, the rate of muon candidate per hour, averaged on 20 8-hr files, for the three years running period is shown in Figure 4.3 for the Top modules in coincidence with the lower level and for the North modules in coincidence with the lower level. In the North modules, the muon rate is almost flat and evenly distributed along the time. The rate is slightly decreasing due to the ageing of the PMTs. The slope is more pronounced for the Top modules due to a clear loss of effective light output of one of the modules.

In parallel to the veto data analysis, a GEANT-4 [186] detailed 3-D simulation of muons in the LSM laboratory was performed [184], including the full topology of events and the profile of the mountains. An overview of the comparison of experimental rates with Geant-4 simulations is given in Table 4.1. The difference of rates for each side are discussed together with the mean energy deposit in Section 4.4.

The muon flux was earlier measured by the Fréjus experiment for a horizontal area at the LSM to  $\Gamma_\mu = 4.73 \pm 0.1 \text{ m}^{-2}\text{d}^{-1}$  [185]. In the simulation, muons are gen-

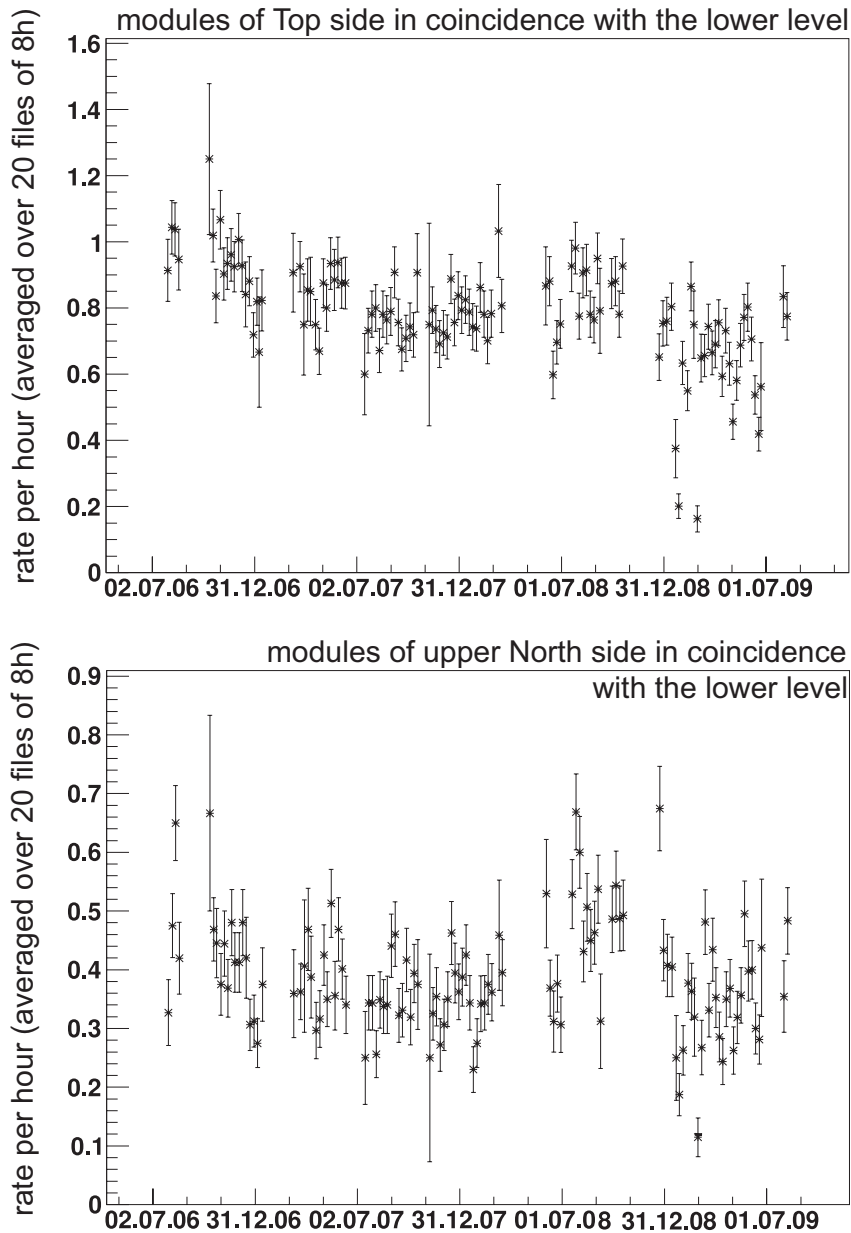


Figure 4.3: *Muon candidate rate of the muon veto of the Top side modules (top) and the North side modules (bottom) in coincidence with modules of the lower level.*

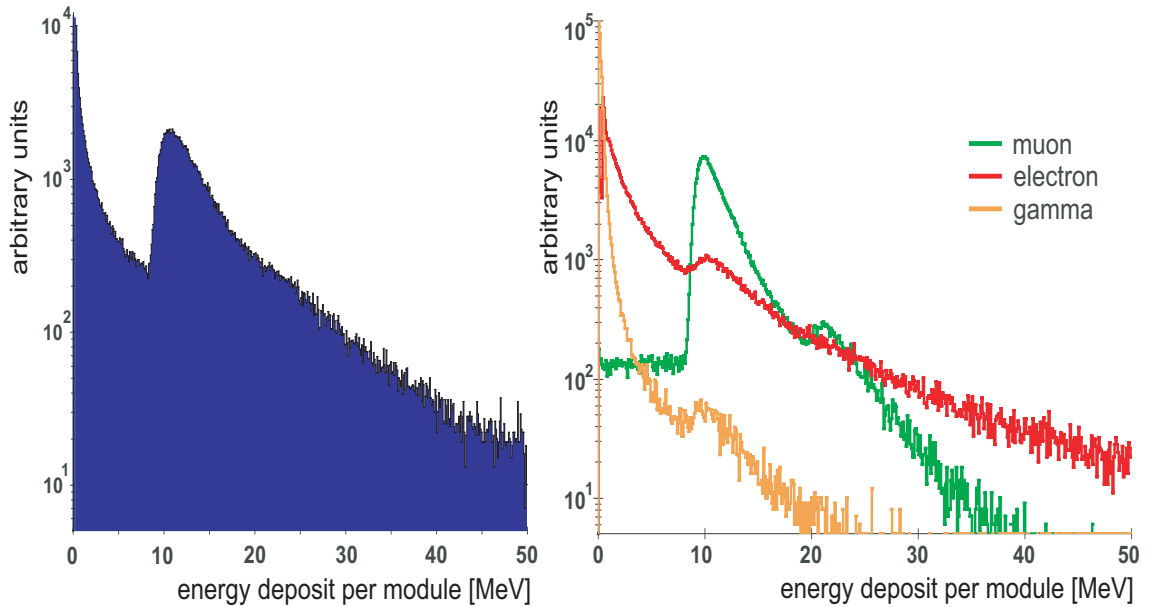


Figure 4.4: Simulated total energy deposit (left) and associated to muons (green), electrons (red) and photons (yellow) per horizontal Top modules from [184].

erated within the complete geometry in the energy range of  $200 < E_\mu < 2000$  GeV, which represents only  $\sim 35\%$  of the total muon flux. The simulation has thus been normalized to the measured muon flux by an arbitrary horizontal area  $A \approx 15$  m<sup>2</sup>, which is the intersection of the upper and lower level. However, whereas in the simulation the muon rate is exclusively made of muons, the muon candidates from the data are *candidates*, they can be real muons, but also muon-induced secondaries or showers.

Not only muons deposit energy in the scintillator modules. While traversing the rock above the experimental hall, the muon develops an electromagnetic shower. Relativistic muons lose energy in matter primarily by ionization and atomic excitation, and produce electrons and photons. The produced photons can have an energy sufficiently high to interact with matter mainly via electron-positron pair production. The electrons and positrons in turn emit Bremsstrahlung photons. The two processes continue to take place alternately until the particle energies are below the production threshold. The total energy deposit simulated for Top modules is shown in Figure 4.4. One can see that the Landau distribution of what would be called muon candidates in the corresponding data analysis in Figure 4.4 left is actually composed of muons (green), electrons (red) and photons (yellow) in Figure 4.4 right.

For the muon spectrum, the second peak, around  $E_{\text{dep}} \approx 22$  MeV, arises from the increased thickness of the plastic scintillator modules at the end due to the light guides, *cf.* [169] for a detailed discussion of these effects. High energy vertical electrons are traversing the thickness  $d = 5$  cm of plastic scintillator by depositing  $E_{\text{dep}}^{e^-} \approx 10\text{--}12$  MeV. The exponential rise in the energy deposit spectrum is from the electrons in the electromagnetic shower induced by the muon in the rock overburden, which lose energy primarily via scattering processes. The energy deposit associated to photons is dominated by the Compton scattering effect. Again, the curve shows an exponential rise towards low energy deposits in the scintillator module.

In principle, detecting high energetic secondary particles in the veto system can

condition	Geant-4 geom. rate (d <sup>-1</sup> )	measured rate (d <sup>-1</sup> )
Top side and lower level	12.0 ± 0.3	19.2 ± 0.2
North side and lower level	7.0 ± 0.2	9.7 ± 0.2
South side and lower level	6.2 ± 0.2	12.8 ± 0.2
NEMO side and lower level	3.4 ± 0.1	9.1 ± 0.2
East side and lower level	2.4 ± 0.1	5.4 ± 0.1

Table 4.1: Comparison of the rates of muon candidates of the EDELWEISS-II muon veto system with Geant-4 simulations from [184] for various geometrical coincidence conditions. Measured muon candidates are coincidences of a side of the upper level with any side the lower level.

be associated with a muon passing nearby. The energy deposit of secondary particles of a muon-induced electromagnetic shower offers the possibility to increase the muon detection efficiency for further coincidences with bolometers.

## 4.4 Mean muon energy deposit per module

Underground cosmic ray muons, as high energy charged particles, lose energy in matter through ionization process, described by Bethe-Bloch's formula. The plastic scintillator modules have material density of  $\rho_{\text{module}} \approx 1 \text{ g/cm}^3$ . Muons with high kinetic energies of  $\langle E_{\mu} \rangle_{\text{LSM}} \approx 300 \text{ GeV}$  will lose in a thin layer of matter, as a flat horizontal plastic scintillator module,

$$\frac{dE_{\mu}}{dX} \approx 2 \text{ MeV/cm.} \quad (4.4)$$

As a result, the mean muon energy deposit for vertical muons in a module of thickness of  $d = 5 \text{ cm}$  is approximately

$$\langle E_{\text{dep}} \rangle \approx 10 \text{ MeV.} \quad (4.5)$$

The fluctuations in energy loss can be described by a Landau-distribution, as already shown in Figure 4.1 and for each distribution is defined a *Landau Most Probable Value* (LMPV).

However, not all modules are flatly horizontally oriented as the Top and Bottom sides. Since the modules are placed in a cubic geometry around the cryostat and the shielding, most of the modules are in fact placed vertically on their side. Moreover, the muon flux in the underground laboratory LSM depends on the shape of the mountain and varies in terms of angular distribution. The direction of the muons, thus the average muon track length in the modules and, hence, the muon energy deposit and the muon candidate rate, differs considerably for the different sides of the veto system.

The simulated mean energy deposit  $\langle E_{\text{simu}} \rangle$  and the most probable value of the Landau fit of the data  $E_{\text{LMPV}}$  for all sides of the EDELWEISS-II veto system is given in Table 4.2. The statistical errors on simulation on the determined values are negligible. A systematical error of  $\sigma_E \approx 0.2 \text{ MeV}$  can be accounted to the muon generator of the Monte Carlo simulations. The most probable value of the Landau fit is most likely at higher energy than the simulated mean energy for muon candidates, *i.e.* coincidences of a module of a level with the other level. Particles hitting

the muon veto have a higher energy than estimated in the simulation, despite the higher measured rate. This tends to show the discrepancy in rates is due to (high energy) secondaries and showers rather than (low energy) background. On the other hand, this comparison works only if all modules are perfectly calibrated to the same gain, which is not the case, and will be further studied.

The angular distribution depends strongly on the shape and orientation of the mountain overburden. The muon flux increases with the zenith angle\*. However, for large zenith angles, as the mountain range above the LSM underground laboratory is stretched dominantly along the geographical East-NEMO axis, and due to adjacent mountains, the rock overburden strongly increases in the East-NEMO direction, which further lowers the muon flux. The muon flux in direction of  $\theta > 70^\circ$  is suppressed by two orders of magnitude and can be neglected [184]. Therefore, the average track length of muons in the Top and Bottom side modules is thus approximately the thickness of the modules. In the simulation, muons hitting the muon veto are defined as particle going through an imaginary plane, which is the intersection of the upper and the lower level. The comparison of the simulated and measured rate is then more straightforward for the horizontal module of Top and Bottom.

As at large zenith angles, more muons are entering the underground laboratory from the North-South direction, *i.e.* from the valleys, rather than from the East-NEMO, the muon flux also depends on the azimuth angle†. This directional difference can be held responsible for a higher mean of muon energy deposit in the vertical veto modules on the East and NEMO side of the experiment. On these sides, there is less muons at high zenith angles which make short tracks, thus the mean muon track length is longer and the mean energy deposit is higher.

Muons going through modules vertically oriented on their side have typically longer track lengths. Therefore more energy is lost along the module, and the mean of the muon energy loss increases. As modules on the lower level are laid out on the long sides, a slight difference can be determined for modules of the North and South lower sides to the upper side ones. Therefore, very high energy deposits by muons traversing the full length of the module are not possible, because the maximal track length for vertical muons is limited to the width of the modules. The mean value is thus slightly lower than for modules laid out on the short sides, as on the upper level.

## 4.5 Tracking muon candidates

### 4.5.1 Position of the event along the module axis

The time difference of a signal coming from both ends of a module is due to the scintillation light path along the module axis and can be translated to the position of the muon candidates along the axis of this module. The sample is defined as clear as possible requiring the condition to have muon candidates, *i.e.* coincidences of a module of a level with the other level. The modules are grouped in set depending

---

\* The zenith angle is the angle made from the vertical direction opposite to the gravitational force at a given location. That is:  $0^\circ$  in the zenith,  $90^\circ$  on the horizon. The local muon distribution as a function of zenith angle is integrated over all azimuth angles.

† An azimuth is defined as a horizontal angle measured clockwise from a North base line or meridian. The true North is measured as a  $0^\circ$  azimuth.

side		orientation	$\langle E_{\text{simu}} \rangle$ (MeV)	$E_{\text{LMPV}}$ (ADC-ch)
upper level	Top	horizontal	11.8	686.8
	North	vertical (ss)	20.8 (1.8)	1254.3 (1.8)
	South	vertical (ss)	20.7 (1.7)	1269.0 (1.8)
	NEMO	vertical (ls)	23.7 (2.9)	1565.5 (2.3)
	East	vertical (ls)	24.0 (2.0)	1887.3 (2.7)
lower level	East	vertical (ls)	23.8 (2.0)	1984.7 (2.8)
	South	vertical (ls)	19.6 (1.7)	1914.0 (2.8)
	North	vertical (ls)	19.9 (1.7)	1719.8 (2.5)
	NEMO	vertical (ls)	23.9 (2.0)	1670.7 (2.4)
	Bottom	horizontal	12.2 (1.0)	1263.2 (1.8)

Table 4.2: Mean muon energy deposit (simulation and experimental) in plastic scintillator modules for different orientation in the EDELWEISS-II setup. Vertical modules are laid out either on the short side (ss) or on the long side (ls). In brackets are the relative contribution of a side compare to the Top one. The muon generation is from [184]. The measured LPMV is for muon candidates of a side of a level, which are in coincidence with the other level. This comparison works only if all modules are perfectly calibrated to the same gain, which is not the case.

on their length (4 m , 3.75 m, 3.15 m and 2 m) rather than individually to increase the statistics. The resulting spectrum of the time difference coming from both ends of a module is shown per set in Figure 4.5. Each end of a spectrum can be fit by a Gaussian function. The size of the module is set to correspond to the number of channels between the two Gaussian fits at mid-height:

$$4 \quad \text{m module} \equiv 76 \text{ TDC-ch} \quad (4.6)$$

$$3.75 \text{ m module} \equiv 68 \text{ TDC-ch} \quad (4.7)$$

$$3.15 \text{ m module} \equiv 60 \text{ TDC-ch} \quad (4.8)$$

$$2 \quad \text{m module} \equiv 36 \text{ TDC-ch} \quad (4.9)$$

The spatial resolution of a module is defined looking at the time difference of coincidences between a module  $n$  and its neighbor  $n + 1$  of one level and further in coincidence with the other level of the veto system. Three sets of modules are now defined depending on their position: Top modules, vertical modules along their shorter side (North and South of the upper level), and vertical modules along their longer side (North and South of the lower level, and East and NEMO). The biplot of the time difference within the neighboring module  $n + 1$  versus the time difference within module  $n$  is shown per set in Figure 4.6. The width of this biplot distribution is the spatial resolution of a type of modules. The projection of the biplot can be fit by a Gaussian with a width of  $2\sigma$ . The resolutions obtained are in TDC channels:

$$\sigma_{\text{top}} = 10.20 \text{ TDC-ch} \quad (4.10)$$

$$\sigma_{\text{ss}} = 10.33 \text{ TDC-ch} \quad (4.11)$$

$$\sigma_{\text{ls}} = 6.53 \text{ TDC-ch} \quad (4.12)$$

The sets defined per size are associated to the sets defined per position. The 4 m module are modules from the Top side and the North and South lower sides, they have a resolution  $\sigma_{\text{top}}$ . The 3.15 m modules are the vertical modules along their

shorter side (North and South of the upper level) with a resolution of  $\sigma_{ss}$ . The 2 m modules, which are the small one of the Bottom side, have also a resolution  $\sigma_{ss}$ . The 3.75 m modules are the rest with a resolution of  $\sigma_{ls}$ . Therefore, we obtain:

$$\sigma_{4m} \simeq 54 \text{ cm} \quad (4.13)$$

$$\sigma_{3.75m} \simeq 36 \text{ cm} \quad (4.14)$$

$$\sigma_{3.15m} \simeq 54 \text{ cm} \quad (4.15)$$

$$\sigma_{2m} \simeq 57 \text{ cm} \quad (4.16)$$

Note that the spectrum of the time difference within a module is not symmetric for the 3.15 m modules (the North and South upper level ones) in Figure 4.5. The time difference is the difference in TDCs recorded in both ends of a module, which is, for these modules, the upper end minus the lower end. There are as many events occurring in the upper part as in the lower part of these modules, there is no restriction, as they are in the valley direction. However, less events occurring in the lower part of these modules are in coincidence with the lower level, as there is one module missing for the North lower side. The spectrum is, thus, asymmetric.

With the translation of the time difference into a position along the module axis and with the resolution of a module, it is now possible to reconstruct the muon candidate tracks in a 3-D muon veto system, as it has been done in Chapter 5, pages 112-113.

## 4.5.2 Through going muon candidates

If the TDC difference of a signal coming from both ends of a module gives information about the position of a hit in the module, the average value of the TDC can be used as an absolute time between modules within one event. This average becomes larger as the internal coincidences arrive later in an event. The average value of the TDC from the three Top modules closer to the NEMO side compared to the one of the long Bottom modules, as shown in Figure 4.7, should give the time of flight of the muon candidates.

A TDC channel corresponds to 0.8 ns. The spectrum of the time difference is fit with a Gaussian, which is centered on

$$\begin{aligned} \langle \Delta t \rangle_{\text{Gaus}} &= \langle t_{\text{top}} - t_{\text{bottom}} \rangle_{\text{Gaus}} \\ &= (24 \pm 2) \cdot 0.8 \text{ ns} \\ &= 19 \pm 2 \text{ ns}. \end{aligned} \quad (4.17)$$

Given the muon candidates propagate at  $c = 3 \cdot 10^8 \text{ m/s}$ ,

$$l = \Delta t \cdot c = (5.7 \pm 0.6) \text{ m}. \quad (4.18)$$

The distance from the Top side to the Bottom side of the muon veto is  $d = 5.52 \text{ m}$ , which is the length of a vertical module on its shorter side, plus the length of three vertical modules on their longer side and the space between them, plus the space due to the structure to hold the modules on the lower level on the ground and to the structure of the first floor and the clean room, in two words the top to bottom length of the muon veto. Given that muons do not privilege directions from a zenith angle  $\theta = 0$ , because of the shape of the mountain, but have a more diagonal, thus longer track length, we have predominantly downward going muons.

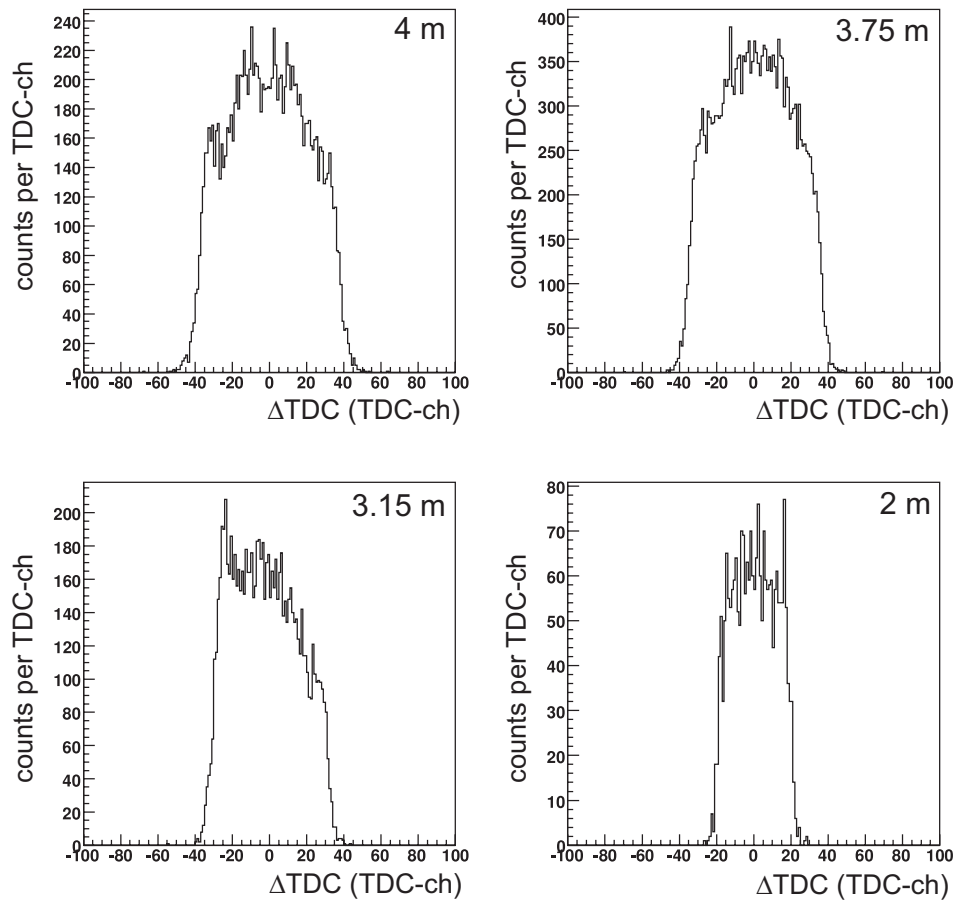


Figure 4.5: *Time difference of the TDCs from both ends of a module in coincidence with the other level per sets of modules per size: 4 m modules (top left), 3.75 m modules (top right), 3.15 m modules (bottom left), 2 m modules (bottom right). See Figure 3.11 for position in the muon veto.*

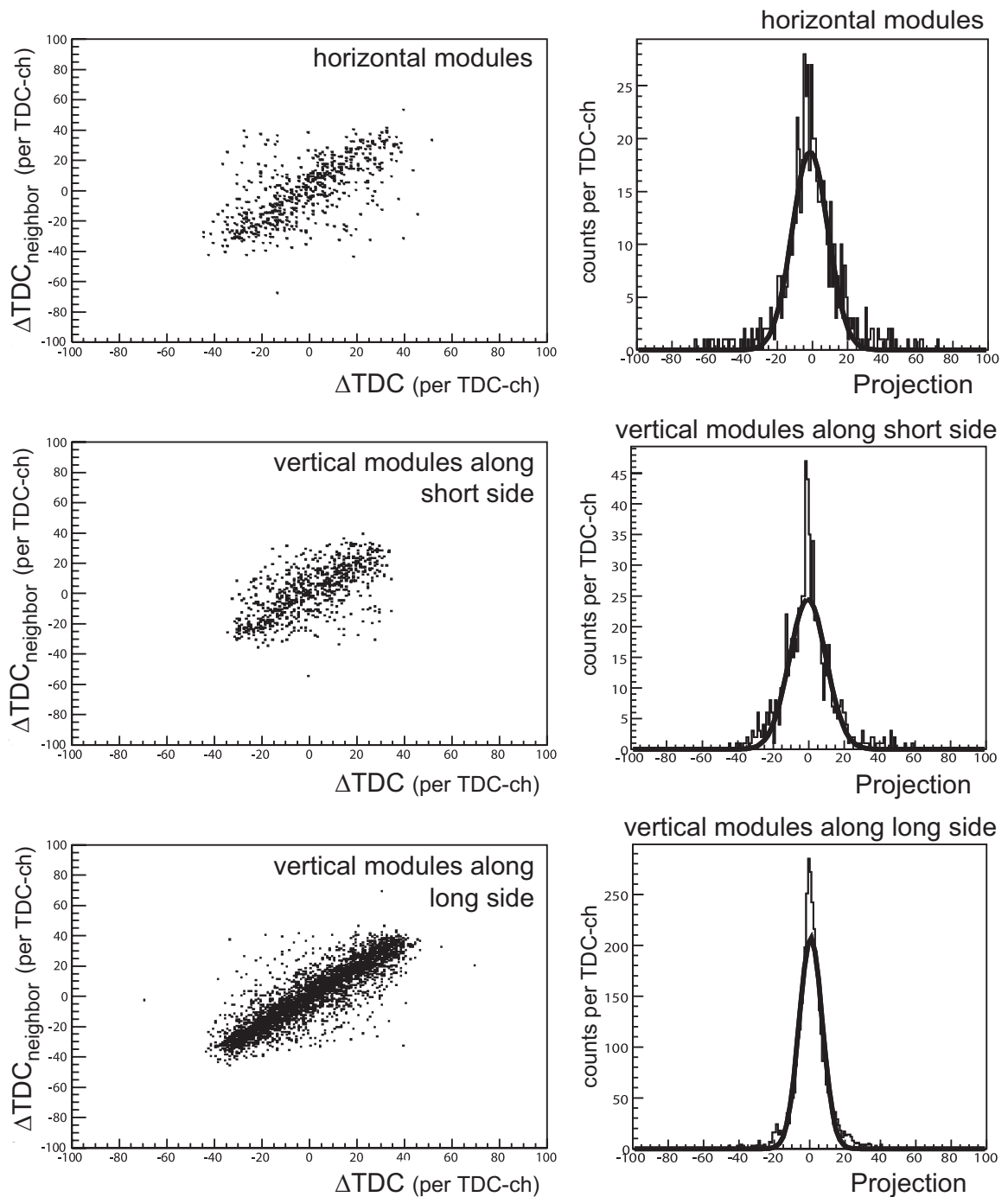


Figure 4.6: *Left: Biplot of the time difference within the neighboring module  $n + 1$  versus the time difference within module  $n$  of a level, further in coincidence with the other level of the veto system. Right: Projection of these biplots. On top are represented the Top modules, in the center the vertical modules along their shorter side (North and South of the upper level), and on bottom the vertical modules along their longer side (North and South of the lower level, and East and NEMO).*

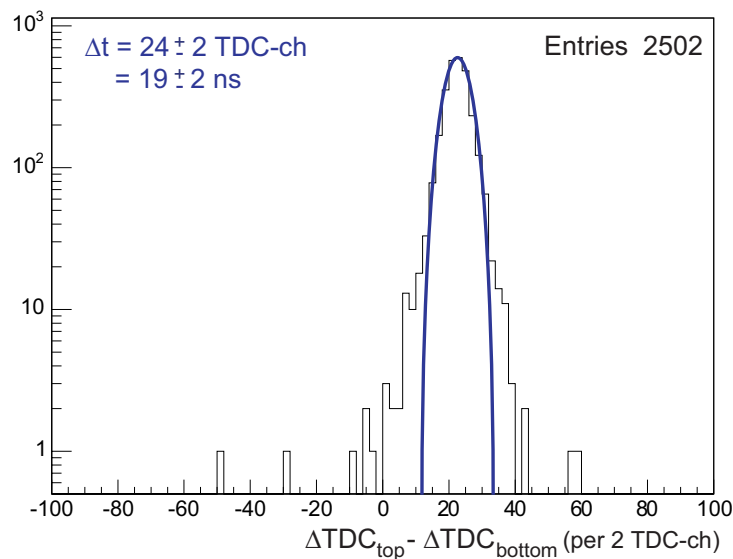


Figure 4.7: Time difference of through going muon candidates from both ends of the three Top modules closer to the NEMO side and the long Bottom modules.

There are events with  $\Delta t < 0$ . They could be upward going muons from interactions of neutrino, passing through the Earth. However, these events have a high multiplicity ( $multi_{\text{veto}} = 17$  to 34) and, thus, more likely to be muon-induced showers, which products arrive later in the Top modules compared to the muon hitting the Bottom ones.

The EDELWEISS-II muon veto has already run for three years and is continuously taking data. Despite some discrepancies with the simulation, the analysis of the events yields a good detection and identification of muon candidates and their showers. On a pure muon detection point of view, the complicated shape of the mountain and the deep overburden of rock make it difficult, even after three years, to collect high statistics in all sides of the muon veto. Of course, from a Dark Matter search point of view, less muons means also less induced neutrons and a better final sensitivity. Muon veto-bolometer coincidences are the subject of the next Chapters.



# 5

## Analysis of Run 8

### Contents

- 5.1 Status of the experiment
- 5.2 Muon veto data
- 5.3 Bolometer data
- 5.4 Coincidences between the muon veto and the bolometers
- 5.5 Summary

*How do you want me to understand you!...  
You're talking to me against the light,  
I can't see what you're saying!*

G. Feydeau.

THE ULTIMATE SENSITIVITY of a WIMP experiment is set by its rate of background events which are indistinguishable from WIMP candidates. In the EDELWEISS-II experiment, natural radioactivity, from the rock or the materials, is under control thanks to the new shielding made of polyethylene, of lead and of the self-shielding of the cryostat and to the use of radio-pure material. But to reach the high sensitivity goal, it is important to consider also formerly negligible background sources. Neutrons induced either directly by cosmic ray muons or indirectly by electromagnetic processes in the shower of a muon have to be considered as a limiting background source. The active muon shield, so called muon veto, of the EDELWEISS-II experiment is made to reject muon-induced background, by associating cosmic ray muons in the vicinity of the experiment with neutron recoil events in the bolometers.

### 5.1 Status of the experiment

The following study is based on the analysis of the bolometer Run 8 and the corresponding period for the muon veto. Run 8 lasted from November 24<sup>th</sup> 2007 to March 18<sup>th</sup> 2008. The muon veto system worked completely and properly, all 42 modules were ready for data acquisition. For the bolometer system 16 standard Germanium bolometers are considered, set on 3 different acquisition computers, called *s1*, *s2*, *s3*.

To look for coincidence events between the muon veto and the bolometers, the idea is to have a central clock with a 10  $\mu$ s-beat, which dispatches the time over the whole system. The central time stamp from the clock is transferred via a fiber connection from the bolometer set up to the time board of the veto.

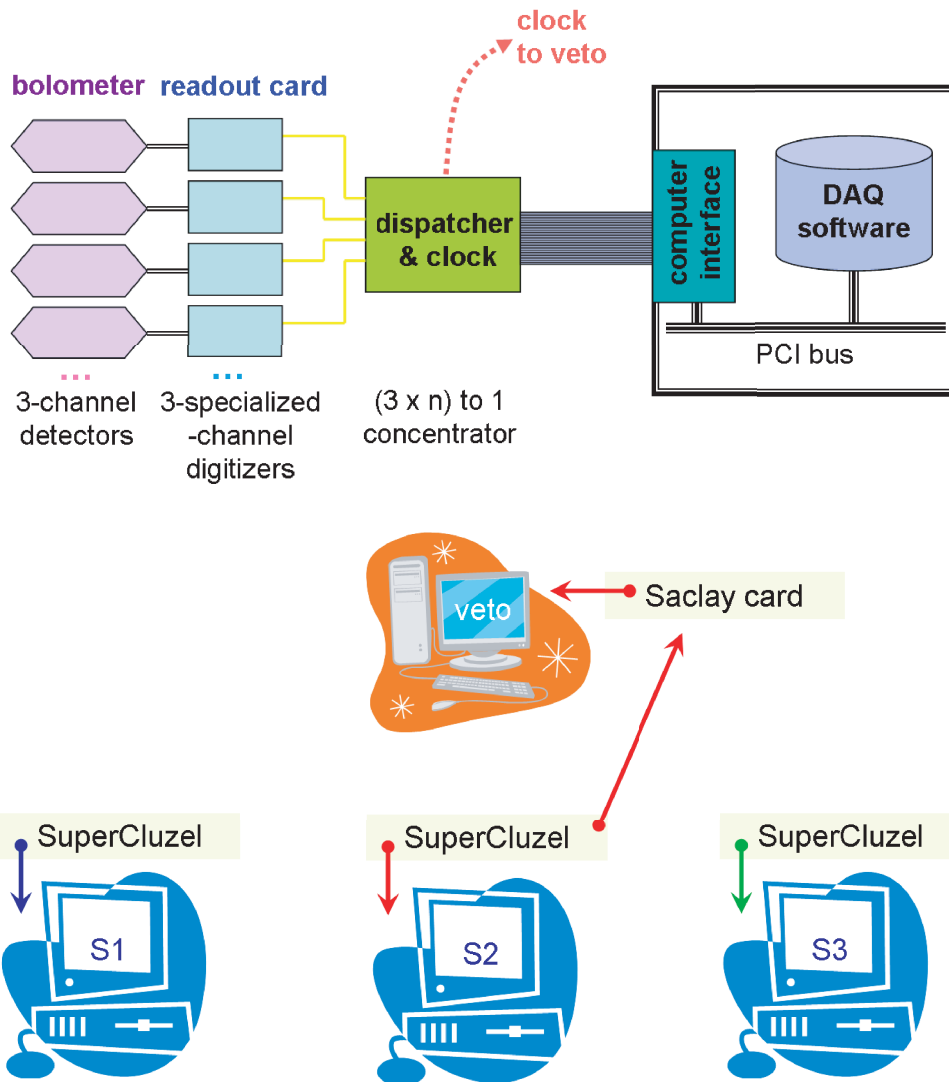


Figure 5.1: *Top: Electronic chain of the bolometers during Run 8. There were 3 similar chains to run the 16 bolometers. Since the number of channels is different depending on the type of bolometer (from 3 for standard Ge bolometer to 7 for ID bolometer), each bolometer is assimilated to an ensemble of 1 or 2 or 3 pseudo-detector(s) with 3 readout channels. Figure adapted from [187]. Bottom: Distribution of the time over the EDELWEISS-II experiment, during Run 8.*

However, as already mentioned in Section 3.1.7, the data acquisition of bolometers is split between different computers to handle the number of bolometers, and each DAQ is independent. The clock is part of the electronic chain of the bolometers, between their individual electronic readout cards and their computer, as shown in Figure 5.1 top. The clock is reset as a new run is started, as any other parameters. Each data acquisition starts and ends without regards to the others, and the most important point, each DAQ restarts its own clock from zero with every new run. Therefore, there is no overall clock, but three independent clocks, with only one among them connected to the veto time board (the one from the computer called *s2*), as naively illustrated on Figure 5.1 bottom.

Due to this complex time recording which was corrected only from Run 10 on, considerable work had to be performed within the analysis to reconstruct a common time basis for all the bolometers and the muon veto. This will be described in the following.

## 5.2 Muon veto data

To have well-defined geometric conditions, coincidences between the bolometers and the veto system were searched for only when the EDELWEISS-II upper level was closed.

On one hand, when there is a background run in the bolometer system, the upper level of the experiment is closed. Since the clock of the veto is linked to the clock of the bolometer DAQ computer *s2*, every restart of the clock of *s2* defines a starting point of a closed period for the veto. But, when the run ends on *s2*, its clock continues to run until a new run starts on *s2*, and in between, the veto can be opened. However, the running period of the closed veto can not only be defined by the running period of *s2*, because even if the run is finished on *s2*, it does not mean it is finished on *s1* or *s3*.

On the other hand, during Run 8, the muon veto is known as closed only by manual entries into the logbook\*. The muon veto system is considered as closed, if the opening is less than 2 hours in an 8-hour muon veto data file.

Therefore, periods, when the veto is closed, are defined as periods in between two restarts of the clock, out of files which have an opened period greater than 2 hours. From 24/11/2007 to 18/03/2008, the muon veto ran as closed for  $t_{\text{veto}} \simeq 98.8$  days.

It corresponds to a mean rate of

$$\Gamma_{\text{veto}} = 0.173 \text{ Hz} \quad (5.1)$$

$$\Gamma_{\text{veto}}^{\text{multi}_{\text{veto}} > 3} = 4.46 \text{ mHz} \quad (5.2)$$

$\Gamma_{\text{veto}}$  is the rate for all events,  $\Gamma_{\text{veto}}^{\text{multi}_{\text{veto}} > 3}$  is the rate for events which make strictly more than one internal coincidence within a module (a multiplicity  $\text{multi}_{\text{veto}} > 3$ , cf. Section 3.3.2). The rate of the muon veto over time is shown in Figure 5.2. The rate is not as constant as one can expect (left plot), still the distribution of the rate is Gaussian (right plot). The differences are probably due to short periods with the veto opened, which are not disregarded with the condition used. Movements to

---

\* Note that since March 12<sup>th</sup> 2008, the muon veto is known as closed independently of users thanks to two laser devices, which measure precisely the position of the wagons of the muon veto every 15 min.

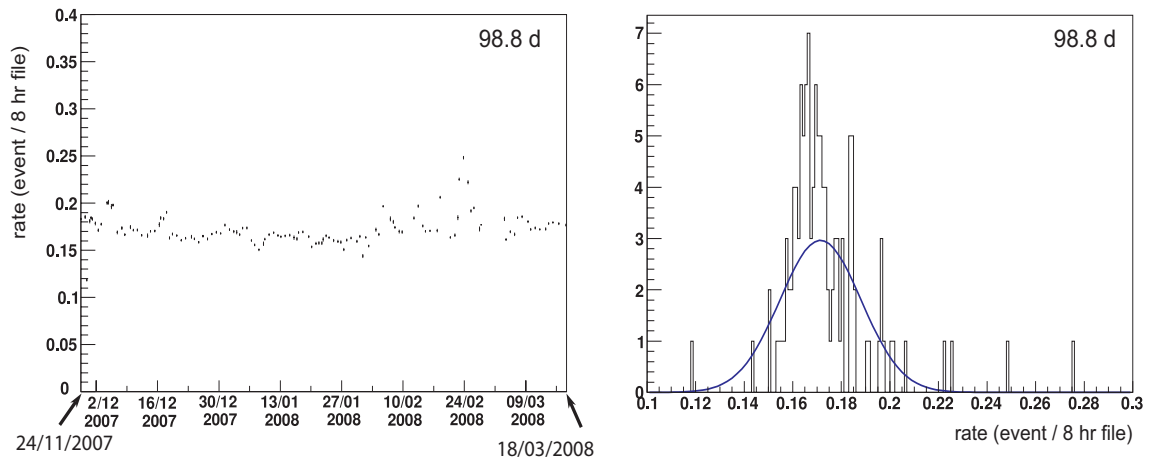


Figure 5.2: Rate of the muon veto per 8-hour file when the veto is closed, see text for details. The rate is shown over time (left) from 24/11/2007 to 18/03/2008 and as a histogram (right) with a Gaussian fit. The mean of the Gaussian fit is 0.173 Hz (calculated rate from data is also 0.173 Hz).

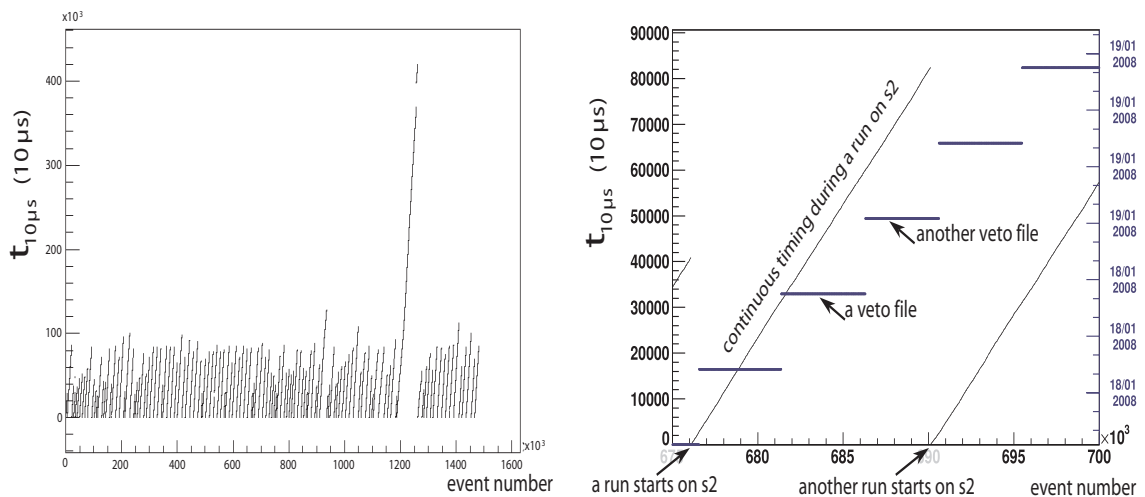


Figure 5.3: Timeline of the veto events during Run 8 (left) and zoomed on one bolometer period (right). Since a bolometer run lasts  $\sim 24$  hours, there are typically three 8-hour veto files to cover the same period.

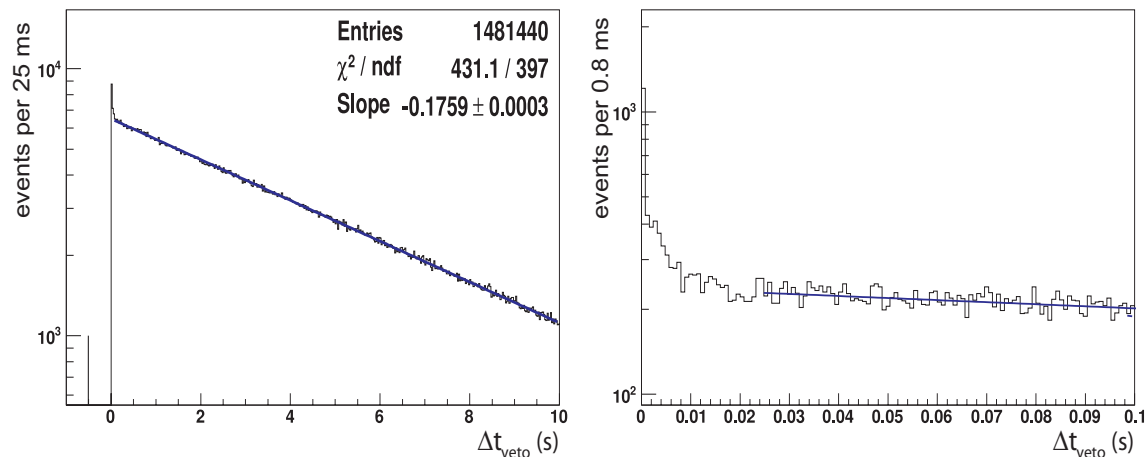


Figure 5.4: Time difference of consecutive muon veto events (left) and zoomed on 0.1 s in a finer binning (right). The negative  $\Delta t_{\text{veto}}$  at  $-0.5$  s indicate restarts of the clock.

close and open the wagons create vibrations, which perturbate the PMTs of the veto module. If the opening and closing happened in a short time interval, it is then not removed from the analysis and extra events (sparks) increase artificially the rate.

Due to the restart of the clock with every bolometer runs on  $s_2$ , the timeline of the veto looks like as in Figure 5.3. On left is shown the time in seconds over the veto event number. The diagonal lines are the periods for a bolometer run. Only bolometer runs which last more than 24,000 s ( $> 6.6$  h) are selected for the coincidence analysis, the reason is detailed in Section 5.4. The timing looks rather discontinuous. However, on right is the same plot, but zoomed over one period, *i.e.* zoomed over one bolometer run. Over one bolometer period, the timing is perfectly continuous.

Considering now Figure 5.4 left, is plotted the time difference of consecutive muon veto events up to 10 s. The negative  $\Delta t_{\text{veto}}$  due to the restarts of the clock are all plotted at  $-0.5$  s. Excluding the first 25 ms, which contains only  $\sim 8000$  events out of a total of  $\sim 1.5 \cdot 10^6$  events, as shown more explicitly on right, the time distribution follows an exponential, which can be fit giving a  $\chi^2/\text{ndf} = 431.1/397$ . The slope of the exponential can be used to cross-checked the rate, The slope of the exponential fit is 0.176 Hz, which is a bit higher than the rate already mentioned.

## 5.3 Bolometer data

The bolometers in use during Run 8 are shown in Figure 3.5 in Section 3.1.6, and are summarized in Table 5.1. The selected bolometers for the muon veto-bolometer coincidence analysis are the one shown in blue without striped on Figure 3.5, minus GGA1, which was intentionally polluted for calibration purpose. Figure 5.5 is a 3-D representation of the position of the selected bolometers during Run 8. The bolometer data used come from the analysis B from the PAW-based software ANA developed in Lyon [161, 188].

In the analysis B, the events left are those from good periods in terms of heat and ionization baseline and are defined as at least one bolometer with a hit, *i.e.*

DAQ	bolometer	status	remarks
s1	ID	out	interdigitised bolometer for test purpose
s1	GSA9	out	switched OFF
s1	GGA14	✓	
s1	GGA13	✓	
s1	GSA11	✓	
s1	GGA10	✓	
s1	GGA7	✓	
s1	GSA10	✓	
s1	GGA6	out	switched OFF
s1	GGA3	✓	
s2	GSA6	out	switched OFF
s2	GGA5	✓	
s2	GGA11	✓	
s2	GGA12	out	switched OFF
s2	GGA8	✓	
s2	GSA8	✓	
s2	GSA4	out	switched OFF
s2	GGA4	✓	
s2	GGA9	✓	
s3	GSA7	✓	
s3	GSA5	out	switched OFF
s3	GSA1	✓	
s3	GGA1	out	$^{210}\text{Po}$ source
s3	GSA3	✓	large alpha background
s3	IAS	out	sapphire detector

Table 5.1: *Bolometer status during Run 8.*Figure 5.5: *3-D visualization of the selected bolometers for the muon veto-bolometer coincidence analysis during Run 8.*

with an ionization energy which passed the threshold, defined as an individual value for each bolometer. The study is made per DAQ computer, *i.e.* per data set of bolometers. The files have one line per event. If several bolometers are hit, the sum of energies are calculated per set of bolometers from a DAQ computer. The ionization and heat channels have been calibrated in keV from the calibration runs and the recoil energy calculated from the heat energy corrected by the Luke effect, as explained in Section 3.1.5. All events are ordered per increasing real time in days from the computer internal clock  $t_{PC}$ , which is not the ever-restarting clock of the dispatcher  $t_{10\mu s}$  in 10  $\mu s$ -beat. Quality cuts have also been performed to cut out the bolometers which do not fit certain conditions and to restrict the final events to a defined fiducial volume. However, these quality cuts are not used for the muon veto-bolometer coincidence search and will be discussed in Section 5.4.3.

In general, if there is a coincidence between the muon veto system and the bolometer system, then these events are expected to be muon/shower-induced neutrons or gammas. Since neutrons are likely to interact in more than 1 bolometer crystals, such a coincidence potentially imply multi-hit event. The idea is thus to define global bolometer events, occurring in 1 up to 16 bolometers, and to look whether these events are in coincidence with a muon veto event. Therefore, we first need to define a common bolometer time and to look for bolometer coincidences between the events of the different DAQ.

Since the clock from all DAQ computers are independent, the first thing to do was to define a global time stamp. The DAQ computer  $s2$  is chosen to be the reference computer, as it shared its clock with the muon veto. The time stamp of  $s1$  and  $s3$  events have been “renormalized” to the one of  $s2$ , under certain restrictions.

The “renormalization” is actually a shift, so that the time stamp of  $s1$  and of  $s3$  refer to the run start of  $s2$  instead of their own start. This calculation of shifts was done by identifying an accumulation in the distribution of the time difference  $\Delta t_{\text{shift}}$  of consecutive events of  $s2$  and  $s1$ , and of  $s2$  and  $s3$ , per couple of coincident runs. If at least two  $\Delta t_{\text{shift}}$  fall within a 20 ms bin, the shift to apply is the mean of these  $\Delta t_{\text{shift}}$ . Else the stamp is not reconstructed, and the run is rejected. The  $\Delta t_{\text{shift}}$  between  $s2$  and  $s1$ , and  $s2$  and  $s3$  is shown in Figure 5.6. There is no systematic shift between the DAQ of the different computers. For corresponding runs from different computers, the DAQ is started with a delay of a few minutes up to 5 hours.

There are runs of  $s1$  or  $s3$ , which start or stop within the corresponding run of  $s2$ . In this case, their time stamps are reconstructed and they are part of the muon veto coincidence analysis. Then, runs of  $s1$  or  $s3$  can be longer than this of  $s2$ . At the end of the run, the clock of  $s2$  continues to deliver a time stamp to the veto, until a new restart. If the run of  $s1$  or  $s3$  is longer, the time stamp, and the correction applied, is still reliable and can be compared with the muon veto time stamp up to the next restart on  $s2$ . Actually there is no run from  $s1$  or  $s3$  which are long enough to encounter another restart of  $s2$ . Runs on the different computers more or less start together in a 5 min length, except for some runs which were restarted. And usually, they stop in the same 10 min. Finally, if the run of  $s1$  or  $s3$  starts earlier than the run of  $s2$ , the reconstructed time stamps of these events are negative. The corresponding time stamp of the veto is a high number from the end of another run (calibration or regeneration or (short) physics runs). Thus, to compare this high muon veto time stamp and the negative  $s1$  or  $s3$  time stamp, the time stamp of the muon veto would also have to be reconstructed to be made as if it is part of the

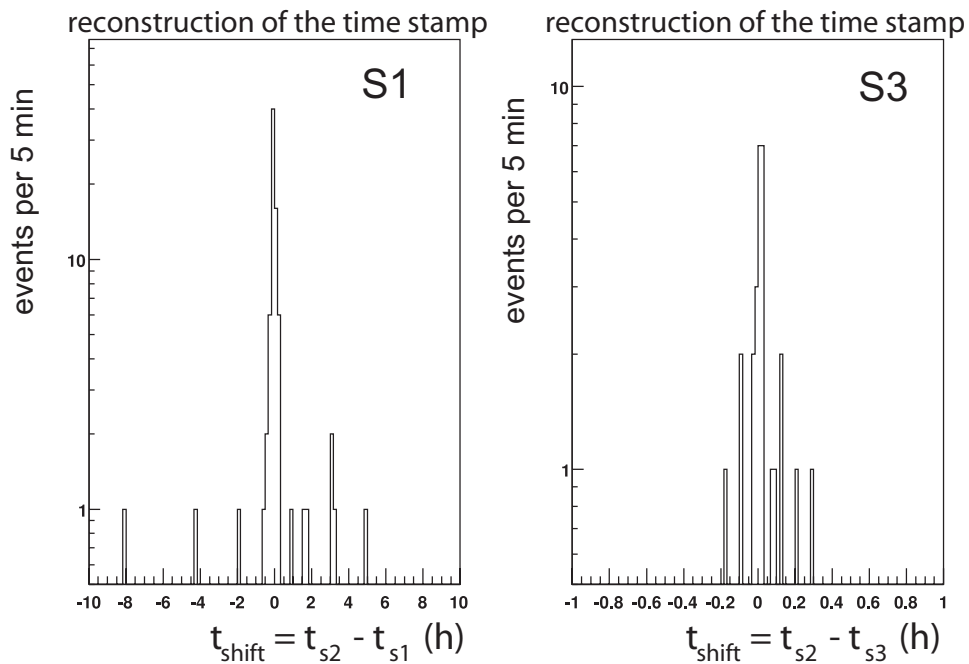


Figure 5.6: Shift applied to reconstruct the time stamp of  $s_1$  (left) and the time stamp of  $s_3$  (right) to correspond to this of  $s_2$ , shown in a 5 min binning. There is no systematic shift between the different clocks, and in the mean  $\Delta t_{\text{shift}}$  is  $\sim 1.5$  min.

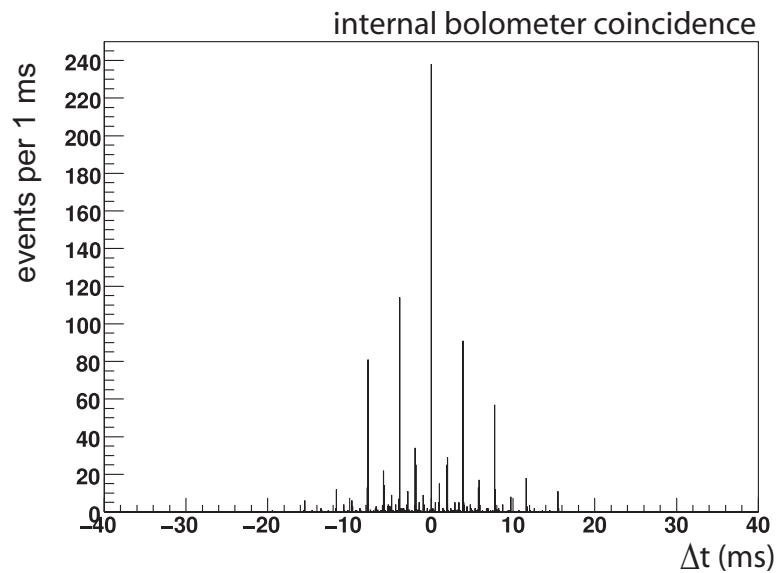


Figure 5.7: Time difference of the events which are in coincidence between the three sets of bolometers. The distribution is discrete as the timing in heat trigger is rounded on 1 ms. The additional feature comes from the reconstruction of the stamp

current run of  $s2$ . This manipulation has not been done. The events with a negative time stamp are excluded.

Once the time stamp is reconstructed, it is possible to look for coincidences between the three sets of bolometers, *i.e.* the three bolometer DAQ computers and to define bolometer system events. In Figure 5.7 are shown the time difference of consecutive events  $\Delta t_{\text{bolo in coincidence}}$  from coincident runs of different DAQ computers. The coincident bolometer events are selected in a 20 ms interval centered on zero. The structure of the bolometer coincidences is due to the reconstruction of the time stamp.

Note that when comparing with the muon veto time stamp, the time stamp of  $s2$  is preferably used, since it has not been manipulated. If the bolometer coincidence is between  $s1$  and  $s3$ , the time stamp used is the sum of their time stamps weighted by their total heat energy deposit.

The bolometer system life time for this analysis is the one of  $s2$ , plus the life time of  $s1$  and  $s3$  if their runs have been longer, all weighted by the mass of their bolometers. With 16 Ge bolometers of 320 g, the exposure of the bolometer system under investigation here amounts to  $t_{\text{bolo}} = 285.4 \text{ kg}\cdot\text{day}$ .

A new file is defined for further analysis, ordered per increasing real time in days from the computer internal clock  $t_{\text{PC}}$ . This file contains the global event number, the run number from analysis B, the event number in this run, the time stamp in seconds  $t_{10\mu\text{s}}$ , the real time in days  $t_{\text{PC}}^{\text{norm}}$  (normalized to 01/01/2008), the recoil, ionization and heat energies  $E_R$ ,  $E_I$  and  $E_H$ , the factor  $Q = E_I/E_R$ , the number of bolometers with a hit, *i.e.* the bolometer multiplicity  $multi_{\text{bolo}}$ , the identity of the bolometer with a hit (relevant only if  $multi_{\text{bolo}} = 1$ ) and a flag. The energies are in keV and are the sum of the energies of the bolometers with a hit in the event. The flag allows to know if the time stamp of the event has been reconstructed or not ( $f = 1$  or  $0$ ) and to know the coincidence status of the event. For  $s2$ , the flag is at least 1, as it is the reference computer. If the flag is zero, then the time stamp of  $s1$  or  $s3$  is the original one. If the event, if reconstructed, is in coincidence with the next event/line in the file  $f = f + 10$  per line. The final event in coincidence has an extra flag of 50 instead of 10 and summarizes the variables about the coincidence. The energies on this line are the sum of the energies of all the bolometers in the coincidence, as well as the multiplicity is the total sum of bolometer with a hit. For example, an event with a flag  $f = 71$  is a coincidence of the three computers, its recoil, ionization and heat energies and multiplicity are the sum of the hit bolometers of the three computers together.

The muon veto events are all kind of entries, which trigger the muon veto system, to keep the statistics high. On the contrary, the bolometer system events are events of a good quality, since they have already been selected on physics criteria. Two conditions have been yet added. First, only bolometer runs which lasted longer than 24,000 s ( $\sim 6.6 \text{ h}$ ) are selected, *cf.* Section 5.4. Then, on the left hand side of Figure 5.8 is plotted the time difference of consecutive bolometer system events up to 10 s. The negative  $\Delta t_{\text{bolo}}$  due to the restarts of the clock are all plotted at  $-0.5 \text{ s}$ . For the muon veto-bolometer analysis, a further cut of  $\Delta t_{\text{bolo}} > 500 \text{ ms}$ , which corresponds to twice the bolometer dead time of 250 ms, is applied to make sure the bolometer events are uncorrelated. This condition only cuts 686 of the bolometer events and make the sample clean of any kind of after-pulses, leading to a nice exponential distribution with a fit value  $\chi^2/ndf = 2581/2133$ . The slope of the exponential fit is 0.0164 Hz. On the right hand side is shown the distribution

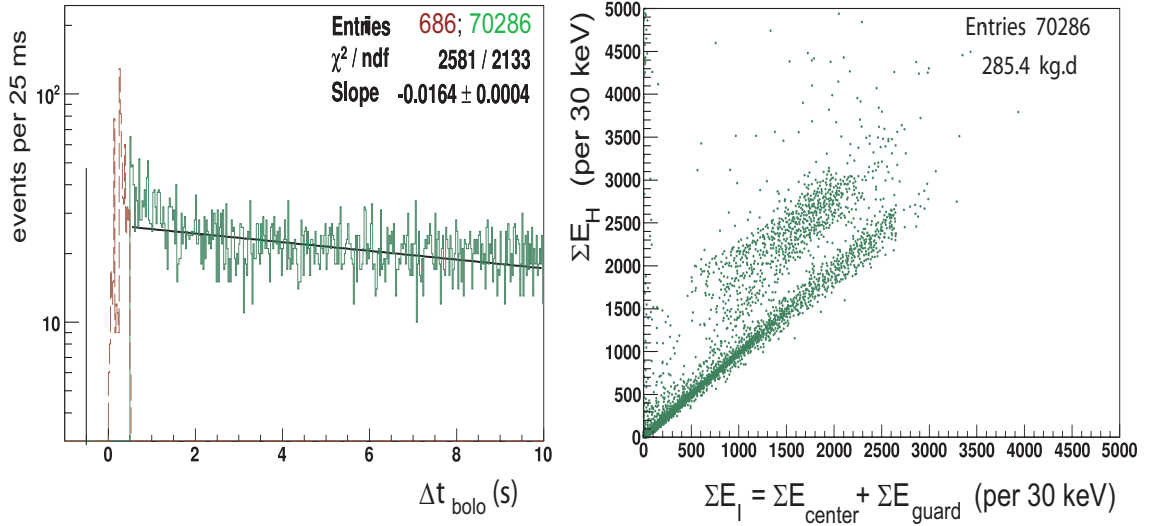


Figure 5.8: *Quality of the bolometer system events. Left: Time difference of consecutive bolometer events. The negative  $\Delta t$  at  $-0.5$  s are due to the restarts of the clock. The slope of the exponential fit does not exactly correspond to the calculated rate, which may suggest, we could have used a higher cut rather than  $\Delta t_{\text{bolo}} > 500$  ms. Right: Recoil energy versus ionization energy with  $\Delta t_{\text{bolo}} > 500$  ms. These energies are the sum of all contributed bolometers for an event.*

of events in the recoil channel versus the ionization channel. The distribution is predominantly set on a line  $E_R = E_I$  as expected these events are mainly gamma-like background with  $Q = 1$ . There is no particular behavior at low energy, as these events are already a selection, but there is an extra feature around  $E_R \sim 2500$  keV, parallel to  $E_R = E_I$ , which may come from the saturation in ionization at high energy or from a bolometer with bad features (a high figure of merit, a bad resolution on a channel) or with a large background, like GSA3. Note that not all bolometers, which are part of the coincidence analysis, are actually part of the WIMP analysis, *cf.* Section 5.4.3. There are 70286 events in the final bolometer selection for coincidence search, corresponding to an exposure of 285.4 kg·d, which makes a rate of

$$\Gamma_{\text{bolo}} = 14.6 \text{ mHz}. \quad (5.3)$$

## 5.4 Coincidences between the muon veto and the bolometers

The muon veto and the bolometer samples are defined from the preceding sections. Although the bolometer time stamp has been reconstructed to have a bolometer system event sample which seems to rule on a single clock, the time stamp still restarts from zero with every new run on *s2*, the reference computer. On the one hand, for the bolometer system, there are the time stamp from the clock in 10  $\mu\text{s}$ -beat  $t_{10\mu\text{s}}^{\text{bolo}} = t_{\text{bolo}}$  and the real time with the precision of 1 s from the computer clock  $t_{\text{PC}}$ . On the other hand, for the muon veto system, there are the time stamp from the clock in 10  $\mu\text{s}$ -beat  $t_{10\mu\text{s}}^{\text{veto}} = t_{\text{veto}}$  and the time of creation of a file with the precision of 1 s, which is part of the file name. The analysis of coincidences between the muon veto and the bolometer systems is made such that the real time

of a bolometer system event is associated with a muon veto file according to its start time. Then, step-by-step the time stamp in 10  $\mu$ s-beat of events of the two systems is compared.

To avoid misassociations of events, especially when searching to compare small time stamps, only bolometer runs which lasts longer than 24,000 s ( $\sim 6.6$  h) are selected. This value has been chosen experimentally to balance the number of bolometer runs kept and the number of periods on the veto. On the bolometer side, data runs longer than 24,000 s are in the selection. On the veto side, any periods corresponding to short runs or regeneration runs ( $< 6.6$  h) are removed. For calibration runs, they are likely to happen another day than physics runs, and then be excluded by the comparison of the real time.

If  $|t_{\text{veto}} - t_{\text{bolo}}| < 1$  s, the event is considered as a potential coincidence and studied in more detail. The result can be seen on left in Figure 5.9, where is shown the heat energy in keV for bolometer system events versus  $t_{\text{veto}} - t_{\text{bolo}}$  in a  $\pm 100$  ms interval. There is a clear excess of high energy events, which indicates correlated events between the muon veto and the bolometers.

### 5.4.1 Definition of coincidence region and rates

The time interval for coincidences is defined by the position of the peak at high heat energy events  $E_H > 6.5$  MeV and no multiplicity condition on the veto, as shown on left in Figure 5.10. The time interval of coincidences is set to

$$t_{\text{veto}} - t_{\text{bolo}} = \Delta t_{\text{coinc}} \in [+15, +35] \text{ ms.} \quad (5.4)$$

The fact that  $t_{\text{veto}} - t_{\text{bolo}} > 0$  seems at first completely unphysical, since the veto system is first hit and then the bolometers. This is discussed in Section 5.4.3 and with all technical details in Appendix C. As one can see in Figure 5.10 on right, the events at high energy are not clustered in real time. They are no artefact due to specific condition, they are spread all along the 4 months of investigation.

Two regions are now defined, one as the coincidence region and one as outside the time interval  $\Delta t_{\text{coinc}}$ . However, in Figure 5.9 on right is shown only the  $\Delta t_{\text{coinc}} = t_{\text{veto}} - t_{\text{bolo}}$  on a  $\pm 100$  ms interval. One recognizes a flat distribution. There are no correlated events, which means the coincidence events are background dominated, even inside the coincidence time interval. The condition of having more than one muon veto module with a hit ( $multi_{\text{veto}} > 3$ ), as shown in Figure 5.11, underlines the coincidence peak. It allows to reduce the number of accidental coincidences and to concentrate on candidates induced by muons.

The first test for the events in coincidence is to check if the measured rate reproduces the expected one in terms of accidental events. Assuming uncorrelated stochastic<sup>†</sup> event samples for both muon veto and bolometer system, the expectation is calculated from their rate as defined in the Equations 5.2 and 5.3:

$$N_{\text{acc}}^{\text{exp}} = (\Gamma_{\text{veto}}^{multi_{\text{veto}} > 3} \cdot \Gamma_{\text{bolo}} \cdot \Delta t_{\text{win}}) \cdot t \quad (5.5)$$

$$= (0.00446 \text{ s}^{-1} \cdot 0.0146 \text{ s}^{-1} \cdot \Delta t_{\text{win}}) \cdot \frac{285.4 \text{ kg} \cdot \text{d}}{5.12 \text{ kg}} \quad (5.6)$$

<sup>†</sup> The stochastic quality is justified by the exponential distributions of the muon veto and bolometer system events as shown in Figure 5.4 and 5.8 on left, respectively, and by the very small sample of correlated muon veto-bolometers coincidences.

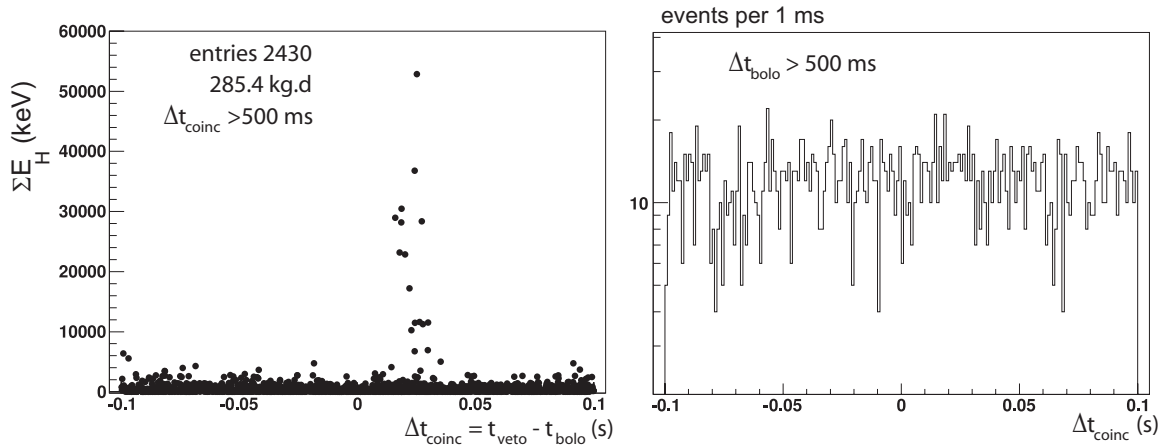


Figure 5.9: *Muon veto-bolometer events in coincidence. Left: Heat energy in keV for bolometer system events vs.  $t_{\text{veto}} - t_{\text{bolo}}$  in seconds in a  $\pm 100$  ms interval. The heat energy is the sum of the heat energy of the bolometers which have triggered. Right:  $\Delta t_{\text{coinc}} = t_{\text{veto}} - t_{\text{bolo}}$  of the muon veto-bolometer events in coincidence, in a  $\pm 100$  ms interval. The plot is zoomed on an interval of  $\pm 100$  ms, instead of the full  $\pm 1$  s technical window, to focus on the position of the possible peak region. There is no further condition applied on muon veto events.*

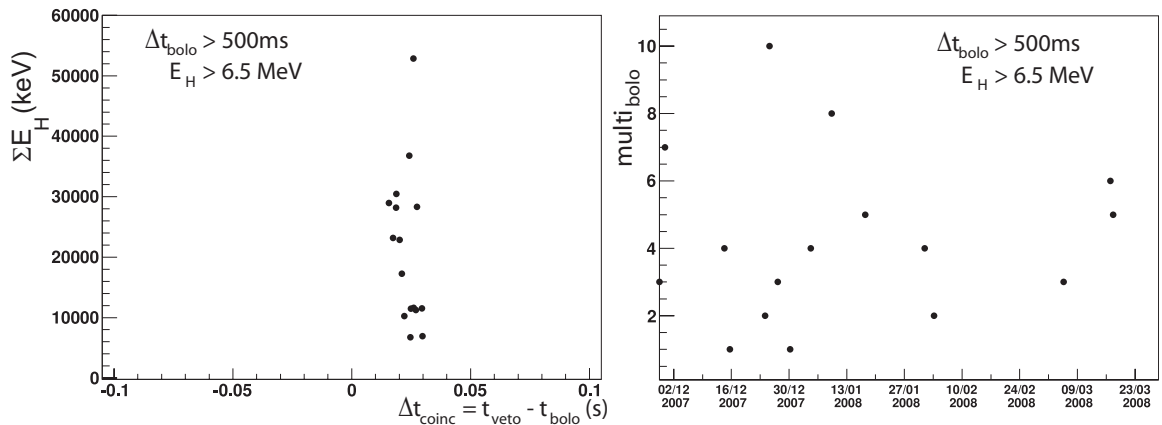


Figure 5.10: *Coincidences at high heat energy  $E_H > 6.5$  MeV to define the coincidence interval. The heat is the sum of the heat of the bolometers which have triggered. Left: Heat energy in keV for bolometer system events versus  $t_{\text{veto}} - t_{\text{bolo}}$ . Right: Distribution of the same events in bolometer multiplicity over measuring time.*

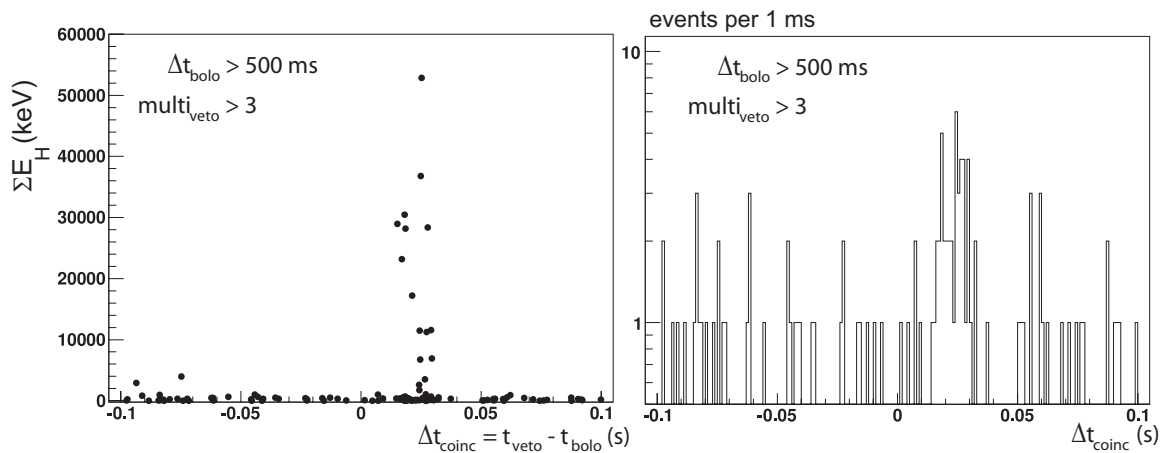


Figure 5.11: *Muon veto-bolometer events in coincidence with  $\text{multi}_{\text{veto}} > 3$ . Left: Heat energy in keV for bolometer system events vs.  $t_{\text{veto}} - t_{\text{bolo}}$ . The heat energy is the sum of the heat energy of the bolometers which have triggered. Right:  $\Delta t_{\text{coinc}} = t_{\text{veto}} - t_{\text{bolo}}$  of the muon veto-bolometer events in coincidence. The condition on the muon veto is to have strictly more than one veto module by applying  $\text{multi}_{\text{veto}} > 3$ .*

On a time window of  $\Delta t_{\text{win}} = 2 \text{ s}$  (*i.e.*  $\pm 1 \text{ s}$ ),  $N_{\text{acc}}^{\text{exp}} \simeq 627 \pm 3$ . Inside the coincidence time interval, the events are a mixing of real coincidences and background events. The number of accidental events inside the coincidence time interval can be evaluated from the number of events outside the coincidence time interval, which are only accidental events. The results for the accidental events are in Table 5.2. The second column is the number of accidental events expected and measured outside the coincidence region. In the third column are extrapolated values from the second column in the coincidence region. The rates of accidental events are reproduced by the measurement. They agree within the statistical uncertainties.

Inside the coincidence time interval, it is interesting to differentiate between the high recoil energy events  $E_R \geq 250 \text{ keV}$ , which are probably fast neutrons or even passing through muons, and low energy recoil events  $E_R < 250 \text{ keV}$ , which are more interesting muon-induced phenomena as in the energy region of interest for the WIMPs. Since we would like to focus at low energy, we now switch from the heat energy  $E_H$  to the more refined recoil energy  $E_R$ . The list of principal characteristics of these events at low and high energy can be found in Appendix A.3. The real number of coincidence candidates has yet to be extracted subtracting the accidentals for this region. The results of this calculation is shown in Table 5.3. The signal over background confirms the clear excess of events inside the time window of the expected coincidences. The excess coincidences are the muon-induced candidates. One can deduce the coincidence event rate to compared with the simulated rate from [184].

However, the center of the time interval defined via high heat energy events is 23.45 ms and the length of the interval is somewhat arbitrarily chosen to fit the events. Thus, one can ask how well defined the coincidence time interval of  $25 \pm 10 \text{ ms}$  is, especially at low recoil energy  $E_R < 250 \text{ keV}$ , where the WIMP is expected to interact. The results of possible coincidence intervals are summarized in Table 5.4.

events in	$[-1000, +15] \vee [+35, +1000]$ ms	$[+15, +35]$ ms
expectation $N_{\text{acc}}^{\text{exp}}$	$621 \pm 7$	$6.3 \pm 0.1$
measurement $N_{\text{acc}}$	$647 \pm 26$	$6.6 \pm 0.2$

Table 5.2: *Measured and extrapolated rate of accidental coincidences.*

$t_{\text{veto}} - t_{\text{bolo}} \in [+15, +35]$ ms	low energy events $E_R < 250$ keV	high energy events $E_R \geq 250$ keV
measured events	16	28
expected accidentals	$3.7 \pm 0.2$	$2.9 \pm 0.2$
excess coincidences	$12.3 \pm 4.2$	$25.1 \pm 5.5$
signal / background	$3.3 \pm 1.4$	$8.7 \pm 2.4$

Table 5.3: *Events at  $E_R < 250$  keV and  $E_R \geq 250$  keV in the coincidence region.*

time intervals (ms) for the coincidences	low energy excess $E_R < 250$ keV	high energy excess $E_R \geq 250$ keV	total number of excess events
<b><math>t = 25 \pm 10</math></b>	<b>12.3</b>	<b>25.1</b>	<b>37.4</b>
$t = 25 \pm 15$	10.5	25.7	36.2
$t = 24 \pm 10$	12.3	26.1	38.4
$t = 23.45 \pm 10$			
$t = 23.5 \pm 10$			
$t = 23 \pm 10$			
$t = 24 \pm 15$	10.2	26.2	36.4
$t = 23.45 \pm 15$			
$t = 23.5 \pm 15$			
$t = 23 \pm 15$			
$t = 20 \pm 10$	11.3	24.1	35.4
$t = 20 \pm 15$	11.5	26.7	38.2

Table 5.4: *Evaluation of the coincidence interval.*

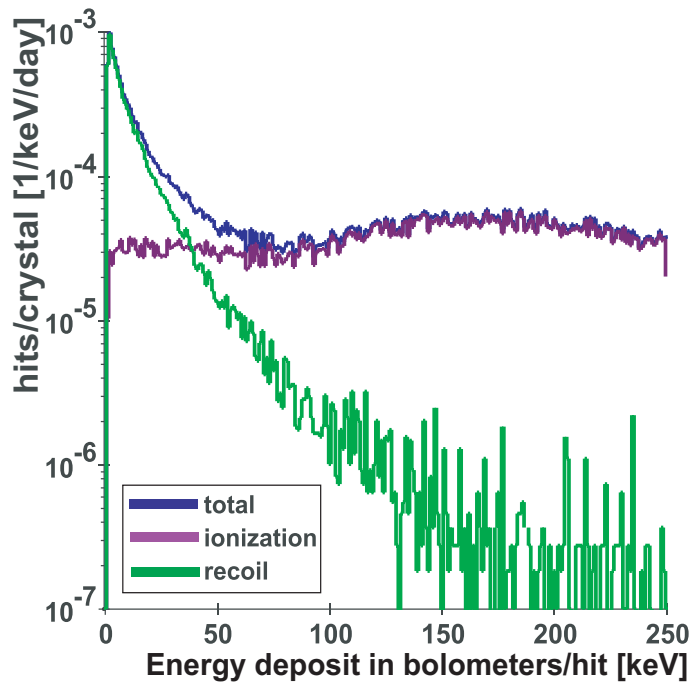


Figure 5.12: *Geant-4* simulation of muon-induced Germanium hits. The total energy deposit (blue) can be assigned to electron recoils by electrons and photons (green) and nuclear recoils mainly by neutrons (purple). Figure from [184].

Even if we decide to change the time interval and to go for *e.g.*  $23 \pm 10$  ms, the number of correlated excess events remains almost unchanged.

The simulated rate is extracted from Figure 5.12. In Figure 5.12 is shown the simulated energy deposit spectrum in Ge bolometers as a result of muon-induced electromagnetic and hadronic showers. The contribution of nuclear recoil clearly dominates below 50 keV, which is also a feature of the measured coincidences, *cf.* Figure 5.13. However, there is a small threshold of 15 keV on the bolometer heat channel, which allows to disregard a part of the exponential contribution and allows to estimate the expected rate in the following way. There are  $4 \cdot 10^{-5}$  hits per crystal ( $1/\text{keV}\cdot\text{day}$ ) at 250 keV, this corresponds to  $\Gamma_{\text{coinc}}^{\text{simu}} = 4 \cdot 10^{-5} \times 250/0.320$  events $\cdot(\text{kg}\cdot\text{d})^{-1}$ . For  $1 < E_R < 250$  keV, the coincidence rates are

$$\Gamma_{\text{coinc}}^{\text{simu}} \sim 0.03 \pm 0.01 \text{ events}\cdot(\text{kg}\cdot\text{d})^{-1} \quad (5.7)$$

$$\Gamma_{\text{coinc}}^{\text{meas}} = 0.043 \pm 0.015 \text{ events}\cdot(\text{kg}\cdot\text{d})^{-1} \quad (5.8)$$

The measurement is well reproduced by the expectation, but note that the simulation is made for the full range of energy deposit below 250 keV and for the compact geometry of all 120 bolometers. For  $E_R \geq 250$  keV, the measured coincidence rate is  $0.09 \pm 0.02$  events $\cdot(\text{kg}\cdot\text{d})^{-1}$ .

## 5.4.2 Identification of the coincidence events

It is not possible to define which of the 44 events are accidental events and which are the muon-induced events, but it is possible to visualize them on a Q-plot to

events in		$[-1000, +15] \vee [+35, +1000]$ ms	$[+15, +35]$ ms
$E_R \geq 50$ keV	$Q < 0.6$	23 (6.3%)	0 (0%)
	$Q \geq 0.6$	245 (67.5%)	11 (68.8%)
$E_R < 50$ keV	$Q < 0.6$	11 (3.0%)	4 (25.0%)
	$Q \geq 0.6$	84 (23.2%)	1 (6.2%)

Table 5.5: Number of events outside and inside the coincidence interval in 4 different regions defined by the conditions  $E_R \geq 50$  keV or  $E_R < 50$  keV and  $Q \geq 0.6$  or  $Q < 0.6$ .

determine which kind of events they are.

The resolution lines for the Q-plot are defined in Section 3.1.5, with input variables as listed in Appendix A.1. The results for the 16 events at  $E_R < 250$  keV and  $\Delta t_{\text{coinc}} \in [+15, +35]$  ms is shown in Figure 5.13. Most of the events are enclosed in the  $\gamma$ -region band around  $Q \sim 1$  and are likely to be  $\gamma$ -particles, except for 4 events. Although, there is no condition on the bolometer multiplicity in this Q-plot, all events are the coincidences of the muon veto with only 1 individual bolometer. These 4 events would not have been removed under the condition of multiple hits to exclude neutron-like events.

The distribution of coincidence events inside the coincidence window can be compared to the one outside over  $\Delta t_{\text{win}} = \pm 1$  s, which is pure uncorrelated background. The comparison can be made defining 4 regions with the conditions  $E_R \geq 50$  keV or  $E_R < 50$  keV and  $Q \geq 0.6$  or  $Q < 0.6$ , see Table 5.5. In brackets is the percentage of the selection compared to the total number of events. The ratio of events for the region ( $E_R < 50$  keV,  $Q < 0.6$ ) and ( $E_R < 50$  keV,  $Q \geq 0.6$ ) is 4/1 inside  $\Delta t_{\text{coinc}}$  and 11/84 outside. Therefore the events inside the coincidence region  $\Delta t_{\text{coinc}} \in [+15, +35]$  ms are not a background like distribution. These events are clearly identified as muon-induced neutrons.

Information from the veto can also be added to have more detail on the coincidences. A 3-D visualization has been implemented in the C++ based ROOT software. The position of the hit on a veto module is from the study made in Section 4.5.1. The results for the 4 events are shown in Figure 5.14. Except for the one with the lowest  $E_R$ , the muon track is very clear, and they are all likely to be muon-induced events. For the other one the track is not so evident, it is not possible to decide if it is not a muon.

Examples of events with  $E_R \geq 250$  keV are shown in Figure 5.15. Events at high energy are as different as a single bolometer with a very high or relatively low energy (top and bottom left), or few bolometers which totalize a high or relatively low energy (top and bottom right). The second type of events, for which the recoil energy is the sum of the recoil energy of the bolometers, are particularly interesting. The individual bolometers, which constitute a coincidence event, may fall into the region of interest for WIMPS at  $E_R < 250$  keV, especially when quality cuts exclude the second bolometer. The results of the individual contribution is shown in Figure 5.16. Three events fall in the nuclear recoil band with ( $E_R = 35$  keV,  $Q = 0.33$ ), ( $E_R = 34.9$  keV,  $Q = 0.47$ ) and ( $E_R = 16$  keV,  $Q = 0.22$ ). Note that the first two are associated with one or two bolometers of some tens of MeV, clearly a muon, and the other one with two bolometers of hundreds keV. Muon-induced background

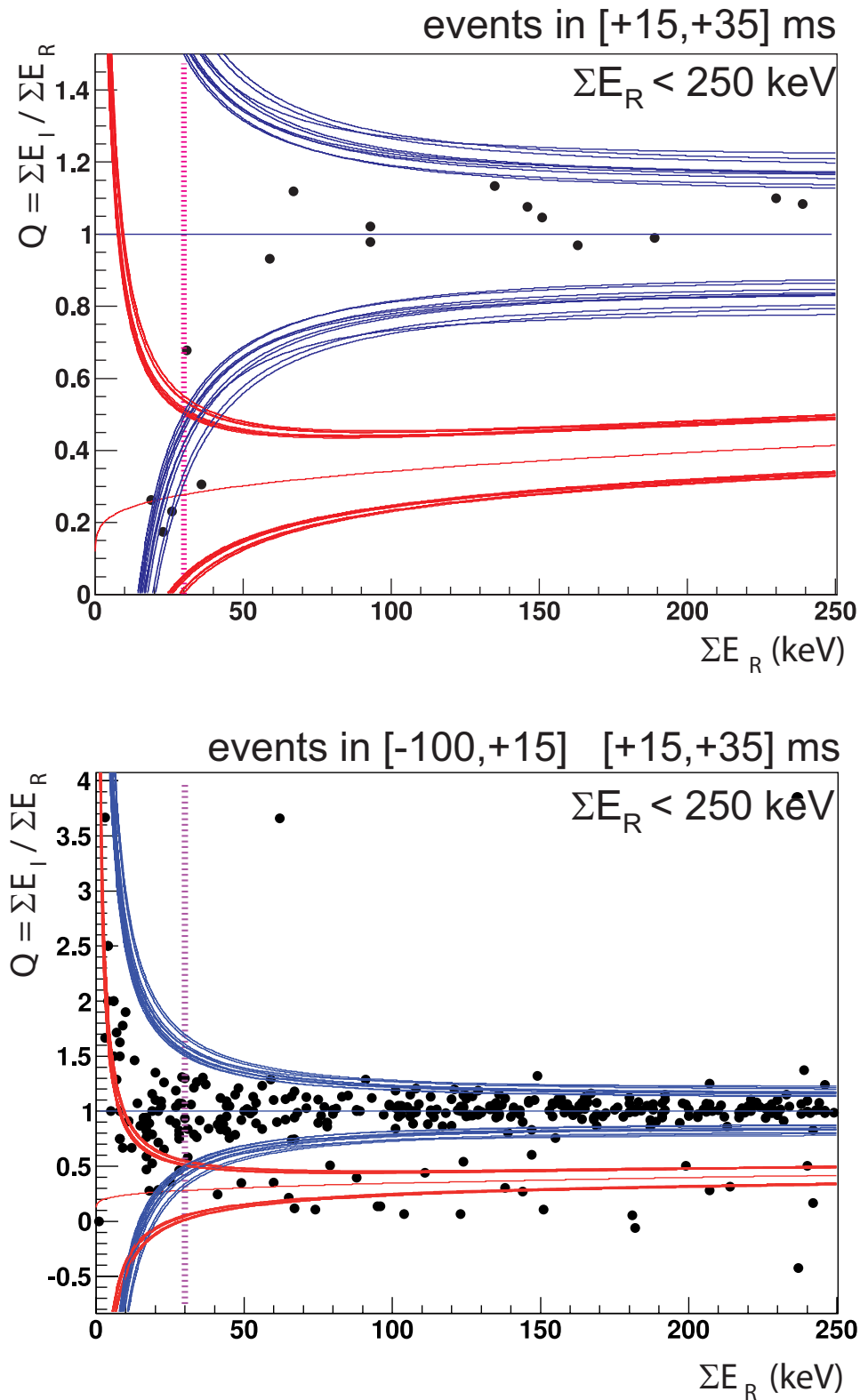


Figure 5.13:  $Q$ -plot of events in coincidence with  $E_R < 250$  keV inside (top) and outside (bottom) the coincidence time interval  $\Delta t_{coinc} \in [+15, +35]$  ms. The pink line is plotted as a reference at  $E_R > 30$  keV, this is not a threshold applied in this analysis.

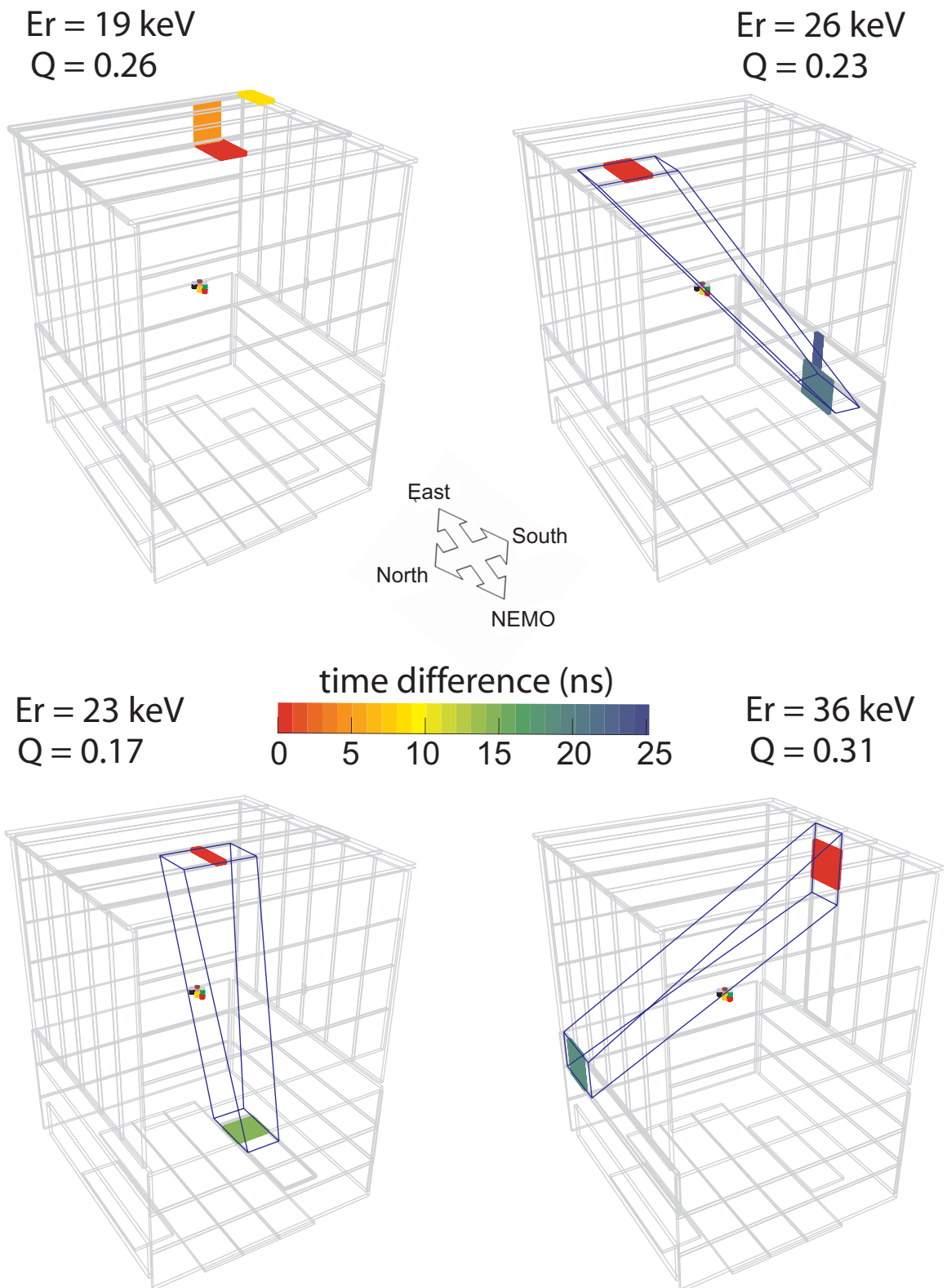
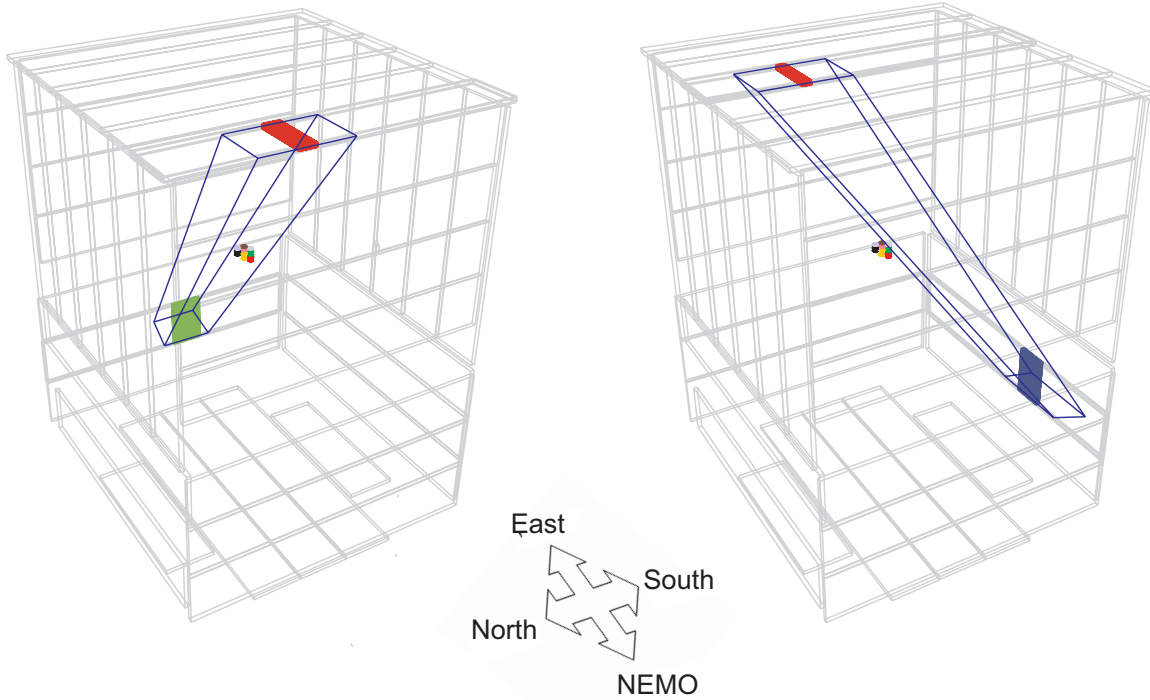


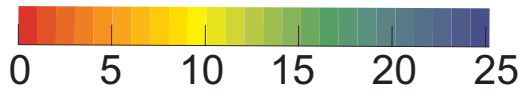
Figure 5.14: 3-D visualization of the four coincidence events with  $E_R < 250$  keV in the nuclear recoil band in  $\Delta t_{\text{coinc}} \in [+15, +35]$  ms. In a veto module, the size is proportional to the energy deposit, and the color to the timing.

$E_R = 3956 \text{ keV}$   
 $Q = 0.84$

$E_R = 38453 \text{ keV}$   
 10 bolometers



time difference (ns)



$E_R = 348 \text{ keV}$   
 $Q = 0.97$

$E_R = 513 \text{ keV}$   
 2 bolometers

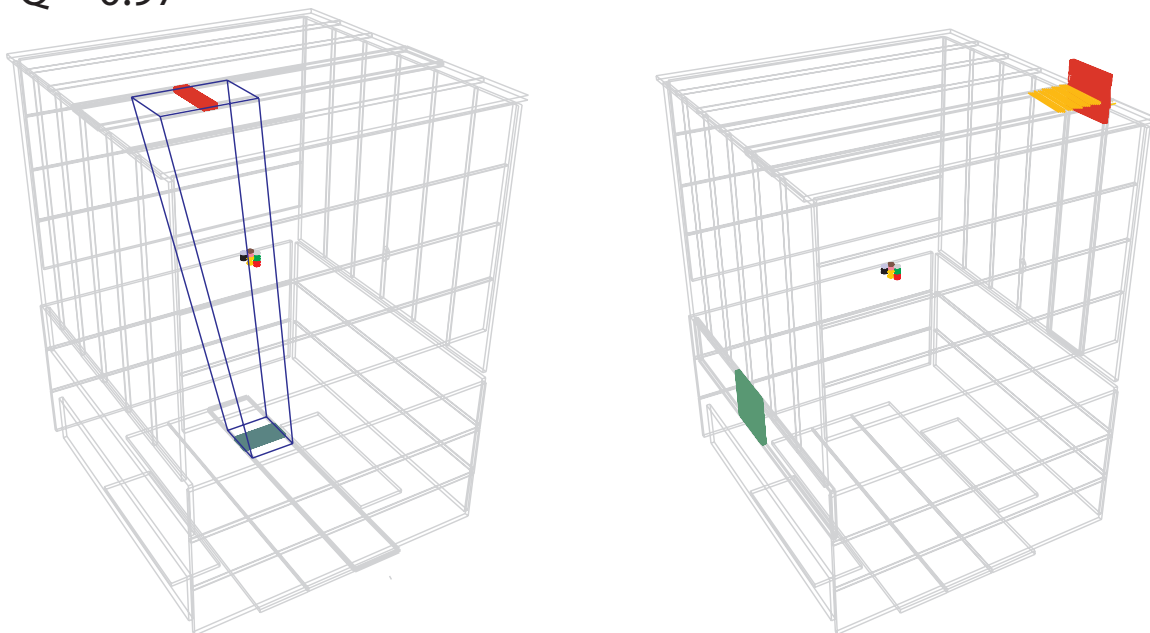


Figure 5.15: Examples of muon veto-bolometer coincidence events with  $E_R \geq 250 \text{ keV}$  in  $\Delta t_{\text{coinc}} \in [+15, +35] \text{ ms}$  in 3-D visualization. In case of multi bolometer hits, the recoil energy is the sum of the recoil energy of the hit bolometers, the value of  $Q$  is then not relevant and the number of bolometers is mentioned instead. In a veto module, the size is proportional to the energy deposit, and the color to the timing.

event in the bolometers or accidental bolometer in coincidence with the others, it is not possible to conclude. These events would be in any case removed from the WIMP analysis, as they are multiple hits event.

### 5.4.3 Discussion: Comparison with the pure bolometer analysis and position of the peak

The first point to discuss is to compare the events left at  $E_R < 250$  keV with the pure bolometer analysis, which is performed on the same files but with some quality additional cuts [188].

The figure of merit (or magic point, MP) is defined as the intersection of the  $\gamma$  band at 99.9% and the neutron band at 90%. This value is based on the baseline and the 356 keV-calibration-peak resolutions for the heat and the ionization, which are different from a bolometer to another. The list of figure of merit for the different bolometers is shown in Appendix A.2. For the bolometer analysis, the figure of merit has been set to 30 keV.

In Figure 5.13 and 5.16, the resolutions drawn are the one from good bolometers with  $MP < 30$  keV, and with no calibration or background problem. The resolutions of GSA11 (noise), GSA7 (no Feb. data), GSA1, GGA11 (both calibration trouble), GSA3 and GGA8 (both  $MP > 30$  keV) are thus not drawn. Then, one can ask if there are events from these bolometers in coincidence with the veto. There are three events from these bolometers: ( $E_R = 93$  keV,  $Q = 1.1$ ) from GSA11, ( $E_R = 93$  keV,  $Q = 0.98$ ) and ( $E_R = 151$  keV,  $Q = 1.04$ ) from GGA8. There is a fourth event ( $E_R = 59$  keV,  $Q = 0.93$ ) from GSA7, but it happened the 23/01, when there was no problem with this bolometer. All these events are in the electronic recoil band.

More interesting, the muon veto-bolometer coincidence analysis shows that 4 events are left in the nuclear recoil band for  $E_R < 250$  keV. However, these events does not show up in Q-plots of the full bolometer analysis [188]. Although there are quality cuts on the data of the full analysis, that reject some bolometers and noisy periods, it has been cross-checked that these four low  $Q$  events are part of the surviving events after the cut.

A bolometer is disregarded, if its figure of merit is above 30 keV. Therefore, to have a constant number of kg·d along the recoil energy scale, *i.e.* to avoid dependence on the individual figure of merit, events are considered above 30 keV. Since three of the coincidence events have a  $E_R < 30$  keV, they are below the threshold and not seen by the bolometer analysis.

The last event has  $E_R > 30$  keV, but this event is a guard event. The fiducial volume defined in [188] is made only by the central electrode, and the guard electrode acts a veto. Therefore, the last coincidence event at low  $Q$  is also out of the bolometer analysis.

It is important to notice that the muon veto-bolometer coincidence analysis and the pure bolometer analysis are two different and complementary analyses with different conditions. Thus, there is no reason that the events rejected in the bolometer analysis are dismissed from the coincidence events.

The second point to discuss is the position of the coincidence time window  $\Delta t_{\text{coinc}} = [+15, +35]$  ms. The time window is  $\Delta t_{\text{coinc}} = t_{\text{veto}} - t_{\text{bolo}}$ . And as an event in coincidence in the veto and the bolometers happens almost simultaneously

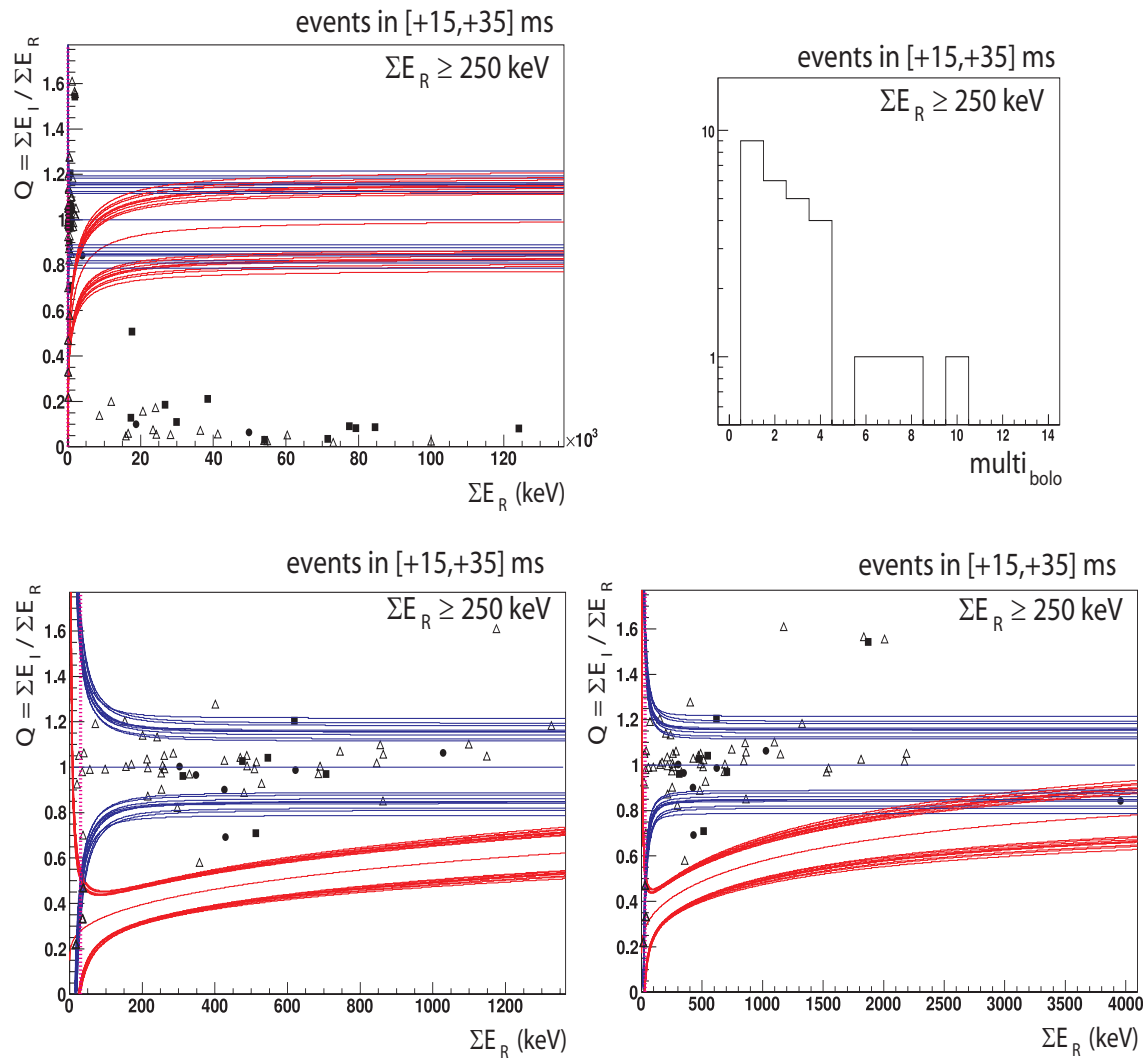


Figure 5.16:  $Q$ -plots of events in coincidence with  $E_R \geq 250$  keV inside the coincidence time interval  $\Delta t_{\text{coinc}} \in [+15, +35]$  ms on the full energy scale (top left), for  $E_R < 1350$  keV (bottom left) and for  $E_R < 4$  MeV. The pink line is plotted as a reference at  $E_R > 30$  keV, this is not a threshold applied in this analysis. The bolometer multiplicity of the coincidence is shown in the top right figure. In the  $Q$ -plot this information is translated as: Coincidence with  $\text{multi}_{\text{bolo}} = 1$  are plotted as full circles, with  $\text{multi}_{\text{bolo}} > 1$  are full rectangles. The individual bolometer from an event with  $\text{multi}_{\text{bolo}} > 1$  are plotted in open triangles.

in both system with a hit first in the muon veto,  $\Delta t_{\text{coinc}}$  should be a negative number, close to zero, see Figure C.1 page 155.

To compare events in different systems, in addition to an overall and unique time, the best is to define the real time of an event in a system as the beginning of the pulse in this system, which real time will be the same for the muon veto, the bolometer heat and ionization. However, during data acquisition, the time of the bolometer event is defined to the time of the maximum of the heat signal  $t_H^{\text{max}}$ . In contrast, in the analysis, the time is or the time of the beginning of the ionization interval  $TH$ , in which is registered the ionization pulse, or the relative time of the maximum of the pulse compared to the center of the interval  $TC$ . The full discussion can be found in Appendix C. The conclusion is that this time interval makes sense. Instead of comparing the real time of the event in both system, we compared the beginning of the ionization interval from the bolometer to the beginning of the pulse in the muon veto, which leads to typically

$$\Delta t_{\text{coinc}} = t_{\text{veto}} - t_{\text{bolo}} \quad (5.9)$$

$$\simeq 20 \text{ ms} \quad (5.10)$$

And then the bolometer signal seems earlier than the muon veto signal.

## 5.5 Summary

The analysis of the coincidence between the muon veto and the bolometer system is summarized in Table 5.6. The sample is clear and understood, the accidental rate is reproducible. The coincidence rate and features at  $E_R < 250$  keV is reproduced by the simulation and it leads to

$$\text{for } E_R < 250 \text{ keV, } \Gamma_{\text{coinc}}^{\text{meas}} = 0.043 \pm 0.015 \text{ events} \cdot (\text{kg} \cdot \text{d})^{-1} \quad (5.11)$$

$$\text{for } E_R \geq 250 \text{ keV, } \Gamma_{\text{coinc}}^{\text{meas}} = 0.09 \pm 0.02 \text{ events} \cdot (\text{kg} \cdot \text{d})^{-1} \quad (5.12)$$

The events at low  $Q$  and low  $E_R$  are different from a background distribution and are identified as muon-induced neutron events. The analysis of the coincidences is successful for Run 8.

However, the definition of the time of the event in the analysis B makes the coincidence events to be artificially centered at  $25 \pm 10$  ms. Furthermore, defining the time of the different sets of bolometers has been difficult, since each data acquisition had its own independent clock. Runs of  $s1$  and  $s3$  have been removed irregardless of the quality of the data, because the reconstruction of their timing was not possible. Runs have also been removed because they were shorter than 24,000 s, because the risk of misassociation with the veto events was greater than the gain of having these very short runs in the analysis. The analysis of the coincidences is successful for Run 8, but it could have been even more efficient, if all runs could have been selected. The lack of one global clock for the entire system was a huge problem during Run 8.

	muon veto	bolometer system
rate	0.173 Hz for all events 4.46 mHz for $multi_{\text{veto}} > 3$	14.6 mHz
life time	98.8 d	285.4 kg·d
condition	more than one veto module with a hit, $multi_{\text{veto}} > 3$	$\Delta t_{\text{bolo}} > 500$ ms
time window of the coincidence	$\Delta t_{\text{coinc}} = 25 \pm 10$ ms $t_{\text{veto}} - t_{\text{bolo}} \in [+15, +35]$	

Table 5.6: *Summary of the results for the muon veto-bolometer coincidence analysis.*



# 6

## Analysis of Run 10

### Contents

- 6.1 Status of the experiment
- 6.2 Muon veto data
- 6.3 Bolometer data
- 6.4 Coincidences between the muon veto and the bolometers
- 6.5 Summary and conclusion

*No observational problem  
will not be solved by more data.*

V. Rubin.

COINCIDENCES between the muon veto system and the bolometers are of great interest to reduce and understand the muon-induced background. The first analysis of coincidences between the muon veto and the bolometer systems during Run 8 was successful, the EDELWEISS-II experiment does identify coincidences as expected. But the analysis was not as complete as it could have been, since there was no overall clock on the experiment. For Run 10, a new device to dispatch a unique time for all sub-systems was installed. The analysis of coincidences during Run 10 is, above all, meant to check if the new timing works properly and allows to see coincidences between the muon veto and the bolometers.

6

### 6.1 Status of the experiment

The following study is based on the analysis of the bolometer Run 10 and the corresponding period for the muon veto. Run 10 lasted from July 25<sup>th</sup> 2008 to November 24<sup>th</sup> 2008. The muon veto system worked completely and properly, all 42 modules were ready for data acquisition. For the bolometer system, 12 standard Germanium bolometers and 2 interdigitised bolometers (of 400 g and 320 g) are considered, set on 3 different acquisition computers, called *s1*, *s2*, *s3*.

For Run 10, a central clock was installed. Every data acquisition of the bolometers, via ethernet, as well as the DAQ of the muon veto system, via a fiber connection, get the time stamp in 10  $\mu$ s-beat from a separate and dedicated electronic card, as shown in Figure 6.1. This electronic card is independent and is not reset with each bolometer DAQ.

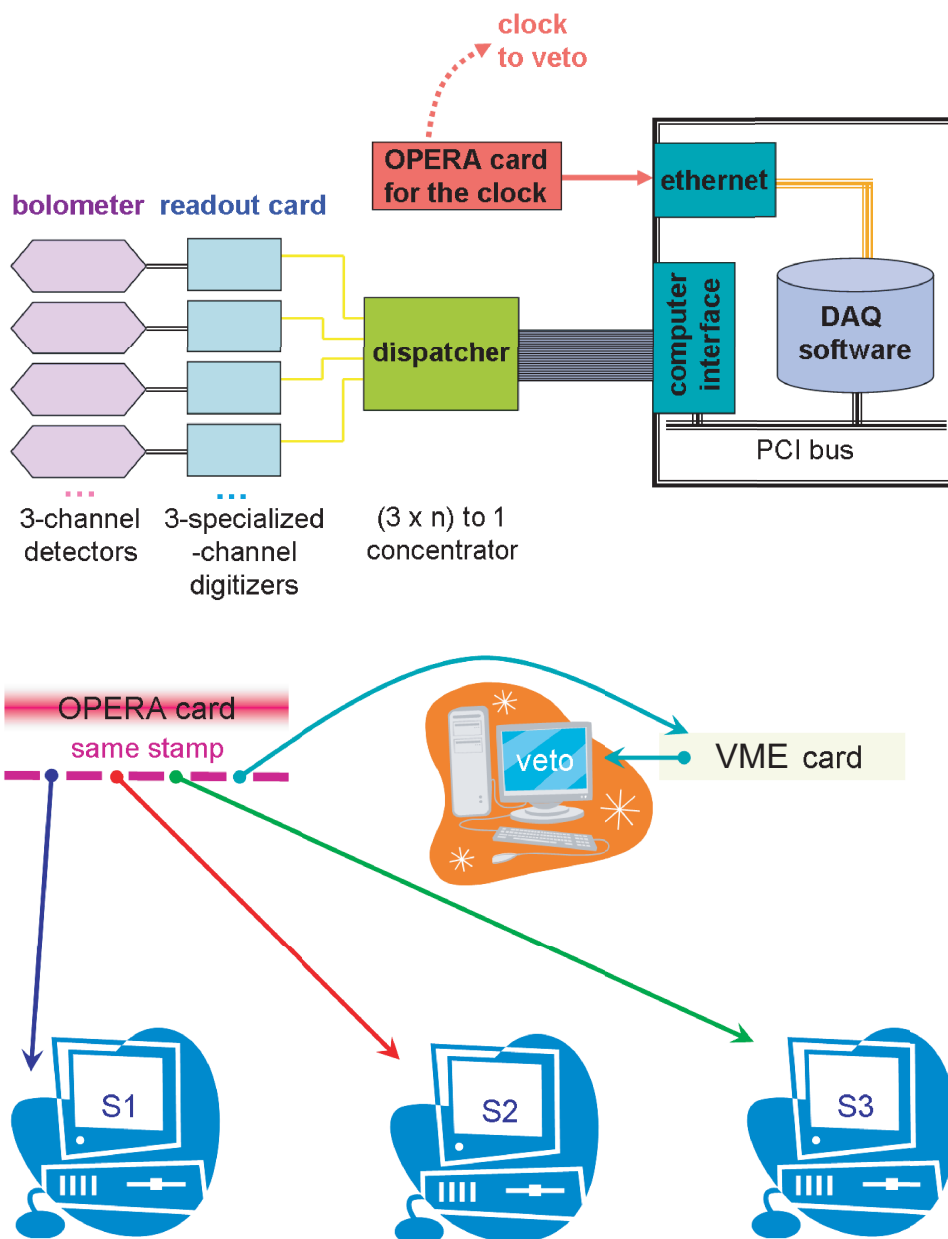


Figure 6.1: *Top: Electronic chain of the bolometers during Run 10. There were 3 similar chains to run the 14 bolometers. Since the number of channels is different depending on the type of bolometer (from 3 for standard Ge bolometer to 7 for ID bolometer), each bolometer is assimilated to an ensemble of 1 or 2 or 3 pseudo-detector(s) with 3 readout channels. Figure adapted from [187]. Bottom: Distribution of the time over the EDELWEISS-II experiment, during Run 10. The so-called OPERA card distributes a unique time for all sub-systems since June 4<sup>th</sup> 2008.*

## 6.2 Muon veto data

Since March 12<sup>th</sup> 2008, the position of the wagons of the upper level of the muon veto is precisely known thanks to laser measurements, which are made every 15 min. If the distance between the two wagons is less than 28.5 cm, the system is considered as fully closed. The condition is large, but actually or the system is widely opened of more than a meter or it is tiny closed of less than 1 cm. Between 25/07/2008 to 24/11/2008, the muon veto system ran as closed for a total of 84.3 days.

In October 2008, the muon-induced neutron counter has been installed in the LSM laboratory, *cf.* Section 3.4.2. The DAQ of the neutron counter is included into the DAQ of the muon veto since then. It is included as a real module for the muon veto module, which lies on top of the neutron counter, and as a pseudo-module which corresponds to the internal 2" PMTs in the paraffin. Additionally to physics data, the neutron counter is regularly fired by a LED system every 8 hours for calibration purpose. It creates so many events in the data file, that it increases the rate for almost a third ( $\sim 0.3$  Hz compared to the expected  $\sim 0.2$  Hz). All events from the neutron counter are not physically linked to the muon veto, and consequently have to be removed from the analysis.

Events are selected following three encased conditions. If the event is at least one internal coincidence in a veto module, it is a clear muon veto event, the event is kept. Else, if it makes an internal coincidence in a neutron counter module (and thus not in the muon veto), it is a pure neutron counter event, the event is disregarded. Else, the events which are not a clear muon veto event or a pure neutron counter event are kept for further analysis. With only the first condition, it would have been as if the condition on the veto events was  $multi_{veto} \geq 3$ , *i.e.* at least one complete module has to be hit, which is already a cut on the veto data. With only the second condition, we would have missed events which occur simultaneously in the neutron counter and the muon veto (passing through muon-candidates outing the veto in the NEMO side, showers ...). The last condition is made in case of a module has one of its ends missing in terms of TDC or ADC. These encased conditions are the most effective way to remove the neutron counter events and to keep the number of possible entries high for further analysis with the bolometers.

The rate of the muon veto, during Run 10, has a mean value of

$$\Gamma_{veto} = 0.161 \text{ Hz} \quad (6.1)$$

$$\Gamma_{veto}^{multi_{veto}>3} = 5.22 \text{ mHz}, \quad (6.2)$$

as shown in black in Figure 6.2. The rate is flatter over time than for Run 8, since the accuracy on the veto position is better and thus the “closed veto” condition more accurate. The veto wagons are also more carefully closed. With the mechanization of the source inside the shielding for calibration or regeneration purposes, the upper level is less often opened. The upper level is then completely closed for long periods, which increases the veto efficiency.

One can see the rate is slightly decreasing over time. Events, which have a very high energy, are stored in an overflow bit in the ADC data. If we remove the events from the overflow, the rate is flatter, as shown in grey in Figure 6.2. Very high energy events are from very high energy muons or from sparks on the edge of the PMTs. The more the system is stable, the less sparks are likely to happen. As the system ran on long continuous periods in stable conditions, the rate is slightly decreasing

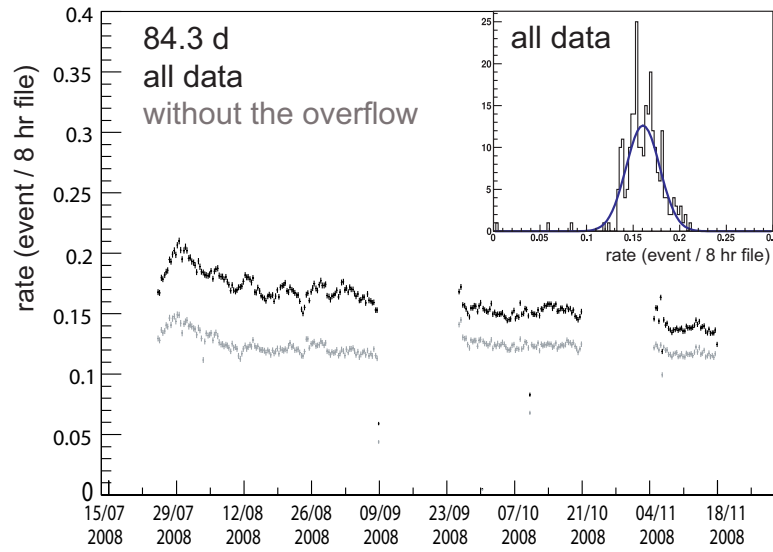


Figure 6.2: Rate of the muon veto per 8-hour file when the veto is closed, see text for details. The rate is shown over time (left) and as a histogram (right) with a Gaussian fit. The points with a much smaller rate are from files less than 8-hours long. In lighter shade is the rate without the very high energy events. The mean of the Gaussian fit is 0.161 Hz (calculated rate from data is also 0.161 Hz).

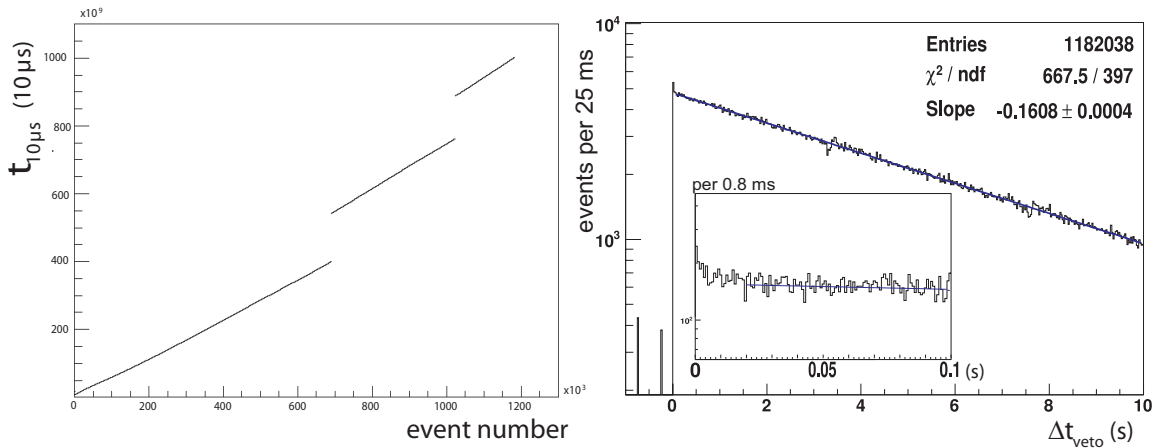


Figure 6.3: Left: Timeline of the veto events during Run 10, with the condition of having a time difference of consecutive events lower than 600 s. The timeline is broken twice when the muon veto DAQ was stopped, due to the installation of the neutron counter, see also Figure 6.2. Right: Time difference of consecutive muon veto events in log scale up to 10 s and zoomed over the first four 25 ms. At  $-0.25$  s are plotted  $\Delta t_{veto} > 600$  s, at  $-0.75$  s are plotted  $\Delta t_{veto} < 0$  s.

and stable when removing the sparks. The gaps during the data acquisition on Sept. 09–25, Oct. 21 to Nov. 4 and Nov. 18–24 are the periods of installation and tests of the neutron counter. The rate is greater after the restart of the system, as the PMTs need some time to stabilize.

In contrast to Run 8, the timing from the universal 10  $\mu\text{s}$ -beat clock is now continuous as shown in Figure 6.3. However, there are  $\sim 10^{-3}$  jumps in the timing due to misreading of the time stamp bits by the time card of the veto system. To avoid these misread time patterns in the analysis of coincidences, events which have a time gap to the preceding one of  $\Delta t_{\text{veto}} > 600$  s are disregarded. Figure 6.3 right shows the time difference of consecutive veto events up to 10 s. Excluding the first 25 ms, which contain only  $\sim 1000$  events out of  $\sim 1.18 \cdot 10^6$ , the distribution follows an exponential, which can be fit giving a  $\chi^2/\text{ndf} = 647.5/397$ . The slope of the exponential fit is 0.161 Hz, which is the rate previously mentioned.

## 6.3 Bolometer data

The bolometers in use during Run 10 are shown on Figure 3.6 in Section 3.1.6, and are summarized in Table 6.1.

The bolometers for the analysis of the coincidences with the muon veto are 12 standard Germanium bolometers from *s1*, *s2* and 2 interdigitised bolometers ID401 (400 g) and ID3 (320 g)\* from *s3*. Figure 6.4 is a 3-D representation of the position of the selected bolometers during Run 10.

For the analysis performed in this work, there was no calibrated data available yet for Run 10, as there is for Run 8. The following analysis is based on the “ntp” files, which are the online pre-processed data, usually used for the monitoring, *cf.* Section 3.1.8. The analysis of the bolometers with the ntp is not meant to be a full standard reference analysis, but it allows to have a first look into the bolometer data and to further look for coincidences with the muon veto.

There is one ntp file per run. An ntp file has one event per line and contains variables such as the event number, the name of the corresponding data files for this event, the real time  $t_{\text{PC}}$  from the computer clock in seconds, the time stamp  $t_{10\mu\text{s}}$  in 10  $\mu\text{s}$ -beat, the identity of the bolometer which triggered, the multiplicity of the event  $m_{\text{bolo}}$ , the time difference of the event with the previous one  $\Delta t_{\text{bolo}}$ , the amplitude, the baseline, and the noise of the heat channel and of the ionization channels from the center and the guard electrodes per standard bolometer in arbitrary units. In case of interdigitised bolometers, there are the amplitude, baseline and noise for the heat channel. But the same variables for the ionization channels are triple to store the information of each side (two faces plus guard). The collecting electrodes are stored in the variables labeled center and the veto electrodes in the ones labeled guard. The baseline is the value without event. The noise is the value of the *rms* of the pre-trigger. The amplitude per channel and per bolometer is already filtered, and corresponds to the energy per channel. The time stamp  $t_{10\mu\text{s}}$  registered in 10  $\mu\text{s}$ -beat is the time of the heat channel, when the maximum amplitude is reached. The ntp files are reorganized in one single C++/ROOT file per DAQ computer with only

---

\* ID401 and ID3 have a different mass, because they are manufactured differently. Their geometry is also different. What has already been said in Section 3.1.4 is true for ID401, however, for ID3 the electrode readout channels are reversed, the collecting electrodes are the veto channels and *vice-versa*.

DAQ	bolometer	status	remarks	
s1	GSA9	out	bad heat channel + $\alpha$ -contamination  no heat channel  large noise on center channel  no guard channel  small detectors (50 g)	
s1	GGA14	✓		
s1	GGA13	out		
s1	GGA10	✓		
s1	GGA7	✓		
s1	GSA10	✓		
s1	GGA6	out		
s1	GGA3	✓		
s1	GGA12	out		
s1	GSA8	✓		
s1	pgsa2, pgsa3	out		
s2	GSA6	✓		no ionization channel switched OFF
s2	GGA5	✓		
s2	GGA11	✓		
s2	GSA4	✓		
s2	GGA4	✓		
s2	GGA9	✓		
s2	ID2	out		
s2	GGA1	out		
s3	ID401	✓	unstable + $\alpha$ -contamination  small detector (50 g)	
s3	ID201	out		
s3	ID3	✓		
s3	Ge73	out		
s4	NbSi409	out	NbSi detectors	
s4	NbSi407	out		
s4	NbSi410	out		
s4	NbSi408	out		
s4	NbSi402	out		
other	GSA11	out	as test for a new readout electronic	
other	GGA8	out		
other	GSA3	out		
other	GSA7	out	switched OFF	
other	GSA5	out	too noisy	
other	GSA1	out	too noisy	
other	Gc1, Gc2, Gc3	out	pure heat channel detectors	
other	IAS	out	sapphire detector	

Table 6.1: *Bolometer status during Run 10.*



Figure 6.4: 3-D visualization of the selected bolometers for the muon veto-bolometer coincidence analysis during Run 10.

the selected bolometers.

The bolometers have been calibrated, as explained in Appendix B.1, with  $^{133}\text{Ba}$  runs: *ik24a019*, *ik24b011*, *ik24c005*, which correspond to runs of November 24<sup>th</sup> 2008.

To select the physics runs of Run 10, a very simple trick has been used. During physics runs, the individual threshold on the heat channel of the bolometers is adapted to keep a stable and constant rate. The information about the so-called adaptative threshold per bolometer are stored in a special file, called “seuils”, which means thresholds in French. If this seuils file exist, it is assumed that the run is a low background run and not a calibration or a regeneration run. Figures of the behavior of the threshold per bolometer during Run 10 and a table of the individual mean threshold can be found in Appendix B.2.

Once calibrated and their threshold known, bolometer events can be defined per set of bolometers, *i.e.* per data acquisition, with a heat and ionization energy as the sum of the ones from bolometer, which pass their threshold. In Figure 6.5 is shown the heat channel *vs.* the sum of the ionization channels from guard and center from *s1*, *s2* and *s3*. In red is shown the events which survive the adaptative threshold. This threshold is very low from 1.1 to 9.8 keV. Events at low heat and more prominently at low ionization are not cut out by the adaptative thresholds. The rate of the events, which survive the adaptative threshold, is per data set *s1*, *s2*, *s3*:

$$\Gamma_{s1}^{\text{thresh}} = 0.072 \text{ Hz} \quad (6.3)$$

$$\Gamma_{s2}^{\text{thresh}} = 0.146 \text{ Hz} \quad (6.4)$$

$$\Gamma_{s3}^{\text{thresh}} = 0.122 \text{ Hz} \quad (6.5)$$

which is up to a factor 10 higher than  $\Gamma_{\text{bolo, Run 8}} = 0.0146 \text{ Hz}$  for the whole bolometer system during Run 8.

Such a high event rate indicates a sample containing also misconstructured events, or events from particularly noisy periods, or potentially mislabeled runs (a regeneration run with a seuils file). One can also notice the events should be aligned diagonally ( $E_H \simeq E_I$ ) Due to the preliminary calibration, this is not completely assured. The purpose of the bolometer analysis in the context of this work is to look for

coincidences with the muon veto. With such a high bolometer event rate, any search for correlated coincidences would be dominated by accidental muon veto-bolometer coincidences.

To be able to look for real coincidences, a further cut has been chosen leaving events shown in green in Figure 6.5. It is a 30 keV threshold on the ionization channel and a 30 keV threshold on the heat channel for each individual bolometer. The event rate then becomes

$$\Gamma_{s1}^{30/30} = 5.46 \text{ mHz} \quad (6.6)$$

$$\Gamma_{s2}^{30/30} = 4.34 \text{ mHz} \quad (6.7)$$

$$\Gamma_{s3}^{30/30} = 1.84 \text{ mHz} \quad (6.8)$$

*i.e.* slightly smaller than  $\Gamma_{\text{bolo, Run 8}}$ . The advantage is that the 30/30 keV condition removes all low ionization and low heat events, without applying a complex bolometer period analysis as the one which has been performed in [161] for the analysis of Run 8. The disadvantage is that it will also cut any low  $Q$ , low  $E_R$  muon-induced neutron-like events, as the 4 found in Run 8. However, once a complete analysis and calibration of Run 10 is available [189], a full coincidence search can be easily performed based on this work.

The bolometer system event sample is defined by looking for coincidences between the three data sets  $s1$ ,  $s2$ ,  $s3$ . In Figure 6.6 is shown the time difference of coincidences between  $s1-s2$  and  $s1-s3$ . The Gaussian fit is expected to be centered on zero, since the three sets share the same global clock. However, there is a systematic shift between the different computers. These shifts are under further investigation and seem at first to be linked to the synchronization with the time card at the start of a run [190].

The time stamps of one of the computers have been chosen as time reference. In Figure 6.7 is shown the heat energy in keV for bolometer events from  $s1, s2$  or  $s3$  *vs.*  $t_{\text{veto}} - t_{\text{bolo}}$  in an interval of  $\pm 100$  ms, with the only condition of high energy events  $E_H > 6.5$  MeV. The time window of the muon veto events in coincidence with high energy events of  $s1$  is closer to zero than for the others. The  $10\mu\text{s}$ -stamp from  $s1$  is chosen as the reference timing. The time stamp from  $s2$  is corrected by the mean of the Gaussian fit of the  $t_{s1} - t_{s2}$  distribution,  $\langle t_{s1} - t_{s2} \rangle = -13.47$  ms and same for  $s3$  with the  $\langle t_{s1} - t_{s3} \rangle = -11.03$  ms.

To further analyze the data, a new C++/ROOT file has been defined with one event per line, even if it is a coincidence of two/three sets of bolometers. The events are organized per increasing time stamp  $t_{10\mu\text{s}}$ . All the variables of the preceding files are stored in this file, plus a global event number, the correction applied on the time stamp for  $s2$ ,  $s3$  and a specific variable for the coincidences. This variable called *WhicMac* is  $i$  if the event is from  $si$ ,  $ij$  if the event is a coincidence of from  $si$  and  $sj$ , and  $ijk$  if all computers are in coincidence, with  $i, j, k = 1, 2$  or  $3$ .

The bolometer system life time is the one of  $s1$ ,  $s2$ ,  $s3$ , all weighted by the mass of their bolometers. With 14 Ge bolometers of 320 g and 1 ID of 320g and 1 ID of 400 g, the exposure of the bolometer system under investigation here amounts to  $t_{\text{bolo}} \simeq 294.7$  kg·day.

In Figure 6.8 is shown the time difference of consecutive bolometer events. As for Run 8, for the muon veto-bolometer analysis, a further cut of  $\Delta t_{\text{bolo}} > 500$  ms, which corresponds to twice the bolometer dead time of 250 ms, is applied to make sure the bolometer events are uncorrelated. This condition only removes 526 bolometer

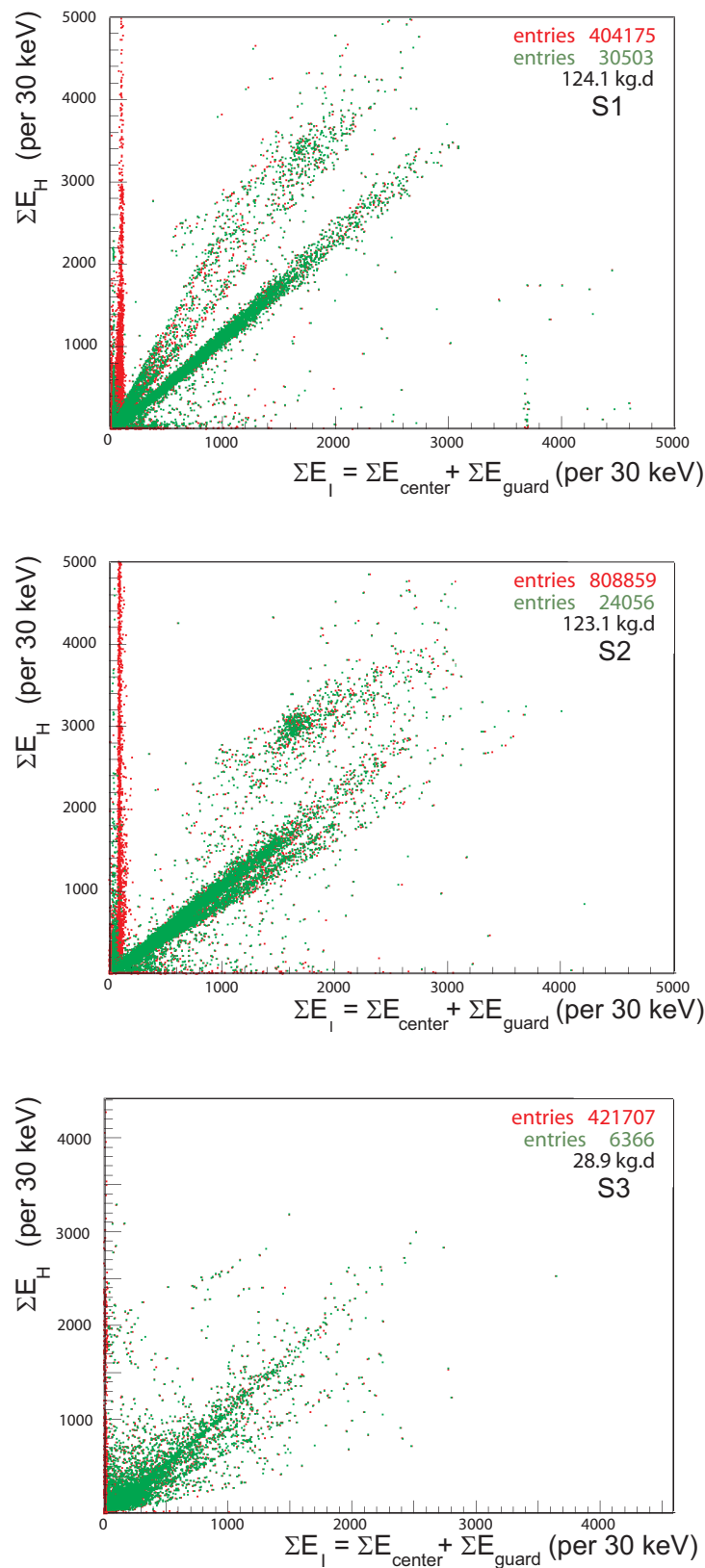


Figure 6.5: Biplot of the heat channel versus the sum of the ionization channels from guard and center from s1, s2 and s3 for energies below 5 MeV. Events in red survive the adaptive threshold, events in green have  $E_H > 30$  keV and  $E_I > 30$  keV.

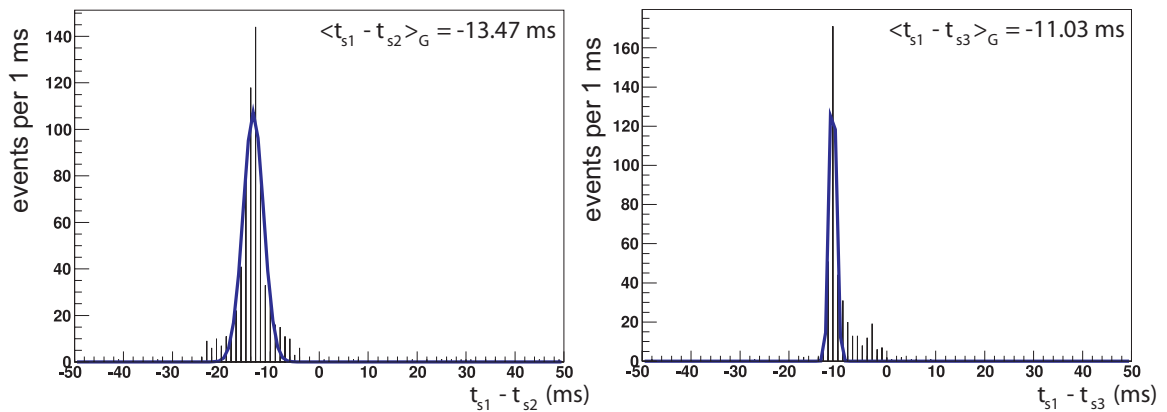


Figure 6.6: Time difference of coincidences between  $s_1$ - $s_2$  and  $s_1$ - $s_3$ . The distribution is discrete, because the time in heat trigger is rounded to 1 ms due to the slow risetime of the heat signal.

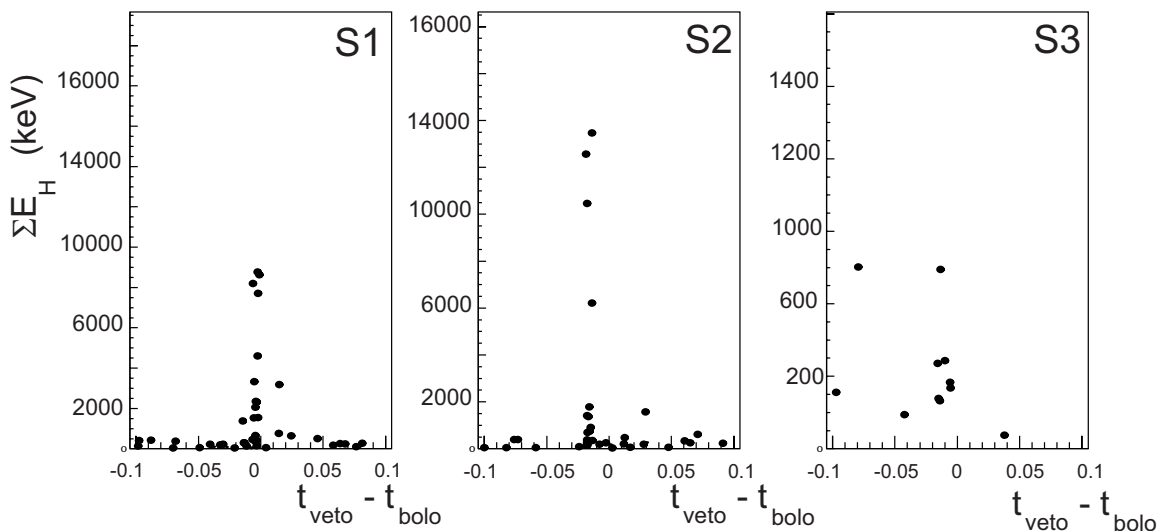


Figure 6.7: Muon veto-bolometer events in coincidence per data set  $s_1$ ,  $s_2$ ,  $s_3$ . Top: Heat energy in keV for bolometer events versus  $t_{veto} - t_{bolo}$  in a  $\pm 100$  ms interval. The heat energy is the sum of the heat energy of the bolometers which have triggered. The high energy coincidence at  $E_H > 6.5$  MeV helps to define a coincidence interval. There is no further condition applied on muon veto events.

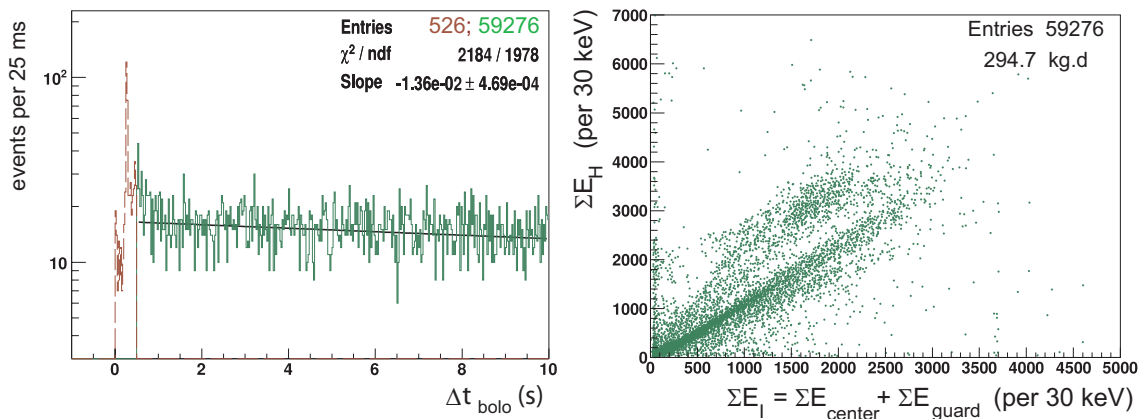


Figure 6.8: *Quality of the bolometer system events. Left: Time difference of consecutive bolometer events. Right: Recoil energy versus ionization energy.*

events and makes the sample clean of any kind of after-pulses, leading to a nice exponential distribution with a fit value  $\chi^2/\text{ndf} \simeq 2184/1978$ . The slope of the exponential fit is 13.6 mHz, which is not exactly the final rate for the bolometer system. There are more event at low  $\Delta t_{\text{bolo}}$  than in the mean, the cut could have been chosen to a higher value. Figure 6.8 right shows the distribution of events in the recoil channel versus the ionization channel. There are 59276 events (with 1093 coincidences of two bolometer DAQ, 5 coincidences of three bolometer DAQ) in the final selection on 294.7 kg·d, or a rate of

$$\Gamma_{\text{bolo}} = 10.7 \text{ mHz}. \quad (6.9)$$

The events are not set on a straight line in Figure 6.8 on right, because of the rough selection and calibration. The 30 keV cut in heat and in ionization removes part of the noise at low energies, but despite of the lower rate than Run 8, it is clearly not the best quality events which are left. Nevertheless, it is sufficient enough to look for coincidences with the muon veto.

## 6.4 Coincidences between the muon veto and the bolometers

The muon veto and the bolometer samples are defined from the preceding Sections. In comparison to Run 8, the search of muon veto-bolometer coincidences

The time stamp from both systems is step-by-step compared. If  $|t_{\text{veto}} - t_{\text{bolo}}| < 1 \text{ s}$ , the event is considered as a potential coincidence for further analysis. The result is shown on left in Figure 6.9, where is shown the heat energy in keV for bolometer system events versus  $t_{\text{veto}} - t_{\text{bolo}}$ . As for Run 8, there is a clear sample of high energy bolometer events correlated with the muon veto events.

### 6.4.1 Definition of coincidence region and rates

The coincidence events with no further condition suffer from double counting (one bolometer event links to more than one muon veto event or *vice-versa*), 1.6 % of

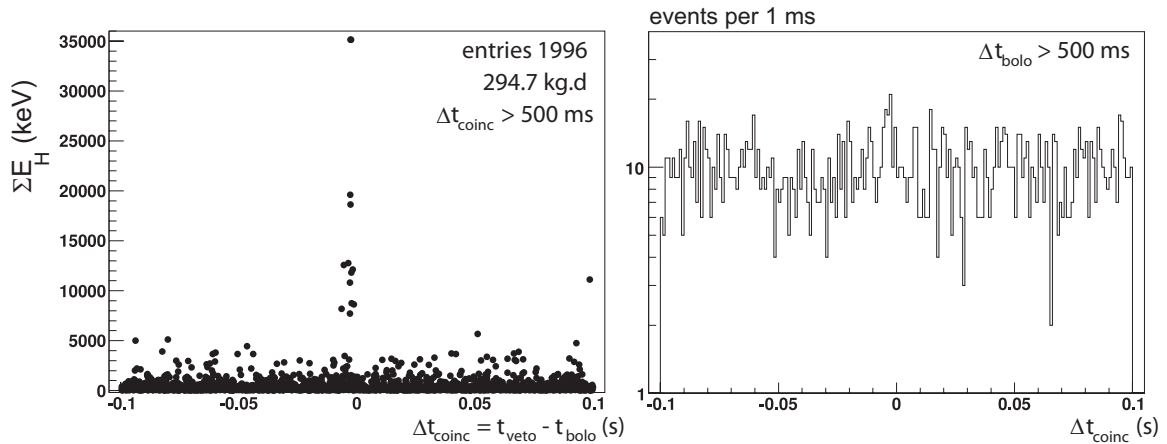


Figure 6.9: *Muon veto-bolometer events in coincidence. Left: Heat energy in keV for bolometer system events vs.  $t_{\text{veto}} - t_{\text{bolo}}$  in a  $\pm 100$  ms interval. The heat energy is the sum of the heat energy of the bolometers which have triggered. Right:  $\Delta t = t_{\text{veto}} - t_{\text{bolo}}$  of the muon veto-bolometer events in coincidence, in a  $\pm 100$  ms interval. The plot is zoomed on  $\pm 100$  ms, instead of the full  $\pm 1$  s technical window, to focus on the peak region. There is no further condition applied on muon veto events.*

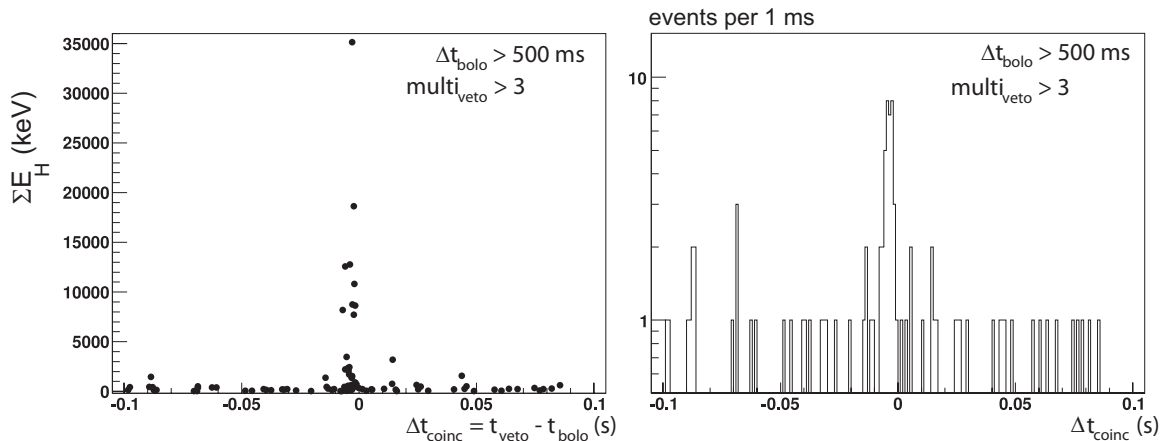


Figure 6.10: *Muon veto-bolometer events in coincidence with  $\text{multi}_{\text{veto}} > 3$ . Left: Heat energy in keV for bolometer system events versus  $t_{\text{veto}} - t_{\text{bolo}}$ . The heat energy is the sum of the heat energy of the bolometers which have triggered. Right:  $\Delta t = t_{\text{veto}} - t_{\text{bolo}}$  of the muon veto-bolometer events in coincidence. The condition on the muon veto is to have more than one veto module by applying  $\text{multi}_{\text{veto}} > 3$ .*

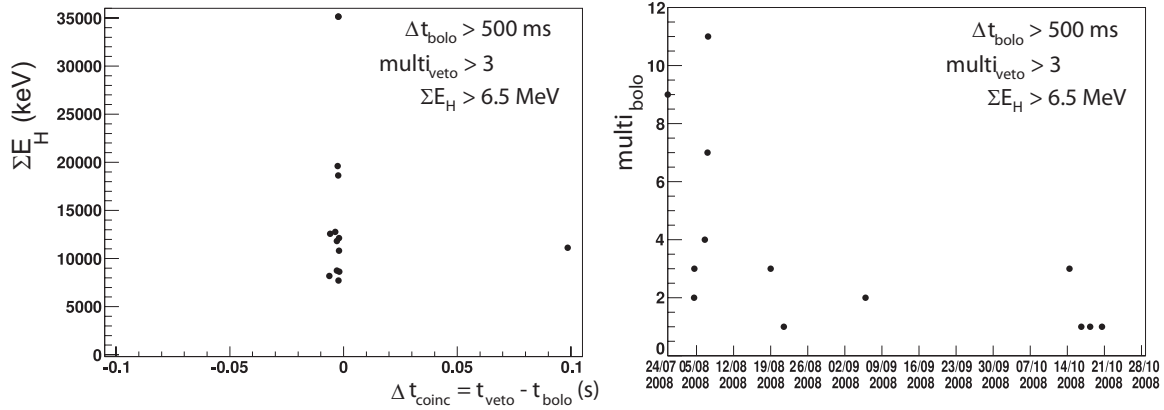


Figure 6.11: Coincidences at high heat energy  $E_H > 6.5$  MeV and with  $multi_{veto} > 3$  to define the coincidence interval. The heat is the sum of the heat of the bolometers which have triggered. Left: Heat energy in keV for bolometer system events versus  $t_{veto} - t_{bolo}$ . Right: Distribution of the same events in bolometer multiplicity over measuring time.

time windows (ms) for the coincidences	low energy excess $E_R < 250$ keV	high energy excess $E_R \geq 250$ keV	total number of excess events
$\Delta t = -5 \pm 5$	4.4	28.6	32.9
<b><math>\Delta t = -5 \pm 10</math></b>	<b>6.7</b>	<b>30.2</b>	<b>36.9</b>
$\Delta t = -5 \pm 15$	7.1	28.8	35.9
$\Delta t = -5 \pm 20$	6.4	30.4	36.9
$\Delta t = 0 \pm 5$	3.3	22.6	25.9
$\Delta t = 0 \pm 10$	6.7	27.2	33.9
$\Delta t = 0 \pm 15$	7.1	31.8	38.9
$\Delta t = -10 \pm 5$	3.3	7.5	10.8
$\Delta t = -10 \pm 10$	4.7	30.2	34.9

Table 6.2: Evaluation of the coincidence interval.

the coincidences are double counted in a  $\pm 100$  ms interval. In Figure 6.9 on right is shown only the  $\Delta t = t_{veto} - t_{bolo}$  on a  $\pm 100$  ms interval. Since, as for Run 8, the coincidence events are background dominated, the condition of having more than one muon veto module with a hit ( $multi_{veto} > 3$ ) is added. The result is shown in Figure 6.10. It allows to reduce the number of accidentals and the number of double counting and to concentrate on candidates induced by going through muons. The two double counted events left are carefully studied to decide to which event they are most likely to be linked.

The time interval for the coincidences is defined by the position of the peak at high heat energy events  $E_H > 6.5$  MeV and with  $multi_{veto} > 3$ , as shown on left in Figure 6.11. The time interval of coincidences is set to  $\Delta t_{coinc} = -5 \pm 5$  ms. As one can see in Figure 6.11 on right, the events at high energy are not clustered in real time. They are no artefact due to specific condition, they are spread all along the 4 months of investigation.

events in	$[-1000, -15] \vee [+5, +1000]$ ms	$[-15, +5]$ ms
expectation	$618 \pm 3$	$6.2 \pm 0.1$
measurement	$595 \pm 25$	$6.1 \pm 0.2$

Table 6.3: *Measured and extrapolated rate of accidental coincidences.*

$t_{\text{veto}} - t_{\text{bolo}} \in [-15, +5]$ ms	low energy events $E_R < 250$ keV	high energy events $E_R \geq 250$ keV
measured events	10	33
expected accidentals	$3.3 \pm 0.2$	$2.8 \pm 0.2$
excess coincidences	$6.7 \pm 0.4$	$30.2 \pm 5.5$
signal / background	2.4	9.1

Table 6.4: *Events at  $E_R < 250$  keV and  $E_R \geq 250$  keV in the coincidence region.*

The time interval defined at high energy is very sharp. The small number of events may mislead to a too small windows. Different positions of the excess and different windows are tested in Table 6.2. Note that the exact mean position of the time interval defined at high energy is 3.30 ms. The number of low energy events ( $E_R < 250$  keV) is the same for  $\Delta t = 0 \pm 10$  ms and  $\Delta t = -5 \pm 10$  ms and for  $\Delta t = -5$  ms, the maximum of excess events at high energy ( $E_R \geq 250$  keV) is reached for a window length of 10 ms and is the same as  $\Delta t = -10 \pm 10$  ms. The time window is selected to be  $\Delta t = -5 \pm 10$  ms rather than  $\Delta t = -5 \pm 5$ . The time window of coincidences for Run 10 is set to

$$\Delta t_{\text{coinc}} = -5 \pm 10 \text{ ms} \quad (6.10)$$

$$t_{\text{veto}} - t_{\text{bolo}} \in [-15, +5] \text{ ms.} \quad (6.11)$$

The events in Table 6.2 are excess coincidence candidates after subtraction of the accidental background. The expected number of accidental events  $N_{\text{acc}}$  is calculated from the bolometer and muon veto rates as in Equation 5.5, with  $\Gamma_{\text{veto}}^{\text{multiveto} > 3} = 5.22$  mHz,  $\Gamma_{\text{bolo}} = 10.7$  mHz,  $t = 294.7/4.56$  d. On a time window of  $\Delta t_{\text{win}} = 2$  s (*ie.*  $\pm 1$  s),  $N_{\text{acc}}^{\text{exp}} \simeq 624 \pm 3$ . The comparison with the experiment is in Table 6.3.

The calculated rates of accidental events is reproduced by the measurement, they agree within the statistical uncertainties.

Inside the coincidence time interval, it is interesting to differentiate between the high recoil energy events  $E_R \geq 250$  keV, which are probably fast neutrons or even passing through muons, and low energy recoil events  $E_R < 250$  keV, which are more interesting muon-induced phenomena as in the energy region of interest for the WIMPs. The real number of coincidence candidates has to be extracted subtracting the accidentals for this region. The results of this calculation is shown in Table 6.4. The signal over background confirms the clear excess of events inside the time window of the expected coincidences. The excess coincidences are the muon-induced candidates and can be compared with the simulated rate from [184].

The simulated rate is extracted from the the simulated energy deposit spectrum in Ge bolometers in Figure 5.12, as explained previously in Chapter 5. It gives  $\Gamma_{\text{coinc}}^{\text{simu}} \sim 0.03 \pm 0.01$  events $\cdot$ (kg $\cdot$ d) $^{-1}$  for  $1 < E_R < 250$  keV. However, since the data

in Run 10 are cut at 30 keV in heat and ionization, it is not relevant to compare with the simulation, which is made on the full range of energy deposit below 250 keV. From the measurement, we would have still

$$\text{for } 30 < E_H < 250 \text{ keV, and } E_I > 30 \text{ keV} \quad (6.12)$$

$$\Gamma_{\text{coinc}}^{\text{Run10}} = 0.023 \pm 0.01 \text{ events} \cdot (\text{kg} \cdot \text{d})^{-1} \quad (6.13)$$

$$\text{for } E_H \geq 250 \text{ keV, and } E_I > 30 \text{ keV} \quad (6.14)$$

$$\Gamma_{\text{coinc}}^{\text{Run10}} = 0.10 \pm 0.02 \text{ events} \cdot (\text{kg} \cdot \text{d})^{-1} \quad (6.15)$$

The rate at  $E_H \geq 250$  agrees within the statistical uncertainties with the rate of  $E_R \geq 250$  for Run 8. Since events at high energy are not affected by the 30/30 keV cut, the fact that the rates agree shows that muon-induced background measurements are reproducible. Therefore, the EDELWEISS-II experiment is able to measure and detect muon-induced background.

### 6.4.2 Identification of the coincidence events

Visualization in a Q-plot is helpful to determine the kind of events, which make a coincidence. The resolution lines for the Q-plot are defined in Section 3.1.5, with input variables as listed in Appendix B.3.

The results for the 10 events at  $E_R < 250$  keV and  $\Delta t_{\text{coinc}} = -5 \pm 10$  ms is shown in Figure 6.12. There is no event in the nuclear recoil band. All events are enclosed in the  $\gamma$ -region band and are likely to be  $\gamma$ -particles. The 30 keV condition on the heat and the ionization channels has cut out any chance of low energy muon-induced neutrons.

All events shown in this Q-plot have a bolometer multiplicity of one. There is one extra event with  $E_R < 250$  keV, with a  $multi_{\text{bolo}} = 2$ . This event is in the gamma-band, and thus anonymously plotted together with the higher energy events  $E_R \geq 250$  keV, as shown in Figure 6.13. There are 16 events at high energy with  $multi_{\text{bolo}} = 1$ , and 17 events with  $multi_{\text{bolo}} > 1$ . And eventually one event falls in the nuclear recoil band. The list of principal characteristics of these events at low and high energy can be found in Appendix B.4.

## 6.5 Summary and conclusion

The analysis of the coincidence between the muon veto and the bolometer system is summarized in Table 6.5. The accidental rate is reproducible, despite the rough analysis of the bolometers with the ntp files. The limitation of the bolometer analysis with the ntp files does not allow to find muon-induced neutron like events, but the position of the peak has a physics sense and is well define close to zero. Typically the heat signal has a risetime of  $\sim 10$  ms, whereas the muon veto of few ns. Since we compare the time of the event in the muon veto and the time in the ntp, which is the maximum of the heat channel, the result is to have an interval centered on the mean risetime of the heat pulse, *cf.* Appendix C for a detailed discussion.

	muon veto	bolometer system
rate	0.161 Hz for all events 5.22 mHz for $multi_{\text{veto}} > 3$	10.7 mHz
life time	84.3 d	294.7 kg·d
condition	$\Delta t_{\text{veto}} < 600$ s more than one veto module with a hit, $multi_{\text{veto}} > 3$	$\Delta t_{\text{bolo}} > 500$ ms 30 keV ionization cut 30 keV heat cut
time interval of coincidences	$\Delta t_{\text{coinc}} = -5 \pm 10$ ms $t_{\text{veto}} - t_{\text{bolo}} \in [-15, 5]$ ms	

Table 6.5: *Summary of the results for the muon veto-bolometer coincidence analysis.*

The coincident rates are

$$\text{for } 30 < E_H < 250 \text{ keV, and } E_I > 30 \text{ keV} \quad (6.16)$$

$$\Gamma_{\text{coinc}}^{\text{Run10}} = 0.023 \pm 0.01 \text{ events} \cdot (\text{kg} \cdot \text{d})^{-1} \quad (6.17)$$

$$\text{for } E_H \geq 250 \text{ keV, and } E_I > 30 \text{ keV} \quad (6.18)$$

$$\Gamma_{\text{coinc}}^{\text{Run10}} = 0.10 \pm 0.02 \text{ events} \cdot (\text{kg} \cdot \text{d})^{-1} \quad (6.19)$$

We can not compare the coincidence rate with the simulation because of the heat and ionization 30 keV cut, however, the rate at  $E_H \geq 250$  agrees within the statistical uncertainties with the rate of  $E_R \geq 250$  for Run 8, which shows the muon-induced background measurements are reproducible.

It is a bit early to proclaim the analysis of the coincidences is successful for Run 10, further analysis at low  $E_H$  are awaited, but the feasibility of such an analysis is proved successful with the new overall distribution of the timing.

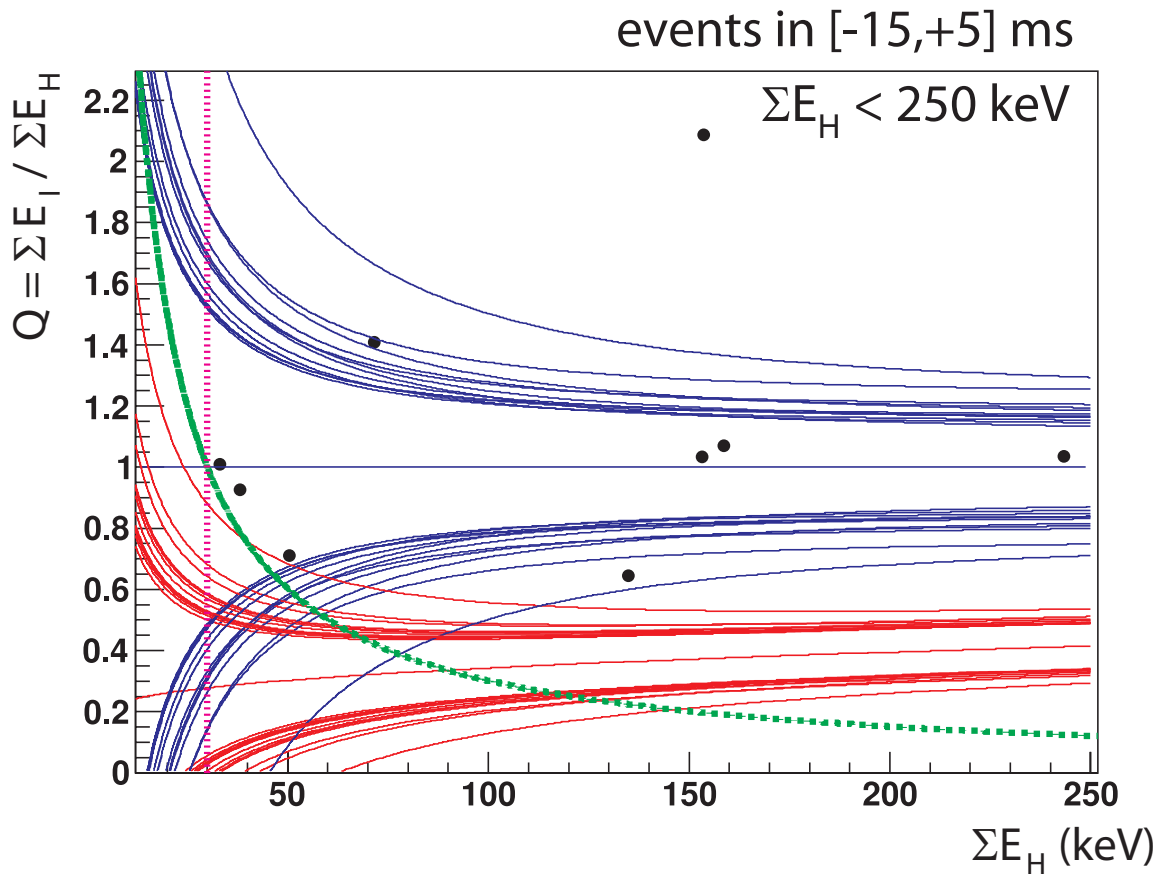


Figure 6.12:  $Q$ -plot of events in coincidence with  $E_H < 250$  keV inside the coincidence time interval  $\Delta t_{coinc} \in [-15,+5]$  ms. All events have a  $multi_{bolo} = 1$ . The green hyperbole is the threshold  $E_I > 30$  keV, the pink line is  $E_H > 30$  keV.

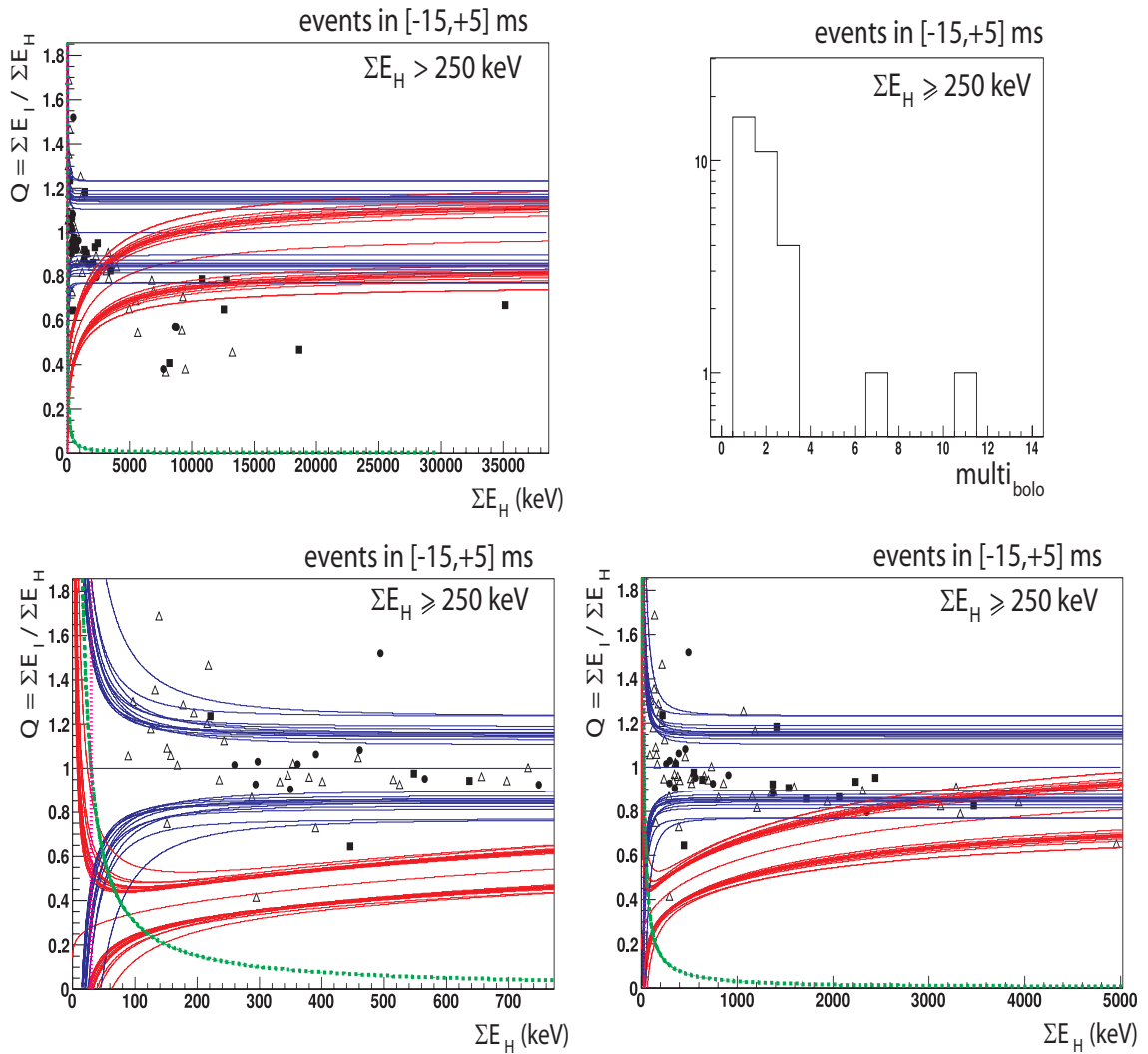


Figure 6.13:  $Q$ -plots of events in coincidence with  $E_H \geq 250$  keV inside the coincidence time interval  $\Delta t_{\text{coinc}} \in [-15, +5]$  ms on the full energy scale (top left), for  $E_H < 750$  keV (bottom left) and for  $E_H < 5$  MeV. The green hyperbole is the threshold  $E_I > 30$  keV, the pink line is  $E_H > 30$  keV. The bolometer multiplicity of the coincidence is shown in the top right figure. In the  $Q$ -plot this information is translated as: Coincidence with  $\text{multi}_{\text{bolo}} = 1$  are plotted as full circles, with  $\text{multi}_{\text{bolo}} > 1$  are full rectangles. The individual bolometer from an event with  $\text{multi}_{\text{bolo}} > 1$  are plotted in open triangles.

# Conclusion

THE SENSITIVITY of a WIMP experiment is set by its rate of background events which are indistinguishable from WIMP candidates. Neutrons induced either directly by cosmic ray muons or indirectly by electromagnetic processes in the shower of a muon have to be considered as a limiting background source. The active muon shield, so called muon veto, of the EDELWEISS-II experiment is made to reject muon-induced background, by associating cosmic ray muons in the vicinity of the experiment with neutron recoil events in the bolometers.

The EDELWEISS-II muon veto has already run for three years and is continuously taking data. Despite some discrepancies with the simulation, the analysis of the events yields a good detection and identification of muon candidates and their showers.

Coincidences between the muon veto system and the bolometers are of great interest to reduce and understand the muon-induced background. The first analysis of coincidences between the muon veto and the bolometer systems during Run 8 is successful. Although the definition of the time of the event in the analysis B makes the coincidence events to be artificially centered at  $25 \pm 10$  ms, the EDELWEISS-II experiment does identify coincidences between bolometer events and muon candidates of the veto as a clear excess compared to the expected accidental rate. The coincidence rates are

$$\text{for } E_R < 250 \text{ keV, } \Gamma_{\text{coinc}}^{\text{Run8}} = 0.043 \pm 0.015 \text{ events} \cdot (\text{kg} \cdot \text{d})^{-1} \quad (6.20)$$

$$\text{for } E_R \geq 250 \text{ keV, } \Gamma_{\text{coinc}}^{\text{Run8}} = 0.09 \pm 0.02 \text{ events} \cdot (\text{kg} \cdot \text{d})^{-1} \quad (6.21)$$

which can be compared and are in agreement with the simulated rate at low energy.

However, the analysis was not as complete as it could have been, since there was no overall clock on the experiment. Since each data acquisition had its own independent clock, defining the time of the different sets of bolometers has been difficult, and periods have been removed regardless of the quality of the data. The lack of one global clock for the entire system was a huge problem during Run 8.

For Run 10, a new device to dispatch a unique time for all sub-systems was installed. However, in contrast to Run 8, there was no calibrated data available yet for Run 10. The second analysis is based on the “ntp” files, which are the online pre-processed data, usually used for the monitoring. Using the ntp files, the rate of bolometer was 10 times higher and the coincidences with muon veto, if any, completely overwhelmed in background. To perform the analysis, a drastic cut has been applied: only events with  $E_H > 30$  keV and  $E_I > 30$  keV are kept. The advantage of the cut is that it removes all low ionization and low heat events, without applying a complex bolometer period analysis as the one which has been performed for the analysis of Run 8. The disadvantage is that it will also cut any low  $Q$ , low  $E_R$  muon-induced neutron-like events, as the ones found in Run 8.

The analysis of the bolometers with the ntp is not meant to be a full standard reference analysis, but it allows to have a first look into the bolometer data and to further look for coincidences with the muon veto. And the analysis of coincidences

is also successful for Run 10. Even if there is no event in the nuclear recoil band, there is a clear excess of events compared to the accidental rate. The coincidence rates are

$$\text{for } 30 < E_H < 250 \text{ keV, and } E_I > 30 \text{ keV} \quad (6.22)$$

$$\Gamma_{\text{coinc}}^{\text{Run10}} = 0.023 \pm 0.01 \text{ events} \cdot (\text{kg} \cdot \text{d})^{-1} \quad (6.23)$$

$$\text{for } E_H \geq 250 \text{ keV, and } E_I > 30 \text{ keV} \quad (6.24)$$

$$\Gamma_{\text{coinc}}^{\text{Run10}} = 0.10 \pm 0.02 \text{ events} \cdot (\text{kg} \cdot \text{d})^{-1} \quad (6.25)$$

We can not compare the coincidence rate with the simulation because of the heat and ionization 30 keV cut, however, the rate at  $E_H \geq 250$  agrees within the statistical uncertainties with the rate of  $E_R \geq 250$  for Run 8, which shows the muon-induced background measurements are reproducible. Therefore, the EDELWEISS-II experiment is able to measure and detect muon-induced background.

The feasibility of a muon veto-bolometer coincidences analysis is proved successful with the new overall distribution of the timing, which is very promising for future Runs. Muon-induced background are awaited to be seen by the coincidence analysis, and to be removed from the low background analysis to increase the sensitivity on the WIMP detection.

# A

## Parameters of Run 8

### Contents

- A.1 Resolution parameters**
- A.2 Figure of merit**
- A.3 List of events in the coincident region**

### A.1 Resolution parameters

The equations to make the mean and the resolution lines are described in Section 3.1.5. The input parameters of these equations are the variables  $\sigma_{\text{center}}(356)$ ,  $\sigma_{\text{guard}}(356)$ ,  $\sigma_H(356)$  and  $\sigma_{\text{center}}(0)$ ,  $\sigma_{\text{guard}}(0)$ ,  $\sigma_H(0)$ . These variables depend on the Run and on the bolometers. Their values are summarized in the table below.

The ionization and heat baseline resolutions at 356 keV are the mean full width at half maximum (FWHM) in keV for all  $^{133}\text{Ba}$  run in January 2008.

The low background ionization and heat baseline resolutions are the mean FWHM in keV for the data acquisition period Nov. 2007 to March 2008.

All values in Table A.1 are after quality cut from Section 8.1 and 8.2 of [188].

### A.2 Figure of merit

The figure of merit (or magic point, MP) is the intersection of the  $\gamma$  band at 99.9% and the neutron band at 90%. Thus, this value is based on the baseline and the 356 keV-calibration-peak resolutions for the heat and the ionization, which are different from a bolometer to another. For the bolometer analysis of [188], this figure of merit has been set to 30 keV. All bolometers with a figure of merit greater are disregarded.

The figure of merit for the bolometers of Run 8 are from Section 9 of [188], and are shown in Table A.2.

### A.3 List of events in the coincident region

The characteristics of coincidence events found during Run 8 are summarized in Table A.3 for events with  $E_R < 250$  keV and in Table A.4 for events with  $E_R \geq 250$  keV. These characteristics are the bolometer run number of the analysis  $B\ run_{\text{bolo}}$ , the event number in this run  $N_{\text{bolo}}$ , the ionization and recoil energies  $E_I$  and  $E_R$  in keV, the ratio  $Q = E_I/E_R$ , the bolometer multiplicity  $multi_{\text{bolo}}$ , the veto event number  $N_{\text{veto}}$ , the veto multiplicity  $multi_{\text{veto}}$ , the time difference of the event in the muon

DAQ	bolometer	$^{133}\text{Ba}$ calibration runs at -7 V			low background runs		
		$\sigma_{\text{center}}(356)$	$\sigma_{\text{guard}}(356)$	$\sigma_H(356)$	$\sigma_{\text{center}}(0)$	$\sigma_{\text{guard}}(0)$	$\sigma_H(0)$
s1	GGA14	4.9	4.6	6.8	1.5	1.6	1.9
s1	GGA13	3.9	4.4	9.1	1.7	1.8	1.3
s1	GSA11	3.6	7.2	6.7	1.5	2.5	1.7
s1	GGA10	5.3	3.6	8.1	1.7	1.7	1.4
s1	GGA7	4.5	4.6	10.5	1.8	1.7	2.5
s1	GSA10	6.8	5.5	5.9	2.2	1.8	1.5
s1	GGA3	3.4	4.2	9.0	1.5	1.4	2.3
s2	GGA5	3.2	5.0	5.1	1.3	1.8	1.6
s2	GGA11	5.8	4.3	6.2	2.2	2.8	1.6
s2	GGA8	7.1	4.9	9.1	4.7	2.5	1.9
s2	GSA8	5.2	5.5	10.6	2.1	1.5	2.6
s2	GGA4	4.5	5.4	12.4	1.6	2.2	1.2
s2	GGA9	4.4	4.8	5.4	1.7	1.7	1.1
s3	GSA7	4.4	—	5.6	2.3	3.2	2.9
s3	GSA1	4.1	7.6	12.5	1.7	3.2	3.2
s3	GSA3	5.2	15.5	12.3	3.7	4.0	4.2

Table A.1: Resolutions of heat and ionization channels per bolometer during calibration and physics runs of Run 8.

DAQ	bolometer	magic point (keV)
s1	GGA14	19.0
s1	GGA13	17.0
s1	GSA11	17.5
s1	GGA10	18.0
s1	GGA7	24.5
s1	GSA10	22.0
s1	GGA3	21.5
s2	GGA5	16.0
s2	GGA11	22.5
s2	GGA8	45.5
s2	GSA8	27.5
s2	GGA4	16.0
s2	GGA9	16.0
s3	GSA7	30.0
s3	GSA1	29.5
s3	GSA3	49.0

Table A.2: Figure of merit per bolometer for Run 8.

veto and the bolometers  $\Delta t_{\text{coinc}} = t_{\text{veto}} - t_{\text{veto}}$  in second and a flag  $f$ . The flag is  $f = 1$  if the coincidence is in between the muon veto and one set of bolometers,  $f = 61$  with two set of coincidences,  $f = 71$  with the three set of bolometers.

$run_{\text{bolo}}$	$N_{\text{bolo}}$	$E_I$	$E_R$	$Q$	$multi_{\text{bolo}}$	$N_{\text{veto}}$	$multi_{\text{veto}}$	$\Delta t_{\text{coinc}}$	$f$
110205	3104	6	26	0.230	1	443303	7	0.01834	1
212400	987	4	23	0.173	1	196446	5	0.01852	1
213000	1811	91	93	0.978	1	278004	5	0.03011	1
213101	5092	187	189	0.989	1	295527	5	0.02055	1
213101	7100	158	163	0.969	1	299625	7	0.02030	1
220102	2173	153	135	1.133	1	306606	5	0.02336	1
120205	1551	11	36	0.306	1	319151	5	0.02105	1
220708	4346	5	19	0.263	1	2735	7	0.01968	1
221904	4559	259	239	1.083	1	174318	5	0.02831	1
122210	2809	55	59	0.932	1	218243	5	0.02710	1
230312	4803	75	67	1.119	1	380737	4	0.02285	1
131713	3894	95	93	1.021	1	596269	5	0.02447	1
231826	4315	158	151	1.046	1	622413	4	0.02916	1
241206	4528	253	230	1.100	1	7331	11	0.02506	1
241300	1737	157	146	1.070	1	16792	4	0.02239	1
241502	850	21	31	0.677	1	45073	12	0.02656	1

Table A.3: *Short list of parameters of coincidence events at  $E_R < 250$  keV.*

$run_{\text{bolo}}$	$N_{\text{bolo}}$	$E_I$	$E_R$	$Q$	$multi_{\text{bolo}}$	$N_{\text{veto}}$	$multi_{\text{veto}}$	$\Delta t_{\text{coinc}}$	$f$
102902	67	2482	71486	0.034	3	393909	5	0.01744	1
203001	2539	10096	124151	0.081	7	415251	4	0.02538	71
110104	2185	297	429	0.692	1	436259	7	0.01603	1
210309	2422	336	348	0.965	1	466500	5	0.02663	1
211200	4470	746	619	1.205	3	24537	5	0.02963	61
211401	1468	4970	26733	0.185	4	52251	12	0.02455	61
211500	6446	569	546	1.042	4	68772	5	0.03277	61
211600	700	1851	18736	0.098	1	72637	5	0.02975	1
212400	1401	7288	84501	0.086	2	197700	5	0.01836	61
112502	5579	384	426	0.901	1	208398	4	0.01618	1
212501	5746	8144	38453	0.211	10	212586	5	0.02109	71
212703	7696	226	122061	0.002	3	240503	6	0.02471	1
120104	6255	304	303	1.003	1	311578	4	0.03282	1
120104	7550	3336	3956	0.843	1	313677	5	0.02700	1
220405	4146	2221	17354	0.127	4	358253	5	0.02487	61
120502	7871	2889	1873	1.542	2	374349	4	0.02429	1
220903	5960	8944	17612	0.507	8	34440	5	0.02936	71
121001	4924	489	476	1.027	2	49724	7	0.02515	1
121203	2224	685	706	0.970	2	69783	4	0.01869	1
221501	1248	1093	1028	1.063	1	109460	19	0.02622	1
121504	5805	-46	5905	-0.007	1	116787	4	0.02452	1
230108	3974	3265	29868	0.109	4	352020	5	0.02762	61
230312	6044	1612	92784	0.017	2	382745	5	0.01590	1
231003	2404	300	312	0.961	3	497150	4	0.02749	61
240601	979	6513	79278	0.082	3	900973	5	0.02791	1
240701	2581	364	513	0.709	2	923013	10	0.01991	61
141706	3288	7064	77455	0.091	6	82722	5	0.01812	61
241800	7936	614	622	0.987	1	101271	5	0.01769	1

Table A.4: Short list of parameters of coincidence events at  $E_R \geq 250$  keV.

# B

## Parameters of Run 10

### Contents

- B.1 Calibration factor of conversion**
- B.2 Adaptative threshold**
- B.3 Resolution parameters**
- B.4 List of events in the coincident region**

### B.1 Calibration factor of conversion

The bolometers have been calibrated with  $^{133}\text{Ba}$  runs: *ik24a019*, *ik24b011*, *ik24c005*, which correspond to runs of November 24<sup>th</sup> 2008. The values found have been cross-checked with the  $^{133}\text{Ba}$  runs: *ih13a000*, *ih13b000*, *i13c000*, which correspond to runs of the August 13<sup>th</sup> 2008, to test their stability during Run 10.

The values for the calibration run in August are less precise because the run is shorter than the one in November, thus there is less statistics. Sometimes it is even not possible to specify the position of the 356 keV, the probable values are then mentioned. The factors of conversion used in the analysis of Run 10 are the one of November.

In a biplot of the heat channel *vs.* the sum of the ionization channels from guard and center, the 356 keV peak gives the factor of conversion Results are summarized in Table B.1.

### B.2 Adaptative threshold

An event is defined during Run 10, if the energy deposit in the heat channel passes a certain threshold. It is the so-called heat trigger. This threshold is defined per bolometer and changes during the run to keep a stable and constant event rate. The mean of the threshold per bolometer is summarized in Table B.2.

### B.3 Resolution parameters

The equations to make the mean and the resolution lines are described in Section 3.1.5. The input parameters of these equations are the variables  $\sigma_{\text{center}}(356)$ ,  $\sigma_{\text{guard}}(356)$ ,  $\sigma_H(356)$  and  $\sigma_{\text{center}}(0)$ ,  $\sigma_{\text{guard}}(0)$ ,  $\sigma_H(0)$ . These variables depend on the Run and on the bolometers. Their values are summarized in the table below.

The ionization and heat baseline resolutions at 356 keV are the mean full width at half maximum (FWHM) in keV for  $^{133}\text{Ba}$  runs in August 2008.

DAQ	bolometer	position of the 356 keV peak			
		heat channel		ionization channel (center + guard)	
		24 <sup>th</sup> /11/2008	13 <sup>th</sup> /08/2008	24 <sup>th</sup> /11/2008	13 <sup>th</sup> /08/2008
s1	GGA14	-725	-750	+660	+665
s1	GGA10	-600	-490 or -600	+675	+545 or +670
s1	GGA7	-380	-400	+680	+695
s1	GSA10	-370	-380	+575	+605
s1	GGA3	-700	-725	+650	+665
s1	GSA8	-610	-575	+700	+675
s2	GSA6	-1350	-1350	+658	+670
s2	GGA5	-1075	-1025	+670	+620
s2	GGA11	-1250	-1300	-483	+455
s2	GSA4	-750	-700 or -800	+645	+575 or +660
s2	GGA4	-810	-860	+425	+435
s2	GGA9	-950	-975	+670	+680
s3	ID401	-1375	-830	+710	+705
s3	ID3	-875	-650	+680	-655

Table B.1: Calibration conversion table of heat and ionization channels per bolometer for Run 10. Position of the 356 keV peak as measured in a biplot of the heat channel vs. the sum of the ionization channels from guard and center during  $^{133}\text{Ba}$  runs in ADU units.

DAQ	bolometer	adaptative threshold on heat channel	
		ADU	keV
s1	GGA14	-20	9.8
s1	GGA10	-10	5.9
s1	GGA7	-8	7.5
s1	GSA10	-9	8.7
s1	GGA3	-10	5.1
s1	GSA8	-8	4.7
s2	GSA6	-6	1.6
s2	GGA5	-10	3.3
s2	GGA11	-4	1.1
s2	GSA4	-10	4.7
s2	GGA4	-3	1.3
s2	GGA9	-5	1.9
s3	ID401	-7	1.8
s3	ID3	-8	3.3

Table B.2: Mean adaptative threshold on the heat channel per bolometer during Run 10.

DAQ	bolometer	$^{133}\text{Ba}$ calibration runs at -7 V			low background runs		
		$\sigma_{\text{center}}(356)$	$\sigma_{\text{guard}}(356)$	$\sigma_H(356)$	$\sigma_{\text{center}}(0)$	$\sigma_{\text{guard}}(0)$	$\sigma_H(0)$
s1	GGA14	4.0	2.0	7.6	1.5	2.0	1.7
s1	GGA10	5.1	1.4	8.0	1.7	1.4	1.6
s1	GGA7	2.4	2.0	9.3	1.5	2.0	2.8
s1	GSA10	7.8	2.6	13.5	2.6	2.6	2.7
s1	GGA3	2.4	2.3	12.3	1.9	2.3	1.9
s1	GSA8	4.6	2.0	10.8	2.3	2.0	2.5
s2	GSA6	4.8	3.4	9.4	2.7	3.4	1.6
s2	GGA5	2.9	2.5	6.7	1.8	2.5	2.1
s2	GGA11	5.7	1.6	8.5	1.8	1.6	1.4
s2	GSA4	10.3	2.9	13.4	5.1	2.9	5.6
s2	GGA4	3.0	1.9	10.2	1.7	1.9	1.0
s2	GGA9	2.5	1.3	9.7	2.1	1.3	2.0
s3	ID401	—	—	—	—	—	—
s3	ID3	—	—	—	—	—	—

Table B.3: Resolutions of heat and ionization channels per bolometer during calibration and physics runs of Run 10.

The low background ionization and heat baseline resolutions are the mean FWHM in keV for August 2008.

The resolution  $\sigma_{\text{guard}}(356)$  is taken as  $\sigma_{\text{guard}}(0)$ .

All values in Table B.3 are preliminary and before quality cut from [189], and do not include the interdigitised bolometers, which have their dedicated analysis.

## B.4 List of events in the coincident region

The characteristics of coincidence events found during Run 8 are summarized in Table B.4 for events with  $E_H < 250$  keV and in Table B.5 for events with  $E_H \geq 250$  keV. These characteristics are a flag, the bolometer multiplicity  $multi_{\text{bolo}}$ , the heat and ionization energies  $E_H$  and  $E_I$  in keV, the ratio  $Q = E_I/E_H$ , the veto event number  $N_{\text{veto}}$ , the veto multiplicity  $multi_{\text{veto}}$ , the time difference of the event in the muon veto and the bolometers  $\Delta t_{\text{coinc}} = t_{\text{veto}} - t_{\text{veto}}$  in 10  $\mu\text{s}$ . The flag is  $i$  for an event occurring in the set of bolometers  $i$ , *i.e.* in the DAQ computer  $si$ . The flag is  $ij$  if the event is a coincidence of the computer  $i$  and  $j$ , and  $ijk$  for three computer called  $i$ ,  $j$ ,  $k$ .

which DAQ ?	$multi_{\text{bolo}}$	$E_H$	$E_I$	$Q$	$N_{\text{veto}}$	$multi_{\text{veto}}$	$\Delta t_{\text{coinc}}$
1	1	134.840	87.001	0.645	154079	5	-1126
1	1	71.620	100.905	1.408	296130	4	-530
2	1	153.191	158.395	1.034	416039	5	-416
1	1	38.110	35.317	0.926	792405	4	-737
1	1	158.633	169.686	1.069	34908	4	-362
3	1	243.382	251.818	1.035	52407	4	122
1	1	50.386	35.846	0.711	58055	6	372
2	1	153.674	320.627	2.086	75806	5	-357
23	2	221.291	273.498	1.235	100450	7	-1008
1	1	33.104	33.398	1.008	130275	4	-730

Table B.4: *Short list of parameters of coincidence events at  $E_H < 250$  keV.*

which DAQ ?	$multi_{\text{bolo}}$	$E_H$	$E_I$	$Q$	$N_{\text{veto}}$	$multi_{\text{veto}}$	$\Delta t_{\text{coinc}}$
12	2	445.594	287.155	0.644	142381	5	-1363
2	1	349.933	316.348	0.904	161195	4	-34
1	2	2062.519	1783.570	0.864	244135	5	-427
1	1	2354.751	1871.214	0.794	246412	5	-413
2	1	259.836	264.063	1.016	258588	4	-406
2	2	1411.331	1671.678	1.184	276167	5	-373
2	2	18624.430	8701.237	0.467	304258	6	-258
12	7	10810.090	8500.136	0.786	344528	5	-254
12	11	35138.337	23521.013	0.669	346042	36	-240
1	1	1373.890	1220.832	0.888	375822	4	-1442
1	1	293.670	272.303	0.927	378862	4	-1350
1	1	390.669	415.552	1.063	380390	5	-422
12	3	12769.037	10000.569	0.783	521619	5	-393
2	2	1370.675	1265.294	0.923	545801	10	-337
1	1	8758.417	4995.244	0.570	558170	5	-237
3	1	493.995	750.712	1.519	559966	5	-283
12	3	2224.988	2080.840	0.935	566467	5	-503
13	2	3468.626	2862.216	0.826	590698	5	-575
2	1	747.953	692.074	0.925	731905	4	-186
13	2	1719.995	1472.135	0.855	745465	5	-464
1	1	565.245	538.250	0.952	775784	5	-430
2	2	12562.936	8153.084	0.648	781534	6	-553
12	3	2443.128	2326.530	0.952	803388	27	-450
2	1	908.934	877.077	0.965	42444	5	-151
13	2	636.566	600.712	0.943	189560	5	-369
1	3	8197.378	3341.394	0.407	96323	5	-674
2	1	361.287	368.281	1.019	111294	4	-540
1	1	8634.692	4931.154	0.571	198743	19	-151
1	1	296.722	305.890	1.030	206063	5	-272
1	1	7711.451	2933.823	0.380	256291	7	-213
1	2	1537.799	1393.901	0.906	126348	6	-286
23	2	547.584	534.956	0.976	158137	7	-375
1	1	460.956	499.543	1.083	221393	4	-634

Table B.5: *Short list of parameters of coincidence events at  $E_R \geq 250$  keV.*



# C

## Definition of the bolometer timing

### Contents

- C.1 Time variables from the ntp**
- C.2 Time variables from the analysis**
- C.3 An example for Run 8**
- C.4 An example for Run 10**
- C.5 Conclusion**

THE FIRST ANALYSIS of coincidences between the muon veto and the bolometers during Run 8, see Chapter 5, is successful, the EDELWEISS-II experiment does identify coincidences in a time interval  $\Delta t_{\text{coinc}}^{\text{Run8}} = t_{\text{veto}} - t_{\text{bolo}} = [+15, +35]$  ms. The second analysis of coincidences with Run 10, see Chapter 6, is also successful, however, the time interval defined is  $\Delta t_{\text{coinc}}^{\text{Run10}} = t_{\text{veto}} - t_{\text{bolo}} = [-15, +5]$  ms.

The result of Run 8 seems to have no physics sense, since when a muon event occurs, it happens simultaneously in all systems, see Figure C.1, or in case of secondaries, *i.e.* muon-induced neutrons, who have to travel a bit before reaching the bolometers, the hits in the bolometers happen later. Thus,  $t_{\text{coinc}}$  should be a negative number, close to zero. In contrast, for Run 10, the interval defined makes more sense.

This difference in  $t_{\text{coinc}}$  could have been explained with the installation of a new device to dispatch a unique time for all sub-systems for Run 10, but thus it suppose that the results for Run 8 are completely out and the timing unreliable. The good agreement of the results of Run 8 with the simulation, the comparison with the expected background and the analysis of the characteristic of these events tend to show that the coincidences found during the Run 8 analysis are not accidental.

Then, the only difference between the two analyses is the files from which is extracted the bolometer information. The bolometer data used in Run 8 are from the analysis of the raw data with the PAW-based software ANA, whereas the bolometer data used in Run 10 are the ntp files, the online pre-processed data, creating online during a run from the information stored in the raw data.

In this Appendix is reviewed the different definitions of the time in the ANA analysis and the ntp files with all technical details to fully and exhaustively discuss the position of the coincidence interval for Run 8 and for Run 10.

## C.1 Time variables from the ntp

Ntp files are the online pre-processed data, usually used to monitor the bolometers during a run, *cf.* Section 3.1.8 and 6.3. Variables, which contain time information in the ntps, are defined in Table C.1. These time variables are the same than those stored in the raw data files and later used for the analysis.

name of the variable	meaning
$run_{ntp}$	name of the ntp file.
$t_H^{\max}$	time of the maximum of the filtered heat pulse, in 10 $\mu$ s-beat, labelled “GigaStamp”, “Stamp”.
$t_{PC}^0$	time of the beginning of the run, from the UNIX time with a precision of the order of 1 s.
$t_{PC}$	time of the event in the run, from the UNIX time with a precision of the order of 1 s, labelled “Date (s)”, “Date (mus)”, $t_{PC} = t_{PC}^0 + t_{10\mu s} \cdot 10^{-5}$ .

Table C.1: *Time variables from the ntp files.*

For Run 8, the distribution of the clock in 10  $\mu$ s-beat has to be corrected by a factor of  $126/125 = 1.008$  to be translated into seconds. Since a new device to dispatch a unique time for all sub-systems was installed this correction is not relevant any more for Run 10 on.

## C.2 Time variables from the analysis

The analysis of the bolometer used in this work is this realized with the PAW-based software ANA developed in Lyon, *cf.* Section 5.3 and see [161, 188, 189].

First, we define variables, from which the time is evaluated in the analysis, for the heat channel in Table C.2 and for the ionization channel in Table C.3.

Final variables, which contain time information in the analyzed files from ANA, are defined in Table C.4.

Note that, for Run 8, since the clock restart to zero with each run,  $TH$  corresponds to the time of the beginning of the event interval of ionization ( $TH_{Run8} = t_I^0$ ).

The time of an event is the time of the beginning of the heat pulse, which is also the time of the beginning of the ionization pulse, see Figure C.1. Therefore, we have the relation

$$t_I^p = t_H^p \quad (C.1)$$

which corresponds to

$$t_I^0 + \Delta t_I \cdot 0.5 + TI = t_H^0 + \Delta t_H \cdot 0.5 + TC \quad (C.2)$$

If we develop, indeed, from Tables C.2, C.3, C.4, we obtain

$$\begin{aligned} & t_I^0 + \Delta t_I \cdot 0.5 + TI \\ &= t_H^{\max} - \Delta t_I \cdot f_I + \Delta t_I \cdot 0.5 + t_I^p - t_H^{\max} - \Delta t_I \cdot (0.5 - f_I) \\ &= t_I^p \end{aligned} \quad (C.3)$$

name of the variable	meaning
$\Delta t_H$	size of the event interval for heat, $\Delta t_H = 512 \text{ samples} = 512 \cdot 1.008 \text{ ms}$ .
$f_H$	fraction of the pre-sample (pre-trigger) in $\Delta t_H$ , <i>i.e.</i> position of the maximum of the heat pulse, $f_H = 0.5$ .
$t_H^0$	time of the beginning of the event interval for heat, $t_H^0 = t_{10\mu s} - \Delta t_H \cdot f_H$ .
$t_H^p$	time of the beginning of the heat pulse.

Table C.2: *Useful time variables for the heat channel.*

name of the variable	meaning
$\Delta t_I$	size of the event interval for ionization, Run 8, $\Delta t_I^{\text{Run8}} = 4096 \text{ samples} = 40.96 \cdot 1.008 \text{ ms}$ , Run 10, $\Delta t_I^{\text{Run10}} = 5000 \text{ samples} = 50.00 \text{ ms}$ .
$f_I$	fraction of the pre-sample (pre-trigger) in $\Delta t_I$ , <i>i.e.</i> position of the maximum of the <i>heat</i> pulse, Run 8, $f_I^{\text{Run8}} = 0.75$ , Run 10, $f_I^{\text{Run10}} = 0.80$ .
$t_I^0$	time of the beginning of the event interval for ionization, $t_I^0 = t_{10\mu s} - \Delta t_I \cdot f_I$ .
$t_I^p$	time of the beginning of the ionization pulse.

Table C.3: *Useful time variables for the ionization channel.*

name of the variable	meaning
$run_{\text{ANA}}$	name of the file in ANA.
$TH$	difference of the time of the beginning of the run and the time of the beginning of the ionization interval ( $t_I^0$ ) in seconds (corrected by the factor 1.008).
$TC$	time of the <i>beginning</i> (not maximum) of the heat pulse relative to the <i>center</i> of the heat interval (0.5), <i>i.e.</i> difference of the beginning and the maximum of the heat pulse, maximum which is already at $f_H = 0.5$ , $TC = t_H^p - t_H^{\text{max}}$ .
$TI$	time of the <i>beginning</i> (not maximum) of the ionization pulse relative to the <i>center</i> of the ionization interval (0.5), <i>i.e.</i> difference of the beginning and the maximum of the ionization pulse, PLUS the difference of the factor 0.5 and $f_I$ of the ionization interval, $TI = t_I^p - (t_H^{\text{max}} + \Delta t_I \cdot (0.5 - f_I))$ .

Table C.4: *Time variables from the analysis files.*

and

$$\begin{aligned}
 & t_H^0 + \Delta t_H \cdot 0.5 + TC \\
 &= t_H^{\max} - \Delta t_H \cdot f_H + \Delta t_H \cdot 0.5 + t_H^p - t_H^{\max} \\
 &= t_H^p
 \end{aligned} \tag{C.4}$$

### C.3 An example for Run 8

The event chosen as example for Run 8 is the 3<sup>rd</sup> event of the run of Jan 2<sup>th</sup> 2008, which correspond to  $run_{ntp} = ia02a005$ , and  $run_{ANA} = 120205$ .

From the data analysis file, we have the time difference of the beginning of the run and of the beginning of the ionization interval, which is for Run 8 the time of the beginning of the ionization interval:

$$TH = t_I^0 = 15019.483 \text{ ms} \tag{C.5}$$

$TH$  is already corrected by the factor 1.008. We also have the time of the beginning of the ionization pulse relative to the center of the ionization interval:

$$TI = 0.68573 \cdot 1.008 \text{ ms} \tag{C.6}$$

From the data acquisition, *i.e.* the ntp file, which contain the same information than the corresponding raw data files, we have the time of the maximum of the filtered heat pulse:

$$\begin{aligned}
 t_H^{\max} &= 1493100 \text{ unit of the } 10 \mu\text{s clock} \\
 &= 14931.000 \cdot 1.008 \text{ ms} \\
 &= 15050.448 \text{ ms}
 \end{aligned} \tag{C.7}$$

Thus, it is clear that  $TH$  and  $t_H^{\max}$  are different and have a different signification, despite a misleading name in the bolometer analysis ANA.  $TH$  is the beginning of the ionization interval and  $t_H^{\max}$  is the maximum of the heat pulse.

The time of the maximum of the heat pulse in ANA can be evaluated if we add the pre-trigger  $f_I = 0.75$  of the sample window to the time of the beginning of the ionization window:

$$(t_H^{\max})_{ANA} = t_I^0 + \Delta t_I \cdot f_I \cdot 1.008 \tag{C.8}$$

$$\begin{aligned}
 &= TH + \Delta t_I \cdot f_I \cdot 1.008 \\
 &= 15019.483 \text{ ms} + 40.96 \cdot 0.75 \cdot 1.008 \text{ ms} \\
 &= 15050.449 \text{ ms}
 \end{aligned} \tag{C.9}$$

Comparing Equations C.7 and C.9, we have  $(t_H^{\max})_{ANA} = t_H^{\max}$ , we find back the ntp time stamp from the time of the analysis. We are now certain that the time used in the analysis and the time used in the ntp is the same and is the one coming from the device which dispatch the clock in 10  $\mu\text{s}$ -beat, and not some arrangements from  $t_{PC}$ .\*

\* About  $t_{PC}$ , the real time read in the ntp file is  $t_{PC} = 1199263394.124085$ , then  $t_{PC} - t_{PC}^0 = 1199263394.124085 - 1199263379.193085 = 14931.000 \text{ ms}$ . Therefore  $t_{PC} - t_{PC}^0 = t_H^{\max} \cdot 10^{-5}$  still holds as it is defined in Table C.1.

For Run 8 muon veto-bolometer analysis, we compared  $TH$  and  $t_{veto}$ . We have  $TH = t_I^0$  the beginning of the ionization interval, since the clock of Run 8 restart with each runs. And we have  $t_{veto} = t_I^p$  the real time of the event, since an event in coincidence in the veto and the bolometers happens almost simultaneously in both system.

In Table C.4, we have defined

$$TI = t_I^p - t_H^{\max} - \Delta t_I \cdot (0.5 - f_I) \quad (\text{C.10})$$

$$\begin{aligned} \text{hence, } TI \cdot 1.008 &= t_I^p - TH - \Delta t_I \cdot f_I \cdot 1.008 - \Delta t_I \cdot (0.5 - f_I) \cdot 1.008 \\ &= t_I^p - TH - \Delta t_I \cdot 0.5 \cdot 1.008 \end{aligned} \quad (\text{C.11})$$

Therefore, the time of the beginning of the ionization pulse, *i.e.* the real time of the event is:

$$t_I^p = TH + (0.50 \cdot \Delta t_I + TI) \cdot 1.008 \quad (\text{C.12})$$

$$\begin{aligned} &= 15019.483 \text{ ms} + (0.50 \cdot 40.96 + 0.68573) \cdot 1.008 \text{ ms} \\ &= 15040.818 \text{ ms} \end{aligned} \quad (\text{C.13})$$

Therefore in the particular case of the example, the time difference of  $t_{veto} - t_{bolo}$  is

$$(\Delta t_{\text{coinc}}^{\text{Run8}})_{\text{example}} = 21.335 \text{ ms.} \quad (\text{C.14})$$

The risetime of the heat pulse can be evaluated as the time difference of the maximum of the heat pulse and the real time of the event

$$t_H^r = t_H^{\max} - t_I^p \quad (\text{C.15})$$

$$\begin{aligned} &= 15050.449 - 15040.818 \\ &= 9.631 \text{ ms} \end{aligned} \quad (\text{C.16})$$

The risetime is of  $\sim 10$  ms.

The ionization pre-trigger, pre-sample factor has been chosen to  $f_I = 0.75$  relative to the maximum of the heat pulse  $t_H^{\max}$ , so that the ionization pulse is centered in the ionization interval at 0.50 for bolometers with a heat risetime of  $\sim 10$  ms:

$$\begin{aligned} (f_I - 0.50) \cdot \Delta t_I &= (0.75 - 0.50) \cdot 40.96 \\ &= 10.24 \sim 10 \text{ ms} \end{aligned} \quad (\text{C.17})$$

When the ionization pulse is centered at 0.5,  $TI \sim 0$ . Thus, the time difference of the coincidences can be defined in a more general way:

$$t_{veto} - t_{bolo} = t_I^p - TH \quad (\text{C.18})$$

$$\begin{aligned} &= TH + (0.50 \cdot \Delta t_I + TI) \cdot 1.008 - TH \\ &= (0.50 \cdot \Delta t_I + TI) \cdot 1.008 \\ &\sim (0.50 \cdot \Delta t_I) \cdot 1.008 \\ &\sim 0.5 \cdot 40.96 \cdot 1.008 \text{ ms} \\ &\sim 20.644 \text{ ms} \end{aligned} \quad (\text{C.19})$$

In the general case of the ionization pulse centered in the ionization interval, the time difference of  $t_{\text{veto}} - t_{\text{bolo}}$  is

$$(\Delta t_{\text{coinc}}^{\text{Run8}})_{\text{general}} = 20.644 \text{ ms} \quad (\text{C.20})$$

Therefore, the result of the analysis of the muon veto-bolometer coincidences for Run 8, which is  $\Delta t_{\text{coinc}}^{\text{Run8}} = [+15, +35]$  ms can be explained by a misunderstanding when picking variables for the analysis, instead of the beginning of the ionization or heat pulse  $t_I^p$ , which is the real time of the event, the comparison was done with the time of the beginning of the ionization interval  $TH$ .

## C.4 An example for Run 10

For Run 10, the muon veto-bolometer coincidence analysis is made directly with the ntp files, as there was no calibrated data available yet for the Run 10, when the analysis in this work was performed.

The time difference of the coincidences is the time difference of the real time of the event and the maximum of the heat pulse:

$$t_{\text{veto}} - t_{\text{bolo}} = t_I^p - t_H^{\text{max}} \quad (\text{C.21})$$

$$\begin{aligned} &= -t_H^r \\ &\sim -10 \text{ ms} \end{aligned} \quad (\text{C.22})$$

which is the risetime of the heat pulse, see also C.15.

The result of the analysis of the muon veto-bolometer coincidences for Run 10 is  $\Delta t_{\text{coinc}}^{\text{Run10}} = [-15, +5]$  ms, which is the order of the risetime of the heat pulse.

## C.5 Conclusion

The risetime of the muon veto pulse is of  $\sim$  ns. For the ionization pulse of the bolometer, the risetime is of  $\sim \mu$ s, and for the heat pulse of some ms, see Figure C.1. Thus, to compare events in different systems, the best is to define the real time of an event in a system as the beginning of the pulse in this system, which real time will be the same for the muon veto, the bolometer heat and ionization. None of the two analyses compare the real time of the bolometer event with the real time of the muon veto event. However, both coincidence intervals are understood and can be explained

When the analysis will be performed again for Run 10 with calibrated data and future Runs, the real time of the pulse in ANA to be compared with the muon veto will be defined as

$$t_I^p = TH + (0.50 \cdot \Delta t_I + TI) \quad (\text{C.23})$$

$$\begin{aligned} &= TH + (0.50 \cdot 50.00 + TI) \text{ ms} \\ &= TH + 25.00 + TI \text{ ms} \end{aligned} \quad (\text{C.24})$$

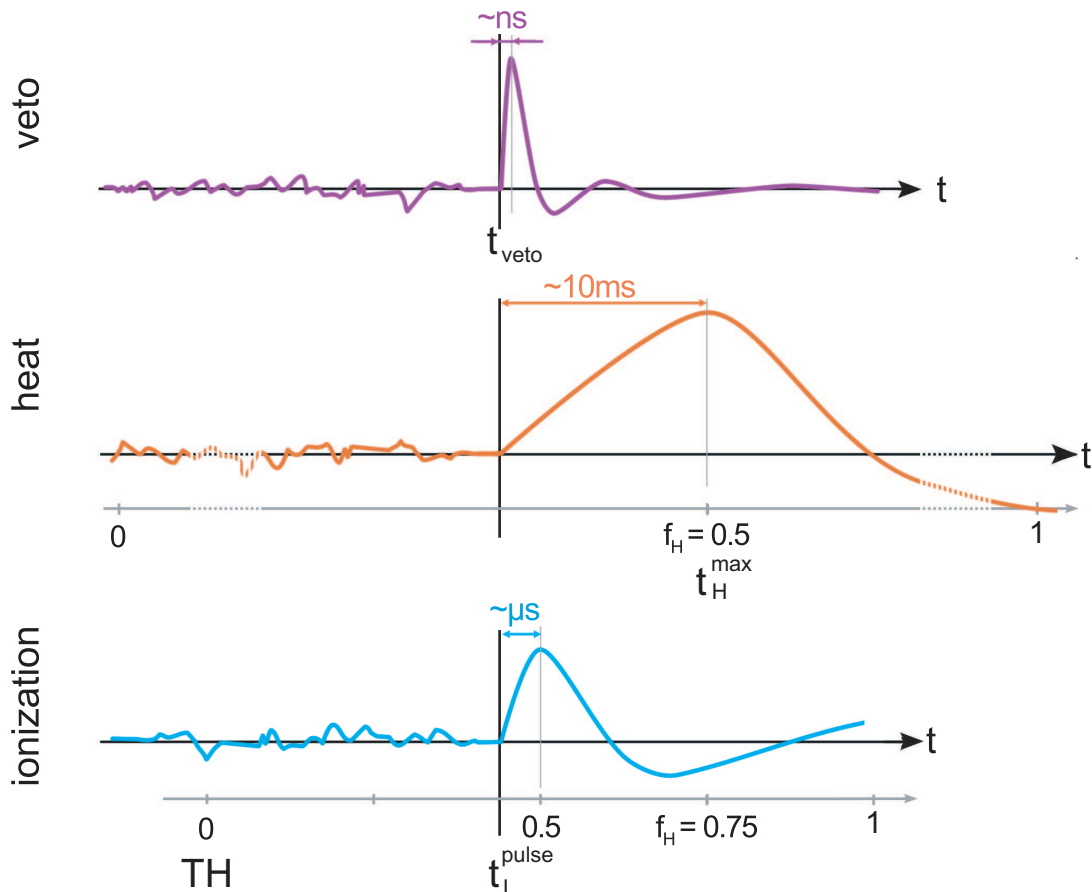


Figure C.1: Schematic of the signals induced in all sub-systems by a coincidence event in the EDELWEISS-II experiment. An event in coincidence in the muon veto and the bolometers happens almost simultaneously in both systems. The muon veto signal has a very brief risetime of  $\sim ns$ . The ionization signal has a risetime of  $\sim \mu s$ . And the heat signal is the slowest one with a risetime of  $\sim 10 ms$  to reach its maximum amplitude. The pulses are not to scale. In grey is represented the heat or ionization interval, in which the corresponding pulse is recording. Noticeable variables for the discussion are also shown. Picture credit GLCH.



# Bibliography

- [1] F. Zwicky, *Helv. Phys. Acta*, **6**, 110 (1933); republished in *Gen Relativ Gravit*, **41**, 207 (2009).
- [2] V. Rubin and W.K. Ford, *Astrophysical Journal*, **159**, 379 (1970).
- [3] Edvige Corbelli and Paolo Salucci *MNRAS*, bf 311, 441 (1999).
- [4] M. Persic, P. Salucci and F. Stel, *MNRAS*, **281**, 27 (1996).
- [5] J. F. Navarro, C. S. Frenk and S. D. M. White, *Astrophysical Journal*, **490**, 493 (1997).
- [6] A. Toomre, *Evolution of Galaxies and Stellar Populations*, ed. B. M. Tinsley & R. B. Larson, New Haven: Yale Univ. Press, p. 401 (1977).
- [7] G. A. Mamon, *ApJL*, **401**, L3.
- [8] C. M. Baugh, S. Cole and C. S. Frenk, *MNRAS*, **283**, 1361 (1996).
- [9] V. Springel, S. D. M. White, G. Tormen and G. Kauffmann, *MNRAS*, **328**, 726 (2001).
- [10] A. Dekel et al., *Nature*, 437, 707-710 (2005); 21st IAP meeting, *Mass Profiles and Shapes of Cosmological Structures*, ed. G. A. Mamon, F. Combes, C. Deffayet & B. Fort (Paris: EDP).
- [11] A. Romanowsky, N. Douglas, M. Arnaboldi et al., *Science*, **301**, 1696 (2003).
- [12] F. Zwicky, *Astrophysical Journal*, **86**, 217 (1937).
- [13] P. Schneider, J. Ehlers, and E. E. Falco, *Gravitational Lenses.*, Springer-Verlag (1992).
- [14] R. Narayan and M. Bartelmann, *Lectures on gravitational lensing.*, arXiv:astro-ph/9606001 (1996).
- [15] J. D. Bekenstein, *Phys. Rev. D*, **70**, 083509 (2004).
- [16] NASA, Andrew Fruchter and the ERO Team [Sylvia Baggett (STScI), Richard Hook (ST-ECF), Zoltan Levay (STScI)] (STScI) <http://hubblesite.org/newscenter/archive/releases/2000/07/image/b/>, News Release Number: STScI-2000-07 (2000).
- [17] H. Dahle, *The NOT in the 2000s*, ed. N. Bergvall, L. O. Takalo and V. Piirola (Piikkio: Univ. Turku), **45** (2000).
- [18] H. Dahle et al., *Astrophysical Journal*, **579**, 227 (2002).

- [19] N. A. Bahcall, L. M. Lubin and V. Dorman, *Astrophysical Journal*, **447**, L81 (1995).
- [20] N. Bahcall et al., *Astrophysical Journal*, **541**, 1 (2000).
- [21] E. W. Kolb and M. S. Turner, *The Early Universe*, Frontiers in Physics, Vol. 69 (1990).
- [22] D. N. Spergel et al., *Astrophysical Journal*, **170**, 377 (2007).
- [23] W. Freedman et al., *Astrophysical Journal*, **553**, 47 (2001).
- [24] Burles, Nollet and Turner, arxiv:astro-ph/9903300.
- [25] C. Amsler et al. (Particle Data Group), *Phys. Lett. B*, **667**, 1 (2008)
- [26] J. C. Mather et al., *Astrophysical Journal*, **420**, 445 (1994).
- [27] G. Hinshaw et al., *Astrophysical Journal*, **170**, 288 (2007).
- [28] W. C. Jones et al., *Astrophysical Journal*, **647**, 623 (2006).
- [29] C. L. Kuo et al., *Astrophysical Journal*, **600**, 32 (2004).
- [30] A. C. S. Readhead et al., *Astrophysical Journal*, **609**, 498 (2004).
- [31] C. Dickinson, *MNRAS*, **353**, 732 (2004).
- [32] W. Baade, *Astrophysical Journal*, **88**, 285 (1938); C. Kowal, *Astrophysical Journal*, **73**, 1021 (1968).
- [33] A. Reiss et al., *Astrophysical Journal*, **116**, 1009 (1998).
- [34] S. Perlmutter et al., *Astrophysical Journal*, **517**, 565 (1999).
- [35] L. D. Bradley et al., *Astrophysical Journal*, **678**, 647 (2008).
- [36] S. Perlmutter, *Physics Today*, **56**, 53 (2003).
- [37] M. M. Colless et al., *MNRAS*, **328**, 1039 (2001).
- [38] M. Tegmark et al., *Astrophysical Journal*, **606**, 702 (2004).
- [39] S. Cole et al., *MNRAS*, **362**, 505 (2005).
- [40] S. D. M. White, C. S. Frenk and M. Davis, *Astrophysical Journal*, **274**, L1-5 (1983).
- [41] B. Paczyński, *Astrophysical Journal*, **304**, 1 (1986).
- [42] K. Griest, *Astrophysical Journal*, **366**, 412 (1991).
- [43] R. J. Nemiroff, *Astron. Astrophys.*, **247**, 73 (1991); A. De Rujula et al., *Astron. Astrophys.*, **254**, 99 (1992).
- [44] C. Afonso et al., *Astron. Astrophys.*, **400**, 951 (2003).

- [45] Alcock, C. et al., *Astrophysical Journal*, **542**, 281 (2000).
- [46] KATRIN Collaboration, *KATRIN Design Report 2004*, **4FZKA7090**, NPI ASCR Rez EXP-01/2005, MS-KP-0501 (2005).
- [47] D. Clowe et al., *Astrophysical Journal*, **609**, 596 (2004).
- [48] D. Clowe et al., *Astrophysical Journal*, **648**, 109 (2006).
- [49] A. Mahdavi et al., *Astrophysical Journal*, **668**, 806 (2007).
- [50] M. Bradac et al., *Astrophysical Journal*, **687**, 959 (2008).
- [51] C.-J.Ma et al., *Astrophysical Journal*, **693**, 56 (2009).
- [52] R. D. Peccei, H. R. Quinn, *Phys. Rev. Lett.*, **38**, 1440 (1997); *Phys. Rev. D*, **16**, 1791 (1977).
- [53] P. G. Harris et al., *Phys. Rev. Lett.*, **82**, 904 (1999).
- [54] J. Preskill, M. B. Wise, and F. Wilczek., *Phys. Lett. B*, **120**, 132 (1983).
- [55] P. Sikivie, *Phys. Lett. B*, **567**, 1 (2003).
- [56] P. Sikivie, *Phys. Rev. Lett.*, **51**, 1415 (1983); *Phys. Rev. D*, **32**, 2988 (1985).
- [57] L. D. Duffy et al., *Phys. Rev. D*, **74**, 012006 (2006).
- [58] G. Jungman, M. Kamionkowski and K. Griest, *Physics Reports*, **267**, 195 (1996).
- [59] J. Ellis, J.S. Hagelin, D.V. Nanopoulos, K.A. Olive and M. Srednicki, *Nucl. Phys. B*, **238**, 453 (1984).
- [60] Ya. B. Zel'dovich, *Zh. Eksp. Teor. Fiz.*, **48**, 986 (1965).
- [61] Ya. B. Zel'dovich, L. B. Okun and S. B. Pikelner, *Usp. Fiz. Nauk.*, **84**, 113 (1965).
- [62] H.-Y. Chiu, *Phys. Rev. Lett.*, **17**, 712 (1996).
- [63] B. Lee and S. Weinberg, *Phys. Rev. Lett.*, **39**, 165 (1977).
- [64] E. A. Baltz, M. Battaglia, M. E. Peskin, and T. Wizansky, *Phys. Rev. D*, **74**, 103521 (2006).
- [65] Dan Hooper and Edward Baltz, *Annu. Rev. Nucl. Part. Sci.*, **58** (2008).
- [66] G. Bertone, D. Hooper, and J. Silk, *Physics Reports*, **405**, 279 (2005).
- [67] C. Tyler, *Phys. Rev. D*, **66**, 023509 (2002).
- [68] L. Bergstrom, J. Edsjo, P. Gondolo, and P. Ullio, *Phys. Rev. D*, **59**, 043506 (1999).
- [69] J. Silk, K. A. Olive, and M. Srednicki, *Phys. Rev. Lett.*, **55**, 257, (1985).

- [70] L. M. Krauss, M. Srednicki, and F. Wilczek, *Phys. Rev. D*, **33**, 2079 (1986).
- [71] L. Bergstrom, P. Ullio, and J. H. Buckley, *Astropart. Phys.*, **9** 137, (1998).
- [72] N.W. Evans, F. Ferrer and S. Sarka, *Phys. Rev. D*, **69**, 123501 (2004).
- [73] L. Pieri, E. Branchini and S. Hofmann, *Phys. Rev. Lett.*, **05**, 211301 (2005).
- [74] F. Aharonian et al., *Astron. Astrophys.*, **425**, 13 (2004).
- [75] J. Albert et al., *Astrophysical Journal*, **638**, 101 (2006).
- [76] K. Kosack et al., *Astrophysical Journal*, **608**, 97 (2004).
- [77] K. Tsuchiya et al., *Astrophysical Journal*, **606**, 17 (2005).
- [78] F. Aharonian et al., *Phys. Rev. Lett.*, **97**, 221102 (2006).
- [79] G. Zaharijas and D. Hooper, *Phys. Rev. D*, **73**, 103501 (2006).
- [80] S. Dodelson, D. Hooper and P.D. Serpico, *Phys. Rev. D*, **77**, 063512 (2008).
- [81] W. de Boer et al., *Astron. Astrophys.*, **444**, 51 (2005)
- [82] L. Bergstrom, J. Edsjo, M. Gustafsson, and P. Salati, *JCAP*, **0605**, 006 (2006).
- [83] F. W. Stecker, S. D. Hunter, and D. A. Kniffen, *Astropart. Phys.*, **29**, 25 (2008).
- [84] Christine Meurer, *Proceedings of AIP Conference*, **1085**, 719 (2009)
- [85] P. F. Michelson., Large area telescope first light. NASA teleconference, Credit: NASA/DOE/International LAT Team, (August 26<sup>th</sup> 2008).
- [86] The Super-Kamiokande Collaboration, *NIM A*, **501**, 418 (2003).
- [87] A. Goldschmid et al., *Proceedings of the 27th International Cosmic Ray Conference*, 1237 (2001).
- [88] T. DeYoung, *Int. J. Mod. Phys. A*, **20**, 3160 (2005).
- [89] S. Desai et al, *Phys. Rev. D*, **70**, 083523 (2004) [Erratum-ibid. *Phys. Rev. D*, **70**, 109901 (2004)].
- [90] O. Adriani et al., *Nature*, **458**, 607 (2009).
- [91] S.W. Barwick et al., *Astrophysical Journal*, **482**, 191 (1997); S. Coutu et al, in *Proceedings of 27th ICRC*, (2001).
- [92] J. Olzem, *Talk given at the 7th UCLA Symposium on Sources and Detection of Dark Matter and Dark Energy in the Universe*, Marina del Ray, CA, (2006).
- [93] J. Chang et al., *Nature*, **456**, 362 (2008).
- [94] D. Finkbeiner, *Phys. Rev. D*, **76**, 083012 (2007).

- [95] I. Cholis, L. Goodenough, D. Hooper, M. Simet and N. Weiner, arXiv:0809.1683 [hep-ph] (2008).
- [96] F. Donato, D. Maurin, P. Brun, T. Delahaye and P. Salati, *Phys. Rev. Lett.*, **102**, 071301 (2009); M. Cirelli, M. Kadastik, M. Raidal and A. Strumia, *Nucl. Phys. B*, **813**, 1 (2009).
- [97] J. Hall and D. Hooper, arXiv:0811.3362 [astro-ph] (2008).
- [98] M. W. Goodman and E. Witten, *Phys. Rev. D*, **31**, 3059 (1985).
- [99] R. J. Gaitskell, *Ann. Rev. Nucl. Part. Sci.*, **54** 315 (2004).
- [100] A. Kurylov and M. Kamionkowski, *Phys. Rev. D*, **69**, 063503 (2004).
- [101] J. D. Lewin and P. F. Smith, *Astropart. Phys.*, **6**, 87 (1996).
- [102] G. Dūda, A. Kemper, and P. Gondolo, *JCAP*, **07**, 12 (2007).
- [103] D. R. Tovey, R. J. Gaitskell, P. Gondolo, Y. Ramachers and L. Roszkowski, *Phys. Lett. B*, **488**, 17 (2000).
- [104] M. T. Ressell et al., *Phys. Rev. D*, **48**, 5519 (1993).
- [105] V. Dimitrov, J. Engel, and S. Pittel, *Phys. Rev. D*, **51**, 291 (1995).
- [106] J. Engel, *Phys. Lett. B*, **264**, 114 (1991).
- [107] J. Diemand et al., *Nature*, **454**, 735 (2008).
- [108] V. Springel et al., to appear in *Nature*, arxiv:0809.0894 [astro-ph] (2008).
- [109] A.M. Green, *New Astronomy Reviews*, **490**, 181 (2005).
- [110] L.M. Krauss and C.J. Copi, *New Astronomy Reviews*, **49**, 185 (2005).
- [111] G. Heusser, *Ann. Rev. Nucl. Part. Sci.*, **45**, 543 (1995).
- [112] A. K. Drukier, K. Freese, and D. N. Spergel, *Phys. Rev. D*, **33**, 3495 (1986).
- [113] K. Freese, J. A. Frieman, and A. Gould, *Phys. Rev. D*, **37**, 3388 (1988).
- [114] D. N. Spergel, *Phys. Rev. D*, **37**, 1353 (1988).
- [115] Hank Sobel, *DMSAG Draft Report*, AAAC Meeting (2007).
- [116] J. Angle et al., *Phys. Rev. Lett.*, . **100**, 021303 (2008).
- [117] Elena Aprile, Laura Baudis et al., *Proceedings of the Identification of Dark Matter conference (IDM 2008) Stockholm*, arXiv:0902.4253v1 [astro-ph.IM] (2008).
- [118] Kastens, et al., arXiv:0905.1766v1 [physics.ins-det] (2009).
- [119] V. N. Lebedenko et al., arXiv:0812.1150v2 [astro-ph] (2008).
- [120] P. Benetti et al., *Astropart. Phys.*, **28** 495 (2008).

- [121] R. Lang and W. Seidel, accepted for publication in New Journal of Physics, arXiv:0906.3290v1 [astro-ph.IM] (2009).
- [122] E. Armengaud, *Proceedings of the 1st International Workshop "Radiopure Scintillators for EURECA" (RPScint'2008)*, arXiv:0903.1539v2 [nucl-ex] (2009).
- [123] Z. Ahmed et al., *Phys. Rev. Lett.*, **102**, 011301 (2009).
- [124] R. Bernabei et al., *La Revista del Nuovo Cimento*, **26N1**, 1 (2003).
- [125] R. Bernabei et al., *Phys. Lett. B*, **389**, 757 (1996);
- [126] R. Bernabei et al., *Proc. of the X Int. Works. on "Neutrino telescopes"*, 403 (2003)
- [127] R. Bernabei et al., *Eur.Phys.J.C*, **56**, 333 (2008).
- [128] C. Savage, P. Gondolo and K. Freese, *Phys. Rev. D*, **70**, 123513 (2004).
- [129] P. Gondolo and G. Gelmini, *Phys. Rev. D*, **71**, 123520 (2005).
- [130] E. Behnke et al., *Science*, **319**, 933 (2008).
- [131] C.E. Aalseth et al., *Phys. Rev. Lett.*, **101**, 251301 (2008).
- [132] P.S. Barbeau, J.I. Collar and O. Tench, *JCAP*, **09**, 009 (2007).
- [133] D.B. Cline, W. Ooi, H. Wang, arXiv:0906.4119v1 (2009).
- [134] A. Benoit et al., *Phys. Lett. B*, **513**, 15 (2001).
- [135] A. Benoit et al., *Phys. Lett. B*, **545**, 43 (2002).
- [136] V. Sanglard et al., *Phys. Rev. D*, **71**, 122002 (2005).
- [137] P. Di Stefano et al., *New Astron. Rev.*, **49**, 251 (2005).
- [138] J. Lindhard et al., *Mat. Fys. Medd. Dan. Vid. Selsk.*, **33 10**, 1 (1963).
- [139] E. Simon et al., *NIM A*, **507**, 643 (2003).
- [140] A. Benoit et al., *NIM A*, **577**, 558 (2007).
- [141] S. Fiorucci et al., *Astropart. Phys.*, **28**, 143 (2007)
- [142] X. F. Navick et al., *NIM A*, **444**, 361 (2000).
- [143] G. F. Knoll, *Radiation detection and measurement*, J. Wiley & Sons, New-York (1989).
- [144] X. F. Navick, *Etude et optimisation de bolomètres à mesure simultanée de l'ionisation et de la chaleur pour la recherche de matière noire*, thèse de doctorat, Université Paris VII, France (1997).
- [145] A. Broniatowski et al., *NIM A*, **520**, 178 (2004).

- [146] B. Censier et al., *NIM A*, **520**, 156 (2004).
- [147] A. Benoit et al., *Phys. Lett. B*, **479**, 8 (2000).
- [148] T. Shutt et al., *NIM A*, **444**, 340 (2000).
- [149] V. Sanglard, *Recherche de la matière noire non-baryonique à l'aide de détecteurs cryogéniques à double composante ionisation et chaleur : Analyse et Interprétation des données de l'expérience EDELWEISS-I*, thèse de doctorat, Université Lyon I, France (2005).
- [150] A. Juillard, *Résolution dans des bolomètres équipés de couches minces d'isolant d'Anderson pour des événements impliquant des reculs de noyaux*, thèse de doctorat, Université Paris XI, France (1999).
- [151] B. Neganov, *Otkrytia i izobreteniya*, **146**, 215 (1985); P. Luke, *Appl. Phys. J.*, **64**, 6858 (1988); P. N. Luke et al., *NIM A*, **289**, 496 (1990).
- [152] S. Marnieros, *Couches minces d'isolant d'Anderson. Application à la bolométrie à très basse température*, thèse de doctorat, Université Paris XI, France (1998).
- [153] X. Defay, *Recherche de matière noire au sein de l'expérience EDELWEISS avec des bolomètres germanium à double composante Ionisation/Chaleur, rejet des événements de surface avec la voie ionisation*, thèse de doctorat, Université Montpellier II, France (2008).
- [154] O. Martineau et al., *NIM A*, **530**, 426 (2004).
- [155] A. Juillard et al., *NIM A*, **559** 393 (2006).
- [156] A. Broniatowski et al., *NIM A*, **559**, 378 (2006).
- [157] A. Broniatowski et al., submitted to *Phys. Lett. B*, arxiv:0905.0753v1 (2009).
- [158] O. Martineau, *Recherche de WIMPs par l'expérience EDELWEISS : caractérisation des détecteurs et analyse de données*, thèse de doctorat, Université Lyon 1, France (2002).
- [159] V. Chazal et al., *Astropart. Phys.*, **9**, 163 (1998).
- [160] S. Fiorucci, *Acquisition et analyse des données pour l'expérience de recherche de matière noire EDELWEISS*, thèse de doctorat, Université Paris XI, France (2005).
- [161] S. Scorza, *EDELWEISS-II, direct Dark Matter search experiment: First data analysis and results*, thèse de doctorat, Université Lyon I, France (2009).
- [162] ROOT, *ROOT / A Data Analysis Framework*, <http://root.cern.ch/> (1995-2009).
- [163] *Bolometer monitoring* available within the LSM firewall at <http://lsmmc11.in2p3.fr/~acquis/monitoring>
- [164] A. de Bellefon et al., *Astropart. Phys.*, **6**, 35 (1996).

- [165] M. L'Hour, *Rev. Archeol. Ouest*, **4**, 113 (1987).
- [166] L. Chabert, *Étude du bruit de fond neutron induit par les muons dans l'expérience EDELWEISS-II*, thèse de doctorat, Université Lyon I, France (2004).
- [167] A. Chantelauze, in *Proceedings of SUSY07 Karlsruhe*, arXiv:0710.5849v1 (2007).
- [168] B. Armbruster et al., *Phys. Rev. D*, **65**, 112001 (2002).
- [169] J. Reichenbacher, *Untersuchung der optischen Eigenschaften grossflächiger Plastiksintillatoren für den KARMEN-Upgrade*, Diplomarbeit, Universität Karlsruhe (TH), Germany (2004).
- [170] F. Habermehl, *Entwicklung der Datenaufnahme und Tests der Vetomodule für das EDELWEISS II  $\mu$ -Vetozählersystem*, Diplomarbeit, Universität Karlsruhe (TH), Germany (2004).
- [171] *Muon veto monitoring* available at the password protected website <http://www-ik.fzk.de/~edelweiss>
- [172] R. Lemrani, G. Gerbier et al., *J. Phys. Conf. Ser.*, **39**, 145 (2006).
- [173] E. Yakushev, *Monitoring of the thermal neutron flux in the LSM underground laboratory*, paper in preparation.
- [174] G.S. Vidyakin et al., *Instruments and experimental techniques*, **32(4)**, 809-12 (1989).
- [175] H. Kluck, *Aufbau und Test eines Prototyp-Neutronendetektors für das EDELWEISS Experiment*, Diplomarbeit, Universität Karlsruhe (TH), Germany (2007).
- [176] V. Yu. Kozlov for the Edelweiss Collaboration, in *Proceedings of IDM2008 Stockholm*, arXiv:0902.4858v1 (2008).
- [177] X. F. Navick for the Edelweiss Collaboration, *Proceedings of AIP Conference*, **897**, 65 (2007).
- [178] S. Yellin, *Phys. Rev. D*, **66** 032005 (2002).
- [179] A. Benoit et al., *Phys. Lett. B*, **616**, 25 (2005).
- [180] R. Trotta, F. Feroz, M.P. Hobson, L. Roszkowski, R. Ruiz de Austri, *JHEP 08*, **12**, 024 (2008)
- [181] E. A. Baltz and P. Gondolo, *JHEP 04*, **10**, 052 (2004).
- [182] E. A. Baltz and P. Gondolo, *Phys. Rev. D*, **67**, 063503 (2003).
- [183] R. Gaitskell and J. Filippini, *An interactive plotter for experimental and theoretical data*, <http://dmtools.berkeley.edu/limitplots/> (2007).

- 
- [184] O. M. Horn, *Simulations of the muon-induced neutron background of the EDELWEISS-II experiment for Dark Matter search*, PhD thesis, Universität Karlsruhe (TH), Germany (2007).
- [185] Ch. Berger et al, *Phys. Rev. D*, **40**, 2163 (1989).
- [186] GEANT4, *Geant4: Physics Reference Manual*, Geant4 collaboration: online publication, (2007).
- [187] M. Gros, *News of the acquisition system*, collaboration meeting (Oct. 2008).
- [188] S. Scorza, *Analysis of the data from the 8<sup>th</sup> EDW-II cool down, November 2007-March 2008*, technical note (Jul. 2008).
- [189] V. Sanglard, private communication, (Jul. 2009).
- [190] G. Gerbier and M. Gros, private communication, (Jul. 2009).



## Investigation of the muon-induced background of the EDELWEISS-II experiment

The EDELWEISS experiment aims to detect WIMPs, weakly interactive massive particles, which could possibly amount for all or part of the dark matter in the universe. It measures the energy released by nuclear recoils produced by the elastic collision of a WIMP in an ordinary matter target. Due to the very small interaction cross-section of WIMP with nucleons, which leads to an extremely low expected event rate ( $< 1$  event/kg/year), and due to the relatively small deposited energy ( $< 100$  keV), the nuclear recoil signal of WIMP events can be mimicked by neutrons coming from natural radioactivity or induced by muons. The present work is devoted to study the muon-induced background. Performances of the muon veto of the EDELWEISS-II experiment are presented and detection of muons and showers discussed. The first muon veto-bolometers coincidences has been performed on two 4-month physics runs in 2007 and 2008 and leads to a result of  $0.043 \pm 0.015$  coinc/kg/d for a recoil energy  $E_R < 250$  keV.

---

## Étude du bruit de fond induit par les muons dans l'expérience EDELWEISS-II

L'expérience EDELWEISS a pour but de détecter des WIMPs, particules massives faiblement interactives, qui pourraient composer la matière noire de l'univers. Elle mesure l'énergie libérée lors de la collision élastique d'un WIMP sur un noyau de matière ordinaire. Du fait de sa très faible section efficace d'interaction, qui conduit à un taux d'évènement extrêmement bas ( $< 1$  evt/kg/an), et du fait du faible dépôt d'énergie ( $< 100$  keV), le signal de recul nucléaire des WIMPs peut être imité par des neutrons de la radioactivité ambiante ou induits par des muons. Cette thèse est dédiée à l'étude du bruit de fond induit par les muons. Les performances du veto muon de l'expérience EDELWEISS-II sont présentées et la détection des muons et de leur gerbes discutés. Les premières coïncidences entre le veto muon et les bolomètres ont été réalisées sur deux prises de données de 4 mois de 2007 et 2008 et conduisent à un résultat de  $0.043 \pm 0.015$  coinc/kg/j pour une énergie de recul de  $E_R < 250$  keV.